Bergische Universität Wuppertal
Fachbereich Mathematik und Naturwissenschaften
Fachgruppe Physik

Future polar ozone: predictions of Arctic ozone recovery in a changing climate

Dissertation

vorgelegt von
Diplom Umweltwissenschaftler

Carsten Lemmen

WUB-DIS 2005-04

Erster Gutachter: Prof. Dr. Martin Riese
Zweiter Gutachter: Priv. Doz. Dr. Martin Dameris
Tag der Abgabe: 30. März 2005
Tag der Disputation: 31. Mai 2005

Abstract

Possible recovery of the polar stratospheric ozone layer has previously been assessed with a variety of chemistry climate models (CCMs). With a decreasing load of ozone-depleting substances (ODS), a recovery of Antarctic ozone columns to pre-1980 conditions is expected somewhere around 2050, while Arctic ozone is predicted to recover much earlier. This hemispheric difference is due to the generally warmer and more disturbed North Polar winter vortex. It is unclear, however, whether the net effect of Climate Change leads to a cooling or warming of the Arctic winter polar vortex. It is uncertain, how increasing amounts of greenhouse gases affect the evolution of the ozone layer, which is tightly coupled to the prevailing stratospheric temperature through the formation of polar stratospheric clouds.

On the one hand, the North Polar stratosphere is projected to warm due to additional energy dissipated by planetary and gravity waves. These waves are triggered by tropospheric meteorology, which may be influenced by ongoing climatic changes, for example, regional changes in surface temperatures. On the other hand, the radiative effect of most greenhouse gases which leads to a warmer troposphere cools higher atmospheric layers. Cloud formation depends critically on threshold temperatures, and activation of ODS depends on the availability of surfaces provided by cloud particles.

The prediction of Arctic polar ozone with climate models is difficult given the complex interactions of climate change, stratospheric temperature and ozone depletion. In this thesis, based on a multi-annual CCM time slice experiment with year 2015 boundary conditions, deficiencies, analysis methods and improvements for the assessment of future polar ozone loss are examined. The chemistry transport model CLaMS is employed in combination with the tracer-tracer correlation technique. Dynamical changes to the 2015 ozone column are isolated from chemical changes. Updates to CCM results for springtime Arctic minimum ozone columns and new results for maximum ozone loss columns for 2015 conditions are presented. Recommendations for verification of ozone loss chemistry and the calculation of chemical ozone loss are provided for post-analysis of already performed CCM simulations.

CLaMS simulations show that around 2015 northern hemispheric ozone depletion may be as severe as observed and modelled in medium to cold 1990s winters: at 19 km altitude, up to 1.85 ppm chemical ozone loss is predicted in the polar vortex. Chemical column ozone depletion of 85 Dobson units (DU) is found, while corresponding CCM results show less than 50% of this loss. The apparent recovery of Arctic ozone in the CCM is attributed to dynamical changes rather than decreased stratospheric halogen loading. The new prediction for the 2015 springtime minimal ozone column is 250 DU as opposed to 296 DU found by the CCM alone; from this analysis, there is no indication for Arctic ozone recovery within the next decade.

Zusammenfassung

Eine mögliche Erholung der polaren stratosphärischen Ozonschicht wurde bereits mit Klimachemiemodellen (CCM) untersucht. Bei fallenden Konzentrationen ozonzerstörender Substanzen (ODS) wird eine Erholung der antarktischen Ozonsäule zu Werten, die vor 1980 beobachtet wurden, um 2050 erwartet, für die Arktis wesentlich eher. Der hemisphärische Unterschied kann auf den allgemein wärmeren und gestörteren Nordpolarwirbel zurückgeführt werden. Unklar ist jedoch, ob Klimaänderungen zu einer Nettoabkühlung oder -erwärmung des arktischen Polarwirbels führen, und damit, wie ansteigende Treibhausgaskonzentrationen die Ozonschicht beeinflussen. Diese ist eng verknüpft mit der Stratosphärentemperatur und der Bildung polarer Stratosphärenwolken.

Einerseits wird eine Erwärmung des Nordpolarwirbels durch erhöhte Aktivität von planetaren als auch von Schwerewellen vorausgesagt. Diese Wellen werden durch troposphärische Meteorologie angeregt, welche selbst unter dem Einfluss gegenwärtiger Klimaänderungen stehen, wie zum Beispiel Änderungen der regionalen Temperaturverteilung. Andererseits führt derselbe Treibhauseffekt, der die Troposphäre wärmt, zu niedrigeren Temperaturen in höheren Atmosphärenschichten. Dort hängt die Wolkenbildung kritisch von Schwelltemperaturen ab und damit die Aktivierung ozonzerstörender Substanzen auf Wolkenteilchen.

Erschwert wird die Vorhersage des arktischen polaren Ozons in Klimamodellen durch komplexe Interaktionen von Klimaänderung, Stratosphärentemperatur und Ozonverlust. In dieser Arbeit werden anhand eines mehrjährigen CCM Zeitscheibenexperiments unter Randbedingungen für das Jahr 2015 Fehleranfälligkeit, Analysemethoden und Verbesserungen für die Untersuchung zukünftigen polaren Ozonverlusts vorgestellt. Hierzu wird das Chemietransportmodell CLaMS zusammen mit der Tracer-Tracer-Korrelationsmethode benutzt. Dynamische Änderungen an der Ozonsäule 2015 werden von chemischen Änderungen isoliert. Gegenüber dem CCM aktualisierte Werte für die minimale arktische Frühjahrsozonsäule und neue Werte für den maximalen Ozonverlust unter 2015 Bedingungen werden berechnet. Empfehlungen werden gegeben zur Verifizierung der Ozonverlustchemie und der Berechnung von Ozonverlust bei der nachträglichen Analyse bereits durchgeführter CCM Simulationen.

CLaMS Simulationen zeigen, dass um 2015 der nordhemisphärische Ozonverlust ähnlich stark sein kann wie er in mittelkalten Wintern der 90er Jahre beobachtet und simuliert wurde: auf 19 km Höhe werden im Wirbel bis zu 1.85 ppm chemischer Ozonverlust vorhergesagt. Ein chemischer Säulenozonverlust von 85 Dobson Einheiten (DU) wird festgestellt, während korrespondierende CCM Ergebnisse nur etwa 50% dieses Verlusts zeigen. Die anscheinende Erholung des arktischen Ozons im CCM wird auf dynamische Änderungen zurückgeführt, nicht auf den Rückgang der stratosphärischen Chlorbeladung. Als neue Vorhersage für die minimale arktische Frühjahrsozonsäule wird 250 DU berechnet wohingegen das CCM alleine 296 DU berechnete; innerhalb der nächsten Dekade gibt es anhand dieser Berechnungen keinen Anhaltspunkt für eine Erholung des arktischen Ozons.

Table of Contents

1 Motivation

"Climate change means a change of climate which is attributed directly or indirectly to human activity that alters the composition of the global atmosphere and which is in addition to natural climate variability observed over comparable time periods."
(UNFCCC, 1992)

"Future scientific questions that might be linked to the fate of the ozone hole include whether global warming will begin to affect ozone depletion, whether the Arctic stratosphere will change to be more like the Antarctic in coming centuries; and how possible changes in the atmospheric concentration of methane or nitrous oxide might affect ozone-hole chemistry."
(Solomon, 2004)

1.1 Ozone and Climate Change

Samples of air preserved in ice cores show that global temperature and atmospheric abundance of gases like carbon dioxide and methane were highly variable over the last 400 000 years. Until 100 years ago, methane and carbon dioxide abundances remained within confined ranges of 350–750 parts per billion by volume (ppb) and 180–310 parts per million (ppm), respectively (Petit et al., 1999).

At least since the large-scale transformation of natural landscapes into farm and crop land which started as early as 8 000 years ago, human activity has been influencing the global carbon cycle: Ruddiman (2003) argues that atmospheric levels of methane (CH_4) and carbon dioxide (CO_2) had been raised anthropogenically by 250 ppb and 40 ppm, respectively before 1850.

With the advent of fossil fuel burning in the 19th century, a new level of global anthropogenic influence on climate had been reached. Emissions of CO_2, an important greenhouse gas[1] (GHG) second to water, started to increase in industrialised areas from 1850. Tyndall (1861) found that carbon compound vapours absorbed large amounts of thermal radiation; much lesser absorptivity was found for ozone (O_3). By 1896, Arrhenius had calculated the greenhouse effect of CO_2 and predicted that a doubling of atmospheric CO_2 content would lead to a (fortuitous) temperature increase of 6°C in northern mid-latitudes (Arrhenius, 1896).

Though Högbom (1894) had long before argued that the atmospheric concentration of CO_2 was variable due to volcanic sources, concern about a trend was first issued by Revelle and Suess (1957). They noted that human emissions exceeded oceanic uptake and that CO_2 would thus accumulate in the atmosphere. Measured evidence of CO_2 enrichment was provided by Keeling (1960). The CO_2 trend has been confirmed by many observations (IPCC 2001 and references therein); in 1998, the CO_2 loading in the troposphere reached 370 ppm.

With the First World Climate Conference in 1979, climate change was recognised as a potentially serious problem: international cooperation to investigate the effect of changing climate on human activities was initiated under the direction of the World Meteorological Organisation (WMO) and United Nations Environment Programme (UNEP). Political and scientific efforts of the 1980s culminated in the First Assessment Report of the Intergovernmental Panel on Climate Change (IPCC, 1990)[2] and the United Nations Framework Convention on Climate Change (UNFCCC, 1992) where several countries agreed to reduce their national greenhouse gas emissions to 1990 levels by 2000.

In March 1994, the UNFCCC entered into force; in the Second Assessment Report by the IPCC (1995) stated: "the balance of evidence suggests that there is a discernible human influence on global climate". Most recently, the Third Assessment Report tells of "evidence stronger than ever before" for human influence on climate (IPCC, 2001). A 5% reduction of collective emissions of six GHGs was stipulated in the Kyoto Pro-

[1] Gases that absorb and re-emit infrared radiation; the greenhouse effect ("effet de serre") was described by Fourier (1824) based on prior experiments with staggered bell jars.

[2] The panel itself was established in 1988.

tocol (UNFCCC, 1997), which entered into force on February 16, 2005. Examples of negative consequences of ongoing climate change are sea level rise, increased occurrence of extreme weather events and changed rainfall patterns (IPCC, 2001). On the other hand, past anthropogenic warming may have prevented widespread glaciation that could be expected due to orbital forcing (Ruddiman et al., 2005).

While human activities have merely increased the atmospheric burden of GHG like CO_2, N_2O and CH_4, a wholly anthropogenic class of molecules was released to the atmosphere from the 1940s on: halogenated hydrocarbons, which are chemically inert to troposphere available ultraviolet radiation and oxidation by OH radicals. Chlorofluorocarbons (CFC), methyl chloroform, halons (bromine containing halocarbons), methyl chloride (partly biogenic), and other halogenated hydrocarbons proved valuable as propellants and refrigerants, for isolation and foam-blowing. Most widely used were CFC-11 ($CFCl_3$) and CFC-12 (CF_2Cl_2); these gases are the only absorbers in the so-called atmospheric window, a spectral band between 8–13 μm wave length and thus are very potent GHGs despite their lower concentration compared to water (H_2O) or CO_2 (e.g. Forster and Joshi, 2005).

All GHGs except for water and ozone are well-mixed in the troposphere and enter the stratosphere almost unaffected by transport through the tropical tropopause. At higher altitudes, more energetic photons and atomic oxygen are available which break down these long lived compounds to mainly H_2O, carbon monoxide (CO), nitrogen oxides (NO_x), and hydrogen halogenides.

Direct changes from GHG emissions have been observed in the chemical composition of the stratosphere: most notably (a) the introduction of halogen compounds in significant amounts (e.g. Engel et al., 1998), and (b) an increase in water vapour (Oltmans et al., 2000). Increased chlorine levels in the stratosphere were expected to adversely effect stratospheric ozone in radical reactions involving atomic chlorine (Cl) and chlorine monoxide (ClO, Molina and Rowland, 1974). In a model study, Crutzen (1974) found that Cl and ClO amounts expected from anthropogenic chlorine could be responsible for up to 40% local ozone destruction at 40 km altitude, where the required reactand atomic oxygen is abundant (a profile of atomic oxygen is shown in Figure 2.4 on page 20). Observations confirm high-altitude stratospheric ozone depletion due to chlorine catalysis for mid-latitudes (e.g. Weiss et al., 2001).

For the O_3 column, Crutzen (1974) calculated a worst-case effect of less than 10%: the thickness of the ozone layer[3], which protects the surface of the Earth from harmful ultraviolet radiation, should have been reduced only slightly. However, in 1985, Farman et al. published observations of the total column over Halley Bay, Antarctica, showing that in the early 1980s the October column was lower than the March column. This had not ever been observed in their pre-1973 long-term data. By plotting tropospheric values of CFC-11 together with appropriately scaled austral spring ozone column values, they suggested a relationship between the increase of chlorofluorocarbon loading and the decrease of the polar ozone column.

Farman et al.'s finding that the austral spring ozone column was declining was cor-

[3] all ozone above the planetary boundary layer (UNEP, 1985)

roborated by satellite observations from TOMS (Total Ozone Mapping Spectrometer) and SBUV (Solar Backscatter UV) instruments on the Nimbus 7 satellite (Stolarski et al., 1986). These observations showed a "hole" in Antarctic ozone columns[4], which could be dated back as far as 1980.

An explication of the measurements by (Farman et al., 1985) required at least that all inorganic chlorine (Cl_y) in the lower stratosphere was in the form of reactive Cl and ClO. The chemical mechanisms to activate the chlorine reservoir species hydrogen chloride, chlorine nitrate and hydrochloric acid were uncovered in 1986: Solomon et al. (1986) found that ozone depletion was largest in the lower stratosphere at altitudes around 15–20 km were polar stratospheric clouds (PSC) were frequently observed and proposed heterogeneous reactions for conversion of reservoirs to active chlorine. The condensation of nitric acid (HNO_3) and H_2O makes possible the formation of cloud surfaces on which heterogeneous reactions take place (Crutzen and Arnold, 1986). Toon et al. (1986) further found that the condensation of HNO_3 removes NO_x from the gas phase, thus prolonging ClO_x activity. Further, catalytic ozone destruction cycles involving halogens but not requiring atomic oxygen were proposed by Solomon et al. (1986), McElroy et al. (1986), and Molina and Molina (1987).

The Antarctic ozone hole and severe depletion of ozone in Arctic spring are seasonal phenomena, but also global mean total column ozone has decreased by 3% during the last two decades (Fioletov et al., 2002). This relative decrease is consistent across observations from satellites, ground based observations and assimilated model data. The strongest global trend is seen in southern hemisphere high latitudes, while no significant trend is found for tropical data. Reconstructions of UV surface irradiance show a relative increase of 6%–14% over the last 20 years; half of this trend can be attributed to changes in total ozone, other important factors are changes in clouds and surface albedo (WMO, 2003).

Crutzen had cautioned in 1974 that the effects of CFC release might be observed in the stratosphere with a lag time of 50–100 years and that the possible role of aerosols was uncertain. Based on the evidence that became public in the first half of the 1980s and a political declaration towards ozone layer protection (UNEP, 1985), the Montreal Protocol on Substances that Deplete the Ozone Layer was agreed upon in 1987 (UNEP, 1987): The signatories agreed on a 50% CFC reduction within 13 years. Amendments and adjustments to the Montreal Protocol were made in London (1990), Copenhagen (1992), and Beijing (1999). In London, more than 80 countries agreed to include halons in the Montreal protocol and to discontinue CFC use by 1999; in Copenhagen, the CFC ban was preponed to 1996 and a collective limit on halogenated CFC was agreed upon (Rowlands, 1993). As a result, the burden of ozone depleting substances (ODS) in the stratosphere will be reduced to one third of the present day value within 100 years. The effect of regulation on the expected future stratospheric ODS burden is shown in Figure 1.1.

The effect of emission control became visible as a turnaround of tropospheric CFC

[4]The ozone hole was defined later as the poleward region enclosed by the 220 Dobson unit contour (WMO, 1990).

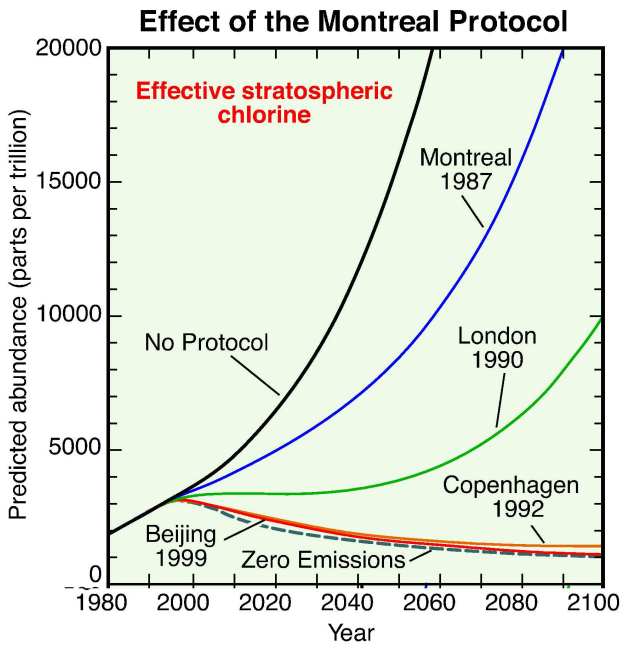

Figure 1.1: Effects of international amendments to and adjustments of the Montreal protocol. From emission scenarios based on the various agreements, predictions for effective equivalent stratospheric chlorine (the equivalent of all ODS in terms of chlorine) show a peak around 1998 and a gradual decrease to values around 1 ppb by 2100 (WMO, 2003).

loading around 1994 (Montzka et al., 1996). To quantify the combined effect of ODS, the term effective equivalent chlorine (EECl) was defined, which accumulates all ODS in terms of chlorine abundance weighted with their ozone destruction potential (ODP). Bromine compounds, for example, are weighted with a factor around 50 due to their higher ODP with respect to chlorine. A lag time of 3–3.5 years has to be added to EECl to quantify stratospheric loading EESC (effective equivalent stratospheric chlorine). The effect on polar ozone depletion lags release by about five years and, in fact, a stagnation of lower stratospheric chlorine loading has been noticed (e.g. Engel et al., 2002).

Hydrochlorofluorocarbons (HCFC) have replaced fully halogenated compounds in many applications; HCFC do have a large ODP but their chemical life time is reduced by an order of magnitude compared to CFC (WMO, 2003). HCFC can only temporarily serve as substitutes for CFC in applications where more "ozone-friendly" chemicals (e.g. butane, propane) are not yet available (Rowlands, 1993). Successfully, hydrofluorocarbons (HFC) like HFC-134a (CH_2FCF_3) replace CFC in refrigeration, air-conditioning and aerosols. Though not directly harmful to the ozone layer, the substitutes may still contribute to global warming (e.g. Forster and Joshi, 2005).

1.2 Interactions

Although effective equivalent stratospheric chlorine (EESC) is expected to decrease slowly in the future (cmp. Figure 1.1), a recovery of stratospheric ozone may be complicated by (a) a change in water vapour content throughout the stratosphere or (b) a temperature decrease in the lower polar stratosphere. Both water vapour increase and

temperature decrease facilitate the existence of polar stratospheric clouds and lead to more ozone depletion (Kirk-Davidoff et al., 1999). Uncertain in sign and magnitude are the (c) effects of changing dynamics on stratospheric ozone, which makes the prediction of future stratospheric ozone difficult.

Observations of water vapour show an increase of about 1% per year since 1979 from balloon experiments above Boulder, Colorado (Oltmans et al., 2000, altitude range 16-28 km). Since the middle 1950s, lower stratospheric water vapour mixing ratio may have increased by as much as 2 ppm (30–50% SPARC, 2000); however, only up to 50% of the observed increase in lower stratospheric water vapour can be explained by the increase in methane (SPARC, 2000). Röckmann et al. (2004) show how the increased oxidation of methane by enhanced chlorine humidifies the stratosphere. Other factors like an increased activity of the tropospheric hydrological cycle or changes in stratosphere to troposphere transport (STT) may be important: for example, radiation calculations by Forster and Joshi (2005) show that increasing CFC amounts should raise, all other things being equal, the cold point temperature (CPT) at the tropical tropopause by 0.4 K. A higher CPT may lessen the efficacy of the cold trap which removes water from ascending air masses in the tropics. In radio sonde observations from 1973 to 1998, Zhou et al. (2001) find a cooling trend of -0.57°C per decade at the tropical tropopause. A recent analysis of satellite observed water vapour by Randel et al. (2004) stresses that there are unresolved issues in the water vapour trend: measurements from HALOE (Halogen Occultation Experiment) and POAM (Polar Ozone and Aerosol Measurement) instruments show a stagnation or decrease of lower stratospheric water vapour since 1997, which may be related to changes in the solar cycle.

Measurements of stratospheric temperature from satellites and radiosondes show significant cooling in the upper stratosphere up to 2 K per decade from the late 1970s on; in the lower stratosphere, the cooling trend is not as strong and confined to middle and high latitudes, while in the tropics, no significant trend has been detected (WMO, 2003). The northern extra-tropical trend is shown in Figure 2.12 in Section 2.4.2 based on Microwave Sounding Unit (MSU) measurements from the late 1950s, exhibiting lower stratospheric cooling of more than 1 K. The more well mixed greenhouse gases (WMGHG, i.e. CO_2, CH_4, N_2O, halocarbons) are probably responsible for most of the observed upper stratospheric cooling (WMO, 1999); increases in stratospheric water vapour may also have contributed to the observed cooling of the mid- to high latitude stratosphere on the same order as ozone depletion (Forster and Shine, 1999). The lower stratosphere cooling is attributed mainly to global ozone decline (e.g. Shine et al., 2003).

A model study by Langematz et al. (2003) confirms that past lower stratospheric northern hemispheric cooling can be partly explained by ozone depletion. The lower temperatures in their simulations lead to a longer lifetime of the Arctic vortex on the order of 7–8 days. Prolonged vortex life time of 15 days between the 1980s and 1990s was attributed by Waugh and Randel (1999) to a decrease of vertical wave propagation into the stratosphere. There may be a positive feedback mechanism as ozone itself is a source of heat in the stratosphere: when the stratosphere is depleted of ozone,

less heat is absorbed by ozone, which increases the potential for PSC occurrence and ozone depletion.

In 1992, Austin et al. reported the possibility of an Arctic ozone hole due to increases of CO_2. Shindell et al. (1998) modelled the effects of GHG changes on ozone loss: radiatively lowered polar temperatures increase the latitudinal temperature gradient and lead to intensification of the polar vortex low-pressure system; this in turn decreases the frequency of stratospheric warming events and stabilises the vortex. Up to 50% increased Arctic column ozone loss was calculated for a lower stratospheric temperature decline by 7 K. While an intensification of Arctic ozone loss is also predicted by a study based on empirical data by Knudsen et al. (2004), Shindell et al.'s prediction of maximum Arctic ozone loss between 2010 and 2019 has been criticised because of the relatively low spatial resolution of their model; more recently there is consensus among many chemistry climate models (CCM) that there will be no significant change over the next decade in Arctic ozone (Austin et al., 2003).

One of the first general circulation models that include a comprehensive chemistry scheme is the ECHAM3.DLR(L39)/CHEM model (succeeded by E39C, see detailed description in Section 3.1) operated by the Deutsches Zentrum für Luft- und Raumfahrt in Oberpfaffenhofen, Germany. In a CCM, changes in atmospheric composition due to chemical reactions are included; these changes in atmospheric composition have a feedback on the underlying circulation model by altering the radiative properties of the atmosphere and thus changing the distribution of heat sources and sinks. The distribution of heat is the dominant driving force for the global circulation (cmp. Section 2.2), and the global circulation model. A great technical challenge in chemistry climate modelling is the parameterisation of chemical reactions to long enough numerical time steps that allow for multi-annual simulation experiments.

GCMs simulate consistent states of the atmosphere together with their corresponding internal dynamics. The specific state simulated by a GCM depends on boundary conditions, provided as prescribed fluxes across the domain boundaries of the model or introduced at locations within the model domain. Common lower boundary conditions for atmospheric GCMs are global fields of sea surface temperature (SST) and surface emissions of chemical compounds to the atmosphere; a typical upper boundary condition is the solar flux received at the model top. Prescribed tracer or temperature fields, for example from observations, may also be introduced during a GCM simulation which drives the GCM simulated atmosphere towards the observed atmosphere, this process is called 'nudging'. The most constrained circulation models are found in numerical weather prediction (NWP), where observational data is continuously fed into the model. When rich sets of observational data are not available, e.g. for the simulation of past and future climates, a GCM may be equilibrated to a current known state of the atmosphere: Given a set of boundary condition (from observations or projections), the model is then allowed to evolve forwards or backwards in time; these types of simulations are termed transient and provide a view of a single possible temporal evolution of the atmosphere.

While NWP models try to simulate the real atmosphere, GCMs can be used to simulate rather a realistic (past, future, present) atmosphere in terms of mean state,

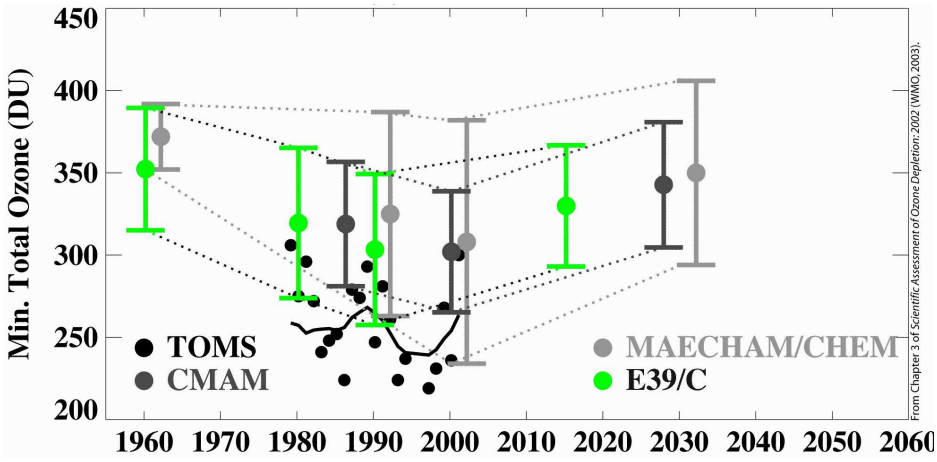

Figure 1.2: Spring Arctic minimum ozone column from a variety of GCM simulations. The four highlighted experiments were performed with a special version of the ECHAM4 model. Of these four, the last experiment shows ozone recovery as early as 2015 (WMO, 2003, updated).

trend, and variability (U. Langematz, personal communication, 2005). If the internal dynamics of a GCM reproduces current climate when provided with a set of current fixed boundary conditions, the same GCM may be used to simulate future climate based on a set of future boundary conditions. The repetitive (usually annually periodic) prescription of one boundary condition for a multi-annual simulation is termed a time slice experiment. Results for the spring Arctic minimum ozone column (AMOC) from time slice experiments simulated with various CCMs are shown in Figure 1.2. This figure includes satellite observations of AMOC and the results from four time slice experiments with the E39C model which are shown in green colour. E39C simulates a decrease of the AMOC from 1960 to 1990, and an increase from 1990 to 2015. This increase is evaluated in WMO (2003) and Austin et al. (2003) as a first sign of possible ozone recovery; this recovery by 2015 is in contrast to predictions of further decreasing ozone by Shindell et al. (1998) and Knudsen et al. (2004); other models simulate no significant change of Arctic ozone by 2020. Based on all model simulations, recovery to 1980 values is predicted in the time frame 2020–2060 (WMO, 2003).

In contrast to CCMs, chemistry transport models (CTMs) simulate the chemistry in more detail, but depend on external meteorological fields from NWP models or GCMs; the results of chemical calculations do usually not feed back into the base GCM. The time period routinely simulated with CTMs is much shorter: for polar stratospheric studies, the integration time is on the order of weeks to a few months. One of the first applications of stratospheric CTMs was presented by Austin et al. (1987) who calculate photochemical reactions in a box which is advected along a trajectory. This box model concept has been extended to multiple trajectories (e.g. Austin et al., 1992; Müller, 1994) and more than 100 000 trajectories (Grooß et al., 2005). Other CTMs calculate chemical reactions on numerical grids that are used in GCMs as well, for example SLIMCAT (Sinnhuber et al., 2000), or REPROBUS (Lefèvre et al., 1998).

The combination of a CCM with a CTM makes possible the calculation of detailed chemistry in a hypothetical future atmosphere. This approach is followed in this thesis, where the CTM CLaMS (McKenna et al., 2002b,a) is operated on the CCM E39C (Hein et al., 2001).

1.3 Aims of this study

Subject of this thesis is the calculation of chemical ozone loss on existing chemistry climate model (CCM) data and its usage for future ozone loss predictions. While changes in ozone are routinely reported for CCMs, for example, as the minimum Arctic spring ozone column (e.g. Austin et al., 2003), the separation of ozone changes due to chemistry from dynamically induced changes is not trivial. With the help of a chemistry transport model (CTM), validity of chemical ozone loss predictions in a CCM is examined. The validation is performed on two so-called time slice experiments from the ECHAM4.DLR(L39)/CHEM (hereinafter referred to as E39C) CCM. The methodology presented in this thesis can, however, be easily extended for validating other CCMs. This effort is in line with recent efforts by Eyring et al. (2004) to establish a framework for the validation of coupled CCMs.

The purpose of this study is threefold. Firstly, chemical ozone loss is analysed for all winters of the E39C time slices 1990 and 2015 with the tracer-tracer correlation technique (e.g. Tilmes et al., 2004a, TRAC). By comparison with total ozone loss the residual ozone change is attributed to dynamical processes. The magnitudes of chemical and dynamical contributions to stratospheric ozone changes from 1990 to 2015 can be assessed in view of changes in the chemical composition of the stratosphere.

Secondly, chemical ozone loss in the CTM CLaMS is calculated with two different methods, (a) TRAC and (b) a passive ozone tracer (e.g. Chipperfield and Pyle, 1998), where the CTM is driven by E39C simulated meteorology. Application of TRAC to model data has attracted criticism (e.g. Sankey and Shepherd, 2003); by comparison with ozone loss calculations obtained with the passive ozone tracer method the validity of the tracer-tracer correlation method is assessed. E39C chemical ozone loss is compared to CLaMS ozone loss. Differences between the two calculations are explored with sensitivity studies on numerical model parameters like horizontal resolution, mixing intensity and sedimentation rate.

As a third goal, the more realistic simulation of future Arctic ozone loss and Arctic minimum ozone columns (cmp. Figure 1.2) is attempted with CLaMS calculations on a cold winter of the time slice 2015. This winter exhibits the largest ozone loss within the 20 winter ensemble of the time slice. CLaMS calculations consider two different but realistic assumptions for stratospheric bromine loading; ozone depletion due to bromine was not considered in the E39C simulations. Further, Arctic ozone loss for scenarios at various stages of the Montreal process is calculated, based on suggestions by Prather et al. (1996) and S. Solomon (personal communication, 2004).

1.4 Outline

Chapter 2 provides a description of the dynamics and chemistry of the stratosphere. Dynamical features of the stratosphere are explained with a focus on the formation of the polar vortex and meteorological properties within the vortex. The section on stratospheric chemistry focuses on the production and loss cycles of ozone and species related to ozone chemistry. Reactions on surfaces (heterogeneous reactions), which transform reservoirs of ozone depleting substances to their active radicals are introduced. Stratospheric chemistry and dynamics in this thesis are investigated in the frame of climate change. A short overview of past, ongoing and expected future climate changes is given, along with established and possible links to stratospheric ozone.

Version E39C of the global circulation model ECHAM and the chemistry transport model CLaMS are described in Chapter 3. While the main data for this thesis are E39C data, multiple experiments are performed with CLaMS driven by E39C results. These experiments are used to assess chemical ozone loss in the CCM; sensitivity studies are designed to look further into possible shortcomings of the CCM in comparison to the CTM. Different methods of chemical ozone loss calculations are presented of which the passive ozone tracer technique and the tracer-tracer correlation method are employed to estimate ozone loss throughout this thesis.

Chemical ozone losses determined for E39C time slices 1990 and 2015 are given in Chapter 4, along with data on minimum spring Arctic ozone columns in these time slices. The later Chapters 5–7 deal with CTM simulations on a specific cold winter of time slice 2015, which is used as a "worst case" (in terms of expected future ozone loss) scenario. Dynamical features of this winter and their relevance for ozone loss determination are discussed in Chapter 5. Formation of polar stratospheric clouds, isolation of the vortex and the establishment of tracer-tracer correlations is examined; denitrification for CLaMS and E39C is calculated.

Chapter 6 considers the polar stratospheric chemistry during one cold 2015 winter with an emphasis on chemical ozone loss and its sensitivities to halogen loading, vortex isolation, and model numerics. A detailed report from the findings on the applicability of TRAC to global climate model data is given.

A further discussion of future ozone loss is provided in Chapter 7. It is shown that within the model uncertainties found, a recovery of Arctic polar ozone due to the reduction of CFC is not evident in the 2015 time slice. Updated results for predictions of polar ozone loss are discussed in view of estimates of future ozone loss reported in the literature. Prospective applications of the methodology developed in this work are outlined. The main text concludes with the major findings of the thesis summarised in Chapter 8.

2 The stratosphere

Earth's atmosphere extends from the surface to a couple of hundred kilometres altitude, of which the upper atmosphere is characterised by free electrons, increasing temperature with height and the separation of atoms, ions and molecules by mass (the thermosphere or heterosphere). Below about 100 km, the homosphere consists mostly of molecules whose distribution is independent of mass but rather governed by the location of sources and sinks, and transport regimes. This middle and lower atmosphere is commonly differentiated into the mesosphere, the stratosphere, and the troposphere, each one characterised by its distinct temperature profile with altitude and each two separated by reversals of the temperature profile called pauses. The troposphere contains about 80% of the mass of the atmosphere, the stratosphere another 19.9% (Wells, 1997).

2.1 Structure

Emission of long wave radiation to space cools the mesosphere (bounded at the top by the mesopause at 85–90 km altitude) and provides for a negative temperature gradient with altitude; absorption of short wave radiation in the stratosphere creates a positive temperature gradient and promotes vertical stability within this layer of the atmosphere between the tropopause (at 10–16 km altitude, 100–200 hPa) and the stratopause (at ≈ 50 km altitude, 1 hPa). From the surface to the tropopause extends the troposphere, characterised by decreasing temperature with altitude, tropical convection, weather systems and the hydrological cycle. The troposphere lower part, the planetary boundary layer, is the most important interface between the atmosphere and other domains of the Earth system, such as the cryosphere, land surface, and oceans; most of the anthroposphere is located within or at the lower boundary of the troposphere; there are several studies on direct stratosphere-anthroposphere interaction (e.g., by aircraft NO_x emissions, Dameris et al., 1998). Figure 2.1 shows an example of the zonal mean temperature vs. pressure from the E39C climate model: the temperature reversal at the tropopause, the decreasing (increasing) temperature profile with altitude in the troposphere (stratosphere), and the very cold tropical tropopause are evident in this simulation[1]. A typical temperature profile is shown in Figure 2.4 on page 20 which relates the temperature structure of the atmosphere to pressure and geometric altitude.

[1]Both Figures 2.1 and 2.2 are based on a model simulation which may not necessarily agree with real atmospheric conditions in detail. For comparison, an ozone climatology based on observations is shown in Figure 2.5.

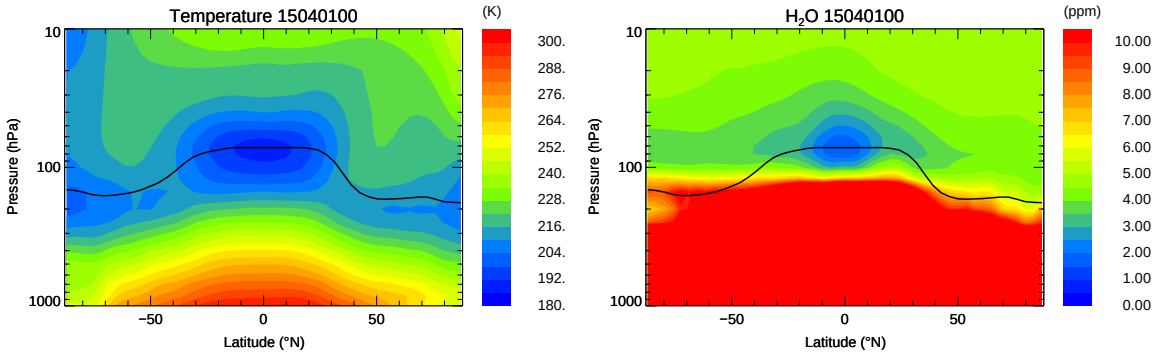

Figure 2.1: Exemplary zonal distribution of temperature **(left)** and water vapour mixing ratio **(right)** in April. The black line shows the temperature minimum. Data based on a 2015 simulation with the E39C chemistry climate model.

2.2 Dynamics

Stratospheric dynamics is largely controlled by the radiation budget within the stratosphere and wave forcing emanating from the troposphere. In addition, stratospheric chemistry is driven by exchange processes across the tropopause and, to a much lesser extent, across the stratopause.

2.2.1 Large scale transport

The global heat budget of the Earth system is in equilibrium, i.e. the amount of energy received from the sun equals the total energy emitted by the Earth. However, there exists a strong meridional gradient in the heat budget, with more energy being received than emitted in low latitudes and a negative energy budget in polar regions. Oceanic and atmospheric transport mediate this gradient which is strongest between the equator and the winter hemisphere pole.

In the equatorial troposphere, warm air ascends, forming the inter-tropical convergence zone (ITCZ) and driving trade winds at the surface. Some of the rising air enters the stratosphere while being dried in the tropical tropopause layer (TTL, Folkins and Appenzeller (1996), some interpret this acronym as the tropical transition layer to emphasise the gradual change from tropospheric to stratospheric properties). It is still under debate, whether most of the water in the stratosphere enters throughout the tropics, over selected "stratospheric fountain regions", or by overshooting of convection cells (Sherwood and Dessler, 2001). The driest part of the atmosphere is the tropical tropopause layer, where most of the humidity is removed from the rising air masses by freeze-drying (Brewer, 1949). This is exemplified in Figure 2.1, where the global zonal mean water vapour distribution is shown: The driest region in the tropical tropopause corresponds to the coldest temperatures. There is irreversible mixing of tropospheric air into the extra-tropical lower stratosphere, as was shown, for example, by Hoor et al. (2004).

Within the tropical stratosphere, air masses ascend slowly and are zonally well

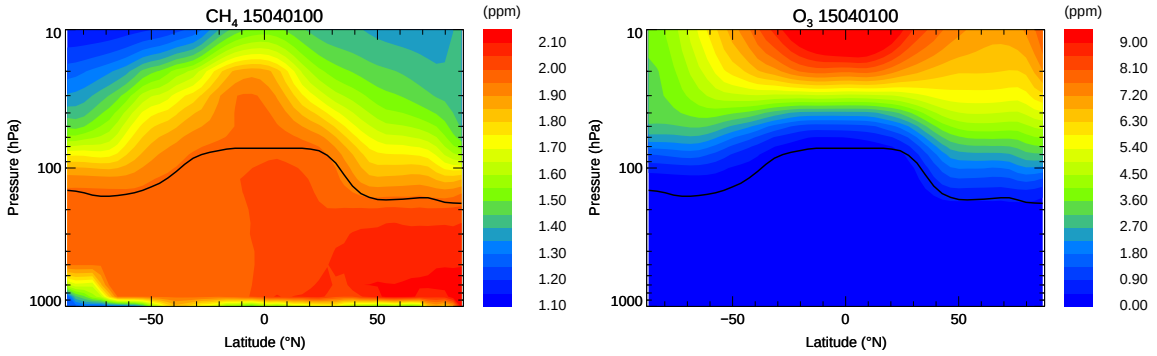

Figure 2.2: As Figure 2.1, but for methane **(left)** and ozone **(right)** mixing ratio.

mixed. There is reduced exchange with mid-latitude air, a so-called tropical pipe forms. Only at high altitudes, transport towards higher latitudes commences Holton et al. (1995). Due to radiative cooling the advected air masses lose heat and descend towards the polar tropopause where exchange is driven by intrusions and subsequent mixing of stratospheric with tropospheric air. The zonal mean transport of air by tropical rise and descent through the polar tropopause became known as the Brewer-Dobson circulation; it can be well illustrated by the distribution of a tracer with a tropospheric source and a stratospheric sink, such as N_2O or CH_4, biogenic molecules which are photolysed in the upper stratosphere. An example of the zonal mean distribution of CH_4 is shown in Figure 2.2 as simulated by the E39C chemistry climate model.

The location of transport barriers is illustrated by isopleths of tracer mixing ratio in altitude-latitude diagrams, for example the 1.72 ppm isopleth of CH_4 in Figure 2.2 (yellow colour): the near-vertical isopleth at 10°N shows the tropical pipe, the diagonal slope between 20–40°N and between 70–80°N the sub-tropical and polar mixing barriers, respectively; In the well-mixed, mid-latitude surf zone 40–70°N, the isopleth is flat (Plumb, 2002).

2.2.2 The lower-most stratosphere

The low temperature of the tropopause separates the troposphere from the stratosphere not only dynamically, but also chemically: the relatively wet upper troposphere (up to 4% water) is clearly distinguished from the dry stratosphere, where water volume mixing ratio is less than 8 ppm (cmp. Figure 2.1). Logan (1999) defines a chemical tropopause at O_3 mixing ratios between 80–150 ppb. In the lower-most stratosphere (LMS), bounded below by the tropopause and above by the 380 K potential temperature surface, a mixture of tropospheric and stratospheric air can be found in model data and in observations. Hoor et al. (2004) find tropospheric influence up to 20 K above the tropopause in mid-latitude CO measurements; M. Krebsbach finds a mixing layer extending 8–10 potential vorticity units (PVU, cmp. Section 2.2.5, personal communication, 2004) from the tropopause into the stratosphere with tracer relations between O_3 and H_2O. Relations between chemical species in the LMS may be different from relations above the 380 K isentrope, in the so-called overworld. In the LMS, the relationship between tracers that have a different source region are very different from the canonical relationships used for tracer correlations (cmp. Section 3.6.1). Stratosphere-troposphere exchange (STE) in the LMS is strongest in summer and weak in winter (C. Schiller, personal communication, 2004): for winter studies in the descending polar vortex it can be suspected that overworld tracer relations are dominant in the LMS, but no quantitative studies exist.

2.2.3 Stratospheric stability

The most important trace species in the stratosphere is ozone (O_3), which is the main absorber of solar radiation at wave lengths between 200 and 300 nm. Absorbed energy

is deposited in the stratosphere as heat, such that the temperature increases with altitude where more short wave radiation is available.

If temperature T increases with altitude z, the atmosphere is stably stratified. More exactly, if the vertical gradient of the potential temperature $\partial\theta/\partial z$ is greater than zero, a dry atmosphere attains static stability (Dessler, 2000). Potential temperature is a useful concept in meteorology and oceanography arising from the first law of thermodynamics:

$$c_p \, \mathrm{d} \, \ln T - R \, \mathrm{d} \, \ln p = 0 \tag{2.1}$$

where c_p is specific heat at constant pressure and R the gas constant of dry air. Dry air can be considered to good approximation as an ideal, diatomic gas, which makes $R/c_p = 2/7$ (e.g. Andrews et al., 1987). Integration of Equation (2.1) from surface pressure p_0 and temperature T_0 at p_0 to p, T yields

$$(T_0/T)^{c_p} = (p_0/p)^R \tag{2.2}$$

such that the temperature an air parcel at pressure p and temperature T assumes at pressure p_0 is given by $T_0 = \theta$

$$\theta = T \cdot (p_0/p)^{R/c_p} \tag{2.3}$$

On time scales of a few weeks, stratospheric motion is adiabatic, thus preserving potential temperature, and, from Equation (2.1) preserving entropy (Hoskins et al., 1985). Adiabatic motion is thus also referred to as isentropic motion and potential temperature levels are identified with isentropic surfaces. In Figure 2.4 on page 20, a profile of potential temperature vs. pressure is included, showing the monotonic increase of θ with altitude in the stratosphere.

Stratospheric motion on long time scales is driven by radiation and thus non-adiabatic. The time derivative of potential temperature $\dot{\theta}$ is proportional to the heating rate Q (Brasseur and Solomon, 1984)

$$\frac{\mathrm{d}}{\mathrm{d}\, t}\theta \propto Q \tag{2.4}$$

In isentropic coordinates the "vertical" velocity is $\dot{\theta}$.

2.2.4 The polar stratosphere

With the Brewer-Dobson circulation, the large scale stratospheric motion has so far been described as two-dimensional, i.e. in coordinates of latitude and pressure (or altitude, potential temperature) as were to be expected if the Earth was an inertial reference frame. When in polar night the lower stratosphere cools, a temperature gradient between the warm mid-latitudes and the polar regions forms. The meridional gradient causes an eastward zonal flow around 60° latitude in the winter hemisphere. This strong flow, referred to as the polar night jet, extends from 100 hPa throughout the stratosphere and attains wind speeds of up to $100\,\mathrm{m\,s^{-1}}$ (Holton, 1992).

The area enclosed by the jet is termed the polar vortex and circulates eastward around the pole. It is well isolated from the mid-latitudes and creates a special winter polar vortex regime: The mean flow within the vortex is zonal, though disturbances of the vortex can lead deformations and displacements of the circular flow. Freqently, in Arctic regions, the deformations lead to a "vortex split"; over Antarctica, only one such event has ever been observed (in winter 2002, e.g Grooß et al., 2004); usually, the vortex reforms after a split during winter. Inside the vortex there is strong diabatic descent in late autumn and early winter. The vertical descent ceases towards spring when adiabatic heating by compression and beginning solar heating are in equilibrium with long-wave radiative cooling. Over Antarctica, this equilibrium is reached much sooner due to lower temperatures. When sunlight warms the polar regions, the jet and the vortex circulation weaken until finally the vortex breaks down.

2.2.5 Potential vorticity and vortex isolation

The local measure of circulation is absolute vorticity, which is calculated from the curl of the relative wind field (relative vorticity $\boldsymbol{\nabla} \times \boldsymbol{u}$) plus twice the angular velocity of the rotating reference frame (planetary vorticity $2\boldsymbol{\Omega}$). The quantity potential vorticity q, defined as

$$q = \frac{1}{\rho} \left(\boldsymbol{\nabla} \times \boldsymbol{u} + 2\boldsymbol{\Omega} \right) \cdot \boldsymbol{\nabla}\, \theta, \tag{2.5}$$

with density ρ, is conserved for adiabatic (no heating or viscous forces) motion (Ertel, 1942a,b):

$$\frac{\mathrm{d}}{\mathrm{d}\, t} q = 0 \tag{2.6}$$

In large-scale atmospheric flow, the horizontal velocity scale is much larger than the vertical scale, such that only the vertical component of vorticity needs to be considered, leading to the commonly used form

$$\mathrm{PV} = -g \left(\xi + f \right) \frac{\partial \theta}{\partial p}. \tag{2.7}$$

The vertical component of the curl of the wind field ξ is calculated on isentropes $\xi = \frac{\partial v}{\partial x} - \frac{\partial u}{\partial y}$ (Müller and Günther, 2004), $f = 2\Omega \sin\phi$ is the Coriolis parameter, with ϕ latitude and Ω the magnitude of Earth's angular velocity. PV is quantified in potential vorticity units (PVU) where $1\,\mathrm{PVU} = 1 \cdot 10^{-6}\,\mathrm{K\,m^2\,kg^{-1}\,s^{-1}}$. PV increases with latitude (increasing f) and is positive in the northern hemisphere.

The polar vortex edge is characterised by a strong meridional gradient of potential vorticity (Rummukainen et al., 1994). The maximum gradient of potential vorticity versus equivalent latitude on isentropic surface was used by Nash et al. (1996) to objectively define the vortex edge; the points of maximum curvature surrounding the largest PV gradient with respect to equivalent latitude (see below) are used to further distinguish the vortex core from the vortex inner edge and the outer edge. This definition of the polar vortex edge is closely followed here and depicted in Figure 2.3.

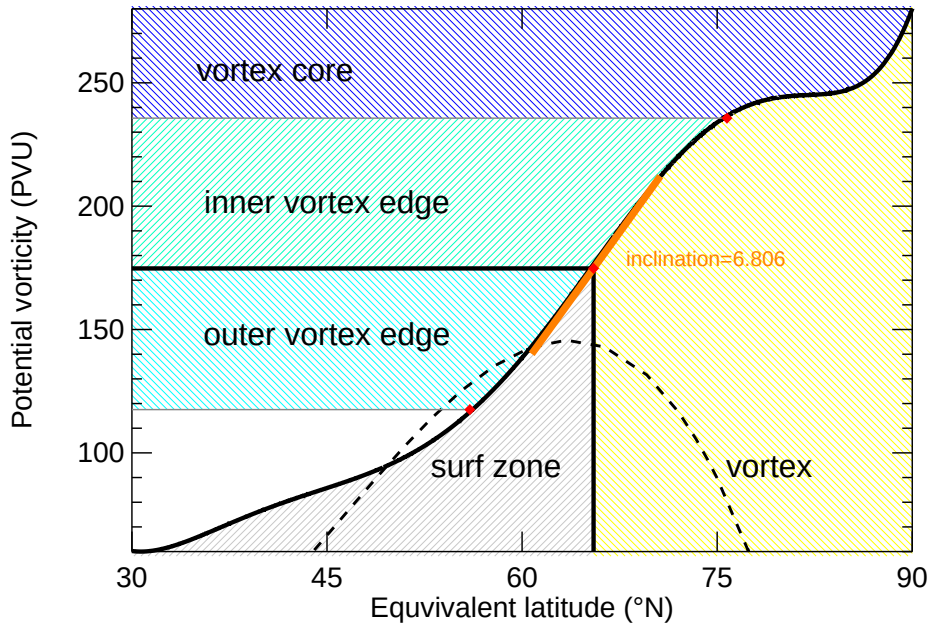

Figure 2.3: Vortex classification based on strongest PV gradient with respect to equivalent latitude. The vortex (yellow shading) is distinguished from the surf zone at the strongest PV(ϕ_{eq}) gradient (orange line, $\nabla_{\phi,\mathrm{eq}}\mathrm{PV}= 6.8\frac{\mathrm{PVU}}{^{\circ}\mathrm{N}}$) which is spatially related to the zonal mean wind maximum (Nash et al., 1996, dashed line, arbitrary units). The broader region enclosed by the points of maximum curvature (red dots) is termed the edge region (cyan shading) and can be differentiated in an outer edge zone (beyond the vortex) and the inner edge zone (within the vortex); the region bounded by the inner edge is the vortex core. Figure kindly provided by I. Kaster, 2005; data based on UKMO wind fields, 16 Nov 2002, 650 K.

The polar vortex isolates the air inside from mid-latitude air during the duration of the polar night: for isentropic transport into the vortex air parcels would have to gain vorticity. Thus the vortex acts a a transport barrier between middle and high latitudes with distinct distributions of tracers inside and outside the polar vortex (Anderson et al., 1989). Steinhorst et al. (2005) examine the isolation of the 1999/2000 Arctic polar vortex with artificial digital tracers and find that the magnitude of the PV gradient at the vortex edge may serve as a measure of vortex permeability.

Scaled potential vorticity and equivalent latitude

Several studies use scaled variants of potential vorticity to reduce the variation of PV with altitude. For comparison with these studies, modified potential vorticity (mPV, Lait 1994) and normalised potential vorticity (nPV, Rex et al. 1998) are used. Both mPV and nPV scale potential vorticity with the pressure dependence of potential vorticity given a reference temperature profile. While Rex et al. (1998) use empirical reference profiles for their scaling, the approach by Lait (1994) is a special case of a polytropic temperature scaling of PV (Müller and Günther, 2003, 2004).

Modified potential vorticity is calculated as

$$\mathrm{mPV} = \mathrm{PV} \cdot \left(\frac{\theta_r}{\theta}\right)^{\beta} \tag{2.8}$$

and shares the conservation properties and dimension of potential vorticity. At the reference level $\theta_r = 475\,\mathrm{K}$, modified potential vorticity equals potential vorticity (mPV= PV). Assuming isothermal scaling, the exponent β is $\beta = 9/2$ (Lait, 1994), which is a valid scaling in the altitude range considered in this thesis.

Rex et al. (1998) introduced a scaling based on a mean potential temperature profile Equation (2.9) from radio sondes referred to as normalised PV (nPV). With a scaling factor $k = 2.65 \cdot 10^5$, the numerical value of nPV, which is measured in s^{-1}, equals the numerical value of PV on the $\theta_r = 475\,\mathrm{K}$ reference level. With the reference polynomial coefficients ($a_0 = 1.248 \cdot 10, a_1 = -3.212 \cdot 10^{-2}, a_2 = 3.708 \cdot 10^{-5}, a_3 = -1.627 \cdot 10^{-8}$), normalised PV is calculated as

$$\ln \frac{p_\theta}{\mathrm{hPa}} = \sum_{i=0}^{3} a_i \cdot \left(\frac{\theta}{\mathrm{K}}\right)^i \tag{2.9}$$

$$\mathrm{nPV} = \mathrm{PV} \cdot \frac{k}{g} \cdot \frac{p_\theta \cdot \partial \ln p_\theta}{\partial \theta} \tag{2.10}$$

Both scalings are contrasted in Figure 5.2 on page 77 as a function of potential vorticity and equivalent latitude for two E39C simulated data sets.

Equivalent latitude ϕ_{eq} is defined as the latitude enclosing the same polar cap area as the area enclosed by a given PV contour. The use of ϕ_{eq} as latitude coordinate eliminates zonal variability of PV: in ϕ_{eq} coordinates, the polar vortex is pole-centred and circular. The equivalent latitude-potential temperature coordinate system was introduced by Hoskins (1991) for applications in meteorology.

Wave interaction

The mean stratospheric circulation is not only driven by the temperature gradient but additionally forced by upward propagating planetary waves which are are triggered by tropospheric weather events, surface topography, and land-sea contrasts. When westerly winds prevail, low frequency waves propagate into the stratosphere. While their amplitude increases due to decreasing pressure with altitude, they are refracted equatorward. Upon breaking, they deposit their energy into the mid-latitude stratosphere. Westward impulse is deposited onto the eastward mean meridional flow: the zonal deceleration (called wave drag) induces poleward residual motion, called Rossby wave pumping (e.g. Plumb, 2002). As the mean meridional circulation drives the transport of chemical tracers from the stratospheric source region (i.e. the tropics) to the poles, planetary waves constitute a link between tropospheric dynamics and stratospheric chemistry.

The stronger land-sea contrast and orographic features of in the northern hemisphere generate more planetary waves: the residual mean circulation is stronger in

the Arctic than in the Antarctic (Randel et al., 1999). The stronger meridional circulation increases adiabatic heating of the polar vortex. On average, the North Polar vortex is 10 K warmer than the Antarctic vortex (e.g. Manney et al., 1996). Zonally asymmetric wave generation in the northern hemisphere is dominated by waves with wave numbers one (displacement of the vortex from the pole) and two (stretching of the circular vortex to an ellipsis). Climatologically, the Arctic vortex is centred over Spitzbergen while over the Aleutians a persistent tropospheric high pressure system is found.

An example of the influence of wave breaking in the stratosphere is provided by Hood et al. (1999) who find that during the last decades increased poleward breaking of planetary waves transports more ozone-poor air from the equator to mid-latitudes, effectively reducing the mid-latitude ozone column purely by transport. While usually refracted towards the equator, poleward breaking planetary waves can, on rare occasions, transport mid-latitude air into the vortex (Nakamura, 2004).

Stratospheric warmings and teleconnections

The slowdown of the mean meridional circulation facilitates propagation of waves with higher wave numbers: more poleward circulation reduces the temperature gradient between the vortex edge and the vortex centre. The reduction of the gradient between 60°N and the pole at 10 hPa indicates a stratospheric warming event, which occurs several times during an Arctic winter, but rarely over Antarctica (a notable example was the 2002 Antarctic winter, see above). Minor reductions of the temperature gradient and zonal mean wind are termed minor warmings; if the wave impact is so large that the mean zonal wind reverses, the warming is characterised as a major warming (WMO, 1992). Wave propagation is blocked by reversed (easterly) zonal wind, if the warmed stratospheric air is in radiative disequilibrium, emission of radiation diabatic cooling and reestablishment of the winter circulation. At the end of the winter, the wave induced warming may coincide with spring radiative heating: the westerly wind cannot reform and the vortex breaks down, a major final warming has terminated the winter circulation.

The strength of the polar vortex has been associated with anomalies in geopotential hight fields (annular modes), hemispheric sea level pressure anomalies (e.g. Arctic oscillation, AO, Thompson and Wallace 1998), or characteristic regional surface pressure differences (e.g. North Atlantic oscillation, NAO, Walker and Bliss 1932). For example, Baldwin and Dunkerton (1999) find a correlation of 0.93 between the polar night jet (PNJ) and the AO, a weakening of the AO corresponds to stratospheric warming events. They show the propagation of the anomaly from the middle stratosphere to the troposphere. Frequency of stratospheric warming events may be connected to the tropical quasi-biennial oscillation (QBO): in QBO east phase, Baldwin and Dunkerton find more likelihood of sudden stratospheric warmings.

Thejll et al. (2003), using the pressure gradient between Gibraltar and iceland as the NAO index, conclude that the NAO has a deep vertical extent into the stratosphere. A connection between NAO index (here defined alternatively as the pressure gradient

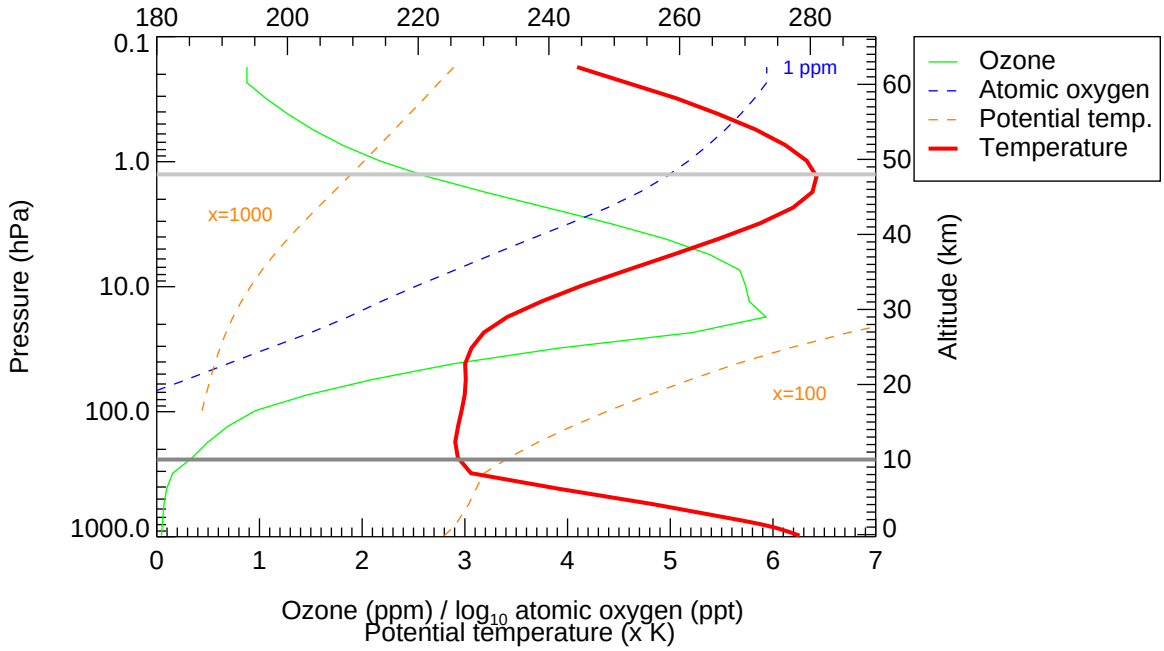

Figure 2.4: Noon profiles for ozone (O_3), atomic oxygen (O), temperature (T), and potential temperature (θ) at $\phi_{eq} = 65°$N on 15 May, 1992 based on Mainz-2D (Grooß, 1996) calculations. For improved visibility, θ is divided by 100 at lower levels (right broken orange line), by 1000 for the upper atmosphere (left broken orange line). The local minimum temperature tropopause (dark grey) is at 10 km altitude (230 hPa, 340 K pot. temp.), the light grey line shows the stratopause slightly below 1 hPa or 50 km altitude.

between the Azores and Iceland) and polar vortex dynamics is confirmed by model experiments with E39C (Schnadt and Dameris, 2003). for positive values of the NAO index they find a strong and cold polar vortex in their model E39C. Schnadt and Dameris discriminate stationary waves —of which propagation is reduced for positive NAO index— and transient waves, which propagate more easily (cmp. Section 3.2.1).

2.3 Chemistry of the Stratosphere

2.3.1 Ozone

Ozone (O_3) is one of the major trace species in the stratosphere and has come into public awareness due to the depletion of ozone in mid-latitudes (WMO, 2003) and the unusually low values of total ozone above Antarctica (Jones and Shanklin, 1995) termed the ozone hole. It is the most abundant reactive compound in the stratosphere with typical volume mixing ratios (vmr) between 2 and 10 parts per million, down to less than 0.1 ppm at the tropopause. Chemical species abundances are given as volume mixing ratio throughout this thesis; this measure is invariant under changes of pressure and temperatures for stratospheric air (which is close to an ideal gas).

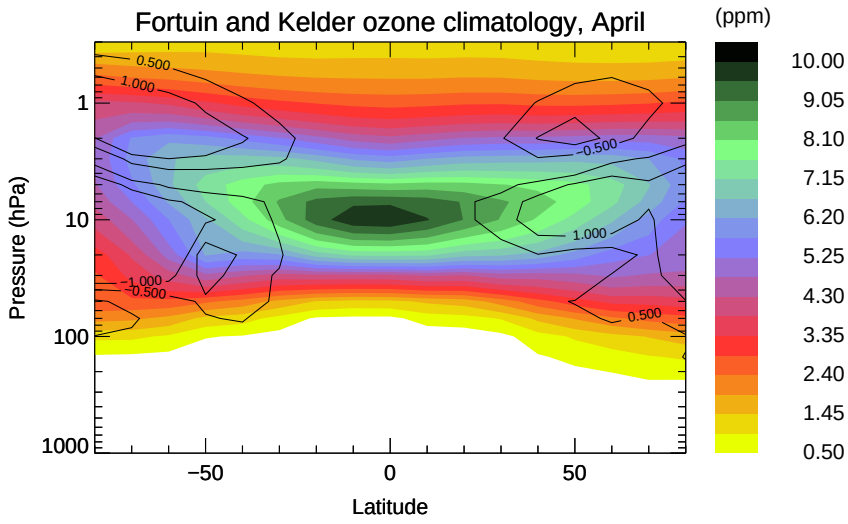

Figure 2.5: April ozone climatology compiled from 30 ozone sonde and SBUV/SBUV2 observations during the 1980s (Fortuin and Kelder, 1998). Contour lines show difference to November climatology.

Ozone is produced photochemically from molecular oxygen (O_2); it is destroyed by recombination with atomic ozone and other oxidised radicals. Thus, its mixing ratio profile with height is a consequence of production and loss reactions with a maximum at 30–32 km (or 10 hPa). This vertical distribution of ozone is illustrated in Figure 2.4. Maximum production occurs in the tropics at 40 km altitude, the highest concentration of ozone is found at 25 km altitude with decreasing concentrations with higher levels (more available radicals) and to lower levels (less production). 90% of all ozone is found in the stratosphere, the term ozone layer denotes the region of maximum concentrations where $\approx 75\%$ of all ozone is located. At the bottom of the stratosphere, ozone mixing ratios fall rapidly below 100 ppb, thus forming a chemopause (e.g. Logan, 1999) apparent in atmospheric data sets as a sharp decline of mixing ratio.

Figure 2.5 shows the climatological mean April distribution for ozone mixing ratio derived from satellite and ozone sonde observations during the 1980s (Fortuin and Kelder, 1998). The zonal distribution of ozone shows the chemopause towards the stratosphere, the high production region in the tropics and the near symmetric distribution of ozone towards higher latitudes. The symmetry is not perfect due to different hemispheric transport and photochemistry. Contour lines show the climatological mean difference between April and November, i.e. changes during boreal winter and austral summer. The increased Brewer Dobson circulation in the northern hemisphere transports more ozone poleward (seen as the increase in mixing ratio around 10 hPa) and downward (decrease at 2 hPa), effectively increasing column ozone during an Arctic winter. Over Antarctica, ozone mixing ratio decreases due to summer photochemistry and less dynamical resupply.

Near the surface, tropospheric ozone is associated with pollution, predominantly as a product of traffic emissions; ozone is also formed by UV irradiation or in high-voltage electric fields. While experimenting with electricity, C. F. Schönbein noticed a pungent smell which he termed "Ozon" (derived from the Greek word $\omega\zeta\varepsilon\iota\nu$ = to reek) in 1839; he observed a similar smell in the atmosphere after lightning. Much later, Soret (1863) proposed the composition of ozone to be oxygen dioxide.

Biological relevance of the ozone layer

The absorption of UV-C (200–280 nm) and UV-B (280–315 nm) by stratospheric ozone was one of the major preconditions for the development of DNA-based life in surface waters and on land, since nucleic acids would be severely damaged by radiation at wavelengths below 295 nm; radiation at higher wavelength (UV-A, 315–400 nm) may inhibit photosynthetic activity or lead to cell membrane damage. For example, Lotze et al. (2002) demonstrate that UV radiation has a detrimental effect on the growth of macroalgae and on the composition of benthic fauna; enhanced mortality of Antarctic krill was found by Newman et al. (1999) when the krill were exposed to UV-B radiation at $\frac{1}{6}$ of the typical spring UV surface irradiation.

Excess exposure of animal or human skin to UV radiation leads to damages exhibited by erythema (skin redding) and burns; Elwood and Jopson (1997), for example, find a significant increase of melanoma with intermittent exposure to sunlight, and especially with sunburns. Hence, the globally declining stratospheric ozone abundance is of great concern for human health, especially since an increase in leisure time and an outdoors-oriented life style contribute additionally to the exposure of human skin to solar radiation: In study by Fears et al. (2002), a 10% increase in hours outdoors lead to increased risks factors of 2.8 for men and 5.8% for women who developed a tan.

While the direct effect of increased radiation in polar regions on humans may be small[2], the impact on polar ecology cannot be neglected (e.g. ACIA, 2004): Antarctic UV surface irradiation is largest in early polar summer, when ozone has not yet recovered and may attain values equal to those observed in sub-tropical latitudes (WMO, 2003). The Arctic Climate Impact Assessment (ACIA, 2004) assumes that with declining (observed and predicted) sea ice extent and thickness, UV radiation increases in coastal areas: much more ultraviolet radiation will be absorbed in the oceans with possible damages especially for marine life and the marine food chain, as shown by Newman et al. (1999).

Column ozone

The protection provided by the ozone layer is given by the number of ozone molecules along a light path through the entire atmosphere. The quantity column ozone describes the total number of ozone molecules at surface pressure integrated vertically over the entire atmosphere; column ozone is commonly measured in terms of Dobson units, where $1\,\mathrm{DU} = 2.69 \cdot 10^{16}\,\mathrm{molecules\,cm^{-2}}$. At surface pressure, 100 DU represent a column of 1 mm height. Globally averaged column ozone is 300 DU, maximum ozone columns of about 500 DU are observed in Arctic spring (cmp. Figure 2.7 on page 24); generally, the northern hemispheric high-latitude ozone column is thicker than the austral column (Dobson, 1966).

A column less than 220 DU has been chosen to define a critically thin ozone layer (WMO, 1990): the ozone hole is the region with ozone columns less than 220 DU

[2]The "ozone hole" is located above the poles, primarily the South Pole, where relatively few people live and those that do live there are well protected by clothing

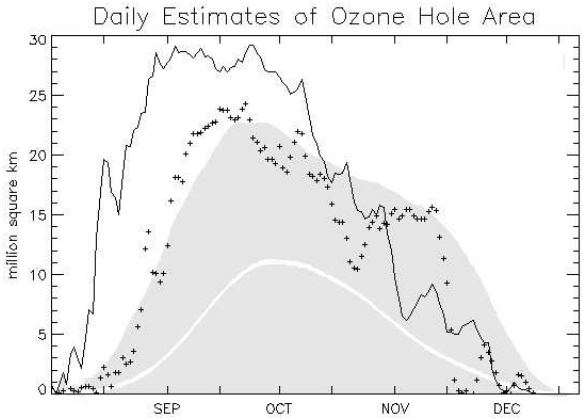

Figure 2.6: TOMS (Total ozone mapping spectrometer) observed Antarctic ozone hole area 2003 (solid line), 2004 (dotted) and 1979–1992 (mean: white line, range: grey shading). The largest extent ($29 \cdot 10^6\,\mathrm{km}^2$) was observed in October during the years 2000 and 2003. Graphics available courtesy of NASA GSFC, EP TOMS web page http://toms.gsfc.nasa.gov/

and its extent is the area enclosed by the 220 DU contour. In the year 2000, a large Antarctic ozone hole covered an area of $29 \cdot 10^6\,\mathrm{km}^2$ (WMO, 2003); a second very large ozone hole has been observed in 2003; recent Antarctic ozone hole extent is shown in Figure 2.6.

Chapman reactions

The source species for ozone is molecular oxygen which photolyses in the stratosphere at wavelengths in the Schumann-Runge band and the Herzberg continuum (wave length λ between 185 and 243 nm) to form two oxygen atoms; with a high ambient concentration of other oxygen molecules, these combine to ozone:

$$\mathrm{O_2} + h\nu \longrightarrow \mathrm{O} + \mathrm{O} \quad \text{for} \quad \lambda < 243\,\mathrm{nm} \tag{2.11a}$$

$$\mathrm{O_2} + \mathrm{O} + M \longrightarrow \mathrm{O_3} + M \tag{2.11b}$$

$$\text{net:} \quad 2\mathrm{O_2} \longrightarrow \mathrm{O_3} + \mathrm{O} \tag{2.11c}$$

The second reaction involves an additional arbitrary molecule M to maintain energy conservation. The reaction speed of the photolysis depends only on available high energy radiation. In Figure 2.4 a logarithmic noon profile of atomic oxygen is shown ranging over six orders of magnitude: surplus atomic oxygen is only available above 25 km.

Equation (2.11) is most effective in the tropics and least effective above the winter pole. The meridional gradient of ozone production is mediated by large scale transport from the tropics to the poles, part of the Brewer-Dobson circulation (see previous section on stratospheric dynamics). Though production is maximal in tropical regions, the observed ozone column is lowest in the tropics and maximal in high latitudes in boreal spring. The meridional distribution of total ozone as observed by the TOMS instrument (Stolarski et al., 1986) is shown in Figure 2.7: In the subtropics the ozone column is below 300 DU, while in middle and high latitudes outside the polar vortex (shown as the thick black contour) ozone has accumulated to columns around 500 DU.

In the stratosphere, only radiation with wavelength longer than 185 nm is available; ultraviolet (UV) light with wavelength < 243 nm penetrates to about 30 km altitude,

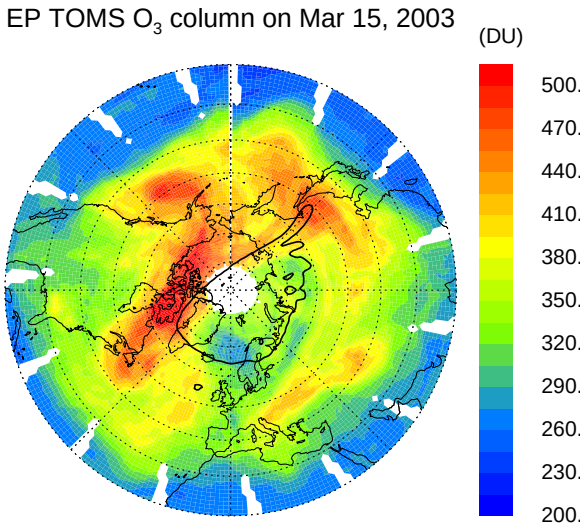

Figure 2.7: Ozone column observed by the TOMS instrument aboard the Earth Probe (EP) satellite on March 15, 2003. The vortex edge on the 475 K isentrope according to Nash et al. (1996) is shown as a solid black line. Grid lines are spaced at 10° latitude. This graphic was kindly supplied by J.-U. Grooß, 2005.

as shown in Figure 2.8. The remaining part of the UV spectrum is almost completely and exclusively absorbed by ozone molecules. Abundance of other strong absorbers of UV (e.g. N_2O_5, NO_x, BrO) is several orders of magnitude less than ozone abundance; short wave absorption cross sections for various atmospheric constituents are displayed in Figure A.1 on page 114. Ozone is photolysed to atomic oxygen in a wide absorption band:

$$O_3 + h\nu + M \longrightarrow O + O_2 + M \qquad \text{for} \qquad \lambda < 1140\,\text{nm} \tag{2.12}$$

Radiation with wavelength shorter than 340 nm can produce atomic oxygen in its high energy singlet state, denoted $O(^1D)$; the production of $O(^1D)$ from O_3 photolysis is quantitative at $\lambda < 306$ nm (Sander et al., 2003). $O(^1D)$ is an important reactand for the breakdown of N_2O and CH_4, for example, yielding nitrogen oxides and hydroxyl (OH); $O(^1D)$ may also relax to the ground state of atomic oxygen, denoted $O(^3P)$. For the purpose of this thesis, no distinction between $O(^1D)$ and $O(^3P)$ is necessary; both are referred to as O.

The radical terminating reaction of O_3 with O completes what has become known

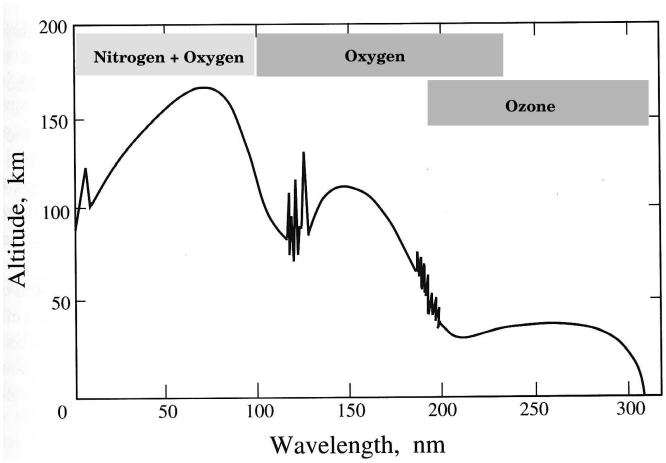

Figure 2.8: Penetration depth of ultraviolet radiation through the atmosphere. Short wavelength radiation (< 185 nm) is absorbed by molecular nitrogen and oxygen and does not reach the stratosphere. O_3 is the major absorber for longer wavelength UV radiation. Figure based on Brasseur and Solomon (1984).

Family		composition
Odd oxygen	O_x	$O_3 + O$
Active chlorine	ClO_x	$Cl + ClO + 2Cl_2O_2$
Inorganic chlorine	Cl_y	$ClO_x + HCl + ClONO_2 + 2Cl_2 + HOCl + ClO_2 + BrCl$
Inorganic bromine	Br_y	$Br_2 + BrO + BrCl + BrCH_3 + Br_2 + BrONO_2 + HBr$
Active nitrogen	NO_x	$NO + NO_2 + NO_3$
Reactive nitrogen	NO_y	$NO_x + HNO_3 + HNO_4 + 2N_2O_5 + CH_3NO_3 + ClONO_2$ $+BrONO_2 + ClONO$

Table 2.1: Examples of chemical family definitions used in this chapter. The definition of a chemical family depends on time scales under investigation; different families are used, e.g. in the E39C chemistry climate model, cmp. Table 3.1.

as the Chapman cycle (Chapman 1930, Equations 2.11–2.13)

$$O_3 + O \longrightarrow 2O_2 \tag{2.13}$$

The family concept

Chemical reaction speeds of different reactions span multiple orders of magnitude: only considering the Chapman reactions the life times of atomic oxygen and ozone would be 0.002 s and 1000 s, respectively, in the lower stratosphere (Sander et al., 2003; Dessler, 2000). It is instructive to group together chemical species that interconvert rapidly in a so-called chemical family (Crutzen, 1974); the choice of family members depends on the time scale under consideration. For example, one can consider the radical forms of oxygen as a family, commonly termed odd oxygen (O_x); the concentration of O_x is the sum of the ozone and atomic oxygen concentration; the ratio of the family members is assumed to be in chemical equilibrium.

The reactions of the Chapman cycle reduce to:

$$O_2 \longrightarrow 2O_x \tag{2.14a}$$

$$2O_x \longrightarrow O_2, \tag{2.14b}$$

provided that there is radiation of sufficient energy $h\nu$ and that there are abundant molecules M to ultimately absorb the energy —and heat the stratosphere.

The life time for odd oxygen, defined as the concentration divided by loss rate, is about five years — if only Chapman cycle reactions are considered. The treatment of family reactions instead of elementary chemical reactions is a technique widely used in chemical modelling. By decreasing the rate constants, the numerical time step used, e.g. in an atmospheric chemistry model, can be increased, thus facilitating an efficient calculation of the state of the atmosphere.

2.3.2 Chlorine and bromine

Halogens do naturally occur in the stratosphere at about 10% of currently observed amounts. Most of the halogen burden in today's stratosphere was introduced by

anthropogenic release of chlorofluorocarbons (CFC) and related halogenated carbon compounds. The majority of the released substances are practically inert in the troposphere and are transported to the stratosphere.

Abundance of biogenic halogen compounds (primarily methyl chloride and methyl bromide) has increased due to their use for industrial purposes; in common with the even more inert CFC and halons (bromochlorofluorocarbons) they are not soluble in water nor are they affected by solar radiation available in the troposphere. After tropical ascent, these primary reservoirs penetrate to the upper stratosphere where they are decomposed by short wave radiation. Figure A.1 shows absorption cross sections for various CFC species. Ultimately, halogen radicals are produced which react with methane to hydrogenhalogenide and with nitrous oxides to halogennitrates. HF, HCl, HBr, $ClONO_2$ and $BrONO_2$ are secondary halogen reservoirs, which are slowly removed from the stratosphere by condensation and wet deposition after having been transported to the troposphere. Hydrogen fluoride is unreactive and is not considered further here. Chlorine and bromine compounds are both important for stratospheric chemistry and ozone loss in particular.

Chlorine

Hydrogen chloride is the major reservoir of inorganic chlorine (Cl_y, all chlorine except CFC, see Table 2.1) in the stratosphere; a second major reservoir is chlorine nitrate ($ClONO_2$). At high altitudes (maximum around 40 km), the chlorine monoxide biradical (ClO) is abundant. Its reactions with atomic oxygen and reformation by reaction of chlorine atoms with ozone were described by Molina and Rowland (1974), and Stolarski and Cicerone (1974):

$$\begin{aligned} & Cl + O_3 && \longrightarrow && ClO + O_2 && (2.15a)\\ & ClO + O && \longrightarrow && Cl + O_2 && (2.15b)\\ \text{net:}\quad & 2O_x && \longrightarrow && 2O_2 && (2.15c) \end{aligned}$$

With the omnipresent O_3, O (and also NO_x), Cl and ClO interconvert rapidly and form the ClO_x family, also termed active chlorine. Volume mixing ratio and concentration within the ClO_x family are calculated on a per Cl atom base, thus in the definition for ClO_x in Table 2.1, Cl_2O_2 is counted twice.

The Cl-ClO cycle of ozone loss had been known in the 1970s along with the awareness of anthropogenic CFC release to the stratosphere: the reaction is most important at 40 km altitude, where the impact on total ozone would not have been significant. The connection to the ozone hole which was observed at altitudes below 25 km had not been made before the mid-1980s.

Several stratospheric radicals other then Cl react as catalysts for ozone destruction in higher regions of the stratosphere where atomic oxygen is available; the general

pattern of odd oxygen loss follows the path

$$\begin{aligned} & \mathrm{X} + \mathrm{O_3} && \longrightarrow && \mathrm{XO} + \mathrm{O_2} && (2.16a) \\ & \mathrm{XO} + \mathrm{O} && \longrightarrow && \mathrm{X} + \mathrm{O_2} && (2.16b) \\ \text{net:} \quad & 2\mathrm{O}_x && \longrightarrow && 2\mathrm{O_2} && (2.16c) \end{aligned}$$

where X= {Cl,NO,HO}. In the lower stratosphere, a catalytic cycle involving OH but no atomic oxygen completes the major loss cycles:

$$\begin{aligned} & \mathrm{OH} + \mathrm{O_3} && \longrightarrow && \mathrm{HO_2} + \mathrm{O_2} && (2.17a) \\ & \mathrm{HO_2} + \mathrm{O_3} && \longrightarrow && \mathrm{OH} + 2\mathrm{O_2} && (2.17b) \\ \text{net:} \quad & 2\mathrm{O}_x && \longrightarrow && 2\mathrm{O_2}. && (2.17c) \end{aligned}$$

The importance of ozone loss cycles at different altitudes has been assessed by, e.g. Crutzen et al. (1995) above 40 km the Equation (2.16) with X = H is dominant (60–80%), around 40 km the chlorine cycle Equation (2.15) is at its maximum (40%, elsewhere $< 10\%$), below 40 km, NO_x-catalysed ozone loss is most important. Below 25 km, Equation (2.17) becomes important. The Chapman cycles account for approximately 10% of chemical ozone loss.

Stratospheric aerosol and polar stratospheric clouds

In the vertical region between the tropopause and ≈ 30 km altitude, a layer of microscopic droplets is described by Junge et al. (1961). These liquid particles are composed of around 75% sulfuric acid (sulfuric acid trihydrate, SAT); sulfur is introduced to the stratosphere by transport of the long-lived biogenic carbonyl sulfide (COS) or volcanic eruptions (SO_x, $\mathrm{H_2S}$). Dessler et al. (1993) show the importance of the surface provided by the stratospheric aerosol for chemical reactions and that the surface area density (SAD) was increased by one order of magnitude after the eruption of Mt. Pinatubo in 1991. The most important stratospheric heterogeneous reaction on sulfate aerosol is the hydrolysis of $\mathrm{N_2O_5}$, described further below.

In the cold polar winter stratosphere, SAT takes up nitric acid at temperatures below 200 K, leading to the formation of supercooled ternary solution (STS) droplets (Tabazadeh et al., 1994); polar stratospheric clouds (PSC) composed of liquid aerosol are classified as type Ib. At temperatures below about 195 K, solid nitric acid trihydrate (NAT) particles form (Fahey et al., 1989), classified as PSC type Ia. The formation of NAT depends on availability of $\mathrm{H_2O}$ and $\mathrm{HNO_3}$, and on temperature (T). A canonical relationship derived by Hanson and Mauersberger (1988) is widely used to determine the saturation vapour pressure of $\mathrm{HNO_3}$ with respect to NAT:

$$\begin{aligned} p_{\mathrm{NAT}} = \exp(& (-2.7836 - 0.00088 \cdot T) \cdot \log p_{\mathrm{H2O}} \cdot \\ & +90.8556 - 26242.6/T + 0.0213885 \cdot T) \end{aligned} \qquad (2.18)$$

At typical lower stratospheric mixing ratios of 10 ppb $\mathrm{HNO_3}$ and 5 ppm $\mathrm{H_2O}$, the partial pressure of $\mathrm{HNO_3}$ exceeds p_{NAT} at temperatures below 195 K.

The existence of solid particles accelerates a number of reactions leading to ozone depletion to an extent that the potential for NAT existence has been employed as a predictor of chemical ozone loss (e.g. Rex et al., 2004). The potential for NAT existence is defined by the area over which $T < T_{\mathrm{NAT}}$ (A_{PSC}, possible PSC area), or a respective volume (V_{PSC}, possible PSC volume). Classified as PSC type II are water ice clouds that exist at temperatures below 185 K.

Heterogeneous chemistry and ClO dimer cycle

Polar stratospheric cloud surfaces facilitate reactions which convert the reservoir species of Cl_y to active forms (e.g. Peter, 1997; Solomon, 1999). These reactions proceed fast, thus converting a reservoir into an active species until one of the reactants is used up. Four of the most important heterogeneous activation reactions are

$$\mathrm{ClONO_2 + HCl} \longrightarrow \mathrm{HNO_3 + Cl_2} \tag{2.19a}$$
$$\mathrm{ClONO_2 + H_2O} \longrightarrow \mathrm{HNO_3 + HOCl} \tag{2.19b}$$
$$\mathrm{HCl + HOCl} \longrightarrow \mathrm{H_2O + Cl_2} \tag{2.19c}$$
$$\mathrm{HCl + HOBr} \longrightarrow \mathrm{H_2O + BrCl} \tag{2.19d}$$

Both $\mathrm{Cl_2}$ and HOCl are photolysed even in low-light polar winter conditions to Cl which rapidly converts to ClO as part of the ClO_x family. Under cold conditions, the self-reaction of ClO forms a dimer (e.g. von Hobe et al., 2005). This dimer can catalyse ozone loss without atomic oxygen (Molina and Molina, 1987):

$$\mathrm{ClO + ClO} + M \longrightarrow \mathrm{Cl_2O_2} + M \tag{2.20a}$$
$$\mathrm{Cl_2O_2} + h\nu \longrightarrow \mathrm{ClO_2 + Cl} \tag{2.20b}$$
$$\mathrm{ClO_2} + M \longrightarrow \mathrm{Cl + O_2} + M \tag{2.20c}$$
$$\mathrm{Cl + O_3} \longrightarrow \mathrm{ClO + O_2} \tag{2.20d}$$
$$\text{net:} \quad \mathrm{2O_3} \longrightarrow \mathrm{3O_2} \tag{2.20e}$$

Bromine

As with chlorine, bromine forms hydrogen bromide and bromine nitrate as reservoir species. In contrast to chlorine, a large part (about 50%) of inorganic bromine ($\mathrm{Br_y}$, cmp. Table 2.1) is present in the form of chemically active bromine oxide throughout the stratosphere.

The ClO dimer cycle Equation (2.20) is the most effective ozone destruction cycle in the cold polar winter stratosphere. Another important loss process is the catalytic BrO-ClO cycle (McElroy et al., 1986):

$$\mathrm{Cl + O_3} \longrightarrow \mathrm{ClO + O_2} \tag{2.21a}$$
$$\mathrm{Br + O_3} \longrightarrow \mathrm{BrO + O_2} \tag{2.21b}$$

the reaction between the halogenmonoxide can then proceed to two different ozone-destroying pathways:

$$\begin{aligned} \mathrm{BrO} + \mathrm{ClO} &\longrightarrow \mathrm{BrCl} + \mathrm{O_2} && (2.21c)\\ \mathrm{BrCl} + h\nu &\longrightarrow \mathrm{Br} + \mathrm{Cl} && (2.21d) \end{aligned}$$

or, alternatively, and with the same net result

$$\begin{aligned} \mathrm{BrO} + \mathrm{ClO} &\longrightarrow \mathrm{ClO_2} + \mathrm{Br} && (2.21e)\\ \mathrm{ClO_2} + M &\longrightarrow \mathrm{Cl} + \mathrm{O_2} + M && (2.21f)\\ \text{net:}\quad 2\mathrm{O_3} &\longrightarrow 3\mathrm{O_2} && (2.21g) \end{aligned}$$

All these reactions can proceed at low altitudes (no O required) and large solar zenith angles (SZA), though cannot proceed in darkness.

2.3.3 Nitrogen compounds

All forms of nitrogen which are not $\mathrm{N_2}$ or $\mathrm{N_2O}$ are combined in the NO_y family, consisting mainly of active nitrogen ($\mathrm{NO}_x = NO, \mathrm{NO_2}, \mathrm{NO_3}$) and nitrogen reservoirs ($\mathrm{N_2O_5}$ and the various nitrates, cmp. Table 2.1). Within the family, each $\mathrm{N_2O_5}$ molecule counts twice, since it can decompose into two NO_x molecules. The major source of stratospheric NO_y is oxidation of $\mathrm{N_2O}$ with $\mathrm{O}(^1\mathrm{D})$ in the upper stratosphere and mesosphere. Minor contributions come from the breakdown of $\mathrm{N_2}$ by cosmogenic particles. NO_x species participate in ozone loss cycles as proposed by Crutzen (1970, cmp. Equation (2.16))

$\mathrm{NO_2}$ reacts with $\mathrm{NO_3}$, hydroxyl, and halogenmonoxides to form the major reservoirs of NO_y, for example:

$$\begin{aligned} \mathrm{NO_2} + \mathrm{NO_3} + M &\longrightarrow \mathrm{N_2O_5} + M \quad \text{at night} && (2.22a)\\ \mathrm{NO_2} + \mathrm{OH} + M &\longrightarrow \mathrm{HNO_3} + M && (2.22b)\\ \mathrm{NO_2} + \mathrm{ClO} + M &\longrightarrow \mathrm{ClONO_2} + M && (2.22c) \end{aligned}$$

In polar winter, the low temperature and light conditions drive most of the available NO_y into the reservoir species, effectively denoxifying the polar stratosphere. All nitrogen reservoir species can be photolysed to form NO_x in back reactions similar to Equation (2.22).

On sulfate aerosol and PSC particles hydrolysis converts $\mathrm{N_2O_5}$, $\mathrm{BrONO_2}$ and $\mathrm{ClONO_2}$ to $\mathrm{HNO_3}$, e.g.:

$$\begin{aligned} \mathrm{N_2O_5} + \mathrm{H_2O} &\longrightarrow 2\mathrm{HNO_3} + \mathrm{OH} && (2.23a)\\ \mathrm{BrONO_2} + \mathrm{H_2O} &\longrightarrow \mathrm{HNO_3} + \mathrm{HOBr} && (2.23b) \end{aligned}$$

The latter reaction is only a minor source of $\mathrm{HNO_3}$, but is an important heterogeneous bromine activation reaction analogous to the respective chlorine reaction Equation (2.19). The uptake of heterogeneous reaction partners on surfaces is described

by a sticking fraction which is very sensitive to temperature and generally approaches one at very low temperatures; with increasing temperature, the efficiency of sticking decreases by orders of magnitude (Dessler, 2000).

Deactivation and denitrification

The sustainable conversion of active forms of chlorine and bromine into their reservoirs is termed deactivation. For the formation of nitrates, deactivation depends on the availability of NO_x: In polar spring, intensified light conditions, higher temperatures and advection of NO_x-rich air from mid-latitudes lead to a termination of halogen-catalysed ozone loss reactions once sufficient NO_2 is available and PSC have disappeared.

The importance of nitrogen chemistry for polar ozone was emphasised by Waibel et al. (1999): a) denoxification at low temperatures and absence of sunlight decreases the availability of NO_x which could otherwise deactivate halogen monoxides; b) high concentrations of HNO_3 increasingly condense to NAT particles, enhancing the surface area density (SAD) where halogen reservoirs are activated; c) NAT particles may be removed from the stratosphere by sedimentation (denitrification), prolonging ozone loss even when the temperatures recover. Waibel et al. estimated that up to 35% (900 ppb) of chemical ozone depletion in Arctic winter 1994/95 can be attributed to denitrification. Denitrification has been observed in several Arctic winters (e.g. Fahey et al., 2001; Mann et al., 2002). In Antarctic winters, the polar stratosphere is completely denitrified and deactivation of chlorine occurs towards the chlorine reservoir HCl:

$$Cl + CH_4 \longrightarrow CH_3 + HCl \tag{2.24}$$

2.4 Climate Change

The term climate describes the statistical properties of weather over periods of time longer than decades. Most frequently reported properties of a regional or the global climate are mean and variability of meteorological quantities like temperature and rainfall. Further aspects of climate are frequency of extreme weather events (e.g. droughts) and the description of systematic seasonal variations (Wordsworth, 1995).

Records of surface temperature preserved in ice cores show that global climate has been changing over the last millennia (e.g. Petit et al., 1999); tree ring analyses and lake sediments indicate regional climate changes. These records however, show an unprecedented rate of temperature change after 1850 and especially in the second half of the 20^{th} century, shown as the pink line in Figure 2.9 for the northern hemisphere.

Climate Change (capitalised) describes this dramatic modern deviation from past climates. Most likely, this dramatic change can be attributed to human interference with the earth system: Taking into account all known natural variabilities, state-of-the-art global circulation models have only been able to simulate about one third of the observed temperature change. According to the model simulations, the remaining

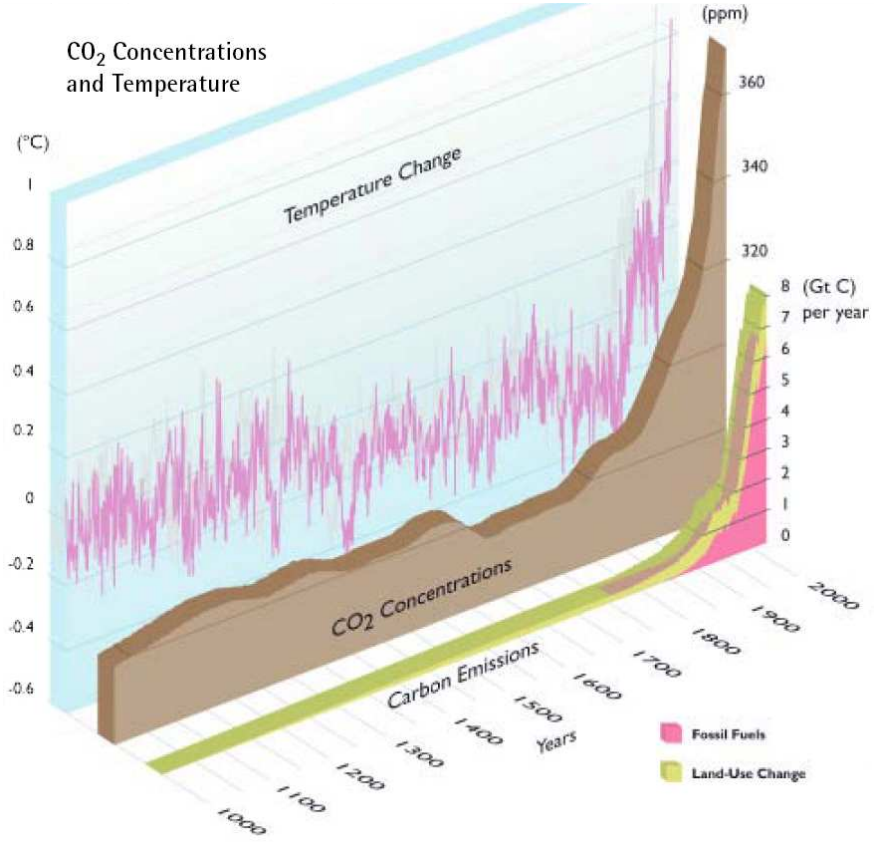

Figure 2.9: Mean northern hemispheric temperature during the last millennium, based on the "hockey stick" reconstruction by Mann et al. (1998, 2004), and showing unprecedented warming during the last century. Global CO_2 concentrations and emissions have increased significantly during the last 150 years. Figure from ACIA (2004).

differences are to be attributed to the additional greenhouse effect of anthropogenically released trace gases (IPCC, 1995, 2001).

For the prediction of future climate, GCM simulations have been performed assuming plausible scenarios of global economic development. In this thesis, climate simulations based on the IS92a business-as-usual scenario IPCC (1994) were used with additional boundary conditions from WMO (2003), which are based on SRES A1 greenhouse gas emissions (IPCC, 2000).

2.4.1 The preindustrial atmosphere

The primordial atmosphere was composed of CH_4, H_2O, N_2, NH_3, and H_2S. Oxygen was introduced in small amounts by the photochemical breakdown of water to H_2, which escaped to space. Methane was oxidised to CO_2; after surface cooling to a temperature where liquid water could exist, CO_2 was dissolved in the oceans and deposited as sediments. At approximately $3.5 \cdot 10^9$ years ago, cyanobacteria started to produce oxygen. First sinks for very early oxygen are uncertain and possible life on

land surfaces (without a protective ozone shield) around $2.6 \cdot 10^9$ years ago is much debated (Copley, 2001). Rocks containing oxidised iron —banded iron formations— were dated to as much $2.22 \cdot 10^9$ years ago, but almost no oxygen could be available in the atmosphere before $2.45 \cdot 10^9$ years ago (Bekker et al., 2004). Along with the subsequent build-up of atmospheric oxygen content from 3% at $2 \cdot 10^9$ years ago to the current level of 20.95%, the stratospheric ozone shield evolved; properties of ozone are described in Section 2.3.

An energy balance model (EBM) calculation of incoming solar radiation, reflected and absorbed light and emitted terrestrial long-wave radiation yields an EBM surface black body temperature of 255 K for our planet. Only by atmospheric infrared absorption and reemission does the surface warm to a global average surface temperature of 288 K (15°C, e.g. IPCC, 2001). The gases contributing to infrared absorption are termed greenhouse gases (GHG); chiefly, these are, in order of importance and naturally occurring: water vapour, carbon dioxide, methane, ozone, and nitrous oxide. Mid 19^{th} century volume mixing ratio of CO_2 was 280 ppm, CH_4 levels were 800 ppb and N_2O 275 ppb. Combined with water, these gases provided a natural greenhouse effect of 33°C at the surface, the effective level of radiation from the Earth is raised by the natural greenhouse effect to approximately 5 km altitude; this is the height of the greenhouse that Fourier (1824) talked about.

2.4.2 Greenhouse gas changes since 1850

As shown in Figure 2.9, from 1850 global concentrations of carbon dioxide started to increase strongly, along with carbon emissions by fossil fuel burning and land use changes. As was predicted by Revelle and Suess (1957), emissions exceed oceanic uptake: of the 8 Pg carbon that are emitted, currently about 4 Pg accumulate in the atmosphere per year (Keeling and Peng, 1995). Since 1850, CO_2 has increased by 30%, the current rate of increase is 0.4% per year.

Even stronger than CO_2, the CH_4 volume mixing ratio has increased to 1745 ppb in 1998 (Ehhalt et al., 2001); its rate of increase has recently been shown to slow down (Dlugokencky et al., 2001). Next to natural wetlands, rice cultivation, cattle herding, energy production, biomass burning and landfills are anthropogenic sources of CH_4; the largest sink for CH_4 is oxidation by OH, stratospheric oxidation is a secondary sink (Ehhalt et al., 2001). The observed CH_4 increase is the strongest increase among the naturally occurring GHG with a relative increase of 120% since 1850. Besides the direct effect of methane on radiation, increases in CH_4 lead to rising values of tropospheric ozone and stratospheric water vapour.

Emissions of CO, NO_x, and volatile organic carbons (VOC), which are not primary greenhouse gases, contribute to the elevation of tropospheric ozone abundance. Stratospheric ozone depletion leads to an increase in tropospheric ozone by permitting more UV radiation to reach the troposphere, which produces surface ozone. Combined changes in tropospheric ozone may be on the order of 40%; the tropospheric ozone column may have increased from 24 DU preindustrial to 34 DU today (Ehhalt et al., 2001).

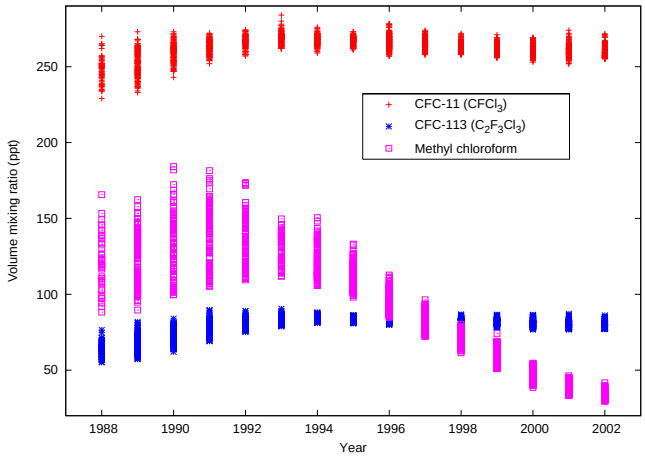

Figure 2.10: CFC and methyl chloroform in whole air samples collected at remote stations. Since their peak in 1994, mixing ratios of the relatively short-lived CFC-11 and CFC-113 have been decreasing, levels of CFC-12 (not shown) remained constant. Abundance of methyl chloroform (the species with the shortest life time) has been severely reduced. Data from Blake (2004).

Nitrous oxide mixing ratio is currently approximately 314 ppb, which is 114% of the 1850 value. The current yearly rate of increase is 0.25%. N_2O is released from soils, at a fraction of 55% from natural soils and 45% from anthropogenically altered soils or land use changes. Its only sink is oxidation and photochemical breakdown in the stratosphere.

Organic chlorine in the troposphere increased from 2.58 ppb in 1985 to 3.53 ppb in 1994 and and 3.64 ppb in 1996. In the year 2000, less organic chlorine was found (3.52 ppm, WMO, 2003). CFC abundance in the troposphere peaked in 2001; although 95% of CFC are released in the northern hemisphere, their concentration is globally homogeneous; inter-hemispheric exchange occurs within 1.1–1.4 years. The temporal evolution of tropospheric CFC and methyl chloroform abundance is shown in Figure 2.10 as observed at remote stations (Montzka et al., 1999; Blake, 2004).

Effective equivalent chlorine (EECl) is the sum of all halocarbons weighted with their ozone depletion potential and considering their decomposition time (WMO, 1995). EECl peaked at 2230 ppt in 1994 (Montzka et al., 1996); since then, EECl has been declining due to the methyl chloroform reduction. When methyl chloroform is removed from the EECl trend, a small increase is still visible (10 ppt per year in 1997, Montzka et al., 1999).

Replacement strategies for CFC include the introduction of hydrogen atoms or the substitution of chlorine atoms with fluorine in CFCs. Hydrochlorofluorocarbons (HCFC) react more rapidly with OH than CFCs, their atmospheric life time is greatly reduced which is reflected in a lower weighting of HCFC for the calculation of EECl. For example, HCFC-141b (CH_3CCl_2F) replaced CFC-11 in many applications, with

Compound	DRF	IRF	RF	%
CO_2	1.4	–	1.4	50
CH_4	0.5	0.2	0.7	25
CFC	0.35	−0.1	0.25	9
N_2O	0.15	–	0.15	5
CO	–	0.15	0.15	5

Table 2.2: Climate radiative forcing (RF) of various gases in excess of the natural forcing. Total forcing is combined direct (DRF, absorption of IR) and indirect (IRF, e.g. ozone depletion) radiative forcing. Numbers are given in $\mathrm{W\,m^{-2}}$ (Waple et al., 2002).

reduced atmospheric life time of 9 years and global warming potential (GWP)[3] of 713 (in contrast to CFC-11 life time of 45 years and 4680 GWP, WMO, 2003). CFC-12 has been replaced by the hydrofluorocarbons HFC-134a (CH_2FCF_3) and HFC-152a (CH_3CHF_2). Degradation of HFC with OH and subsequent solution in water droplets removes HFC from the atmosphere; one of the products of HFC degradation, trifluoroacetic acid (TFA, $CF3CO_2H$) persists very long; initial concerns about its environmental toxicity have been disproved (e.g. Benesch et al., 2002).

Substitution of the chlorine atom with fluorine in CFC to make hydrofluorocarbons or perfluorocarbons (freons) may result in much longer life time and greater GWP, but reduces the ozone depletion potential to zero. Several bromine containing halocarbons (halons) are difficult to replace, for example, Halon-1211; halons that are used in fire extinguishers constitute a large reservoir of ODS that may be released much further into the future. Overall, in equivalents of carbon dioxide, the rate of change in greenhouse gases is approximately 1% per year. The 1% per year increase is often referred to as the "business as usual" scenario.

Radiative forcing

Radiative forcing (RF) of a greenhouse gas or other climate-influencing factor is defined as "the change in net irradiance at the tropopause after allowing for stratospheric temperatures to readjust to radiative equilibrium, but with surface and tropospheric temperatures and state held fixed at the unperturbed values" (Ramaswamy et al., 2001). The tropopause is chosen as the top of the atmosphere for RF calculations since it equilibrates fast (on time scales of months) with the upper atmosphere.

In Table 2.2 the RF of various gases are shown according to the climate assessment by Waple et al. (2002); CO_2 and N_2O influence radiation directly whereas forcing by CFC and CH_4 is composed of direct radiative forcing (DRF) and indirect radiative forcing terms. For CFC, their negative effect on stratospheric ozone is accounted for by the negative indirect forcing (IRF). For methane, the enhancements of tropospheric ozone and stratospheric water vapour are seen as an additional positive IRF. Total and indirect radiative forcing by CO is about one tenth of the forcing by CO_2.

Radiative forcing contributions and the degree of knowledge thereof are summarised

[3]GWP is the relative strength of radiative forcing with respect to CO_2

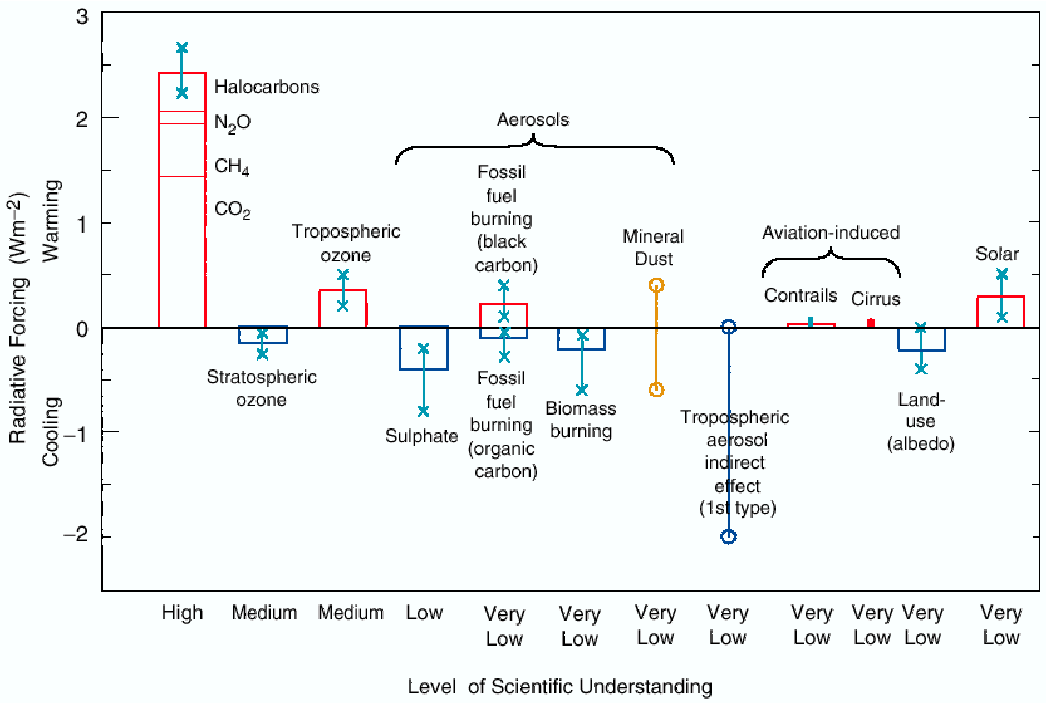

Figure 2.11: Additional climate forcing since the industrialisation and the level of understanding associated with individual forcing terms (Forster and Shine 1999, reprinted in Ramaswamy et al. 2001). The largest radiative forcing is contributed by well-mixed greenhouse gases; the uncertainty for GHG forcing is 10%, while magnitude and direction of cloud and aerosol forcings are very uncertain.

in Figure 2.11 (Ramaswamy et al., 2001). Direct forcing by greenhouse gases is relatively well understood, a medium understanding is assumed for the radiative forcing by ozone; additional radiative forcing by land use changes, solar variability, and aerosols is least understood; the combined aerosol forcing is a approximately $-0.5\,\mathrm{W\,m^{-2}}$.

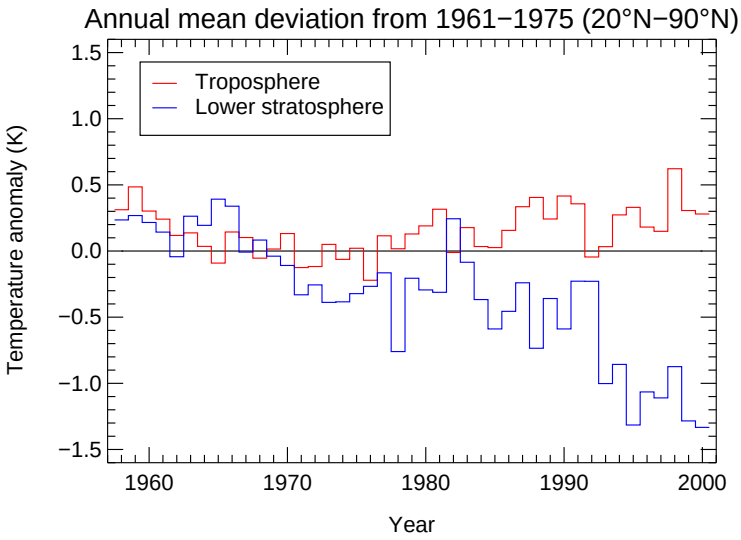

Figure 2.12: Tropospheric and stratospheric temperature in the northern hemisphere (> 20°N) from radiosondes. From 1979 to 1999, the global stratospheric cooling trend is −0.46° per decade and compares well with other observations of lower stratospheric temperature trends. Data Sterin (2001)

Tropospheric and stratospheric temperature

Waple et al. (2002) report that the global surface temperature in 2001 has been the second highest after 1998, the warmest year on record. Deviation from the 1880–2000 mean was +0.51°C (+0.63°C in 1998). Observations from the (Advanced) Microwave Sounding Unit (A)MSU show a tropospheric temperature trend of +0.05°C per decade since 1979. Figure 2.12 shows radiosonde data for northern hemispheric temperature. Radio sonde data is in line with (A)MSU observations which show a lower stratospheric temperature change of −0.5°C between the 1990s and 1990s. A large negative Arctic temperature anomaly, −6°C in January to March 2000, is reported by Waple et al. (2002).

Global surface temperature increased by 0.6°C during the last 150 years. The largest rate of temperature increase (0.17°C per decade) has been seen in the northern hemispheric winter temperature record (Folland et al., 2001). These strong northern hemispheric changes are related to a reduction of high-latitude and an increase of mid-latitude sea level pressure (increase of AO index, Shindell et al., 1999). Along with global increasing temperatures, longer growth and earlier blooming periods have been observed in higher latitudes; a poleward migration of species is noted; glaciers are globally retreating (ACIA, 2004).

Several studies discuss the feedback between observed Arctic stratospheric temperature decline, ozone depletion, and GHG increase. For example, Langematz (2000) finds that observed temperature changes cannot be explained by GHG changes alone: there must be a feedback effect from stratospheric ozone. Taking ozone into account, past changes cannot be completely, but partly explained by ozone depletion and greenhouse gas increase (Langematz et al., 2003). Similarly, Tett et al. (1996) show that observation of atmospheric vertical temperature since 1961 are best modelled including the decrease of stratospheric O_3 in their model.

2.4.3 Future changes

An overview of future expected climate changes is in detail provided by IPCC (2001). Here, selected expectations from the SRES A1B story line are briefly repeated. The A1B story line describes a scenario of rapid economic growth, population growth with a peak around 2050, fast introduction of new and efficient technologies, and a balance across energy sources (IPCC, 2000). As a result of this story line, CH_4 volume mixing ratio is expected to peak in 2050 at 2500 ppb, falling to 2000 ppb by 2100; HFC-134a increases to 900 ppt by 2100, N_2O increases to 370 ppb, OH decreases by 10% (Ehhalt et al., 2001). In the corresponding Ab baseline scenario from WMO (2003), effective equivalent stratospheric chlorine returns to pre-1980 values in 2043.

Surface temperatures are expected to increase by 2.1–3.8°C from 1990 to 2100. This temperature prediction is approximately 0.5°C higher than predictions based on the prior IS92a scenario (Cubasch et al., 2001). A possible massive release of methane from clathrates (Suess et al., 1999) is not considered in the above simulations to 2100; neither are stratospheric or biogeochemical feedbacks regarded.

The effect of N_2O persistent increase and CH_4 decrease after 2050 is examined in a study by Randeniya et al. (2002). Both the increase of N_2O mixing ratio may lead to more ozone depletion (enhancement of NO_x-cycles) and the decrease of CH_4. Methane promotes ozone formation in the by producing OH; OH combines with active nitrogen NO_x to the nitrogen reservoir HNO_3(denoxification). Although this study has received much criticism, it serves well as an example of possible interactions between climate change and ozone depletion in the future.

Circulation changes

Circulation changes can be diagnosed with changes in climatological patterns, for example, a change in the pressure difference between Aleutian high and Iceland low (NAO index). Consistent in climate models and analyses, the NAO index has a positive trend from negative values in the 1960s to positive values in the 1980s and 1990s; this positive trend has been linked to sea surface temperature (SST) increases (e.g. Paeth et al., 2003). The trend towards more positive values of the NAO index was simulated up to 2040 by Paeth et al. (1999). The decadal variability of the NAO index is reduced in Paeth et al.'s simulations which may supply Europe with more westerly and milder climate. A positive trend in NAO index with increasing greenhouse gases was confirmed by simulations extending to 2100 by Ulbrich and Christoph (1999); in spite of the trend, their simulated NAO is for most of their simulation within the variability of a control run without greenhouse gases; a north-eastward geographic shift is found for the northern NAO centre. The increase in storm track activity found by Ulbrich and Christoph exceeds control run variability from 2010 to 2100. The increase in storm track activity is used by Ramaswamy et al. (2001) to report that an increase of cyclone peak wind intensity is likely by 2100.

The studies cited above are consistent with the trend towards a more positive Arctic Oscillation due to GHG increases found by Shindell et al. (1999); an increase in the

AO index would strengthen the polar vortex (Thompson and Wallace, 1998). The past NAO trend is seen as well in time slice experiments with the E39C climate model for 1960, 1980, and 1990 conditions (Schnadt and Dameris, 2003); in their future projection for 2015, Schnadt and Dameris find a marked decrease of the NAO index towards negative values in contrast to results by Ulbrich and Christoph (1999), while both studies use SST from similar ECHAM4/OPYC simulations.

Stratospheric temperature and ozone loss

For the Arctic stratosphere, Kirk-Davidoff et al. (1999) predict a temperature drop of 3.8–11.4°C due to changes in tropical sea surface temperature (SST); these changes would introduce more water into the stratosphere and possibly induce more ozone loss. While an increase in SST temperature can accelerate the hydrological cycle and transport more H_2O to the tropopause by convection, the temperature evolution of cold point is uncertain. While some studies expect an increase of CPT due to greenhouse gases Forster and Joshi (e.g. 2005), other studies show a cooling trend at the tropical tropopause (e.g. Simmons et al., 1999; Zhou et al., 2001)

A cooling of the Arctic stratosphere by 7°C leads to 50% increased Arctic ozone depletion in model simulations by Shindell et al. (1998) which include GHG increases. Rex et al. (2004) found a linear relationship between V_{PSC} (which are related to temperature, cmp. Section 2.3.2) and chemical Arctic column ozone loss. Within the range of observed Arctic column ozone loss (0–100 DU) they relate ozone loss ΔO_3 (in DU) to uniform vortex cooling ΔT with the equation

$$\frac{\Delta O_3}{\Delta T} = 15 \frac{\mathrm{DU}}{\mathrm{K}} \tag{2.25}$$

Their approximation based on temperature only may not hold for winters where the cold pool area is different from the vortex area: Mann et al. (2002) describe the influence of vortex concentricity on the formation of NAT and subsequent denitrification in a chemistry climate model.

Similarly, Tilmes et al. (2004b) relate the volume of possible PSC to total ozone depletion in Arctic winters of the last decade. They find an increase of ozone depletion with V_{PSC} and stress that the amount of sunlight received on PSC surfaces is an additional important factor for chemical ozone loss. Tilmes et al. caution that a linear extrapolation to very large V_{PSC} may not be valid.

3 Models, data, and experiments

Ozone loss analyses are performed on two time slice experiments from the climate chemistry model E39C. Among ozone recovery prediction simulations from a variety of global circulation models, the E39C model shows the earliest signs of ozone recovery, namely in its 2015 time slice (cmp. Figure 1.2, WMO, 2003). This is seen in a significant enhancement of the spring minimum Arctic ozone column.

Chemical ozone loss in time slice experiments 1990 and 2015 is assessed with a methane-ozone tracer correlation. Total changes in ozone column can then be separated from changes due to chemistry.

Focusing on a cold winter (with large ozone loss) of the 2015 time slice experiment, simulations with the Chemistry Transport Model CLaMS are performed. In CLaMS, a passive ozone tracer is used as a quantitative measure of chemical ozone loss in addition to the tracer correlation technique. Chemical loss is investigated towards its sensitivity to loss determination methods and to chemical and numerical processes with CLaMS.

3.1 The Global Circulation Model ECHAM.DLR(L39)/CHEM

The ECHAM model family is based on the European Centre for Medium range Weather Forecast (ECMWF) model which was adapted to a climate model configuration by Roeckner et al. (1992).

3.1.1 The ECHAM model family

The ECHAM suite of models comprises subsequent versions 1 to 5, extensions to the middle atmosphere, and a whole atmosphere configuration. ECHAM models are global and three-dimensional, where the horizontal representation is in spectral space and the vertical coordinate are topography following hybrid sigma-pressure surfaces. ECHAM is categorised as an atmospheric global circulation model (AGCM): The interaction with other components of the Earth system —primarily the cryosphere, ocean and land surface— needs to be prescribed at the model domain boundaries. From early versions on, coupled atmospheric-ocean global circulation models have been realised with ECHAM, for example, ECHAM1/LSG (Cubasch et al., 1992) or ECHAM2/OPYC (Lunkeit et al., 1996). Prognostic variables vorticity, divergence, surface pressure and temperature are represented in spherical space with triangular truncation at wavenumbers 21, 30, 42 or 106; nonlinear quantities are computed after a transformation to a Gaussian grid.

Both ECHAM3 and ECHAM4 standard versions extend from the surface up to 10 hPa on 19 irregularly spaced levels (cmp. Schnadt (2001, Figure 3.1)) with seven stratospheric levels between 200 hPa and 10 hPa. The order of the horizontal diffusion scheme is reduced (from 4 to 2 in ECHAM3, from 10 to 2 in ECHAM4) in upper model layers, thus creating a "sponge" layer with increased wave damping and diffusion. Orographic gravity wave drag is simulated after Miller et al. (1989).

The Global Circulation Model ECHAM4 was presented by Roeckner et al. in 1996 as a successor to the ECHAM3 GCM (DKRZ, 1992; Roeckner et al., 1992). In ECHAM4, cloud water content and specific humidity as prognostic variables and up to 21 tracers are transported by a semi-Lagrangian scheme after Williamson and Rasch (1994). This semi-Lagrangian scheme was found to realistically simulate the polar vortex pattern (Austin et al., 2003). Mass conservation, however, has to be enforced by additional mass fixing corrections. Radiation is calculated according to Fouquart and Bonnel (1980) (shortwave) and Morcrette (1991) (long wave); GHG including chlorofluorocarbons (CFC) are considered in the radiation scheme.

Development is continuing at the Max-Planck Institute for Meteorology in Hamburg towards ECHAM5 (Roeckner et al., 2003, 2004). A middle atmosphere version of ECHAM4 extends up to 0.01 hPa and is described in Manzini and McFarlane (1998), the whole atmosphere version HAMMONIA (Schmidt and Brasseur, 2004; Schmidt et al., 2005) extends up to ≈ 250 km.

Family	Composition
O_x	$O_3 + O(^3P) + O(^1D)$
NOX	$N + NO + NO_2 + NO_3 + 2N_2O_5 + HNO_4$
ClOX	$Cl + ClO + HOCl + 2Cl_2O_2 + 2Cl_2$
HO_x	$H + OH + HO_2$

Table 3.1: Chemical families in E39C; families NOX and ClOX differ from the families ClO_x and NO_x defined in Table 2.1

3.1.2 ECHAM4 at DLR version

At Deutsches Zentrum für Luft und Raumfahrt (DLR) Oberpfaffenhofen, a special 39 layer version of the ECHAM model was constructed with increased vertical resolution around the tropopause (700 m, Land et al., 1999); thus, the effects of damping can be confined to layers above 25 hPa, ensuring a better agreement of lower stratospheric variability in the model with ECMWF reanalyses (Land et al., 1999). High numerical diffusion leads to lower than observed age of air (Hein et al., 2001).

The model dynamics were interactively coupled to the stratospheric chemistry module CHEM (Steil et al. 1998, described in the next section), thus constituting a chemistry climate model (CCM), designated ECHAM3.DLR(L39)/CHEM. The increase in vertical resolution was aimed at performing climate change studies related to the effects of air traffic, particularly of supersonic aircraft and NO_x emissions (e.g. Dameris et al., 1998; Grewe et al., 2001a) and at assessing climate chemistry interactions in the lower stratosphere (e.g. Dameris et al., 1998; Shine et al., 2003; Grewe et al., 2001b). In ECHAM3.DLR(L39)/CHEM the chemical time step is equal to the dynamical time step: for the first time, long-term simulations with online feedback between dynamics and chemistry could be performed. The feedback is realised by passing the chemically altered fields of O_3, CH_4, N_2O, CFC, and H_2O from CHEM to ECHAM at each time step.

The current model version ECHAM4.DLR(L39)/CHEM, is commonly (as within this thesis) abbreviated to E39C. In comparison to its predecessor, the horizontal resolution is increased to T30 truncation (equivalent to 6° resolution for dynamics); tracers and microphysics are calculated on the Gaussian transform of this spherical grid, which has a resolution of $3.75° \times 3.75°$ longitude by latitude. A new radiation scheme (Landgraf and Crutzen, 1998) and orographic gravity wave drag were added; the model does not simulate the quasi-biennial oscillation (QBO).

3.1.3 Stratospheric chemistry module CHEM

The chemistry module CHEM(Steil, 1998; Steil et al., 1998; Hein et al., 2001) describes 107 reactions with 37 chemical species, of which 9 species (CH_4, N_2O, HCl, H_2O_2, CO, CH_3O_2H, $ClONO_2$, HNO_3, H_2O) and 3 families (odd oxygen O_x, oxidised nitrogen NOX, active or oxidised chlorine ClOX, cmp. Table 3.1) are advected. These families were set up to allow for a variable and large integration time step of up to 30 min, which is equal to the dynamical time step of E39C. Boundary conditions for

Scenario	CO_2(ppm)	N_2O(ppb)	CH_4(ppm)	Cl_y(ppb)
1990	353	310	1.69	3.4
2015	405	333	2.05	3.1

Table 3.2: Boundary conditions used in E39C time slice experiments (Surface GHG, stratospheric Cl_y Schnadt, 2001, Table 4.2)

NO_y (=NOX+HNO_3), CFC, and ClOX are based on simulations with the Mainz-2D chemical model (Grooß, 1996).

Polar stratospheric clouds of type I (nitric acid trihydrate, NAT) and type II (water ice) are formed in the model. NAT existence is calculated according to Hanson and Mauersberger (1988), Equation (2.18); for the actual formation of particles, a 10-fold supersaturation is required by specifying a nucleation barrier equivalent to −3 K supercooling. Sedimentation of NAT particles occurs only when ice is present (Steil, 1998). CHEM contains heterogeneous reactions on solid PSC and the stratospheric background aerosol. Heterogeneous reactions on liquid PSC are not considered.

Notably, bromine chemistry is excluded from the current model version, resulting in an underestimation of chemical ozone depletion especially in the northern hemisphere (Schnadt, 2001); Bregman et al. (1997) find that neglect of bromine chemistry leads to an underestimation of ozone loss on the order of 25%.

3.2 Time slice experiments with E39C

Several time slice experiments have been performed with E39C.which depend on scenarios of emissions and oceanic sea surface temperature; they are used to extrapolate current climate to future or past mean climate and climate variability. Time slice experiments are free-running model simulations with a periodically fixed seasonal cycle of boundary conditions. To exclude effects of the initialisation, several model periods (the spin-up phase) at the beginning of a time slice experiment are disconsidered. With E39C, time slice experiments have been performed for 1960, 1980, 1990, 2000 and 2015 climates; this thesis focuses on the time slice experiment with 2015 boundary conditions and analyses chemical ozone loss in time slice 1990.

Within this thesis, the original DLR naming for individual years of time slice experiments is followed: each time slice (1990 and 2015) consists of 24 simulation years, starting with year 39. The spin-up phase is four years, years numbered 39–42 are not used for analysis. The notation 2015/58 thus refers to the 16^{th} analysed simulation cycle within 2015 boundary conditions.

Upper boundary conditions for the time slice experiments 1990 and 2015 are provided by the Mainz-2D model (Grooß, 1996, CFC, Cl_y, NO_y), based on the IS92a scenario (IPCC 1995 and WMO 1999); surface boundary conditions (GHG) are taken from IS92a and summarised in Table 3.2. A description of NO_x boundary conditions including traffic and biomass burning is provided by Schnadt (2001, Chapter 4.1).

3.2.1 Control experiment 1990

Hein et al. (2001) compared the 1990 20-year time slice with NCEP reanalyses for the years 1978–1998 and found that the E39C model captures well the observed dynamics in the northern hemisphere lower stratosphere: The annual cycle of zonal mean zonal wind at 60°N and 30 hPa, as well as the temperature difference to the North Pole agreee reasonably with NCEP and Freie Universität Berlin (FUB) analyses: a slightly stronger zonal wind in the model corresponds to a larger poleward temperature gradient. The calculation of too low polar temperatures, is described for E39C by Schnadt (2001) as −1 K at the 30 hPa level, up to −5 K below, and up to −12 K above. This cold bias may lead to stronger chlorine activation; however, for the Arctic, activation simulated by E39C is found to agree with results from the SLIMCAT model (e.g. Chipperfield, 2003) and HALOE observations (Hein et al., 2001).

The climatological pattern of the zonal mean wind is captured well with E39C in comparison to ECMWF reanalyses for the years 1979–1994. While the summer circulation is not modelled well by E39C, the PNJ and subtropical jet are positioned correctly. The modelled Arctic PNJ at 60°N and 30 hPa is on average 10 $\mathrm{m\,s^{-1}}$ stronger than the analysed jet stream. The inter-hemispheric difference in the residual circulation (stronger in boreal winter) is present in the model. Schnadt (2001) finds satisfactory vertical descent of the vortex at 50 hPa; vertical descent was especially improved with respect to previous model versions where slight ascent had been simulated (cmp. Section 5.1). The temporal distribution of stratospheric warming events slightly underestimates (is in agreement with) observed interannual variability in early (late) winter. The pattern of Arctic March monthly mean column ozone generated in this time slice is found to agree with ECMWF reanalyses. E39C is found to overestimate column ozone by 25 DU on average. Compared to observations, the position of the tropopause is located too high in high latitudes of both hemispheres. The local maximum of ozone loss is simulated at higher than observed altitudes (V. Grewe, personal communication, 2003).

Compared to GOME (Burrows et al., 1999) observations and the ozone climatology by Fortuin and Kelder (1998, cmp. Figure 2.5), the model simulated ozone mixing ratio above 50 hPa is 0.5–2 ppm higher in northern hemispheric winter and spring; between 200 and 70 hPa, ozone mixing ratios are underestimated by up to −0.25 ppm (Hein et al., 2001). In the climatological mean, there is no ozone depletion in time slice 1990 at 30 hPa within the North Polar vortex; at this level, maximum simulated ozone depletion is 1 ppm, the standard deviation from the climatological mean ozone loss is ±0.5 ppm (Schnadt, 2001).

Denitrification is overestimated in the model due to the negative temperature bias: in the climatological mean, vortex core mixing ratio of HNO_3 is 1 ppb. Dehydration removes 50% of the stratospheric polar vortex water vapour from December to February. As noted above, chlorine activation is realistic, maximum activation is 2.2 ppb at 30 hPa and north of 75°N.

	1990 (Jan)	1990 (Apr)	2015 (Jan)	2015 (Apr)	
Temperature	203 ± 4.1	221 ± 6.6	204 ± 4.0	222 ± 5.5	K
Ozone	4.09 ± 0.17	4.26 ± 0.35	4.17 ± 0.16	4.57 ± 0.19	ppm
Methane	1.26 ± 0.02	1.27 ± 0.03	1.56 ± 0.03	1.57 ± 0.04	ppm
N_2O	165 ± 5.3	166 ± 10.8	184 ± 7.9	185 ± 11.2	ppb
Water	3.76 ± 0.14	3.71 ± 0.07	4.29 ± 0.30	4.36 ± 0.09	ppm
NO_y	10.3 ± 0.61	8.95 ± 1.10	11.2 ± 0.9	10.6 ± 1.1	ppb
Cl_y	2.22 ± 0.07	2.07 ± 0.12	1.52 ± 0.10	1.48 ± 0.09	ppb
$ClONO_2$	0.371 ± 0.09	1.13 ± 0.13	0.290 ± 0.09	0.775 ± 0.10	ppb
HCl	0.454 ± 0.07	0.745 ± 0.15	0.295 ± 0.09	0.647 ± 0.10	ppb
NAT	2.12 ± 0.94	(56, 60)	2.13 ± 0.99	–	ppb
ice	165 ± 165	(56, 60)	236 ± 162	–	ppb
Cl-activation	38.2 ± 12.2	6.8 ± 7.2	33.5 ± 13.2	2.6 ± 1.4	percent

Table 3.3: Chemical composition of Arctic stratosphere in 1990 and 2015. Shown are means of chemical species and families averaged over all winters of each time slice 1990 and 2015 on 1 January and 1 April. Numbers are averages of data north of 60° at 50 hPa. In parentheses, the index of years where NAT/ice with volume mixing ratio greater than 1 ppt are present in April.

3.2.2 Experiment 2015

In her detailed analysis of the 2015 experiment, Schnadt (2001) reports an Arctic stratospheric temperature increase (4–6°C) with respect to the 1990 experiment for mid-January to April. NAT formation, ice formation, and A_{PSC} are decreased; denitrification and dehydration are less severe. Within the North Polar winter vortex, significantly less chlorine is activated in 2015 (difference to 1990: -0.7 ppb at 30 hPa) and it is earlier deactivated: ozone loss decreases by up to 0.6 ppm.

For 2015, Schnadt finds increased planetary wave breaking and associated deceleration of zonal circulation. The North Polar vortex is more labile due to more stratospheric warming events (32 versus 23 in 1990). The temperature increase that follows from the weaker vortex over-compensates the temperature decrease that is expected from elevated GHG levels; in fact, a stratospheric cooling is simulated by E39C for the southern hemisphere from 1990 to 2015.

Stratospheric chemical composition 1990 and 2015

The chemical composition of Arctic stratospheric air for 1990 and 2015 in the E39C model is shown in Table 3.3[1]. Activation in this table is defined as the percentage of Cl_y which is not in the reservoirs $ClONO_2$, HCl or HOCl. Large changes between the time slice means are seen in mixing ratios of methane, nitrous oxide and water which increase by 0.3 ppm, 20 ppb and 0.6 ppm, respectively. Total inorganic chlorine

[1] April data for winter 1990/62 were excluded from the time slice mean due to partial data corruption which resulted in unrealistically high NO_y and Cl_y mixing ratios.

decreases by 30% at this altitude and geographic area, while at the model top, a 9% decrease of Cl_y was prescribed. In both time slices, activation is similar in January around 35%, PSC are present in the form of NAT ($\approx$ 20% of NO_y) and ice, and mean temperatures are slightly above 200 K, warming to around 220 K in April. In the later time slice, more water is in condensed phase with less variability ($\approx$ 5.5%) compared to 1990 ($\approx$ 4.8%).

3.3 The Chemical Lagrangian Model of the Stratosphere (CLaMS)

The Chemical Lagrangian Model of the Stratosphere (CLaMS) is a Lagrangian chemical transport model (CTM) hierarchy; details of the model are described in McKenna et al. (2002a,b). The model hierarchy is composed of three core modules which describe (a) Lagrangian advection on isentropes and cross-isentropic motion (b) box model gas phase, photo-reactive and heterogeneous chemistry, and (c) Lagrangian mixing based on flow deformation. Preprocessors for (d) calculation of potential vorticity and equivalent latitude, (e) interpolation of pressure gridded data onto isentropes, (f) heating rate calculation, (g) assimilation of irregular and regularly gridded external chemical data into the model, and (h) tracer-PV mapping tools complement the core modules.

CLaMS has been used in a number of studies describing issues in the Arctic and Antarctic polar stratosphere: the box model chemistry was applied to derive chemical ozone loss on idealised trajectories for winters 1991-92 (Becker et al., 1998) and 1994-95 (Becker et al., 2000b)[2]. The formation of filaments has been modelled in CLaMS in comparison to Eulerian schemes and satellite observations (McKenna et al., 2002b); mixing across at the edge of the polar vortex as observed by the Cryogenic Infrared Spectrometers and Telescopes for the Atmosphere (CRISTA) instrument was realistically simulated with CLaMS (Konopka et al., 2005b); the successful simulation of vortex isolation was shown by McKenna et al. (2002a), comparing CLaMS simulated ClO and O_3 fields to Microwave Limbs Sounder (MLS) and HALOE observations. The influence of vortex remnants was simulated with CLaMS by Konopka et al. (2003a); conversely, the influence of extra-vortex intrusions was examined with CLaMS by Grooß and Müller (2003). CLaMS gas phase and heterogeneous chemistry was found to compare well to other stratospheric chemistry models in an intercomparison study by Krämer et al. (2003).

CLaMS participated in three large international campaigns: the Sage III Ozone Loss and Validation Experiment/Third European Stratospheric Experiment on Ozone (SOLVE/THESEO) in Arctic winter 1999-2000; the European Polar Stratospheric Cloud and Lee Wave Experiment (EUPLEX) in Arctic winter 2002-2003; and the Tropical Convection Cirrus and Nitrogen Oxides experiment (TROCCINOX) over Brasil in early 2005. During SOLVE, Konopka et al. (2003b) validated the mixing

[2]In the study by Becker et al., the original FACSIMILE solver was employed which was later replaced by the ASAD code

scheme in comparison to high temporal resolution *in situ* data from the ER-2 aircraft; for this winter, simulations with a focus on three-dimensional mixing (Konopka et al., 2004) and ozone depletion (Grooß et al., 2002) were performed with CLaMS; chemical ozone depletion during the EUPLEX campaign was studied by Grooß et al. (2004).

Stratospheric chemistry and mixing during the unusual Antarctic vortex split in September 2002 were simulated with CLaMS by Grooß et al. (2005) and Konopka et al. (2005a). Investigations towards and understanding of NO_x induced chemical loss in the upper stratosphere (P. Konopka, in preparation 2005) and the UTLS (Günther et al., 2004) region are ongoing.

3.3.1 Lagrangian concepts

In a Lagrangian view, flow of a fluid is considered as a function of space and time. The flow is represented by an ensemble of air parcels (AP) which are advected with the flow along trajectories. Along individual trajectories, changes of chemical AP properties are uncoupled from the fluid motion. In contrast, a Eulerian description of fluid motion describes the time-dependent change of flow properties at fixed (grid) points in space: a change of chemical properties at any grid point may be a combined result of advection and chemical processes (e.g. Stohl, 1998). Though Eulerian models are more widespread, in a Lagrangian world the separation of different processes is simpler. On the other hand, Lagrangian models do not account for interaction of AP, as it is necessary for diffusive processes to be realised in a CTM. The CLaMS Lagrangian mixing scheme introduces controlled numerical diffusion, triggered by the flow deformations that are generally expected to drive the turbulence in the atmosphere.

3.3.2 Organisation and modularity

The organisation of modules within the CLaMS hierarchy is shown in Figure 3.1. Core modules are called in succession, this succession is repeated for every time step τ. (a) Trajectory module: air parcel (AP) trajectories are calculated based on meteorological data and integrated over τ, typically one day; vertical descent is driven by a radiation scheme. (b) Chemistry module: box model chemistry is calculated on each trajectory, including photolysis and heterogeneous reactions. At the first time step, chemical species are initialised from a 2D model calculation, satellite observations or PV-tracer correlations; at successive time steps, the output of the mixing module is used as input. (c) Lagrangian mixing: a grid adaptation is performed on the deformed AP distribution, thus introducing mixing and creating a new (and more regular) AP distribution which is used as input for the trajectory module; the frequency of mixing is $\frac{1}{\tau}$.

The CLaMS hierarchy is highly flexible. Trajectories can be run in forward or backward mode; asynoptic data can be assimilated in the trajectory module; this module has been used with up to five million AP (Konopka et al., 2005a). Box model chemistry can be applied to any number of trajectories (current simulations use up to 440 000 AP, Grooß et al., 2004); switches for different numerical solvers,

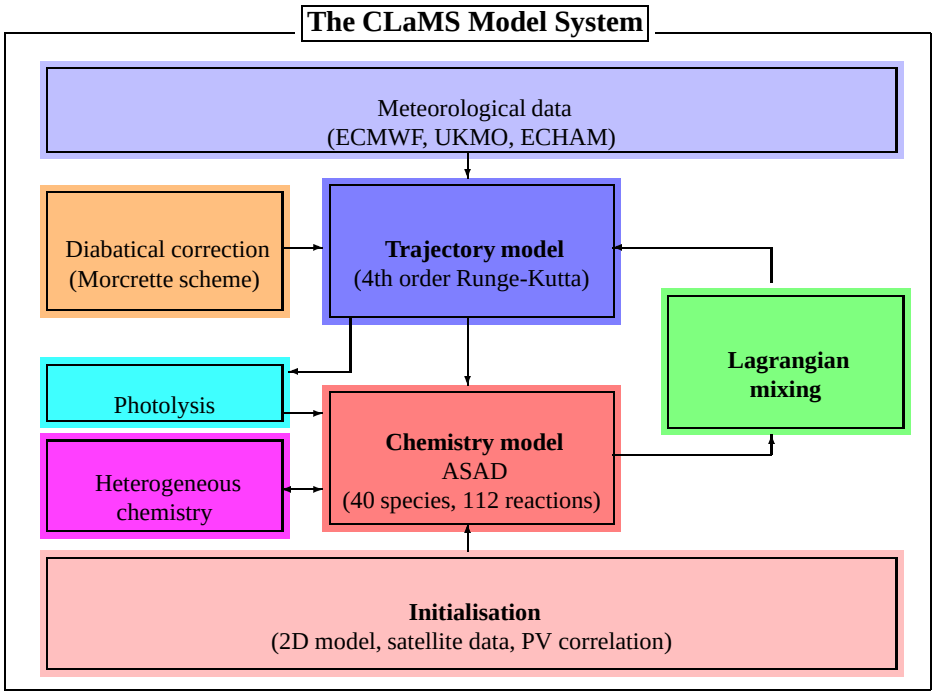

Figure 3.1: The CLaMS model hierarchy. Core components are the calculation of three-dimensional trajectories, box model chemistry, and Lagrangian mixing.

photolysis schemes, heterogeneous chemistry and sedimentation facilitate sensitivity studies. Intensity of mixing is variable, horizontal and vertical domain boundary conditions can be supplied.

3.3.3 Wind fields, heating calculation and trajectories

Like other CTMs, CLaMS depends on external data for wind (U, V), temperature (T) and pressure (p). Different horizontal and vertical resolution, or the frequency of meteorological input data can be accommodated by the CLaMS preprocessors. Previous studies have made use of United Kingdom Meteorological Office (UKMO) and ECMWF find fields, both analysed winds (ECMWF reanalysis, ERA-15 and ERA-40) as well as forecasts (e.g., during the TROCCINOX and EUPLEX campaigns). In this thesis, CLaMS is operated for the first time on climate model output.

Since motion in the stratosphere is isentropic on short time scales, the "natural" vertical coordinate in the stratosphere is potential temperature (θ). Using θ as the vertical coordinate, horizontal motion describes motion on isentropes, while vertical motion is identified with cross-isentropic (diabatic) motion: the local change in potential temperature $\dot{\theta}$ is used as the vertical velocity.

The wind field is interpolated onto potential temperature levels. Diabatic heating rates $(\dot{T})$ on isentropes are calculated from a radiative transport model simulation (Morcrette 1991, with updates from Zhong and Haigh 1995) and converted to $\dot{\theta}$.

Wind velocities $(U, V, \dot{\theta})$ are linearly interpolated to AP locations. Using the scheme

Advected tracers	N_2O_5, HNO_4, HNO_3, H_2O_2, H_2O, CO, HCHO,	
	CH_4, CH_3OO, CH_3OOH, CH_3OOH, CH_3OH, $CH_3O_2NO_2$,	
	Cl_2, ClO_2, HOCl, HCl, $ClONO_2$, ClONO,	
	HBr, HOBr, $BrONO_2$, BrCl, Br_2	
Constant tracers	H_2, CO_2, O_2, N_2, N_2O	
Steady state	OH, HO_2	
Advected families	O_x	$= O_3 + O(^1D) + O(^3P)$
	NO_x	$= NO + NO_2 + NO_3$
	ClO_x	$= Cl + 2Cl_2O_2 + ClO$
	Br_x	$= Br + BrO$

Table 3.4: Chemical species considered for CLaMS chemistry.

of Sutton et al. (1994), which employs a fourth order Runge-Kutta integration with a 30 min time step, air parcel trajectories are calculated. Initial air parcel locations can be arbitrarily chosen in CLaMS; most often, initial positions are chosen as equidistant (quasi uniform) distributions or based on observation locations, for example, aircraft paths or satellite sounding positions.

3.3.4 Box model chemistry, photolysis, and microphysics

The chemistry module is based on "A Self-contained Atmospheric chemistry code" (ASAD) developed at the University of Cambridge. This code provides a flexible and extensible mechanism for the set-up of chemical reactions and chemical families and is described in detail by Carver et al. (1997a) and Carver et al. (1997b). For the experiments discussed in this thesis, 112 reactions and 41 species are considered. To overcome the large difference of reaction time scales, a family concept is employed (cmp. Section 2.3.1) and integrated with the Implicit Algorithm for Chemical Time-stepping (IMPACT, Carver and Scott, 2000) family solver: Of the 41 species, five are treated as constant tracers, 23 as active tracers, 11 are combined into four families, and two odd hydrogen species are calculated in steady-state The chemical families are odd oxygen (O_x), nitrogen oxides (NO_x), active chlorine (ClO_x), and active bromine (Br_x); the composition of families and all tracers are listed in Table 3.4. The internal chemical time step is 10 minutes.

Results with the IMPACT solver were found to compare well with more robust stiff solvers (McKenna et al., 2002a) and its results were validated against a range of CTMs (Krämer et al., 2003). Rate coefficients and absorption cross sections according to DeMore et al. (1997) and Sander et al. (2003) are used for gas phase and photochemical reactions. Heterogeneous reaction rates on STS (supercooled ternary solution droplets), SAT, NAT and ice are calculated with parameterisations by Carslaw et al. (1995a,b, 1997b) and Carslaw and Peter (1997). All reaction rates are updated hourly; a detailed summary of reactions and reaction rate coefficients is provided in McKenna et al. (2002a).

The photolysis scheme is calculated based on ozone and oxygen profiles from the

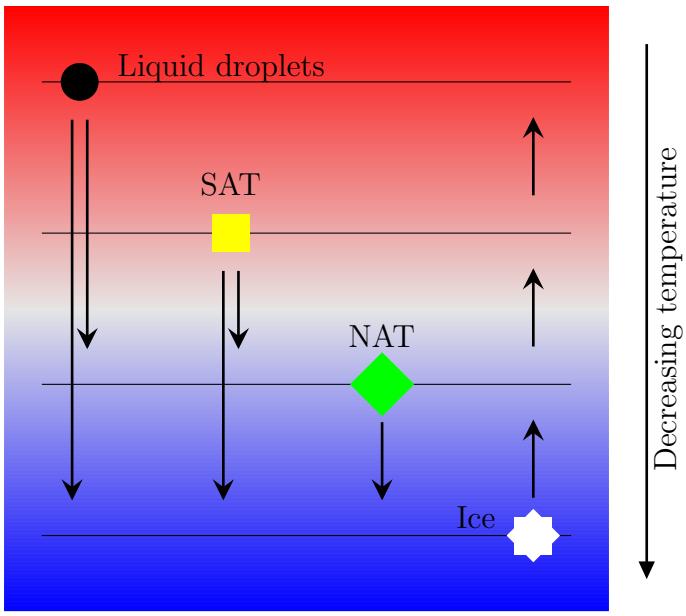

Figure 3.2: Particle state transition diagram used in CLaMS, each possible transition is indicated by arrows. While melting from the four particle types occurs in stages, homogeneous freezing of liquid droplets to SAT is excluded taking into account the high supersaturation required for this freezing process.

Mainz-2D chemical model (Grooß, 1996) using a scheme by Lary and Pyle (1991). This scheme calculates radiative transfer in 100 bands in spherical geometry and was improved by (Becker et al., 2000a). Aerosol microphysics is parameterised with the Carslaw et al. (1997a) scheme. Allowed phase transitions upon cooling are: STS to NAT or ice, SAT to NAT or ice, NAT to ice. NAT is formed from STS when nitric acid supersaturation with respect to NAT exceeds 10, comparable to a required supercooling of −3°C. Melting occurs in a cascade from ice to NAT to SAT to STS. These phase transitions are displayed in Figure 3.2. Sedimentation of large ice and NAT particles is parameterised at a constant fall rate of 250 m day^{-1} (Grooß et al., 2002). An updated sedimentation scheme including renitrification is under development (Grooß et al., 2004) but not included in the model version employed for this thesis.

3.3.5 CLaMS and CHEM in contrast

Both CLaMS and CHEM are are based on chemical models developed at the Max Planck institute for chemistry (MPI-C) in Mainz. In contrast to the Mainz-2D chemical model (Gidel et al., 1983; Brühl and Crutzen, 1988), a box model for use on trajectories was developed by Crutzen et al. (1992) and Müller et al. (1994); this box model is described in detail by Müller (1994): it uses the FACSIMILE chemical solver and includes heterogeneous chemistry. At Forschungszentrum Jülich, the ASAD chemical integration package was integrated into the MPI-C box model, leading to CLaMS (McKenna et al., 2002a). In a different direction, CHEM evolved as an efficient chemistry code for use in global circulation models, including larger chemical families. The fast numerical scheme in CHEM was validated with FACSIMILE (Steil, 1998). Both CLaMS and CHEM share many similarities (e.g. number of species and chemical reactions, heterogeneous chemistry on solids, supercooling), there remain important differences between the two models: (a) Bromine chemistry is not considered in E39C;

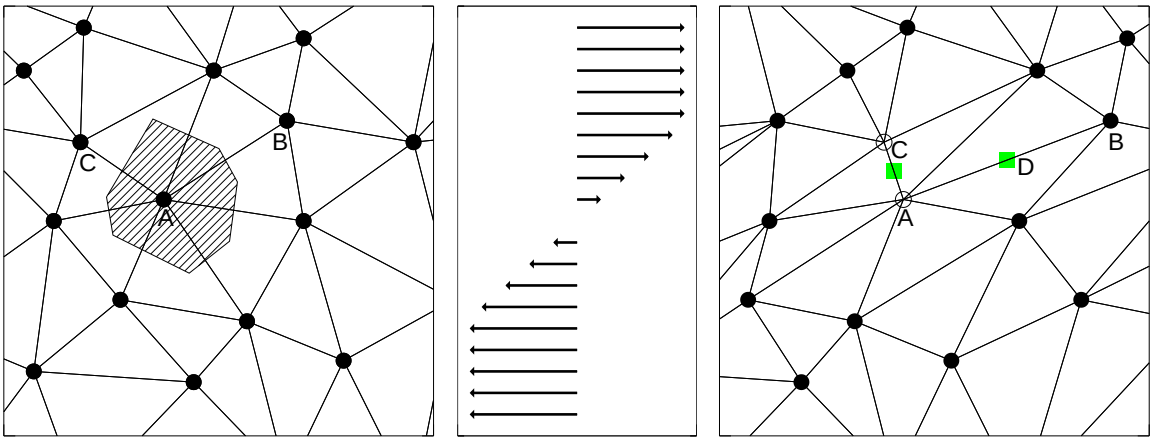

Figure 3.3: Schematic of mixing by grid adaptation. Before advection **(left)** the air parcels are distributed quasi uniformly with mean spacing $\bar{r}_{\text{fine}}$. Nearest neighbours are determined for each AP by Delauney triangulation. Points B and C are two NN of A; the shading around A shows the convex hull of A (Barber et al., 1996). By advection in sheared or strained flow (centre sketch of wind field), the grid is deformed **(right)**. The relative contraction or expansion of NN distance is compared to a critical deformation threshold. If this threshold is exceeded ($\overline{\text{AB}}$), a new AP with average characteristics of AP A and B is introduced in the grid (D); if the inverse of the threshold is exceeded ($\overline{\text{AC}}$), both air parcels are removed from the grid and a new AP is inserted half way between A and C (merging, McKenna et al., 2002a).

(b) CLaMS resolves a larger number of individual tracers, whereas in CHEM larger families are used (having the advantage of a larger integration time step); (c) the larger time step in CHEM requires a faster photolysis scheme (Landgraf and Crutzen, 1998, 9 bands, plan-parallel) than is used in CLaMS (Lary and Pyle, 1991, 100 bands, spherical). (d) the versions of JPL reaction rates (DeMore et al., 1997; Sander et al., 2000b, 2003) differ; (e) different sedimentation schemes are implemented for CLaMS (Grooß et al., 2002) and E39C (Steil et al., 1998); (f) heterogeneous reactions not on liquids are not considered in E39C.

3.3.6 Lagrangian mixing and grid adaptation

Mixing between CLaMS air parcels is based on the deformation of the quasi uniform air parcel distribution or "grid". It is in detail described by McKenna et al. (2002a) and Konopka et al. (2004). Grid deformation occurs in sheared (horizontal) or strained (vertical) flow. Strong shear or strain is physically related to turbulent mixing: mixing in CLaMS is anisotropic and not driven by the tracer gradient in contrast to diffusion schemes in Eulerian models; it only acts at locations of high wind shear and is not uniform across the model domain.

Grid deformation is quantified by the elongation or contraction of nearest neighbour (NN) relationships. NN are determined before advection by Delauney triangulation

(e.g. Preparata and Shamos, 1985); after each advection step, the relative elongation or contraction of the distance between two NN is compared to the critical deformation threshold $\exp \pm \ell_c \tau$, where the signs correspond to elongation and contraction of the grid APs, and ℓ_c is a free parameter. If the critical threshold is exceeded[3], the grid is adapted as described in the figure caption to Figure 3.3 and numerical diffusion is introduced. This grid adaptation ensures that the total number of air parcels is fairly constant for all simulations and that the grid is restored to quasi uniform AP distribution after the mixing procedure.

The Lyapunov exponent ℓ describes the deformation rate of a hypothetical circle around an air parcel to an ellipsis: along the wind, elongation occurs, contraction across the wind. Grid adaptation for conditions where $\ell > \ell_c$ is related to numerical diffusivity by (McKenna et al., 2002a):

$$\begin{aligned} D_+(\ell) &\approx \frac{\bar{r}_{\text{fine}}^2}{4\tau} \exp(+2\ell\tau) \\ D_-(\ell) &\approx \frac{\bar{r}_{\text{fine}}^2}{4\tau} \exp(-2\ell\tau). \end{aligned} \tag{3.1}$$

In two dimensions, D_+ and D_- estimate magnitude of diffusion along and across the wind, respectively. For the reference two-dimensional experiments (Section 3.5, $\ell_c = 1.2\,\text{d}^{-1}$, $\bar{r}_{\text{fine}} = 100\,\text{km}$, $\tau = 24\,\text{h}$) these diffusivities are on the order of $D_+ = 3 \cdot 10^4\,\text{m}^2\text{s}^{-1}$ and $D_- = 2 \cdot 10^2\,\text{m}^2\text{s}^{-1}$.

With the parameter ℓ_c, CLaMS mixing can be tightly controlled. In various comparisons to in-situ and remote sensing tracer observations, optimal values for ℓ_c have been determined. For example, Konopka et al. (2003b) show the realistic simulation of a high resolution tracer (CH_4) measurement from high altitude aircraft (ER-2) with adjusted mixing; McKenna et al. (2002a) validate ℓ_c on CRISTA observed N_2O tracer distributions; Konopka et al. (2004) develop a theoretical framework to optimise ℓ_c to observed time-series variability and tracer-tracer correlations. Suggested values for ℓ_c in the above studies range from 0.8–1.5 d^{-1}.

3.4 Experimental setup of CLaMS

3.4.1 Boundary conditions from Mainz 2D

For the calculation of heating rates and photolysis, and for model initialisation of bromine species, results of a Mainz 2D (Grooß, 1996) transient model simulation extending to 2015 were provided by J.-U. Grooß (personal communication, 2003). This transient simulation is based on greenhouse gas scenarios from the WMO (1999, p 12.7) assessment and prescribes 1825 ppb CH_4 loading in the troposphere, which is a comparable value to the loading suggested in the later IPCC (2001) and WMO (2003) reports (1875 ppb). CFC and related emissions are based on the WMO (2003, p 1.66) Ab baseline scenario; Ab is considered the "best estimate" scenario. Global January

[3] or is undercut, in the case of contraction

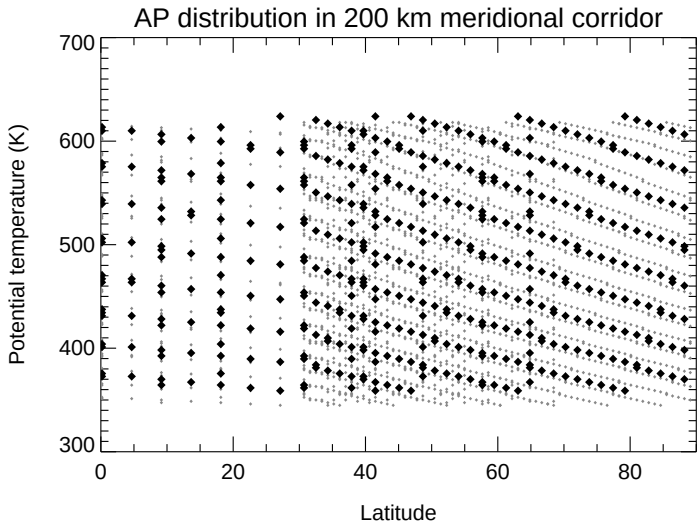

Figure 3.4: Initial air parcel distribution for CLaMS three-dimensional simulations. The large black diamonds are AP locations for a resolution of 200 km, the smaller grey diamonds AP locations at $\bar{r}_{\text{fine}} = 100$ km.

2015 surface mixing ratios for bromine species in Ab are (in ppt): Halon-1211 3.19, Halon-1301 3.52, Halon-2402 0.26, CH_3Br 8.4. Boundary conditions are calculated on a monthly basis in equivalent latitude-pressure space. E39C also uses Mainz-2D output for ClX and NOX boundary conditions.

3.4.2 Parameters and data specific to this study

Meteorological fields (horizontal winds, temperature, pressure) from E39C are available every 12 hours at 0:00 and 12:00 UTC. For all simulation days, these fields are interpolated onto isentropic levels between 350 and 610 K. For the calculation of heating rates, H_2O, CO_2, and O_3 January 2015 profiles from the above described Mainz 2D model calculation are used.

Initial air parcel distribution is quasi-uniform with horizontal mean AP distance of $\bar{r}_{\text{fine}} = 200$ km north of 30°N and a coarser spacing of $\bar{r}_{\text{coarse}} = 500$ km elsewhere. Vertically, AP are distributed onto nine evenly spaced sub-levels around main levels at 370, 395, 422, 450, 480, 513, 547, 579, and 610 K. The location and spacing of vertical main levels is adjusted to the given horizontal resolution as described by Konopka et al. (2004): the aspect ratio between the horizontal and vertical dimension is $\alpha = 250$. Figure 3.4 shows the distribution of individual AP in a 200 km corridor along the 0° meridian for the standard experiment $\bar{r}_{\text{fine}} = 200$ km and a high-resolution experiment $\bar{r}_{\text{fine}} = 100$ km.

Trajectories are calculated over $\tau = 24$ h periods, after which mixing and boundary updates occur. As the standard parameter for mixing intensity $\ell_c = 1.2$ was chosen according to recommendations in McKenna et al. (2002b), variations to this standard setting are described in Section 3.5.3. The upper and lower boundaries are updated by repetitive replacement of the boundary levels with initial conditions.

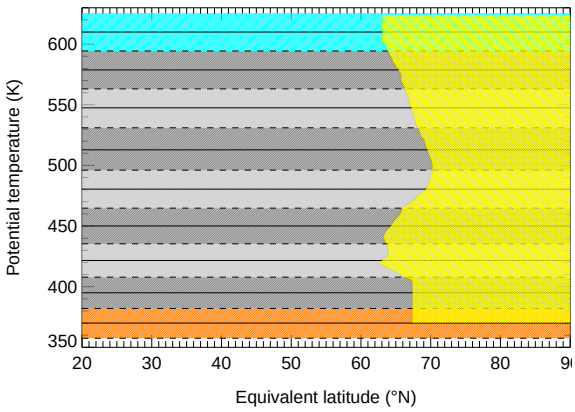

Figure 3.5: Initialisation of artificial tracers for CLaMS experiments. Three digital tracers are used to identify the upper model main layer (Tr_{upper}, cyan shading), the lower model layer (Tr_{lower}, orange) and the domain of the vortex (Tr_{vortex}, yellow), respectively. Also shown are the seven intermediate main layers and their vertical extent.

3.4.3 Chemical species and passive tracer initialisation

Initial mixing ratios for all chemical species are interpolated from the respective E39C field on 1 January. The data set is homogenised such that all tracer fields are in units of volume mixing ratio and the terminology follows the ASAD (Carver et al., 1997a) conventions (e.g. $ClONO_2$ instead of $ClNO_3$). Bromine species are initialised from the Mainz 2D model simulation, resulting in a stratospheric inorganic bromine (Br_y) loading of 11 ppt at 475 K and north of 70°.

Passive ozone (O_3^*) is initialised from the E39C ozone field on 1 January. As indicators of vertical motion, two digital tracers are defined for the lower and upper boundary layer. Tr_{upper} is initialised to 1 in the uppermost model layer and zero elsewhere; Tr_{lower} is set to 1 in the lowest layer, zero elsewhere. A passive potential temperature tracer Tr_θ is initialised with potential temperature at simulation start and transported passively. Vortex export and isolation are examined with a digital vortex tracer Tr_{vortex}, initialised to 1 inside the vortex (as defined by the Nash et al. (1996) criterion) on 1 January, zero outside. The distribution of these artificial tracers is shown in Figure 3.5.

Particle sedimentation and heterogeneous reactions are included in all chemistry simulations if not specified otherwise. Albedo is assumed to be 40%; O_2 and O_3 profiles from the Mainz 2D simulation are utilised to calculate photolysis rates. An overview of CLaMS parameters is provided in the appendix (Tables A.2–A.6)

3.5 CLaMS experiments

With CLaMS, 90-day simulations starting on 1 January, 0:00 UTC and ending on 1 April, 0:00 UTC are performed. The main focus is on three-dimensional simulations including diabatic descent and stratospheric chemistry. Transport only simulations for passive tracers complement these experiments. While over 90 days, stratospheric descent is important, it is shown that for comparison with E39C results an isentropic assumption is justified (cmp. Section 3.5.3). On these grounds, sensitivity studies are performed which exclude diabatic descent.

The various experiments with CLaMS are aimed at three goals: (1) calculate chemical ozone loss and minimum Arctic spring ozone column in one winter of the 2015 time slice to obtain a better estimate of the 2015 maximum chemical ozone loss; (2) assess ozone chemistry in "business as usual" scenarios, including doubled stratospheric chlorine and loading, to quantify impact on ozone of the successful reduction of CFC and related substances production; (3) find model sensitivities towards mixing intensity, resolution, sedimentation and quantify the effect of these parameters on ozone loss.

3.5.1 Bromine loading experiments

In the standard CLaMS initialisation, denoted A, stratospheric bromine loading at 475 hPa is 11 ppt, which is a low value of bromine loading compared to recent measurements: Salawitch et al. (2005) propose 20–30 ppt Br_y in the stratosphere based on SAOZ BrO measurements. Aircraft *in situ* measurements of BrO by the HALOX instrument suggest $\approx$ 18 ppt Br_y at 20 km altitude (M. v. Hobe, personal communication, 2005). A simulation with enhanced loading (22 ppt) is set up and labelled H. A further experiment denoted B is initialised using only the chemistry information contained in the E39C data and does not contain bromine species. Scenario B is used to validate the chemistry scheme in E39C against CLaMS chemistry.

Experiments A and H can provide more comprehensive chemical ozone loss estimates than no-bromine simulations B and E39C. By choosing both a lower and upper estimate for Br_y, the range of sensitivity to bromine chemistry and the relative and absolute impacts of bromine chemistry on ozone loss can be assessed; underestimation of ozone loss due to the missing bromine chemistry in E39C can be quantified. Bromine loading on the 475 K isentropic surface for these scenarios is summarised in Table 3.5.

3.5.2 Non-Montreal experiments

Figure 1.1 in Chapter 1 shows the projections for effective equivalent stratospheric chlorine (EESC) until 2100 assuming different restrictions under the Montreal protocol, its adjustments and amendments, as presented in WMO (2003). Without the Montreal protocol, exponential increase of EESC would have occured, reaching a value of 6 ppb by 2015. The 50% emission reduction in countries participating in the original Montreal protocol would have delayed the increase of EESC but not prevented a further exponential increase. The hypothetical EESC for 2015 under the original Montreal protocol is 4.5 ppb. Amendments in 1992 and adjustment of the protocol to 80 countries would have resulted in a stagnation of EESC at a value of 3.5 ppb until 2050, and an increase of EESC thereafter.

A sustainable decrease of stratospheric halogen loading was effected by the Copenhagen amendment: EESC is projected to decline monotonously after peaking in 1998 at 3 ppb; the prospected value in 2015 is 2.5 ppb. With the Beijing amendment, long-term EESC reduction to 1 ppb will be reached by the year 2100.

$Br_y \backslash Cl_y$	0 ppb	1.83 ppb	3.65 ppb	7.31 ppb
0 ppt	C	B		
11 ppt		A		
22 ppt		H	2	
44 ppt				4

Table 3.5: Matrix of experiment setup for non-Montreal and bromine sensitivity experiments. Columns show variation in bromine loading, rows variation in chlorine loading. Numbers give the average vortex loading in the 475 ± 15 K potential temperature level.

Based on these projections and taking the E39C time slice 2015 as the base line (where EESC is reduced by 9% with respect to the 1990 time slice experiment), the minimum Arctic ozone column and chemical ozone loss under doubled and quadrupled EESC conditions are simulated with CLaMS. For these simulations, denoted 2 (4), fields of all bromine and chlorine species in the A initialisation are doubled (quadrupled). Both scenarios 2 and 4 are based on the conservative assumption for bromine loading which is 28 ppt and 42 ppt, respectively, at 30 hPa. All values for chlorine and bromine loading in these non-Montreal experiments are summarised in Table 3.5 for the 475 K potential temperature level, restricted to the vortex. Multiplication of bromine loading from Table 3.5 with a recommended value for Arctic studies (factor 60, Chipperfield and Pyle, 1998) results in polar vortex EESC at 475 K of 0 ppb, 2.49 ppb, 4.97 ppb, and 9.95 ppb for scenarios C, A, 2, and 4, respectively. The doubled EESC scenario (2) loading corresponds to EESC expected if the Montreal protocol had been implemented but not been amended nor adjusted; scenario 4 describes a situation that would have been reached without any regulation at all in 2030.

3.5.3 Isentropic experiments

Sensitivity experiments require a large number of simulations for each parameter under investigation. To assess model sensitivity to critical mixing parameter ℓ_c, horizontal resolution $\bar{r}_{\text{fine}}$, and sedimentation, high resolution isentropic simulations are performed with CLaMS. Three-dimensional simulations at the same horizontal resolution would require much denser vertical spacing (e.g. Haynes and Anglade, 1997), resulting in too excessive computing costs.

Quasi isentropy in E39C

Motion in the stratosphere occurs along isentropes on short time scales; it is then straightforward to refer to these adiabatic motions as horizontal or two-dimensional. In the 90-day simulations from 1 January to 1 April, the isentropic assumption is not valid. However, based on the vertical displacement of the methane field in the

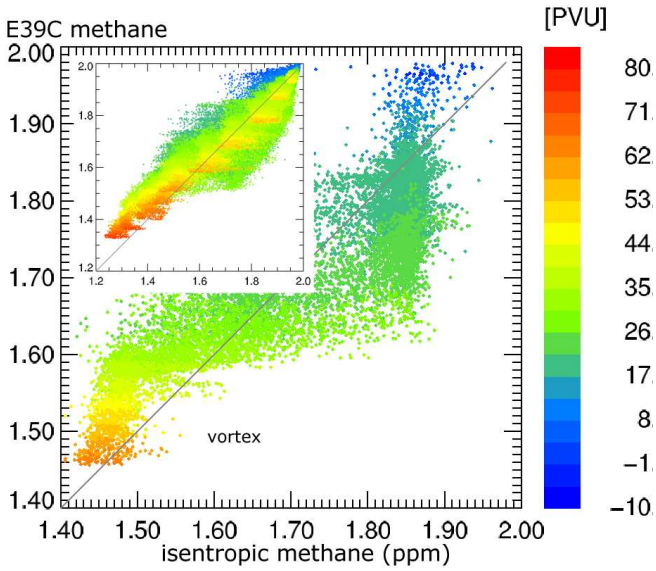

Figure 3.6: Scatter plot of 90-day isentropically advected CH_4 versus E39C CH_4 sampled at the simulation locations. The large plot shows only data at 475 K, the inset data from all simulation altitudes. Colouring denotes modified PV.

E39C data, only a very small diabatic displacement of the layer around $\theta_r = 475$ is found. The vertical displacement of the methane field was used by, for example, Hein et al. (2001) to analyse vertical descent in E39C. In Figure 3.6, an isentropically advected CH_4 field (initialised on 1 January and advected with CLaMS) is compared to the corresponding CH_4 April field in E39C. A relative increase in E39C methane indicates vertical ascent, a decrease descent. The correlation between the advected and sampled methane fields is strong ($r^2 = 0.84$) across the whole data set, and excellent ($r^2 = 0.96$) for data at θ_r in spite of diabatic motion. On the 475 K surface, air within the vortex (yellow and red shading) ascends on average while mid-latitude air (shades of green) descends. The mean CH_4 mixing ratio difference in the vortex is 0.05 ppm, which translates to ≈ 20 K ascent. This very small ascent in CCM data contrasts with radiatively calculated (Zhong and Haigh, 1995) descent rates used for three-dimensional CLaMS simulation which are on the order of 20–80 K per month. For comparison of both models, E39C data at 490 K and isentropic CLaMS simulations at 475 K are used; these levels correspond in both models to the same level in terms of vortex average CH_4 mixing ratio.

Variation of the critical Lyapunov exponent

The critical Lyapunov exponent ℓ_c controls mixing intensities in regions of sheared flow. Within the vortex, the solid-body like rotation ensures that minimal shearing occurs and no mixing events occur: a variation of ℓ_c cannot influence intra-vortex tracer gradients. At the edge and within the outer edge of the vortex, the region of maximum zonal wind is located. Strong shear induces intensive mixing which can be controlled by variation of the critical threshold for mixing, which is the product $\ell_c \cdot \Delta t$. When the time step for mixing is one day, the critical threshold for mixing is numerically identical to the critical Lyapunov exponent.

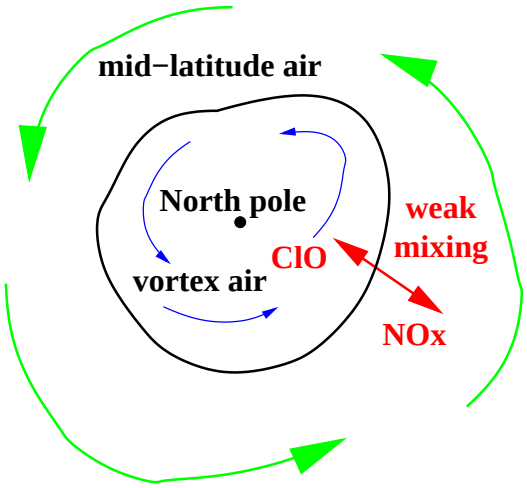

Figure 3.7: Sketch of the influence of mixing on chlorine deactivation. Strong mixing across the vortex edge imports NO_x and leads to deactivation of ClO_x; weak mixing upholds activated chlorine in the vortex. Figure kindly provided by P. Konopka, 2005.

A possible chemical impact of mixing on ozone depletion is the import of NO_x from mid-latitudes into the polar vortex. The gradient of NO_x between the mid-latitudes and the polar vortex is a result of more NO_y photolysis outside the vortex and, inside the vortex, denitrification and special polar chemistry. NO_x import into the vortex can deactivate active chlorine and hence decrease ozone depletion. For the Arctic winter 2000, Konopka et al. (2003b) found only weak impact of mixing on chlorine deactivation within the vortex, whereas, in a complementary study, an effect of mixing on chemistry in vortex remnants was confirmed (Konopka et al., 2003a) for Arctic winters 1997 and 2000.

The range of mixing thresholds proposed by the above studies and McKenna et al. (2002a) is 0.8–1.5, depending on the simulation type (3D vs. 2D) and the dataset validated against (Satellite remote, aircraft in-situ). As the standard threshold for the two-dimensional and three-dimensional experiments in this study $\ell_c = 1.2\,\mathrm{d}^{-1}$ is chosen. To assess the influence of mixing on ozone depletion in winter 2015/58, CLaMS simulations including full chemistry (scenario A) are performed over a range of mixing parameters from 0.0 to 4.0. These simulations are repeated for scenario B (no bromine chemistry) to compare the mixing sensitivities to the E39C simulation.

Variation of horizontal resolution

In preparation for three-dimensional experiments, the sensitivity of chemical ozone depletion to horizontal resolution $\bar{r}_{\mathrm{fine}}$ is tested by a variation of $\bar{r}_{\mathrm{fine}}$ in the range 50–400 km. Simulations are performed for both chemical scenarios A and B. Goals of this sensitivity experiment are (a) to determine an optimal resolution for three-dimensional experiments, (b) to relate experiments to the grid spacing in E39C. The regular $3.75° \times 3.75°$ in E39C translates to an average horizontal spacing of roughly 400 km, which is reduced with a factor $\cos\phi$ towards the pole for the east-west direction. At 60° latitude, east-west grid spacing is about 200 km, at 80° it is 70 km.

For CLaMS, Konopka et al. (2004) found that simulated tracer experiments matched observations only at horizontal AP distance $\bar{r}_{\mathrm{fine}} < 300$ km; optimal agreement was

obtained for $\bar{r}_{\text{fine}} = 100\,\text{km}$; this optimal value is chosen as the reference AP spacing for two-dimensional studies in this thesis. The tested values for $\bar{r}_{\text{fine}}$ apart from the reference simulation are 50 km, 70 km, 120 km, 150 km, 200 km, 250 km, 300 km, and 400 km.

Chemical and sedimentation sensitivities

As in the three-dimensional case, simulations including bromine (scenarios labelled A), excluding bromine (labelled B), excluding chlorine only, and excluding halogens (labelled C) are performed on the 475 K level. Additionally, a simulation is set up with all chlorine species initialised to zero, but standard (as in scenario A, 11 ppt) bromine loading. The effect of sedimentation is examined with simulations initialised as above but without inclusion of sedimentation calculations; these experiments are denoted with lowercase letters. Denitrification may have a severe impact on Arctic ozone loss (up to 35%, Waibel et al., 1999), but depending on the winter, different magnitudes of the influence of denitrification on ozone loss have been reported. For example, Grooß et al. (2002) find a 37% effect at 475 K for winter 1999/2000; in winter 2002/2003, only about 10% of chemical ozone loss can be attributed to denitrification (Grooß et al., 2004).

3.5.4 Tracer experiments

A summary of all sensitivity studies is provided in Table 3.6. The first group (I) of experiments is constituted by three-dimensional CLaMS simulations which include the calculation of stratospheric chemistry as described above. The second group characterises complementary three-dimensional tracer studies with differing mixing intensity; these tracer experiments are performed to test for vortex isolation. The latter groups (III–V) of simulations are composed of two-dimensional simulations; group III enumerates CLaMS simulations including the stratospheric chemistry module and run at various mixing intensities; group IV is an ensemble of simulations with varying air parcel distance. The last group (V) recounts complementary studies for sensitivity to denitrification and presence of halogen families.

3.6 Calculation of chemical ozone loss

The chemical loss rate of ozone or odd oxygen can be calculated from the "known" chemical reactions and reactions constants, as was demonstrated by Crutzen and Schmailzl (1983). This is the method used by Schnadt (2001) for an earlier analysis of chemical ozone depletion in E39C time slice experiments. This theoretical approach to ozone loss can only be performed when the concentrations of all reactants are known (as in a numerical model).

Different approaches are necessary when the state of the atmosphere is not completely known, which is the case for all observation-based —*in situ* and remote

	Scenario	Label	dim	ℓ_c	$\bar{r}_{\text{fine}}$(km)	Br_y (ppt)	Cl_y (ppt)	sed
group I	reference	A	3D	1.2	200	11	1.83	yes
	no Br	B	3D	1.2	200	0	1.83	yes
	no Br,Cl	C	3D	1.2	200	0	0.00	yes
	2× Br	H	3D	1.2	200	22	1.83	yes
	2× EESC	2	3D	1.2	200	22	3.65	yes
	4× EESC	4	3D	1.2	200	44	7.31	yes
group II	tracer	S	3D	1.2	100			
	tracer	[1]	3D	1.2	200			
	tracer		3D	0.0	200			
	tracer		3D	0.1	200			
	tracer		3D	0.4	200			
	tracer		3D	0.8	200			
	tracer		3D	2.0	200			
group III[2]	reference	A	2D	1.2	100	11	1.83	yes
			2D	0.1	100	11	1.83	yes
			2D	0.2	100	11	1.83	yes
			2D	0.4	100	11	1.83	yes
			2D	0.8	100	11	1.83	yes
			2D	1.6	100	11	1.83	yes
			2D	2.0	100	11	1.83	yes
			2D	2.4	100	11	1.83	yes
group IV[2]			2D	1.2	50	11	1.83	yes
			2D	1.2	70	11	1.83	yes
			2D	1.2	120	11	1.83	yes
			2D	1.2	150	11	1.83	yes
			2D	1.2	200	11	1.83	yes
			2D	1.2	250	11	1.83	yes
			2D	1.2	300	11	1.83	yes
			2D	1.2	400	11	1.83	yes
group V		a	2D	1.2	100	11	1.83	no
		b	2D	1.2	100	0	1.83	no
		c	2D	1.2	100	0	0.00	no
			2D	1.2	100	11	0.00	no
			2D	1.2	100	11	0.00	no
	tracer		2D	1.2	100			

Table 3.6: Summary of all experiments performed with CLaMS. Bromine loading and chlorine loading numbers are for the 475 ± 15 K isentropic layer. See text for details.

[1] and further tracer experiments described in the text

[2] this group performed with B chemistry as well

sensing— estimates of chemical ozone loss. They can roughly be classified in approaches using explicit transport calculations and approaches using tracer relations, where transport is implicitly accounted for (Harris et al., 2002; Rex et al., 2002).

Several studies used calculations of vortex average diabatic descent to correct for transport between mean observed ozone profiles (e.g. Manney et al., 1994; Knudsen et al., 1998) from ozone sondes and satellite measurements. In a Lagrangian approach, Manney et al. (e.g. 1995, 1996, 1997) calculate trajectories from locations of satellite observations in a transport model and interpolate to subsequent observations of ozone. The Match technique employs coordinated launches of ozone sondes along pre-calculated trajectories (e.g. von der Gathen et al., 1995; Rex et al., 1997, 2002). Chemical loss is statistically derived from all trajectories within a given time frame. The Match technique has also been applied to satellite measurements (e.g. Terao et al., 2002; Lukyanov et al., 2003).

The accumulated loss with respect to a reference time can be calculated with the help of a model passive ozone tracer in a transport simulation. Ozone loss is then given by the difference between an observation and the simulated passive tracer (e.g. Goutail et al., 1999; Konopka et al., 2004; Hansen and Chipperfield, 1999).

The passive ozone tracer is also used in chemistry transport models along with chemically active ozone, such that at any simulation time step the difference gives an information about the accumulated loss in the model. This method is employed in this study with CLaMS and has been used with various other CTMs (e.g. Sinnhuber et al., 2000; Lefèvre et al., 1998).

The above methods required the knowledge of transport at various degrees, from bulk vertical descent to complete meteorological information. If however, concurrent observations of ozone and a tracer with longer lifetime than the time scale of ozone depletion are available, this tracer can be considered as a proxy for passive ozone on typical time scales of typical ozone loss studies (e.g. Proffitt et al., 1990; Müller et al., 1997; Richard et al., 2001).

3.6.1 Tracer-tracer correlations

The tracer-tracer correlation method (TRAC) postulates that without chemical reactions a tracer-tracer relationship within a closed body of air does not significantly alter while this body of air is advected, deformed or internally mixed. Using an early winter relationship between a passive tracer (e.g. CH_4, N_2O, HF) and ozone within the polar vortex, at any later time an ozone value that would be expected in the absence of chemical change $\hat{O}_3$ can be derived from the correlation established before. The difference between expected and actual (measured or simulated) ozone quantifies the chemical change in ozone, and thus for polar winters, chemical ozone depletion.

Proffitt et al. (1990) first used the change in the relationship of the long-lived tracer N_2O with ozone to calculate chemical loss of ozone. Tilmes (2003) and Tilmes et al. (2004b) characterised the recent Arctic winter ozone losses based on HF-ozone correlations from HALOE measurements for the years 1991/92 until 2002/03.

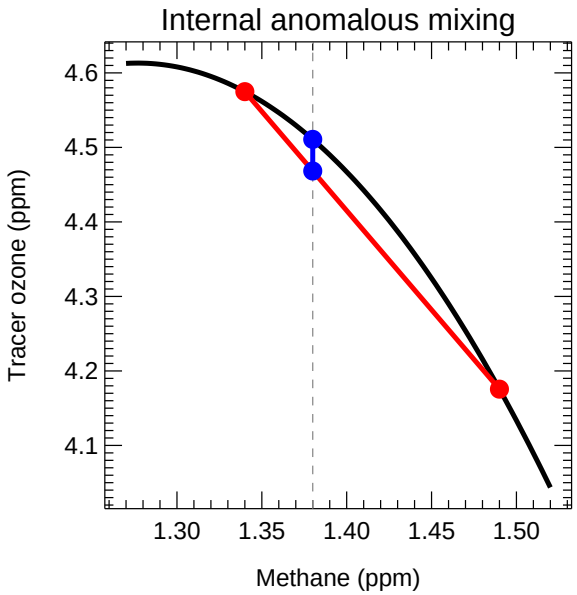

Figure 3.8: Anomalous (in the sense of disturbing the correlation) internal mixing along a mixing line (shown in red) underestimates (blue line) transported ozone with respect to a curved reference correlation (black line).

Beyond ozone, the tracer correlation technique has been used, for example, to quantify denitrification and chlorine activation. With TRAC, Fahey et al. (1989) used an early winter relationship between N_2O and NO_y. While N_2O is long-lived, NO_y is removed from cold air masses by sedimentation of NAT particles (Fahey et al., 2001; Carslaw et al., 2002). The difference between an NO_y^* calculated from the N_2O-NO_y relationship and measured NO_y quantifies denitrification. The relationship between hydrogen chloride and hydrogen fluoride was used by, e.g., Müller et al. (1996) and Tilmes et al. (2004b), to calculate chlorine activation in the polar vortex. In these studies, chlorine activation is found when HALOE observed HCl declines with respect to the reference relation established prior to activation between HF and HCl. TRAC has attracted criticism from several authors, most notably Michelsen et al. (1998), Plumb et al. (2000), and Sankey and Shepherd (2003). For the Arctic winter 1999/2000, Salawitch et al. (2002) found a good agreement between ozone loss derived from a N_2O-O_3relation and ozone loss derived with the Match and vortex average methods. The following paragraphs lay out situations where the tracer-tracer correlation technique may be compromised; a validation of the technique for the E39C data set is provided in Section 6.4.

Internal anomalous mixing

Vigorous internal mixing may lead to errors in a TRAC-like analysis as was demonstrated by Esler and Waugh (2002) for denitrification study using the N_2O-NO_y correlation. If the relationship is highly nonlinear as it is the case for NO_y-N_2O (Esler and Waugh, 2002, Fig. 1), mixing may lead to air parcel configurations which deviate from the reference correlation on so-called mixing lines. Mixing lines are constructed by interpolating linearly between air masses (or water masses in oceanography) with different tracer characteristics: mixing events between these two air masses lead to

new air parcel characteristics that lie on the mixing line. The concept of mixing lines and anomalous internal mixing is sketched in Figure 3.8, with actual vortex data from a CLaMS tracer simulation. A curved vortex reference relationship (black line) between CH_4 and O_3 is derived at simulation start; at the end of the simulation, due to differential descent, on one isentropic level CH_4 mixing ratios over a wide range may be collected, indicated by red solid circles in the above figure. Mixing between air parcels would result in CH_4 and O_3 values that are represented by the red mixing line. At the mean vortex CH_4 mixing ratio, shown as the broken line, the reference correlation overestimates ozone by the magnitude shown as the blue line, if all air parcels in the vortex were mixed. This nonlinear relationship —and the effect of anomalous internal mixing— can be overcome by employing an artificial tracer where the quantity to be predicted is a linear function of this artificial tracer. The artificial tracer technique cannot eliminate the effect of mixing between air masses with different tracer-ozone relations (e.g. the intra-vortex and extra-vortex relationship) even if both are linear.

Cross vortex boundary mixing

Due to non-halogen catalysed summertime ozone depletion and subsequent isolation and descent of polar vortex air masses, different ozone-tracer relations prevail inside and outside the polar vortex. The establishment of these differing ozone-tracer relations are described in detail by, e.g., Proffitt et al. (1993) or Müller et al. (2002). The high-latitude and mid-latitude methane-ozone correlations for a 2015 winter are shown in Fig. 3.9 exhibiting these two different regimes. Thus, a careful selection of profiles used for the establishment of the correlation is essential to the applicability of the TRAC method; the optimal time for derivation of an early winter reference correlation is after the stabilisation of the vortex and before the chemical processes under examination take place (Tilmes et al., 2004b). For a single mixing event during one winter, Rex et al. (1999) proposed to correct for mixing effects on a vortex tracer-tracer correlation by subtracting the change in the mid-latitude correlation between two long-lived tracers (here CH_4 and N_2O).

Intensive investigations by, for example, Müller et al. (2001), Konopka et al. (2003b), or Tilmes et al. (2004b) all agree that if mixing with extra-vortex air occured, this would lead to an overestimation of the TRAC derived proxy for ozone, and an underestimation of ozone loss calculations with TRAC. Plumb et al. (2000) argue that in their study with artificial tracers χ_1 and χ_2, a canonical relationship $\chi_2(\chi_1)$ is altered by mixing across the vortex boundary. Application of the reference relation to χ_1 results in an underestimation of χ_2; if the dependent tracer was ozone, a loss calculation would result in too much ozone loss. The underestimation of χ_2 is shown for a decreasing altitude profile of χ_2 in Plumb et al.. For polar vortex ozone loss studies, the profile of the dependent tracer O_3 increases with altitude. For example, Salawitch et al. (2002) argue that for their calculations in winter 1999/2000 cross vortex boundary mixing leads to a (very small) underestimation of ozone loss when determined with the tracer-tracer correlation method.

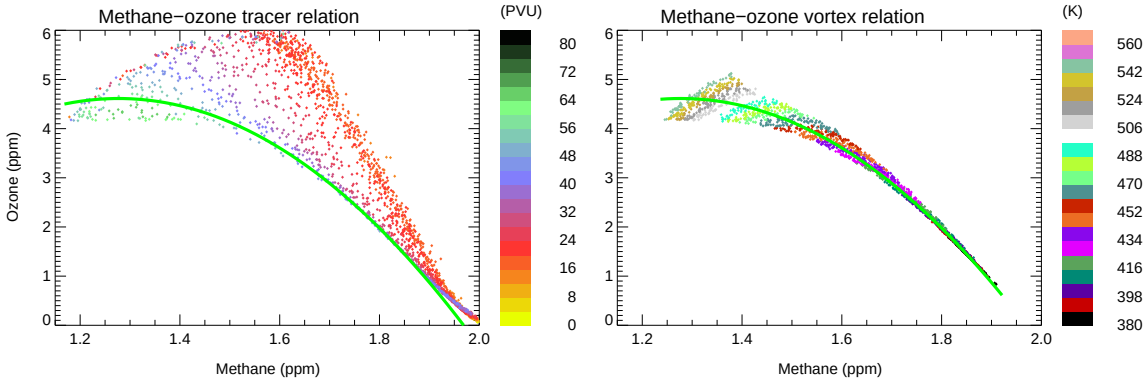

Figure 3.9: (left) Scatter plot of stratospheric E39C 2015/58 January ozone versus methane. Colours denote modified PV in PVU. **(right)** similar as left fingure; here, only polar vortex data between 380–550 K are shown. Colour indicates potential temperature; the green line (shown in both figures) is a second order least squares fit to the polar vortex data.

Calculation of the reference relationship

For all time slice winters 1990 and 2015, an early winter reference CH_4-O_3 correlation is established on the 1 January data set. The DLR chemical and meteorological data are provided on their standard 39 pressure level, latitude by longitude grid. Potential temperature is calculated from the temperature and pressure fields and all data are interpolated onto a potential temperature grid between 340 and 640 K with 20 K spacing. On these isentropes, potential vorticity and equivalent latitude are determined according to Lary and Pyle (1991). The vortex edge is determined separately for each potential temperature level according to Nash et al. (1996, cmp. Section 2.2.5): a 7^{th}-order polynomial is fitted to the PV(ϕ_{eq}) data; first to third order derivatives of these polynomial expressions are evaluated to calculate inflection points and points of maximum curvature.

Methane and ozone fields within the so defined vortex are collected between 380 K and 550 K potential temperature levels, these selected data are displayed in Figure 3.9 on the right hand side. Within each isentropic level (different colours in Figure 3.9), the median values of CH_4 and O_3 are calculated, which are used for the subsequent fitting procedure. Median values on isentropic levels are chosen in preference of the raw data set: the highest isentropic layer is sloped in CH_4-O_3 space, a fit through all data would overestimate the importance of the low-ozone, low-methane values around (1.25 ppm, 4.25 ppm). A second order polynomial is determined with a least squares fit to the median values.

In this winter (like in many others of the time slice, cmp. Table 3.3), Arctic stratospheric temperatures are sufficiently low for existence of PSC and chlorine is already activated. Some chemical ozone loss may have occured prior to the establishment of the reference correlation on 1 January. Because of the very compact vortex relationship and a subsequent analysis of loss rates which are low throughout January (low

light conditions, no Br_y in the model, cmp. also Figure 6.1), not much ozone loss occured prior to January: O_3 loss calculated based on this reference may lead only to a small underestimation of chemical loss due to autumn ozone depletion. The calculated reference relationships for all winters of the E39C time slice experiments 1990 and 2015 are given in Tables 4.1 to 4.2 on page 70.

3.6.2 The passive ozone tracer

A passive ozone tracer O_3^* is routinely employed in a variety of CTMs, such as REPROBUS (Lefèvre et al., 1998), SLIMCAT (Sinnhuber et al., 2000), and CLaMS (McKenna et al., 2002b); it is used primarily for polar winter ozone loss studies (e.g. Grooß et al., 2002; Konopka et al., 2004; Grooß et al., 2004).

The passive tracer is an artificial, chemically inert tracer, initialised at some time t_0 with the values of a corresponding chemically active species. The passive tracer undergoes the same transport active counterpart. This way, the difference between the artificial tracer and the active species at any time $t > t_0$ is equal to the accumulated chemical change of the species under consideration. For ozone

$$\mu\left(\Delta O_3^*\right) = \mu\left(O_3\right) - \mu\left(O_3^*\right) \tag{3.2}$$

where $\mu\left(O_3\right)$ denotes volume mixing ratio of O_3 and ΔO_3^* the accumulated chemical change in ozone over time $t - t_0$.

For polar studies the passive ozone tracer is equated to the chemically active form preferably at the beginning of the winter, after the polar vortex is sufficiently isolated and before severe chemical ozone loss sets in. In reality, the tracer is mostly initialised along with a concurrent atmospheric observation, e.g. a balloon sounding (e.g. Grooß et al., 2002), radiosondes, or from remote sensing measurements (e.g. Grooß et al., 2004).

The passive tracer may —after being transported in a model— be compared to subsequent observations. This approach has been widely used with the Système d'Analyse par Observation Zénithale (SAOZ) observations and the REPROBUS model (e.g. Goutail et al., 1999; Goutail et al., 2004). In the context of this thesis, the passive ozone tracer is used both (a) to assess accumulated chemical ozone loss (see next paragraph) and (b) to validate the tracer-tracer correlation technique.

3.6.3 Quantifiers of chemical ozone loss

A variety of quantifiers to describe chemically lost ozone has been used by other studies, such as the total mass of ozone lost (Knudsen et al., 2004), the integrated instantaneous rates of chemical loss reactions (Schnadt, 2001), the vortex-averaged volume mixing ratio depletion (Rex et al., 2003), or integrated loss profiles (Müller et al., 1996). The variety of quantifiers for polar ozone loss is primarily a consequence of data sampling and availability, such as satellite profiles, Lagrangian trajectories or gridded CCM model output. It is, however, enhanced by the spatial and temporal inhomogeneity of the polar vortex.

Here, chemical ozone loss in the Arctic polar vortex is analysed with two (two-dimensional) criteria accounting for ozone loss on isopleths of potential temperature and methane. Since these first two criteria do not consider the vertical extent of ozone depletion, two further (three-dimensional) criteria are introduced which quantify ozone depletion by specifying the maximum chemical column loss and the minimum observed ozone column in spring. As a (fifth) global quantifier the relative depletion of ozone with respect to the passive ozone tracer is calculated.

1. Local chemical ozone loss is quantified for all experiments around the $\theta_r = 475\,\mathrm{K}$ potential temperature level; the associated layer will be referred to as the reference layer $\Theta_r = 475 \pm 15\,\mathrm{K}$. The thickness of the layer (30 K) is chosen such that, at the resolution $\bar{r}_{\mathrm{fine}}$ of three-dimensional experiments, around 400 data points contribute to the average over all mixing ratio differences between O_3 and O_3^*: $\Delta O^*_{3,475} = [\mathrm{mean}\,\mu\,(O_3) - \mu\,(O_3^*)]$. The sample size of 400 is in accordance with the number of data points enclosed by the vortex on the 475 K isentrope at $\bar{r}_{\mathrm{fine}} = 100\,\mathrm{km}$ resolution used in two-dimensional experiments.

2. As a second quantifier for local ozone loss, the difference between a polynomial fit to the $O_3^*(CH_4)$ relation and a fit to $O_3(CH_4)$ was calculated at a reference CH_4 mixing ratio of 1.35 ppm. This methane value occurs in data (April of simulation year 58) between 460–510 K potential temperature. For the meteorological conditions in this winter with less descent towards the vortex core, a vortex methane isopleth has a positive slope with increasing equivalent latitude. Thus, more data from higher isentropic levels are collected in the core and more data from lower altitudes are collected from the inner edge in comparison to a sampling within an isentropic layer: chemical ozone loss may be overestimated if (which is the case for the analysed winter) ozone loss increases with altitude between 460 K and 510 K. This criterion was chosen because it is the most prominent measure of ozone loss in plots of O_3 vs. CH_4 (cmp. Figures 6.2 to 6.5 on pages 87–90).

3. The effect of ozone depletion on ultraviolet radiation reaching the surface is best captured by considering the total amount of ozone molecules, or the ozone column, above a geographical area. Column ozone $\mathrm{Col}(O_3)$ calculated on the pressure (p) sorted ozone field per unit area and usually expressed in Dobson units (DU):

$$\mathrm{Col}(O_3) = \sum_{i=1}^{n} \frac{1}{2}(\mu_i(O_3) + \mu_{i-1}(O_3)) \cdot (p_i - p_{i-1}) \cdot \frac{N_A}{2.69 \cdot 10^{16} \cdot g \cdot m}, \tag{3.3}$$

where $g = 9.81\,\mathrm{m\,s^{-2}}$ is acceleration due to gravity, $N_A = 6.02252 \cdot 10^{23}\,\mathrm{mol^{-1}}$ is Avogadro's number, $m = 0.028964\,\mathrm{kg\,mol^{-1}}$ is molecular weight of dry air; 1 DU contains $2.69 \cdot 10^{16}\,\mathrm{molecules\,cm^{-2}}$. For E39C gridded data, this column integration is performed directly for each 3.75×3.75 grid cell from 1000 hPa to 10 hPa; CLaMS output is interpolated to the E39C grid and the partial column is subsequently integrated. The amount of column ozone below and above the CLaMS model domain is taken from the E39C field and added to the CLaMS partial column to obtain the total column.

4. Column ozone (also called total ozone) is routinely observed by satellite instruments, e.g., the Total Ozone Mapping Spectrometer (TOMS, Stolarski et al. 1986) or

Global Ozone Monitoring Experiment (GOME, Burrows et al. 1999): the calculation of column ozone allows direct comparison to observational data. In the CCM intercomparison study by Austin et al. (2003), the Arctic minimum ozone column (hereinafter referred to as AMOC, the minimum total ozone value north of 60°N) is used as a quantifier of ozone depletion. This measure may be influenced by tropospheric dynamics when a high pressure system elevates the tropopause and thus dynamically reduces column ozone. On the other hand, its ready availability in observational data and ease of calculation make AMOC a preferred quantity for intercomparison studies; AMOC is used in this thesis along with the maximum column loss calculated as $\max \mathrm{Col}(\Delta \mathrm{O}_3^*)$, or $\max \mathrm{Col}(\Delta \hat{\mathrm{O}}_3)$ if a passive tracer is not available.

5. A measure of ozone loss within the whole vortex body is obtained by a calculation of relative loss $\Delta \mathrm{O}_3^*/\mathrm{O}_3^*$; for this calculation, data north of the vortex edge in ϕ_{eq} space and between 380–550 K in the vertical is averaged and weighted by pressure, yielding the relative amount of ozone molecules destroyed.

4 Ozone loss in E39C time slices

The range of E39C simulated Arctic minimum ozone column (AMOC), has previously been published (Austin et al., 2003; WMO, 2003). Chemical ozone loss averaged over all time slice winters was presented by Schnadt (2001). This chapter is concerned with a reexamination of previously obtained results for AMOC and chemical ozone loss as averages over the time slice experiments 1990 and 2015, and for individual winters. Chemical ozone loss is calculated with the tracer-tracer correlation technique: chemical depletion can be separated from transport induced changes of the AMOC. The differences from 1990 to 2015 in each of these two equally important processes are then assessed separately and contrasted.

4.1 Column ozone and Arctic minimum ozone

4.1.1 Experiment 1990

The 1 January Arctic minimum ozone column (AMOC) in the 1990 time slice ranges from 229 DU to 281 DU; mean and standard deviation within the time slice are 253 ± 17 DU. During the winter, the Arctic ozone column increases due to descent of ozone-rich air from the middle stratosphere. This dynamical resupply balances or exceeds chemical ozone loss in most winters. In April, much higher minimum Arctic ozone column values occur (maximum 374 DU), while in three winters very low April total ozone values are simulated (minimum 218 DU). Winter 1990/56 meets the criterium for an ozone hole with ozone columns less than 220 DU. Mean and standard deviation for April in the 1990 time slice are 297 ± 46 DU. A histogram summarising the minimum total Arctic ozone column is displayed in Figure 4.1. Total ozone in the 1990 time slice is shown in Figures A.2–A.3 for all winters[1].

4.1.2 Experiment 2015

The 1 January AMOC ranges from 228–304 DU in time slice 2015; mean and standard deviation are 263 ± 17 DU. As in experiment 1990, the minimum Arctic column increases during winter, with 1 April values ranging from 296–385 DU and averaging 354 ± 28 DU. The histogram for this time slice is displayed in Figure 4.2.

In both time slice experiments 1990 and 2015, mean and standard deviation of the time slice average January minimum Arctic ozone column are very similar. Spring minimum ozone column is significantly different in the two time slices: For three

[1] except for winter 1990/59 where the archived data were corrupted.

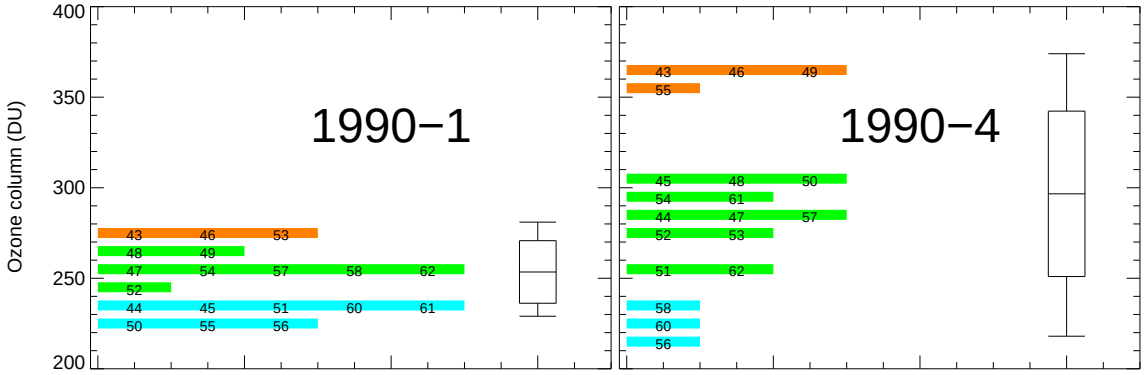

Figure 4.1: Histogram of Arctic minimum ozone column in time slice 1990, binned in 10 DU intervals starting from 215 DU. **(left)** 1 January ozone columns, low ozone winters are shaded cyan, high ozone winters orange. The box-whisker plot indicates mean, standard deviation and range. Small numbers denote individual winters within the time slice according to the E39C naming scheme. **(right)** As left, but for 1 April.

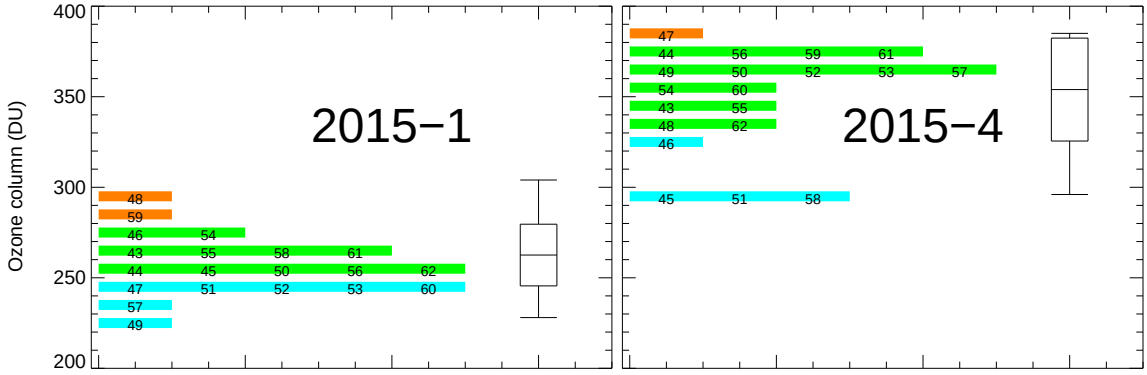

Figure 4.2: As in Figure 4.1, but for the 2015 time slice. The winter numbered 58 is analysed in more detail with CLaMS simulations.

winters of the 1990 time slice, the minimum Arctic spring column is lower than the respective January column whereas for all winters in 2015 the minimum Arctic column increases. From January to April 1990, the mean minimum column increases by 53 DU with considerable spread (the time slice averaged minimum decreases by −11 DU, the maximum increases by 93 DU). Over the same period in 2015, the mean minimum column increase is 91 DU; the histogram of spring minimum Arctic column in 2015 is compact with much less variability than in 1990.

Within time slice 2015, winter 58 is the one with the lowest spring ozone column, and the one with the smallest Arctic minimum column increase from January to April. Total spring ozone column for this cold winter 2015/58 is shown in Figure 4.3, an overview of all 1 January and 1 April total ozone columns in experiment 2015 are displayed in Figures A.4–A.5.

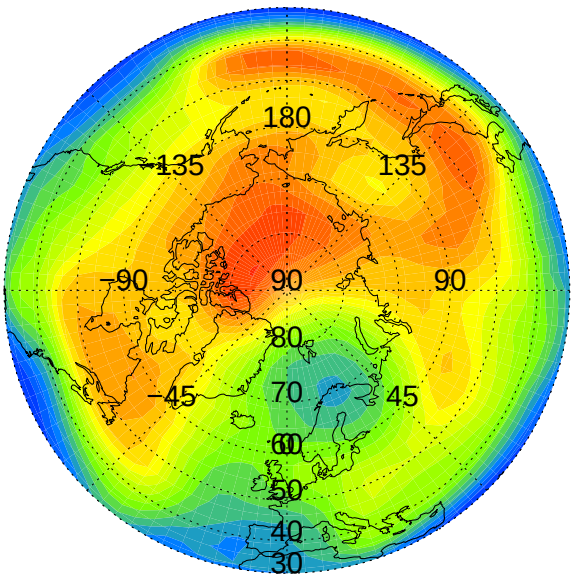

Figure 4.3: Total northern hemispheric ozone column in winter 2015/58, 1 April. The region of minimum ozone (blue colours) is shifted off the pole and centred around 65° N, 45° E with values down to 296 DU. Colour scale and total ozone columns for all winters 1990 and 2015 are displayed in Figures A.4–A.5 in the appendix.

W	b (DU)	a_0	a_1	a_2	W	b (DU)	a_0	a_1	a_2
43	1	−8.64	25.94	−12.75	53	2	−6.86	23.65	−12.10
44	0	−11.65	30.81	−14.66	54	0	−7.79	24.66	−12.32
45	0	−5.65	19.43	−9.80	55	−2	−4.86	20.62	−11.01
46	1	−6.40	23.64	−12.28	56	2	−9.57	27.73	−13.55
47	−1	−0.16	12.58	−7.65	57	0	−5.66	21.07	−10.87
48	−4	−9.22	27.70	−13.67	58	5	−7.40	24.12	−12.21
49	0	−4.53	18.89	−9.95					
50	3	−15.30	37.35	−17.46	60	1	−9.09	26.67	−13.14
51	3	−12.60	32.13	−15.14	61	4	−8.65	26.21	−13.03
52	1	−6.95	23.04	−11.59	62	0	−2.12	16.68	−9.50

Table 4.1: Vortex reference correlations between vortex methane and ozone established on January 1 for winters numbered W in time slice 1990. In the second column, a bias b calculated from the difference of the proxy ozone column and actual ozone column is shown, the last columns give the coefficients of the polynomial fit P with $\mu(\hat{\mathrm{O}}_3) = P(x) = \sum_{i=0}^{2} a_i \cdot x^i, x = \mu(\mathrm{CH}_4), \mu$ mixing ratio in ppm.

4.2 Tracer-tracer reference correlations

For each winter of both time slices 1990 and 2015, reference tracer-tracer correlations are calculated from methane and ozone. For the reference relation, all vortex data (see Section 3.6.1 for polar vortex edge calculation) in the potential temperature range 380–580 K are selected; to the vortex methane-ozone values, a second order polynomial P is fitted. This reference correlation calculates a proxy ozone $\hat{\mathrm{O}}_3$ from the methane field: $\hat{\mathrm{O}}_3 = P(\mathrm{CH}_4)$. The coefficients for the reference polynomials are shown in Table 4.1 for 1990 and in Table 4.2 for 2015.

Ozone column calculations Equation (3.3) are applied to proxy ozone $\hat{\mathrm{O}}_3$, as well. The difference $b = \mathrm{Col}(\mathrm{O}_3) - \mathrm{Col}(\hat{\mathrm{O}}_3)$ can be interpreted as a bias of the reference correlation fit and is also shown in Tables 4.1–4.2. Optimally, this bias is zero, for some

W	b (DU)	a_0	a_1	a_2	W	b(DU)	a_0	a_1	a_2
43	1	−12.77	26.85	−10.36	53	3	−17.12	32.38	−12.11
44	0	−5.35	16.62	−7.02	54	0	−8.20	20.02	−8.01
45	0	−6.38	17.80	−7.34	55	−2	−9.32	23.42	−9.52
46	−1	1.13	9.46	−5.06	56	0	−17.35	32.53	−12.05
47	0	−12.49	25.66	−9.81	57	1	−14.08	28.90	−11.11
48	0	−7.63	20.92	−8.65	58	1	−14.71	29.15	−11.04
49	0	−13.06	26.51	−10.09	59	1	−2.99	14.29	−6.47
50	1	−6.43	17.42	−7.12	60	1	−12.30	27.05	−10.61
51	1	−14.12	28.63	−10.96	61	−6	−10.25	24.44	−9.76
52	−1	−6.79	17.80	−7.19	62	−1	−12.86	26.21	−9.93

Table 4.2: Vortex reference correlations as in Table 4.1 but for time slice 2015

winters, larger positive and negative biases are calculated (largest bias in 1990 winters 48 −4 DU, 58 +5 DU, 61 +4 DU, and in winter 2015/61 +6 DU). These biases are a result of the necessary conversion between the methane coordinate used to establish the relation and the pressure coordinate used to calculate total ozone. The means and standard deviations averaged over each time slice are $+0.8 \pm 2.1$ and -0.1 ± 1.8 DU for experiments 1990 and 2015, respectively.

4.3 Chemical ozone loss

Chemical ozone loss is derived from the column difference $\mathrm{Col}(O_3) - \mathrm{Col}(\hat{O}_3)$, using ozone and methane vortex data on April 1. Proxy ozone $\hat{O}_3$ is calculated from methane with the reference correlation established on January 1 (see previous section). Where possible this reference is applied within the potential temperature range 380–550 K. For several winters, vertical descent of upper boundary air to lower levels is problematic for the tracer-tracer correlation method: enhanced diffusion in this upper boundary leads to contamination of polar with tropical air which invalidates the tracer-tracer correlation analysis for chemical ozone loss. For those winters with top boundary contamination, the analysis of ozone loss with the tracer-tracer correlation is restricted to the maximum potential temperature level exhibiting chemical ozone loss.

4.3.1 Experiment 1990

In all but two winters of the 1990 time slice, chemical loss is quantified with the tracer-tracer correlation method. Column loss in this time slice ranges from −5 DU to −59 DU with an average of −23 DU. Six winters exhibit a column loss greater than 30 DU (winters 51, 56, 58, 60–62). In Table 4.3, the partial O_3 column, the $\hat{O}_3$ column expected from the tracer-tracer correlation and chemically lost column ozone are summarised, along with the range over which the correlation extended.

4.3.2 Experiment 2015

With the tracer-tracer correlation, chemical ozone loss is found in nine winters of the 2015 time slice; an overview of the partial ozone column obtained in the simulation and with the respective tracer-tracer correlation is provided in Table 4.4. The greatest loss occurs in winter 58 with −36 DU, followed by winters 56 (−28 DU) and 62 (−21 DU). While winter 58 is at the same time the winter with the lowest spring Arctic column ozone (cmp. Figure 4.2), all other winters where chemical loss could be diagnosed are within 1 standard deviation of the mean time slice minimum Arctic column. In two winters with very low minimum Arctic ozone column values (45 and 51), the deduced chemical loss of ozone is zero.

W	θ (K)	Col(O_3)	Col($\hat{O}_3$)	ΔCol(O_3)
43	380–475	142	147	−5
44	380–550	162	184	−21
45	380–440	99	114	−15
46	380–550	204	233	−28
47	380–500	182	195	−13
48	380–550	207	227	−19
50	380–475	126	136	−10
51	380–550	193	224	−31
52	380–490	152	173	−21
53	380–550	199	218	−19
54	380–475	161	170	−9
56	380–550	147	207	−59
57	380–490	170	192	−22
58	380–550	204	250	−45
60	380–550	118	156	−38
61	380–525	204	241	−36
62	380–550	196	245	−49

Table 4.3: Chemical vortex ozone loss diagnosed with the tracer-tracer correlation method for 17 winters of the 1990 time slice; column values are given in DU, the loss column Col(Δ) was integrated over the potential temperature range indicated in the second column. There was no chemical ozone loss diagnosed for winters 49 and 55. The vortex edge was determined using the steepest gradient of the PV(ϕ_{eq}) function. Mean loss for the 17 winters shown here is 26 ± 13 DU; mean loss for the time slice is 23 ± 16 DU.

W	θ (K)	Col(O_3)	Col($\hat{O}_3$)	ΔCol(O_3)
43	380–460	165	174	−9
44	380–440	155	158	−2
46	380–440	126	127	(−1)
52	380–440	111	118	−6
53	380–460	136	147	−10
54	380–440	119	124	−5
56	380–500	176	204	−28
58	380–550	214	251	−36
60	380–490	196	201	−4
61	380–460	120	121	(−1)
62	380–500	197	218	−21

Table 4.4: As in Table 4.3, but for 11 winters of the 2015 time slice; no chemical ozone loss is found for winters 45, 47–51, 55, 57, and 59. Values in parentheses are within the standard deviation of the reference correlation. Mean loss for the 9 winters shown here is 13 ± 12 DU, mean loss for the time slice is 6 ± 11 DU.

4.4 Chemical and dynamical changes 1990–2015

Arctic minimum ozone columns for both time slices 1990 and 2015 are shown in Figures A.2–A.5. In both time slices, the January column is —both among individual time slice winters and between time slices— similar and averages 230 DU. April columns are significantly different in both time slices, with the 1990 experiment exhibiting a mean column of about 300 DU with large variability, while the minimum column in the 1990 experiment is larger on average (≈ 350 DU) with less variability.

Chemical vortex column ozone loss differs greatly between the two experiments: 17 winters in time slice 1990 are diagnosed with ozone loss, overall chemical loss is 23 ± 16 DU (mean ± standard deviation). In contrast, chemical loss in 2015 is diagnosed for 11 winters and averages only 6±10 DU over all winters (cmp. Tables 4.3–4.4).

In Figure 4.4, a hypothetical dynamical column is shown, which is derived from the sum of mean Arctic minimum column ozone and absolute overall chemical vortex column ozone loss. This dynamical column indicates that in 1990 from January to April about 70 DU are added to the ozone column by transport, of which 23 DU are lost through chemical processes. In 2015, the column increases from January to April by 100 DU through transport, of which 6 DU are removed by chemistry. There is a large difference of 30–40 DU in dynamical resupply between the two time slice experiments, while the difference due to chemistry is on the order of 10–20 DU.

The difference between the two time slices' Arctic minimum column ozone has been interpreted as a sign of Arctic ozone recovery in Austin et al. (2003) and WMO (2003). The analysis presented here shows that most of this apparent recovery is caused by a difference in the dynamical resupply of ozone and not by changes in

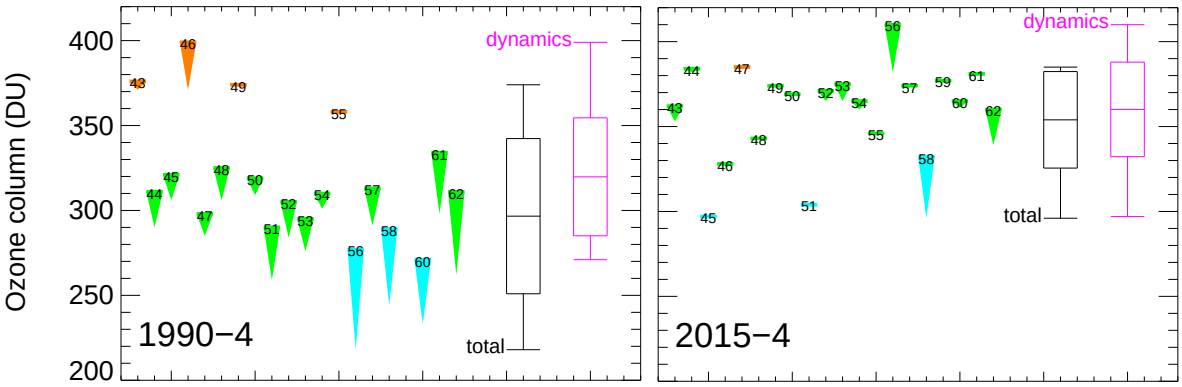

Figure 4.4: Arctic spring minimum ozone column and chemical loss. For each winter of the 1990 **(left)** and the 2015 **(right)** experiment, the vertical extent of the triangle denotes vortex chemical loss, while the lower tip is at the minimum Arctic column value (cmp. Figure A.3 for colours and "total" box-whisker plot). The pink box-whisker plot shows mean, standard deviation and range of a hypothetical "dynamics" column expected in absence of chemical depletion.

chemistry. The attribution of apparent recovery to dynamics had been previously reported by Schnadt (2001), Schnadt et al. (2002), and Schnadt and Dameris (2003); this study further quantifies the magnitude between dynamical ozone resupply and chemical ozone depletion in both time slices 1990 and 2015.

5 CLaMS simulations of the winter 2015/58

Detailed CLaMS simulations were performed for winter 2015/58. This winter is chosen since it shows the largest chemical ozone loss among all time slice 2015 winters. The minimum spring Arctic ozone from winter 58 constitutes the lower bound for the range of E39C simulated spring Arctic minimum ozone column (AMOC) in WMO (2003).

This chapter presents an analysis of dynamics and temperature in winter 58 and assesses PSC formation potential. Artificial digital tracers as indicators of vertical transport and mixing are discussed. The influence of lower and upper boundary conditions is shown. Tracer-tracer reference relationships for N_2O-NO_y and CH_4-O_3 are established. Denitrification derived from the TRAC technique is presented here for CLaMS and the E39C simulation, while chemical ozone loss derived with the tracer correlation method is discussed in the next chapter.

5.1 Polar vortex meteorology

Temperature and wind fields in the archived E39C data are analysed for temperatures below T_{NAT} and indications of stratospheric warmings. Throughout the period 1 January to 1 April of winter 2015/58, cold regions exist north of 60°N where the temperature is below NAT existence temperature T_{NAT} as defined in Equation (2.18); the area covered by temperatures $< T_{\mathrm{NAT}}$ at 50 hPa is shown in Figure 5.1 as cyan shading. The zonal mean temperature at 80°N and 50 hPa is below T_{NAT} for the first 40 days of the year; afterwards, it increases and stays approximately constant around 205 K until 10 March; from mid-March to April the mean temperature increases to 220 K. The minimum temperature at 80°N and 30 hPa stays below the threshold for NAT existence from 1 January to 25 March; thereafter, it oscillates within a 20 K range above the NAT existence temperature.

Changes in the zonal mean temperature difference at 10 hPa between 60°N and the pole at 10 hPa indicate stratospheric warming events. There are three warming events where the temperature gradient is reversed for one to a few days on 12 February, 20 February, and 14 March. On these dates, the zonal mean zonal wind at 10 hPa markedly decreases, but does not reverse: according to the classification of stratospheric warming events by Labitzke (1999), these are minor warmings. A major stratospheric warming event occurs on 25 March with a co-temporal reversal of the

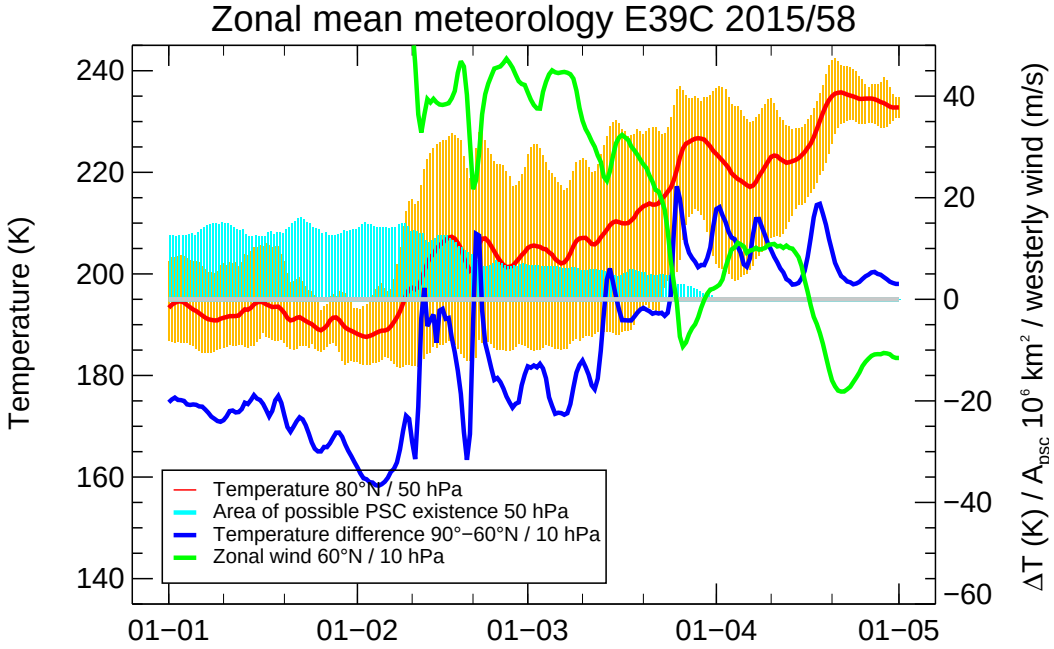

Figure 5.1: Meteorological conditions in winter 2015/58, 1 January to 1 May. The yellow shading shows the range of temperatures at 80°N and 50 hPa; the red line the zonal mean of this temperature field. Cyan shading indicates A_{PSC} north of 60°N at 50 hPa. Blue and green lines visualise the poleward temperature gradient and zonal mean zonal wind at 10 hPa.

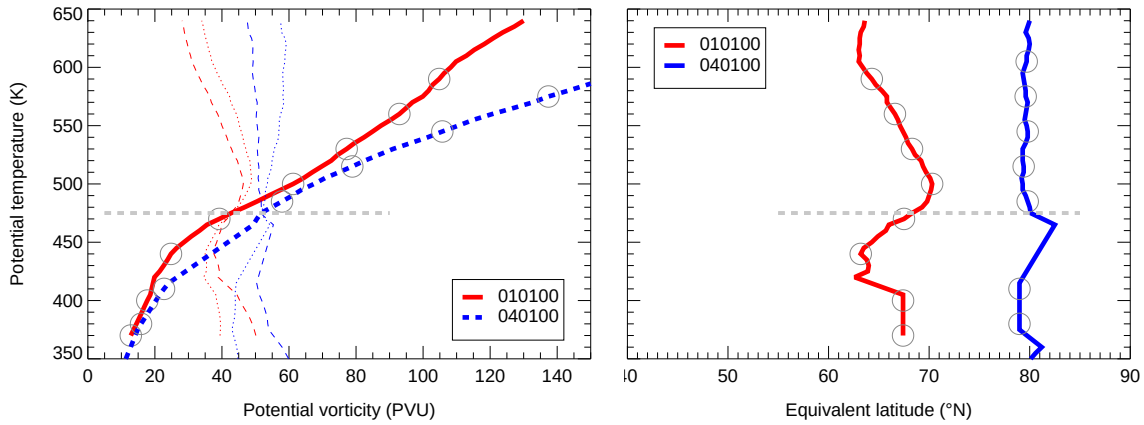

Figure 5.2: Profile of the vortex edge as a function of potential vorticity **(left)** and equivalent latitude **(right)**; the vortex edge is determined by the strongest gradient PV(ϕ_{eq}) on isentropic surfaces (Nash et al., 1996). Red colour indicates 1 January profiles, blue colour 1 April profiles. In the left hand figure, profiles of modified PV (Lait, 1994, dotted) and normalised PV (Rex, 1997, dashed) are added.

temperature difference and the zonal mean wind field. Westerly zonal wind is restored after 30 March until, on 16 April, a final warming ends the winter circulation.

5.1.1 Evolution of the vortex

In the data set for 1 January a stable polar vortex is centred over the North Pole with maximum extent to equivalent latitude $\phi_{eq} = 62°$N at 420 K potential temperature and above 600 K. Below 400 K the vortex area is much smaller ($\phi_{eq} = 68°$N) and nonexistent below 370 K. From 400 K to 490 K, the vortex area decreases to $\phi_{eq} \approx 70°$N, and increases again above 500 K. On the reference level $\theta_r = 475$ K, the vortex extends to 67°N equivalent latitude (the 41 PVU contour); on this level, maximum PV inside the vortex is 62 PVU. Profiles of the vortex edge in potential vorticity and equivalent latitude coordinates are shown in Figure 5.2 for 1 January and 1 April.

The vortex edge profile is stable during January with slight increases around 500 K. At the beginning of February, the vortex reaches its largest extent at 63°N (36 PVU contour at 475 K); after 1 February, the vortex area first decreases around 500 K (to 75°N on 12 Feb.), later in upper levels (to 75°N on 20 Feb.); from 21 February, the vortex edge is unstable above 500 K. Vortex instability is, for example, evident in large daily changes in the geopotential height field (not shown), or intermittent largest PV gradients at multiple equivalent latitudes. The vortex edge stabilises at 77°N after 26 February. The vortex edge below 500 K becomes unstable on 12 March and declines to 78°N until 21 March. Intermittently, instabilities occur below 500 K until the vortex break-up in mid-April. On 1 April, the vortex edge is located at 78°N for most altitudes. The temporal evolution of the vortex edge is shown in Figure 5.3 for multiple isentropic levels. Vortex strength, indicated by the magnitude of maximum PV, increases from 1 January to 10 March on the 475 K isentropic surface from 60 PVU

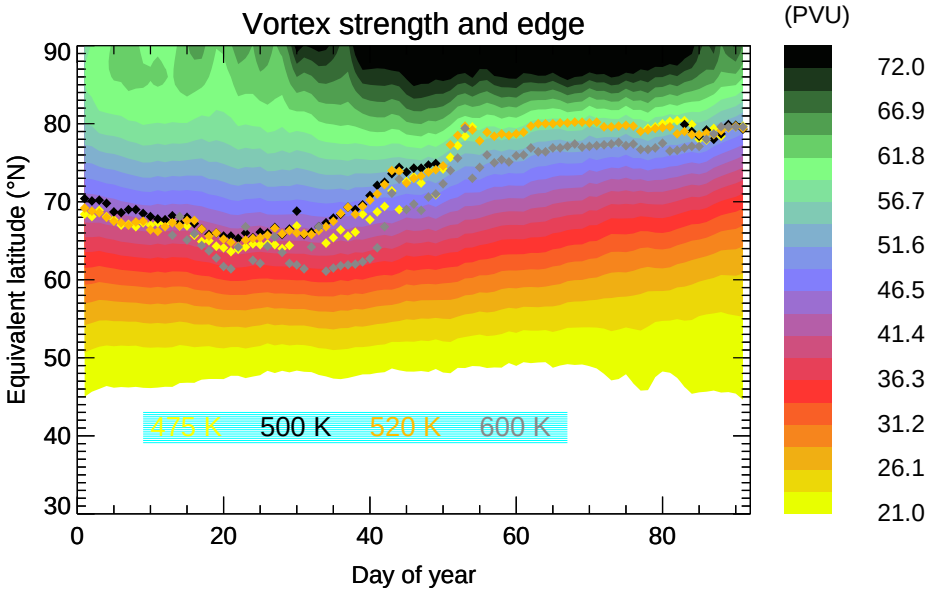

Figure 5.3: Temporal evolution of potential vorticity in ϕ_{eq}-time space over the 90 simulation days on the 475 K isentropic surface; shading indicates modified potential vorticity. The vortex edge at selected isentropic levels is shown as coloured diamonds.

to 85 PVU; until 1 April, vortex core strength is reduced to 60 PVU.

5.1.2 Temperature and PSC

In winter 58, temperatures are low enough for the formation of PSC from January through to the end of March (cmp. Figure 5.1). Assuming typical stratospheric volume mixing ratios[1] of 5 ppm H_2O and 10 ppb HNO_3, the threshold temperature for PSC

[1]Typical stratospheric mixing ratios are used here for comparison among different winters and to other studies using the typical mixing ratio assumption for water and nitric acid content.

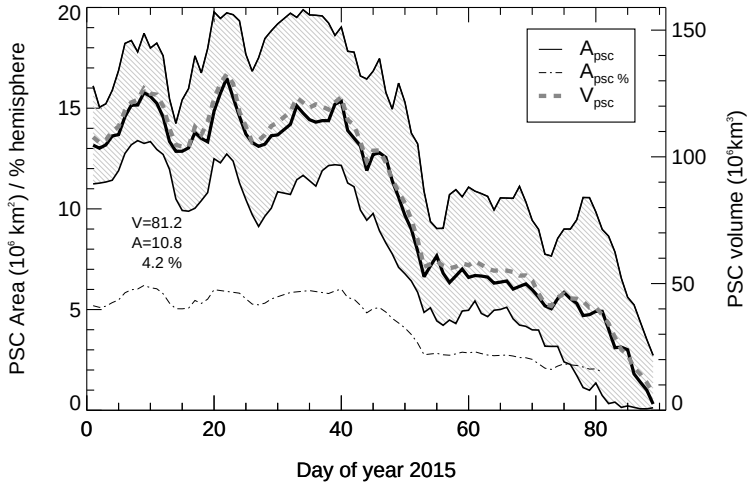

Figure 5.4: Area, hemispheric coverage and volume of possible PSC existence in winter 2015/58 in the altitude range 380–580 K. Shading indicates the range of A_{PSC}. Mean values are averaged over 90 days are given along the side of the figure for volume (V), area (A) and hemispheric coverage (in %).

existence T_{NAT} is calculated (Hanson and Mauersberger, 1988). Potential PSC areas are identified in isentropic gridded data where $T \leq T_{\mathrm{NAT}}$ and $\phi \geq 60°\mathrm{N}$. A_{PSC} is calculated on each isentropic level. To obtain the volume of PSC, vertical extent (in geopotential height) between two isentropic surfaces is multiplied with the mean A_{PSC} of these surfaces. As proposed by Rex et al. (2004), there exists a simple conversion factor between average A_{PSC} and V_{PSC}. For the E39C data, the conversion factor is found to be $8.0\,\mathrm{km^3\,km^{-2}}$ for average A_{PSC} between 380 K and 550 K. Rex et al. (2004) found a lower factor of $5.06\,\mathrm{km^3\,km^{-2}}$ for ECMWF data in the altitude range 400–550 K.

The PSC volume for winter 2015/58 is shown in Figure 5.4 as a function of day of the year. Time-averaged V_{PSC} is $81 \cdot 10^6\,\mathrm{km^3}$, roughly divided in a larger volume during the first 40 days of the year where PSC existence is possible over an area of $A_{\mathrm{PSC}} \approx 14 \cdot 10^6\,\mathrm{km^2}$, and lower values around $A_{\mathrm{PSC}} \approx 6 \cdot 10^6\,\mathrm{km^2}$ during March. This PSC area is one third of the area of a the large ozone hole observed over Antarctica in the year 2000. The northern hemisphere is covered at a fraction of 4.2% during the winter; this calculation is on the same order as calculations by Hein et al. (2001) who find a fractional hemispheric coverage of 4% in E39C simulations for 1990. 4.2% hemispheric coverage is larger than the maximum Arctic fractional coverage calculated for the 1990s by Knudsen et al. (2004), but lower than any of their Antarctic coverage fractions. They show that maximum northern hemispheric PSC fractional coverage was 2.8% in 1997; in all Antarctic winters in their study (1979–1993), 4.2%–6.8% of the hemisphere are covered by temperatures below T_{NAT}[2]

With the CLaMS PSC scheme, 0.2 NAT particles are produced per hour and per air parcel during the first 40 simulation days; NAT formation falls below $0.1\,\mathrm{AP^{-1}\,h^{-1}}$ on day 28, below $0.05\,\mathrm{AP^{-1}\,h^{-1}}$ on day 40. NAT formation ceases by day 86. The surface area density (SAD) provided by NAT particles decreases monotonously from $40 \cdot 10^{-6}\,\mathrm{cm^2 cm^{-3}}$ to $5 \cdot 10^{-6}\,\mathrm{cm^2 cm^{-3}}$ during the first half of the simulation and further to zero on day 86 when the minimum vortex temperature rises above 195 K.

5.2 Descent and boundary influence

As shown in Section 3.5.3, analysed descent in the E39C simulation is weak in the period 1 January to 1 April. Radiatively calculated descent rates used for CLaMS three-dimensional simulations are large on the order of 20–80 K per month. To contrast the different models' descent calculations, Figure 5.5 shows a scatter plot of E39C simulated methane versus CLaMS simulated methane volume mixing ratio: in this plot, CLaMS CH_4 is generally lower than E39C CH_4 (all data above the isoline;

Dehydration and denitrification in E39C and CLaMS simulations can lower these values to 2 ppm and 1 ppb, respectively; thus, the maximum existence temperature for PSC may actually be as low as $T_{\mathrm{NAT}} = 191$ K.

[2]Considering the reduced water vapour and nitric acid content in the CLaMS simulation, which lowers the average NAT existence temperature to $T_{\mathrm{NAT}} \approx 192$ K, the respective values for V_{PSC}, A_{PSC}, and hemispheric coverage are $59 \cdot 10^6\,\mathrm{km^3}$, $8.5 \cdot 10^6\,\mathrm{km^2}$, and 3.3%

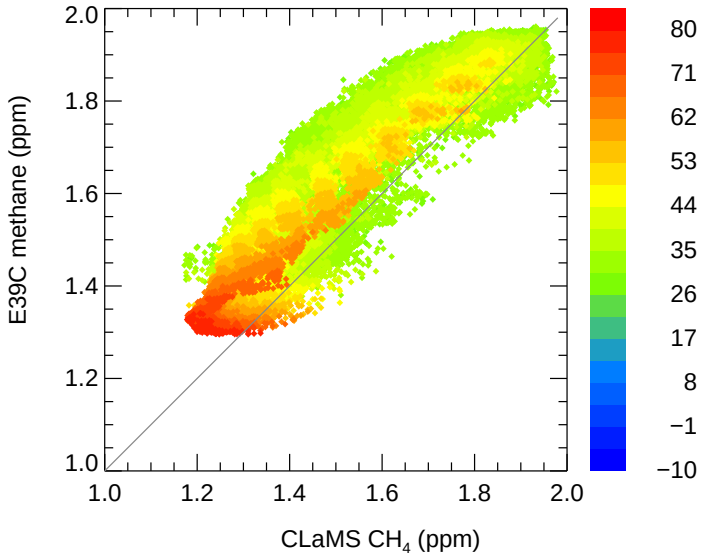

Figure 5.5: As in Figure 3.6, but for CLaMS methane vs. E39C methane. Data with mPV> 30 PVU are shown; the vortex edge is located at 45–55 PVU (colour scale). Data lying above the isoline indicate stronger descent in CLaMS than in E39C.

exceptions are boundaries and some mid-latitude air (green)), indicative of stronger vertical descent in the CLaMS simulation.

5.2.1 Descent of a passive potential temperature tracer

Diabatic motion in CLaMS model simulations is followed with an artificial tracer Tr_θ which is initialised with the potential temperature at simulation start. The difference between potential temperature and Tr_θ indicates at any time the accumulated mean vertical descent of an air parcel. Until 1 February, air with $\phi_{\mathrm{eq}} > 60°$ descends in CLaMS as a compact air mass: on average air descends from 400 K to 380 K, from 500 K to 460 K, and from 560 K to 500 K. There is some early winter differential descent in the 460 K layer which accumulates air from 510 K at the vortex edge and

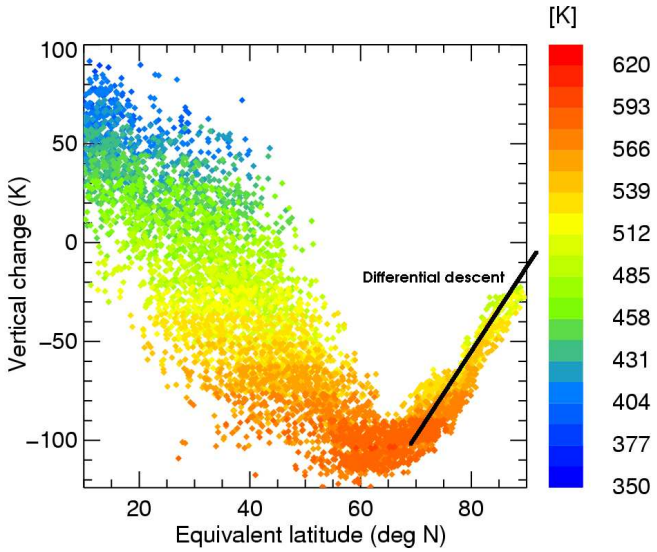

Figure 5.6: Vertical change of air parcels arriving in the 475 ± 15 K isentropic layer on 1 April, derived from a simulation with a passive tracer of potential temperature (Tr_θ); colour indicates AP source altitude. From the vortex outer edge to the core, strong differential descent is indicated by the slope of the black line: air masses outside the vortex are composed of upper boundary air (red), whereas core vortex air descended by ≈ 25 K.

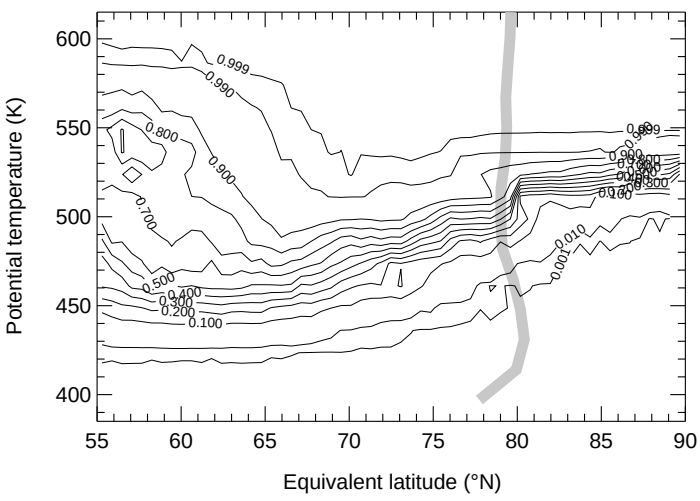

Figure 5.7: Contour plot of the upper boundary tracer (Tr_{upper}) in equivalent latitude-potential temperature space on 1 April of winter 2015/58. The shading indicates the vortex boundary. Within the polar vortex, Tr_{upper} penetrates to 480 K (at the 1% level). The strongest horizontal gradient occurs at the 500 K isentrope, where the tracer mixing ratio increases from 10% to 50% to 90% from vortex core to edge to mid-latitudes, respectively.

from 490 K in the vortex core. While the lower stratospheric vortex air continues its steady descent of $< 20\,\mathrm{K\,month^{-1}}$, there is no further descent above the 420 K level in the core. The origin of air parcels arriving in the 475 ± 15 K layer is shown in Figure 5.6. By 1 April, the strongest descent has occurred in mid-latitudes around $\phi_{eq} = 60°$N; weakest descent is seen in vortex core and sub-tropical data; tropical air ascended by up to 100 K. From $\phi_{eq} = 70°$N to the pole a strong gradient in vertical descent has evolved, shown as the solid black line. Within the vortex, this gradient is approximately 50 K, vortex air masses descend between 22 K in the core and 74 K at the edge. Differential descent results in a methane gradient within the vortex on the 475 K surface: at the vortex edge, methane volume mixing ratio (vmr) is 1.38 ppm. Towards the core, methane mixing ratio rises to a maximum of 1.46 ppm which is the initial 1 January value of CH_4 at 475 K. Isentropic mixing across this methane gradient may lead to overestimation of ozone loss when calculated with the tracer-correlation technique; this issue is further discussed in Section 6.4.

5.2.2 Boundary influence and boundary tracers

The upper boundary tracer (Tr_{upper}) is transported and mixed down from 620 K to 480 K potential temperature within the vortex, down to 425 K outside the vortex during the 90-day CLaMS simulation. Three-dimensional mixing of this tracer influences polar air masses in the 490–530 K layer. Above 530 K, all air originates from the upper boundary layer. Figure 5.7 shows a contour plot of Tr_{upper} on 1 April. Most of the descent occurs in January, air above 530 K which originates in the upper boundary layer may be exposed to perturbed chemistry for a significant amount of time. Column ozone loss estimates for this winter are chosen such as to include data up to 550 K, i.e., the 99% isopleth of Tr_{upper}: it is noted that ozone loss may be underestimated at levels with large amounts of Tr_{upper}. A corresponding experiment for the digital lower boundary tracer (Tr_{lower}) shows that only minute amounts of Tr_{lower} mix into the lower-most model layer (below 370 K, results not shown).

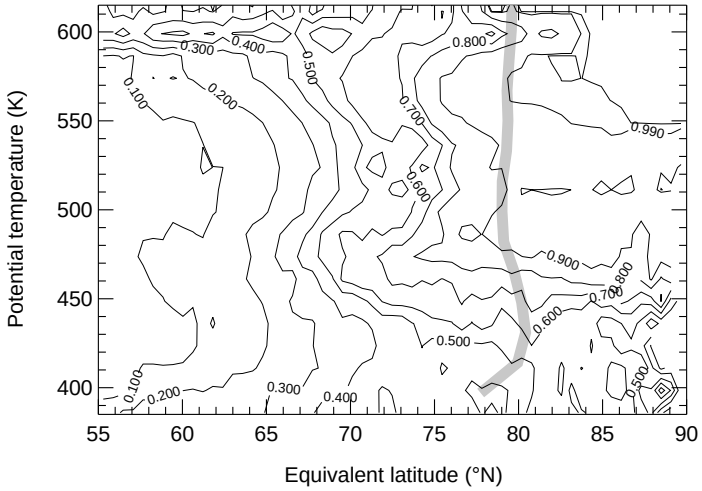

Figure 5.8: Contour plot of the vortex tracer ($\mathrm{Tr}_{\mathrm{vortex}}$) in equivalent latitude-potential temperature space for 1 April of winter 2015/58. The shading indicates the vortex boundary.

5.3 Isolation of and export of air from the vortex

On 1 April, a digital tracer ($\mathrm{Tr}_{\mathrm{vortex}}$) initialised to 100% inside the vortex quantifies the amount of isolation of the polar vortex. Above 450 K, the vortex edge coincides with the 90% isopleth of $\mathrm{Tr}_{\mathrm{vortex}}$, shown in Figure 5.8: the vortex air is well isolated. Towards mid-latitudes the 50% isopleth is located at $\phi_{\mathrm{eq}} \approx 70°\mathrm{N}$ (the extent of the January vortex). Air parcels are composed of half vortex and half mid-latitude air in this outer edge region; during the March warming events the vortex area decreases, depositing initial vortex air in the outer vortex edge. Mid-latitude air fraction at $\phi_{\mathrm{eq}} = 55°\mathrm{N}$ amounts to less than 10%.

Below 450 K the vortex is unstable during the last week of the simulation period. Mid-latitude air is brought to higher latitudes: the 50% isopleth coincides with the vortex edge at $\phi_{\mathrm{eq}} = 80°\mathrm{N}$; throughout the vortex, mid-latitude air fraction is $\approx 40\%$. Figure 5.9 shows a contour plot for two sensitivity studies where the mixing parameter ℓ_c is increased to $\ell_c = 2.4$ (minute mixing) and decreased to $\ell_c = 0.4$ (intense mixing). At both mixing intensities, the distribution of the vortex tracer ($\mathrm{Tr}_{\mathrm{vortex}}$) is similar; at $\ell_c = 2.4$, intrusions of mid-latitude air with $\mathrm{Tr}_{\mathrm{vortex}} < 0.3$ are transported to the vortex centre below 450 K, where they can be found alongside air masses consisting of pure vortex air. The 450 K isentrope separates partly mixed vortex remains below from the isolated vortex above. Whereas the 0.5 isopleth of $\mathrm{Tr}_{\mathrm{vortex}}$ is located at $\phi_{\mathrm{eq}} \approx 75°$ in both cases, reduced mixing extends the 90% isopleth from 80°N to 75°N.

5.4 Reference correlations and denitrification

5.4.1 Early winter reference relations

Tracer-tracer reference correlations are derived from polar vortex data on 1 January of the cold winter 2015/58. Correlations between methane and ozone (cmp. Table 4.2) and between dinitrogen oxide (N_2O) and oxidised nitrogen (NO_y) are calculated to

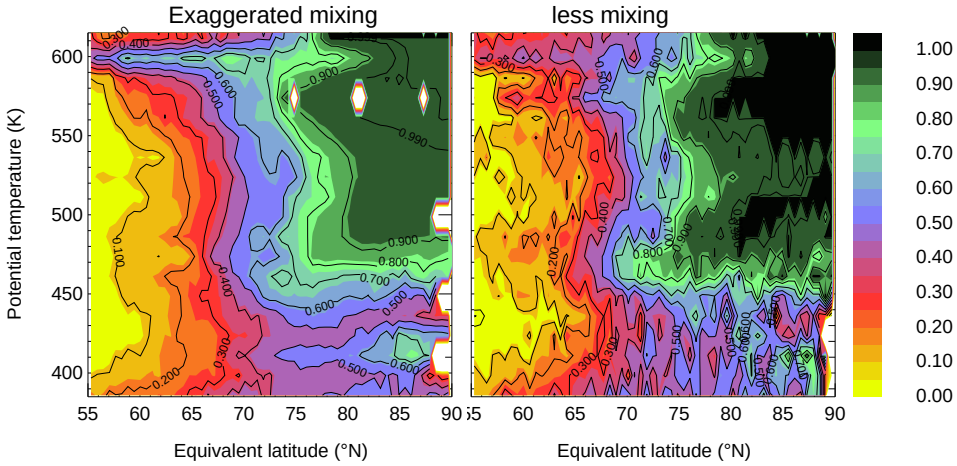

Figure 5.9: As in figure Figure 5.8, but for intense (left, $\ell_c = 0.4\,\mathrm{d}^{-1}$) and dampened mixing (right, $\ell_c = 2.4\,\mathrm{d}^{-1}$) intensity.

derive chemical ozone loss and denitrification, respectively. Table 5.1 shows the second-order polynomial coefficients for the correlations between active tracers y and passive tracers x in this specific winter. As shown in Figure 3.9, the relation between CH_4 and O_3 is compact on 1 January. It is well approximated by a second order polynomial: at higher order fitting as used by Tilmes (2004, 4^{th} order, Table B.3), the respective high-order coefficients $a_{3,4}$ are almost zero; the standard deviation reported here is on the order of, and generally less than, the deviation reported for CH_4-O_3 HALOE reference correlations for Arctic winters of the 1990s by Tilmes (2004).

The relation between N_2O as a passive tracer and NO_y as the active tracer is used to calculate a proxy for NO_y in the absence of denitrification, denoted here and in previous studies (e.g. Esler and Waugh, 2002; Popp et al., 2001) as NO_y^*. As in the study by Popp et al. (2001), a second order polynomial fit is employed to approximate the 1 January tracer relation. This relation is not as compact as the one for CH_4 and O_3: the large A_{PSC} on 1 January (cmp. Figure 5.4) suggests, that denitrification may have occured prior to this date. The derived polynomial relation, however, compares well to the reference relation used by Popp et al. ($a_{0,1,2} = 17.3, -0.0222, -9.85 \cdot 10^{-5}$) and can be here considered realistic, cmp. yellow line in Figure 5.10.

Passive (x)	active (y)	a_0	a_1	a_2	σ
CH_4 (ppm)	O_3 (ppm)	$-1.111 \cdot 10^1$	$2.462 \cdot 10^1$	$-9.64 \cdot 10^0$	$1.519 \cdot 10^{-1}$
N_2O (ppb)	NO_y (ppb)	$-1.71 \cdot 10^1$	$-4.89 \cdot 10^{-3}$	$1.68 \cdot 10^{-4}$	$1.49 \cdot 10^0$

Table 5.1: Early winter reference relations established for 1 January of winter 2015/58. For the relation between mixing ratios of an active tracer y and a passive tracer x a least squares estimate was used to derive a polynomial fit of order n with $y(x) = \sum_i^n a_i \cdot x^i$. The last column describes the standard deviation of the data to the fit. Polynomial fits were established in the range $\mu\,(CH_4) = [1.25; 1.75]$ ppm and $\mu\,(N_2O) = [100; 290]$ ppb.

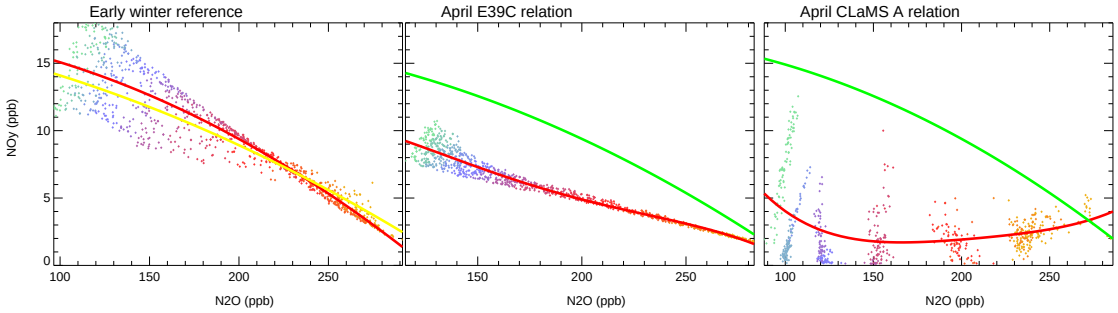

Figure 5.10: Correlation between dinitrogen oxide and NO_y. In the left hand figure, the reference relation (cmp. Table 5.1) on 1 January is shown, the yellow line is the reference relation observed by Popp et al. (2001). The two right hand figures show NO_y versus N_2O on 1 April, in E39C data (centre) and CLaMS three-dimensional simulations (right); in green colour, the reference relation $NO_y^*(N_2O)$ is shown; red colour indicates a fourth order polynomial fit through the data; data colouring and sampling as in Figure 6.2.

5.4.2 Denitrification in CLaMS and E39C

In both CLaMS and E39C, denitrification occurs for all vortex air masses where N_2O mixing ratio is between 100 ppb and 270 ppb, equivalent to the potential temperature range 380–550 K. In E39C (centre panel of Figure 5.10), 5 ppb NO_y are uniformly removed from the vortex air by sedimentation at all levels above 440 K ($\mu(N_2O) = 170$ ppb). In contrast, during the CLaMS simulation, approximately twice the amount of NO_y is lost by sedimentation; loss is more variable with several air parcels (AP) losing all their available reactive nitrogen while few AP retain 90% of the NO_y expected from the reference correlation.

The difference between the models at the lower levels is due to the effects of the lower boundary condition in CLaMS which forces NO_y loss to zero. Away from this lower boundary, the larger loss in CLaMS may be attributed to the difference in sedimentation schemes (cmp. Section 3.3.5). Temperatures from January to mid-March are sufficiently low to fall below the nucleation threshold for NAT in both models (cmp. Figure 5.1) and for NAT to exist for extended periods of time. Temperatures low enough for ice condensation ($T < T_{ice} \approx 185$ K) are present in the vortex but not as persistent as sub-T_{NAT} temperatures. In E39C, sedimentation of NAT —and therefore denitrification— requires the presence of ice particles, whereas in CLaMS, NAT sedimentation is independent of ice: NAT may be removed by the CLaMS sedimentation scheme when temperatures are between T_{ice} and T_{NAT} in CLaMS, but not in E39C. An impact of denitrification on ozone loss has been shown by several authors (e.g. Grooß et al., 2002; Grooß et al., 2004; Waibel et al., 1999); for this winter, the impact of neglection of denitrification on ozone loss is assessed with CLaMS sedimentation sensitivity studies, of which the results are presented in Section 6.5.2.

6 Ozone loss analyses with CLaMS

CLaMS simulations on winter 2015/58 were performed with different chemical boundary conditions. In a base scenario, the full stratospheric chemistry, including bromine reactions, is simulated. This base scenario predicts more chemical ozone loss and a lower Arctic minimum ozone column (AMOC) than the respective E39C simulation, which did not include bromine; Arctic bromine loading used in this base simulation A is $Br_y = 11\,\text{ppt}$ at 475 K. A more reliable estimate of the lower bound for AMOC under 2015 boundary conditions can then be calculated.

Chemical ozone loss is expressed here as accumulated chemical ozone loss over the 90-day simulation period, see Equation (3.2). If not explicitly stated, the calculations refer to the difference between active ozone and the passive ozone tracer O_3^*. The difference between proxy ozone $\hat{O}_3$ (i.e., ozone expected from the early vortex correlation with methane) and active ozone is calculated in addition for comparison to E39C ozone loss.

The underestimation of ozone loss associated with neglect of bromine chemistry is tested by a simulation of the same winter, but without bromine species. This simulation allows a more direct comparison to E39C results. Considering large uncertainties in today's stratospheric bromine loading, a third simulation is performed with doubled Br_y. Effects of Montreal protocol restrictions on emission of CFC and related substances are examined by various simulations which differ in their stratospheric halogen loading from zero to four times the expected 2015 value.

The independent calculation of ozone loss based on the passive ozone tracer in CLaMS allows a validation of the tracer correlation method on climate model data. At last, the sensitivity of chemical ozone loss to numerical and chemical parameters in CLaMS is examined.

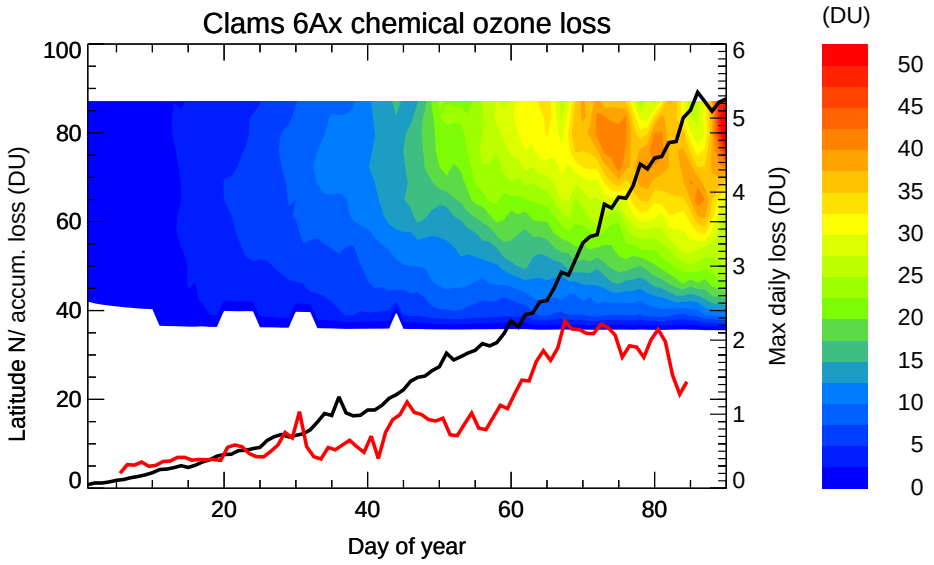

Figure 6.1: Evolution of chemical column ozone loss from 1 January to 1 April for scenario A. The black line indicates maximum Arctic chemical ozone loss (numbers as for latitude, in DU), the red line the day to day chemical column loss with 11-day running mean smoothing. Potential temperature range 340–640 K.

6.1 Evolution of the ozone column

During the course of a typical Arctic winter, the high latitude ozone column increases due to the wintertime mean meridional circulation which transports ozone towards the poles, and due to vertical descent, which brings O_3 rich air to lower altitudes. In CLaMS 3D simulations, this dynamical resupply is evident in the enhancement of the passive ozone tracer during the 90-day simulation period. Between 60°N and 80°N, zonally averaged passive ozone columns increase from 300 DU to 400 DU in the partial column 340–640 K; during the same time, the 300 DU contour widens in hemispheric coverage from 60°N to 45°N. This contour is apparent in the active ozone column at the same latitudes; however, for all CLaMS experiments where ozone loss during the winter is simulated, the mean ozone column between 60°N and 80°N increases from 300 DU to 360 DU during the first month and stays approximately constant until mid-March. North of 70°N, the ozone column declines to January values around 300 DU.

The difference between the passive ozone column and the active ozone column is shown in Figure 6.1 for the reference scenario A (cmp. Table 3.5 for an overview of scenarios). Accumulated zonal mean chemical column ozone loss stays below 10 DU during January; during February, accumulated loss increases to 20–30 DU north of 60°N. From 10 March, accumulated zonal mean loss attains values up to 45 DU, somewhat higher during the last days of March. The black solid line in Figure 6.1 shows the maximum Arctic column chemical ozone loss, along with its day to day change, displayed in red colour. While day to day column loss rates during the first 40 simulation days are on the order of 0.5 DU d^{-1}, about 1 DU is lost per day during late Febru-

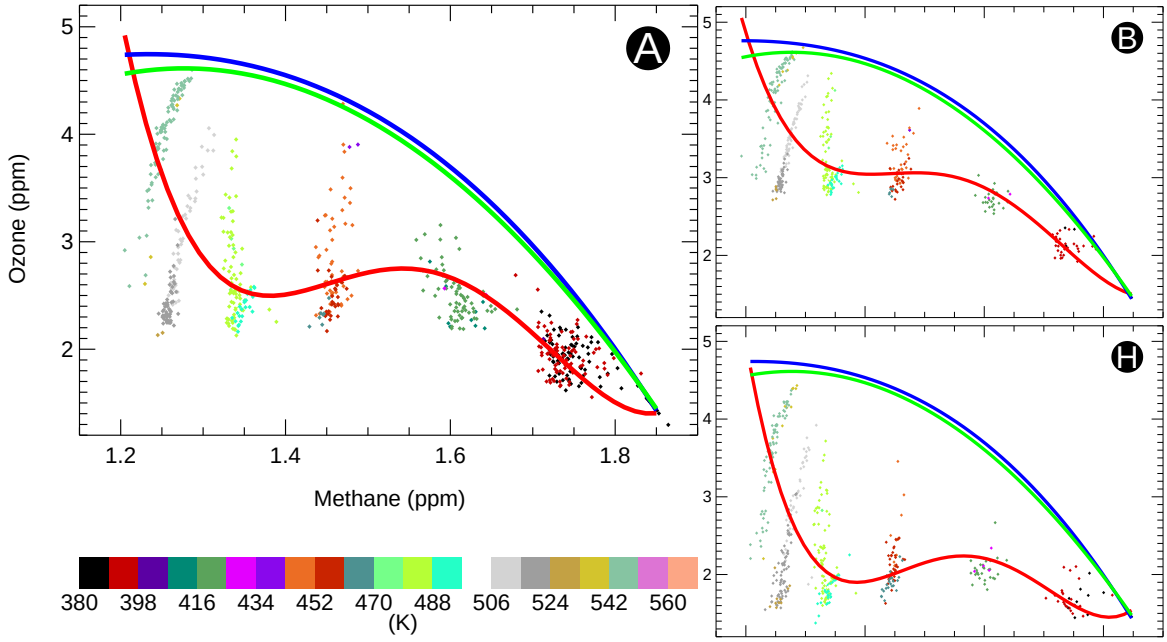

Figure 6.2: Correlation between ozone and methane after 90 simulation days in scenarios B (no Br_y), A (standard Br_y), and H (doubled Br_y). Thick lines (red: ozone, green: proxy ozone, blue: passive ozone) are 4^{th} order fits to the actual data. The difference between the passive tracer and active ozone is due to chemical ozone loss. In this and all following figures of this type, a representative sample of all data points is shown for O_3 to improve visibility; colouring of data points denotes potential temperature.

ary; in early March, daily maximum column ozone loss rises to $2\,\mathrm{DU\,d^{-1}}$. Maximum accumulated column ozone loss on 1 April is 86 DU.

6.2 Bromine chemistry and spring tracer correlations

With respect to the chemically inert CH_4 tracer, chemically active ozone is depleted in the vortex by 1 April. This relative depletion of O_3 vs. CH_4 is shown in Figure 6.2 for vortex data at the end of the simulation period (1 April). In all simulations shown in Figure 6.2 (scenarios B, A, and H, Br_y loading 0 ppt, 11 ppt, and 22 ppt, respectively), ozone values within the vortex are variable with a range up to ≈ 2 ppm within any isentropic layer. The large intra vortex variability of simulated O_3 is evident especially at higher altitudes, or equivalently lower CH_4 volume mixing ratio. A fourth-order fit through the median[1] of ozone values within the main levels emphasises the profile of ozone (shown in red), and thus the profile of vortex-average ozone loss . Largest loss occurs at CH_4 values around 1.35 ppm which corresponds to potential temperatures from 475–500 K. There is a significant increase of ozone loss with an increase in bromine loading. For scenario B (no Br), the median ozone value is 3.1 ppb

[1]The median is used here as a more robust measure of average vortex ozone compared to the mean which is susceptible to outliers

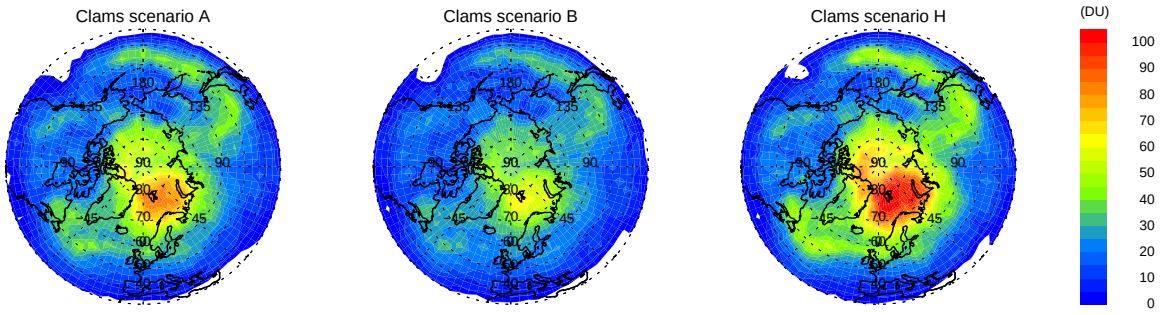

Figure 6.3: 90-day accumulated column ozone loss, calculated with a passive ozone tracer in three experiments with zero Br_y(B), Br_y loading 11 ppt (A), and doubled Br_y(H). The vertical range is 340–640 K, the date is 1 April.

at $\mu\,(CH_4) = 1.35$ ppm, corresponding to a local chemical loss of 1.5 ppm compared to the respective passive ozone value. Realistic but low bromine loading (scenario A) results in $\mu\,(O_3) = 2.5$ ppm, associated with a chemical loss of 2.1 ppm, the higher bromine loading in scenario A results in $\mu\,(O_3) = 1.9$ ppm and a local loss of 2.7 ppm.

The mean vortex column loss profile on 1 April is integrated vertically between 340 and 640 K potential temperature. A chemical loss column is obtained which is shown in Figure 6.3 for scenarios A, B, and H. Ozone loss is largest within, but not confined to the polar vortex. Maximum partial column loss is 87 DU in scenario A, an integral calculation over the mean vortex loss profile evaluates to 67 DU; the Arctic minimum ozone (AMOC) for this partial column is 197 DU. In scenario B (H), maximum loss is 65 DU (114 DU), average profile loss 50 DU (76 DU); AMOC is 221 DU and 179 DU, respectively. Table 6.1 contrasts local loss at $\mu\,(CH_4) = 1.35$ ppm, local loss at $\theta_r = 475$ K, and maximum/average partial column ozone loss for these three bromine scenarios. Additionally, the relative ozone loss per ozone tracer molecule averaged over all vortex data is shown; as defined in Section 3.6.3 this is the pressure weighted volume mixing ratio relation $\Delta O_3^*/O_3^*$. Compared to the partial column between 380–550 K (used when a tracer correlation was applied), chemical column loss within 340-640 K is 5 DU larger. For the indicators shown in Table 6.1 and a variety of other indicators, e.g. pressure-weighted loss, loss based on proxy ozone rather than passive ozone, partial column loss within the 475 ± 5 K layer, ozone loss increases linearly with bromine loading over the three scenarios A, B, H.

	Br_y (ppt)	$\Delta O_3@CH_4,r$ (ppm)	$\Delta O_3@\theta_r$ (ppm)	$\Delta Col(O_3)$ max (DU)	$\Delta Col(O_3)$ (DU)	ΔO_3 (%)
B	0	1.5	1.32	65	50	15
A	11	2.1	1.85	87	67	20
H	22	2.7	2.32	114	76	25

Table 6.1: Local ($\mu\,(CH_4)_r = 1.35$ ppm, $\theta_r = 475$ K) and column chemical ozone loss for three bromine loading scenarios A, B, and H. The last column is the relative ozone loss on a per molecule basis in percent.

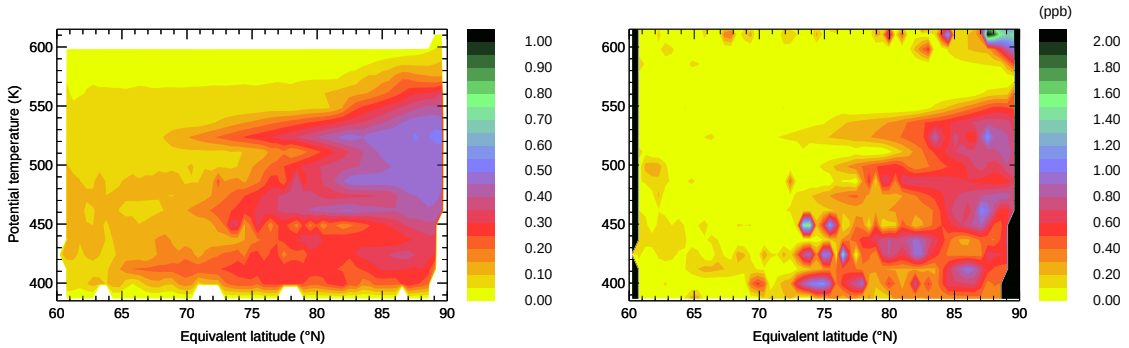

Figure 6.4: Vertical structure and latitudinal extent of ozone depletion and chlorine activation in base scenario A, averaged zonally over equivalent latitude. **(left)** Relative depletion of O_3 with respect to the passive tracer O_3^*. **(right)** Volume mixing ratio of ClO_x species (in ppb). Black edges indicate missing data.

6.2.1 Ozone loss profiles and local loss

Accumulated local ozone loss exhibits a vertical structure with largest depletion between 450 K and 550 K potential temperature. In the standard scenario A, a maximum of 50% of ozone is lost chemically in the vortex; this relative depletion is shown in Figure 6.4. Towards higher altitudes, which are influenced by air from the upper boundary layer, ozone loss decreases sharply. Ozone loss is significantly dampened by the upper boundary above 550 K which corresponds roughly to the 99% isopleth of the upper boundary tracer Tr_{upper}, shown in Figure 5.7. Meridionally, depletion occurs throughout the vortex with excursions of depleted air at 410, 460, and 525 K potential temperature. Beyond these excursions, extravortex ozone loss is small and does not exceed 15%.

A doubling of total bromine (scenario H) intensifies local loss within the vortex, reaching up to 70% (not shown). Likewise, neglection of bromine chemistry leads to reduced loss (maximum 35%) throughout the vortex. The vertical and meridional structure is similar in the bromine sensitivity experiments A, H and B.

6.3 The road not taken — doubled EESC scenarios

Experiments with varying effective equivalent stratospheric chlorine (EESC, the ozone depletion potential weighted sum of halogens) show that chemical ozone depletion under 2015 meteorological conditions depends primarily on halogen loading. Chemically lost ozone is negligible without halogen chemistry (scenario C) in the vortex. With EESC= 0 (scenario C), the chemically lost ozone column is 3 DU, calculated with the passive ozone tracer method. The overestimation of ozone by the tracer correlation method results in an apparent chemical increase of the ozone column by 2 DU; the systematic underestimation of chemical ozone loss calculated with the tracer correlation is on the order of 5 DU for all winter 58 simulations. There is local chemical ozone loss up to 10% in scenario C outside the vortex; within the vortex and Θ_r, the local

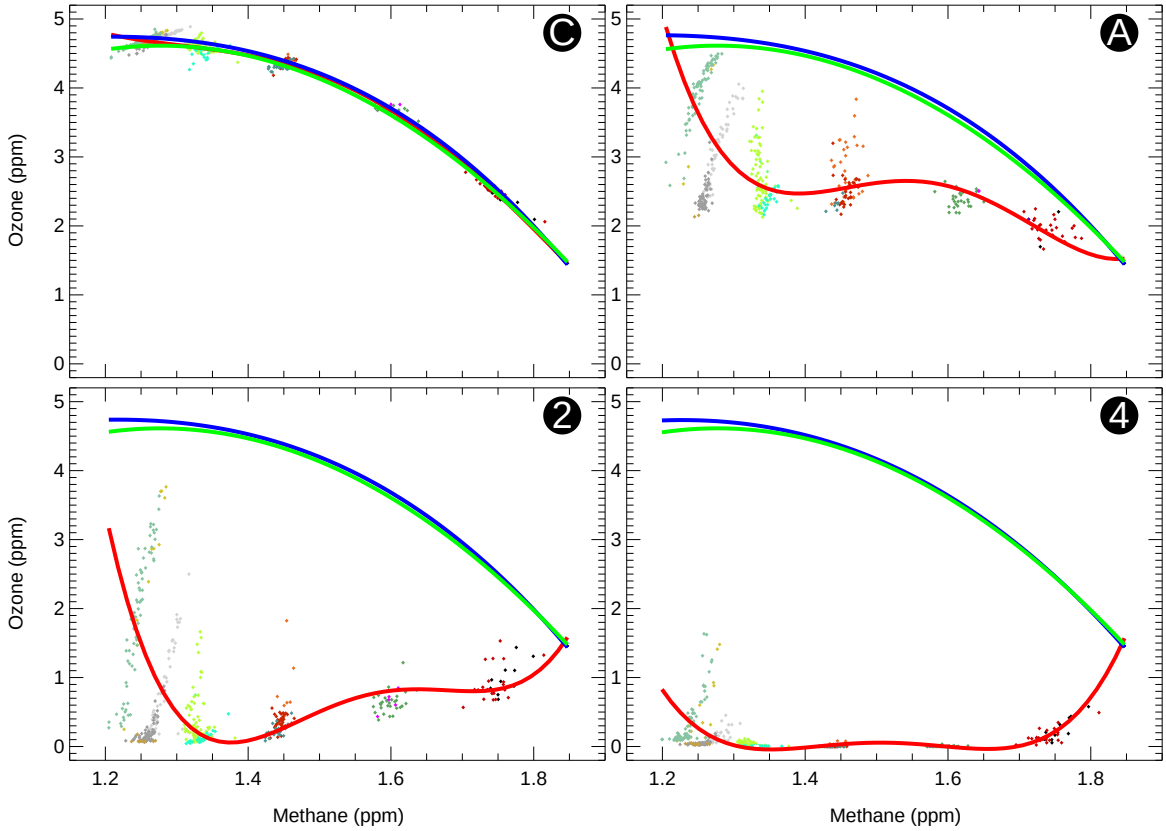

Figure 6.5: As Figure 6.2. The scenarios are (from top to bottom): no chlorine or bromine (C), standard effective equivalent stratospheric chlorine loading (EESC, A), doubled EESC (2) and quadrupled EESC (4). Note the lower ordinate axis in comparison to Figure 6.2

ozone loss is 127 ± 68 ppb, where 68 ppb is the standard deviation.

The depletion of ozone with respect to O_3^* and $\hat{O}_3$ is shown in Figure 6.5 for different halogen loading scenarios C, A, 2 and 4. Scenario A is discussed in the previous section, it is shown here with different scaling to emphasise the impact of doubled and quadrupled halogen loading on ozone depletion in scenario 2 and 4, respectively.

The doubled EESC scenario (2, EESC=4.65–4.97)[2] represents a development of stratospheric chlorine that could have been expected without the implementation of the Montreal protocol. In scenario 2, chemical ozone loss is approximately doubled with respect to A at all levels. Maximum local loss at $CH_{4,r}$ is 4.6 ppm, drawing the residual ozone profile to 0.1 ppm. At the 475 ± 15 K level, vortex-average local loss is 4.1 ± 0.3 ppm. Maximum chemical total ozone loss is 206 DU; 49% of ozone molecules are chemically destroyed with respect to the passive ozone tracer.

Compared to a doubling of bromine only (scenario H), the effect of chlorine doubling can be estimated: Within Θ_r, on a total vortex per-molecule basis and in the maximum

[2]The lower value is derived from weighting of Br_y with factor 45 (WMO, 1995), the higher value for a factor 60 (Chipperfield and Pyle, 1998)

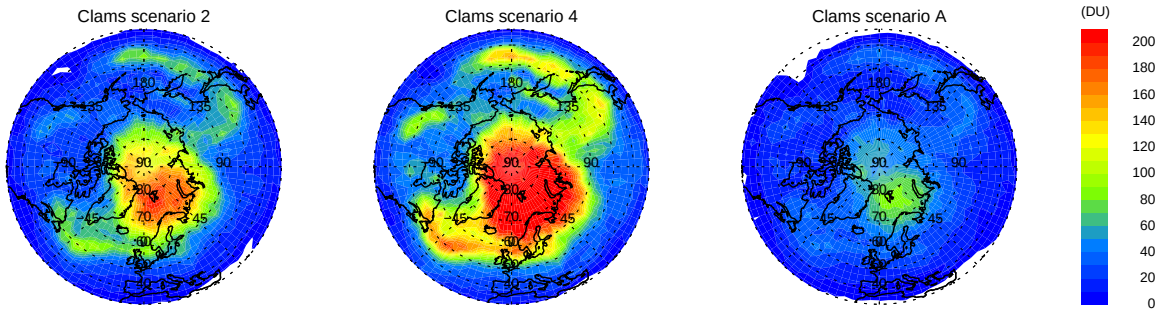

Figure 6.6: 90-day accumulated column ozone loss, calculated with a passive ozone tracer in three experiments with standard EESC (A), doubled halogen loading (2), and quadrupled loading Br_y(4). The vertical range is 340–640 K, the date is 1 April.

column, ozone loss increases by 90% (from 2 to H). Quadrupling the stratospheric halogen loading depletes the vortex of ozone at all levels. Between $\mu\,(CH_4) = 1.3$ ppm and 1.7 ppm, the residual profile is close to zero. Within the 475 ± 15 K level, 4.53 ± 0.08 ppm ozone are lost. Maximum column loss is 248 DU, 71% of all vortex ozone molecules are chemically destroyed. Figure 6.6 displays the accumulated column ozone loss for scenarios A, 2, and 4. Compared to the base simulation, accumulated column ozone loss is higher in all areas of the vortex and vortex edge, as well as in the filamentary structure which is located above the Aleutians. Results form experiments with differing EESC are summarised in Table 6.2

6.4 Validation of TRAC

The relationship of a passive ozone tracer (O_3^*) with CH_4 is influenced in CLaMS by mixing processes across the vortex and within the vortex; while mixing across the vortex edge may lead to underestimation of TRAC calculated ozone loss, internal anomalous mixing may lead to an erroneous overestimation of ozone loss by the tracer-tracer correlation technique (cmp. Section 3.6.1 and Figure 3.8).

By comparing the early winter reference relation with the relation between CH_4/O_3^* at any later time, dynamically induced changes to the correlation may be quantified. Figure 6.7 shows O_3^* as a function of CH_4 on 1 April from a very high resolution three-dimensional CLaMS tracer simulation ($\bar{r}_{\text{fine}} = 100$ km), together with the early winter reference relationship and the current vortex relationship. Data outside the

	EESC (ppb)	$\Delta O_3@CH_4, r$ (ppm)	$\Delta O_3@\theta_r$ (ppm)	ΔCol(O_3) max (DU)	ΔCol(O_3) (DU)	ΔO_3 (%)
C	0.0	0.1	0.1		3	
2	4.8	4.6	4.1	206		49
4	9.6	4.7	4.5	248		71

Table 6.2: As in Table 6.1, but for scenarios C, 2, and 4.

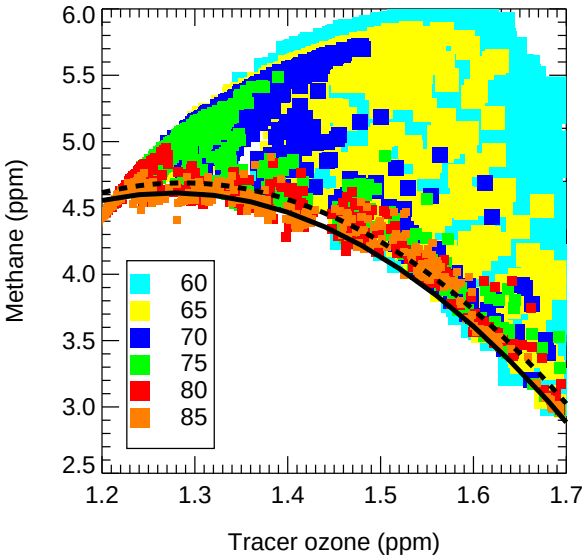

Figure 6.7: Compactness of the CH_4/O_3^* relationship on 1 April in the altitude range 380–550 K. Horizontal extent in units of equivalent latitude is indicated by colour. Red and orange data (north of $\phi_{eq} = 80°N$) are within the vortex. The dashed line is the polynomial relation for vortex data on 1 April, the solid line the reference correlation established on 1 January.

vortex ($\phi_{eq} < 80°N$) cannot be represented well with the early winter correlation. Data inside the vortex are well approximated. It is critical for the TRAC method that only vortex data are considered: including data from the outer edge of the vortex (e.g., $75 < \phi_{eq} < 80°N$, green colour in Figure 6.7) results in a large misrepresentation by the reference correlation.

Passive ozone mixing ratios are greater than ozone mixing ratios expected by the reference correlation: The mean difference between the reference and current relationships is 114 ppm; this number is the bias introduced by using a tracer-tracer correlation instead of a passive ozone tracer for the simulated winter. Too low ozone is predicted, thus calculations of ozone loss yield an underestimation of ozone loss with TRAC compared to the passive tracer loss calculation. At typical vortex-average losses of 1–2 ppm over the winter, the underestimation is 5–10%.

6.4.1 Separation of mixing processes

The influence of cross vortex edge mixing on the tracer-tracer relationship can be overcome by applying the early vortex reference relation to the global methane field at initialisation to generate a proxy of chemically inert ozone which is (a) based on the CH_4/O_3 correlation like $\hat{O}_3$, and (b) passively advected over 90 days, analogous to O_3^*; this tracer is consequently termed $\hat{O}_3^*$. The results of such an experiment are shown in Figure 6.8; again, the reference correlation does not represent data outside the vortex well. Anomalous internal mixing as described by Esler and Waugh (2002) is strongest in the (artificial) extra-vortex $\hat{O}_3^*$ data, which is in accordance with stronger vertical descent outside the vortex. Within the vortex, the effect is much smaller and leads to an underestimation of proxy ozone on the order of 100 ppb. An idealised sketch of internal anomalous mixing is provided in Figure 3.8 on page 61, using CH_4 and O_3^* values from this simulation. At minimum and maximum methane mixing ratio 1.36 and 1.48 ppm within the vortex, mixing between all vortex air parcels to the mean

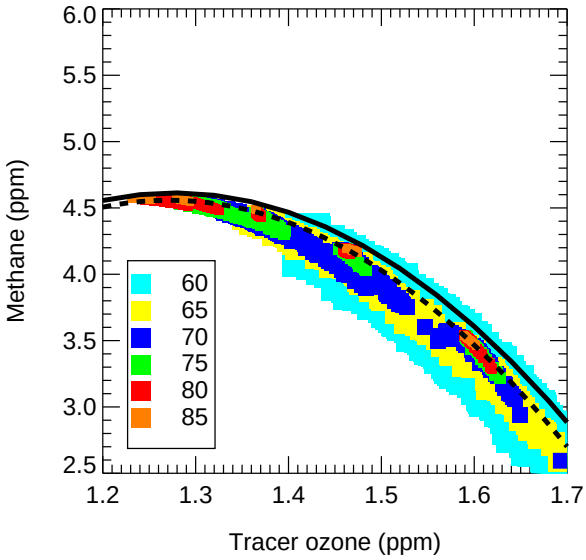

Figure 6.8: As in Figure 6.7, but for a passive tracer which was globally initialised with the reference correlation $\hat{O}_3$ on 1 January.

CH_4 mixing ratio of 1.38 ppm results in an underestimation of tracer ozone by 83 ppb.

While the difference between $\hat{O}_3$ and $\hat{O}_3^*$ captures the effects of anomalous internal mixing for this winter and the difference between $\hat{O}_3$ and O_3^* captures both effects of internal and cross vortex edge mixing, the difference $\hat{O}_3^*$ and O_3^* is equal to effects of cross vortex edge mixing alone. In the potential temperature range 380–550 K the average deviation over all vortex data is -212 ± 161 ppb ozone.

External and internal mixing both contribute to deviations of the CH_4/O_3^* relationship from the early vortex reference relation, but with opposite signs. For the examined winter, the effect of external mixing is larger in magnitude than the effect of internal mixing, both processes combined lead to an underestimation of ozone loss calculations on the order of 100 ppm.

Empirical results for the impact of anomalous internal and cross vortex mixing are published by Salawitch et al. (2002) and Ray et al. (2002) for the Arctic winter 1999/2000. Based on a N_2O-O_3 relation from *in situ* observations, the ozone loss calculated by Salawitch et al. (2002) is not influenced by either anomalous internal nor cross vortex mixing. Ray et al. (2002) examined separately the influences of differential descent and cross vortex mixing on long-lived tracer-tracer correlations. They find that mixing with mid-latitude air only occured below 500 K, and that the more important contribution to the spring vortex profile was differential descent followed by isentropic mixing.

6.5 Sensitivity studies

6.5.1 Numerical sensitivities

For scenarios A (standard EESC, $Br_y = 11$ ppt) and B (no bromine), two-dimensional high resolution studies with varying spatial resolution $\bar{r}_{\text{fine}}$ show that vortex average

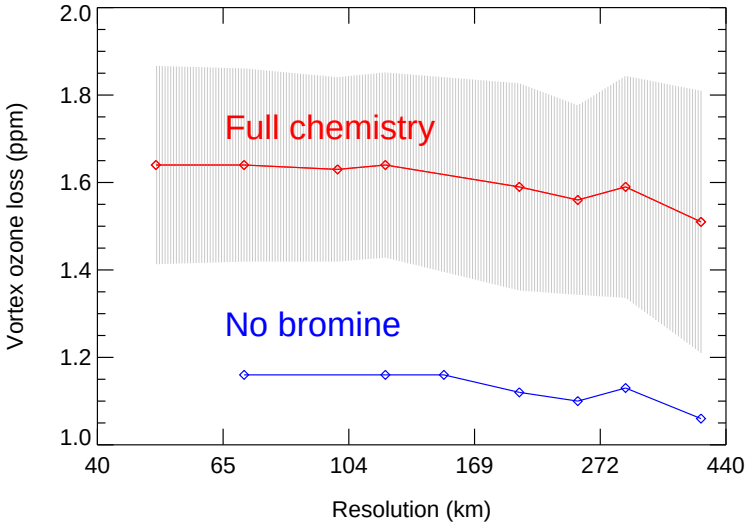

Figure 6.9: Accumulated chemical vortex ozone loss for varying horizontal resolution, ranging from 50 km to 400 km. Shown is the vortex average accumulated loss on 1 April at 475 K from two-dimensional simulations. For the full chemistry simulation, one standard deviation of the simulated vortex average ozone is shown as grey bars.

ozone loss is influenced by numerical resolution of the model on the order of 10%. Figure 6.9 displays the empirical dependence of ΔO_3^* on $\bar{r}_{\text{fine}}$, where $\bar{r}_{\text{fine}}$ is varied from 50 km to 400 km. Similar ozone loss is simulated in all experiments at resolutions better than 120 km; at the standard resolution of three-dimensional experiments ($\bar{r}_{\text{fine}}$=200 km) approximately 60 ppb less ozone loss is simulated, at the coarsest resolution of 400 km, 140 ppb less ozone loss, compared to the mean of the very-high resolution studies.

Results for scenario B resemble those for the full chemistry scenario A, at 70% of the simulated accumulated ozone loss. The reason for different accumulated ozone loss can be found by looking into the activity of chlorine cycles at the end of the simulation where deactivation plays a role: deactivation depends partly on the import of NO_x-rich air from mid-latitudes. If at coarse resolution the numerical diffusion is slightly enhanced, more NO_x is available to deactivate ClO_x and alleviate ozone loss. Relative fractions of ClO_x/Cl_y, NO_x/NO_y, and other parameters related to deactivation are

ℓ_c	$\bar{r}_{\text{fine}}$	N	$\Delta O_3^*/O_3^*$	ClO_x/Cl_y	$ClONO_2/Cl_y$	NO_x	NO_y/N_2O
1.2	50	2100	38.31	8.46	3.08	1.35	1.94
1.2	70	1082	38.40	8.37	3.01	0.92	1.89
1.2	**100**	**521**	**38.21**	**8.27**	**2.96**	**1.58**	**1.95**
1.2	120	358	38.40	8.40	3.03	0.59	1.89
1.2	200	134	37.42	8.35	5.36	0.78	3.26
1.2	250	81	36.71	8.68	4.97	1.26	2.97
1.2	300	57	37.32	8.61	4.97	1.71	2.87
1.2	400	28	35.69	6.82	10.06	0.51	4.83

Table 6.3: Relations between chemical species and families on 1 April for two-dimensional resolution sensitivity experiments. N is the number of vortex data, fractions are given in per cent, NO_x numbers are in units of ppt. Reference simulation results in bold type.

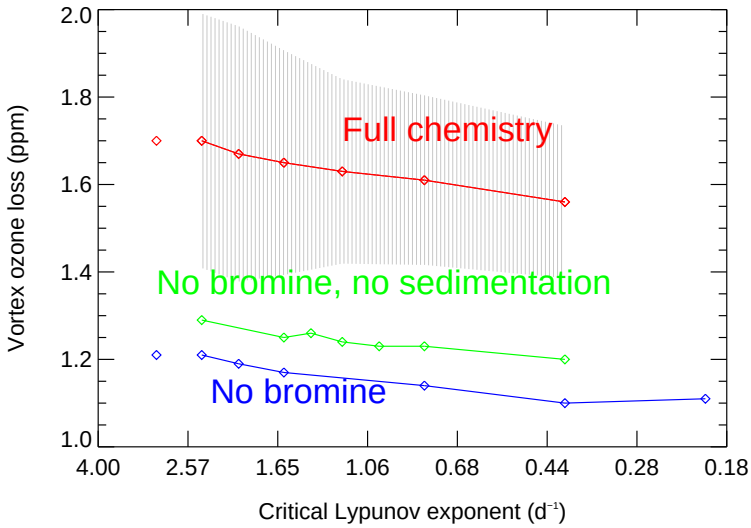

Figure 6.10: As in Figure 6.9, but for constant resolution $\bar{r}_{\text{fine}} = 100\,\text{km}$ and varying mixing intensity; critical Lyapunov exponents ℓ_c are in the range $0.2–\infty\,\text{d}^{-1}$. The single data points on the left hand side of the graph (positioned at $\ell_c = 3.0$) are the values for no mixing.

displayed in Table 6.3. The larger relative formation of $ClONO_2$ by 1 April at coarser resolution shows that, in fact, deactivation is larger in coarse resolution experiments which leads to less accumulated ozone loss; this statement holds even if the very coarse resolution sensitivity experiments are discarded due to the low number of data available for calculation of the vortex average.

Similar to coarse resolution, more intense mixing can lead to more or sooner deactivation if NO_y or NO_x are imported to the vortex. The sensitivity of accumulated vortex ozone loss in two-dimensional experiments is shown in Figure 6.10 for the base scenario A and two scenarios not including bromine. For all three experiment classes, the increase of ℓ_c, i.e. a decrease of mixing intensity, leads to less simulated ozone loss. Tracer relations and partitioning for selected parameters from these sensitivity studies are summarised in Table 6.4.

The evolution of vortex average (here the $\phi_{\text{eq}} = 80°\text{N}$ contour over the entire simulation time is used, which represents the vortex core during the first two months and the vortex edge at the end of the winter) evolution of tracers and tracer relations is shown in Figure 6.11. This figure shows that tracer relations and ozone loss diverge only at the end of the winter between two experiments with very different mixing intensities, where exaggerated mixing is simulated with $\ell_c = 0.4\,\text{d}^{-1}$ and almost no mixing with $\ell_c = 2.4\,\text{d}^{-1}$. In the intense mixing case, from day 60 a larger, but small amount of NO_y is introduced into the vortex from the outer vortex edge air (which is not denitrified). This can be seen in an enhancement of $ClONO_2$ with no corresponding change in ClO_x. During the recovery phase, starting on day 80, the larger available reactive nitrogen pool for intense mixing allows a faster deactivation: NO_x is controlled by the rate of ClO_x decrease and may thus not accumulate as much as in low mixing case.

6.5.2 Sensitivity to denitrification

Figure 6.10 includes the dependence of accumulated ozone loss on the critical Lyapunov exponent for experiments which do not contain bromine nor sedimentation of NAT and

Scenario	ℓ_c	$\bar{r}_{\text{fine}}$	$\Delta O_3^*/O_3^*$	ClO_x/Cl_y	$ClONO_2/Cl_y$	NO_x	NO_y/N_2O
A	0.4	500	36.46	8.66	5.61	0.80	3.50
A	0.8	518	37.74	8.68	3.94	0.90	2.51
A	1.2	521	38.21	8.27	2.96	1.58	1.95
A	1.6	562	38.68	8.52	2.95	1.31	1.76
A	2.0	510	39.41	8.57	2.72	1.51	1.76
A	2.4	500	39.80	9.13	2.24	0.32	1.54
A	∞	558	39.73	9.10	2.44	0.48	1.65
a	1.2	510	39.36	6.04	105.69	43.16	89.58
B	0.2	99	26.02	9.28	8.66	0.58	6.15
B	0.4	500	25.63	9.87	6.43	0.82	3.36
B	0.8	518	26.68	9.87	4.51	0.95	2.41
B	1.6	562	27.48	9.71	3.27	1.38	1.71
B	2.0	510	28.06	9.77	2.97	1.58	1.72
B	2.4	500	28.34	10.42	2.43	0.34	1.50
B	∞	558	28.29	10.38	2.64	0.50	1.61
b	0.4	495	28.23	2.52	117.75	46.60	87.69
b	0.8	498	28.79	3.52	118.04	44.27	88.98
b	1.0	529	28.72	4.07	118.93	48.78	88.74
b	1.2	510	28.96	5.24	119.18	42.19	88.87
b	1.4	550	29.39	5.69	116.48	35.87	88.60
b	1.6	567	29.36	6.72	119.40	41.30	88.91
b	2.4	489	30.30	7.97	119.90	43.99	89.27
b	0.0	557	30.21	7.55	118.88	46.70	89.16

Table 6.4: As in Table 6.3, but for varying mixing intensity. $\bar{r}_{\text{fine}}$ is held constant at 100 km, scenarios denoted with lowercase letters correspond to scenarios A and B, respectively, but do not include sedimentation.

ice particles (green line). From the literature, accumulated ozone loss is reported to be sensitive to denitrification: simulated and observed contribution of denitrification to ozone loss is on the order of 10% to 30% (e.g. Waibel et al., 1999; Grooß et al., 2002; Grooß et al., 2004). Here, the simulation of sedimentation and denitrification decreases vortex average accumulated ozone loss on 1 April. This unexpected result can be explained with the persisting low temperatures in the vortex in winter 2015/58 and the strong denitrification and dehydration associated with such temperatures.

Figures 6.11–6.12 show the temporal evolution of fractional ozone loss, chlorine and nitrogen partitioning, accumulated denitrification and dehydration for two scenarios with different mixing intensities and for two scenarios including and excluding sedimentation. In the no-sedimentation case (Figure 6.11), chlorine activation (ClO_x/Cl_y) is stronger during the first 85 simulation days. During the first 60 days, more chlorine is found in the short-term reservoir species HOCl. Compared to wintertime measurements of chlorine oxides (e.g. Stimpfle, 2004), this partitioning is unrealistic: under the low temperature conditions there should be more ClO_x than HOCl. This partitioning

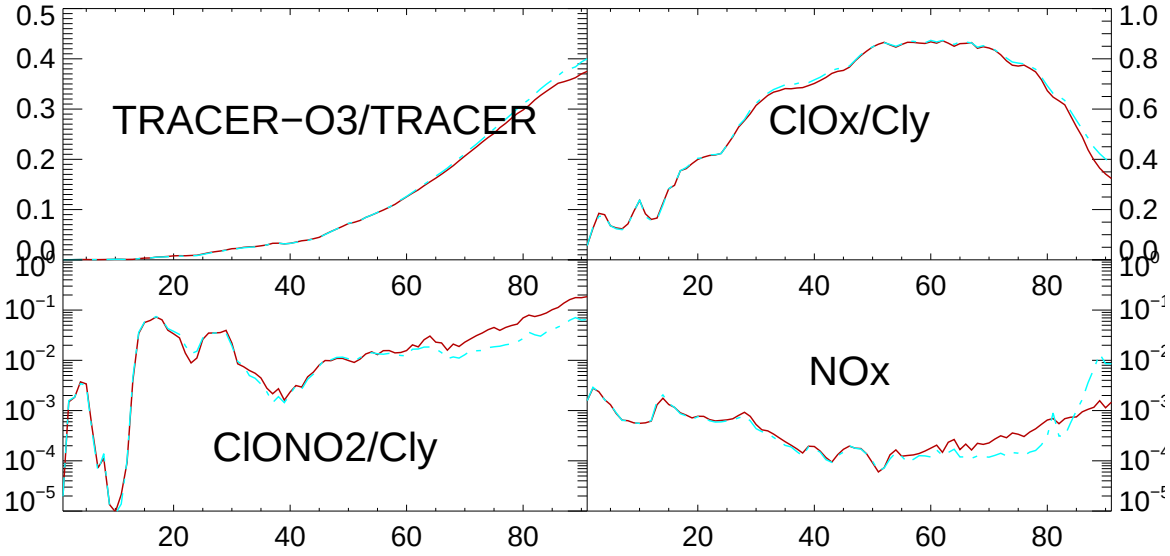

Figure 6.11: Evolution of vortex average tracers and tracer relations for two sensitivity experiments with different mixing intensity: exaggerated mixing ($\ell_c = 0.4\,\mathrm{d}^{-1}$, dark red, solid line) and minute mixing ($\ell_c = 2.4\,\mathrm{d}^{-1}$, cyan, broken line). Tracer relations are given as fractions of one, NO_x mixing ratio in ppb.

may be understood by considering that HOCl is part of the E39C ClOX family and is —in the view of E39C chemistry— active chlorine; values of $ClONO_2$ and HCl are low, which means that the vortex air is activated (no long-term reservoirs) throughout January and February. In CLaMS simulations, however, this partitioning may lead to underestimation of early winter ozone loss rates.

More important for accumulated ozone loss —and different in both simulations considered here— is the time period from day 60 to day 85, where Cl_y partitioning shows higher ClO_x and less chlorine in reservoirs for the no-sedimentation case. On day 70, for example, there is about 5 times less (45 ppt vs. 236 ppt) HCl in the no-sedimentation case. The fast changes in the reservoir fraction can only be attributed to heterogeneous chemistry on PSC: without sedimentation, more PSC can form because more nitric acid (factor 100, on day 70) and water (factor 5) are available compared to a simulation including sedimentation. On these surfaces, more chlorine is activated, accumulating in the ClO_x family and thus increasing chemical ozone depletion.

After day 85, the effect of denitrification is clearly seen in the comparison of both scenarios: without sedimentation, NO_x and $ClONO_2$ increase, accompanied by a decrease in ClO_x and stagnating ozone loss. In the simulation which includes sedimentation, the $ClONO_2$ reservoir starts to increase slowly with a corresponding decrease in activated chlorine: deactivation is not complete by 1 April and ozone loss continues past the end of the simulation.

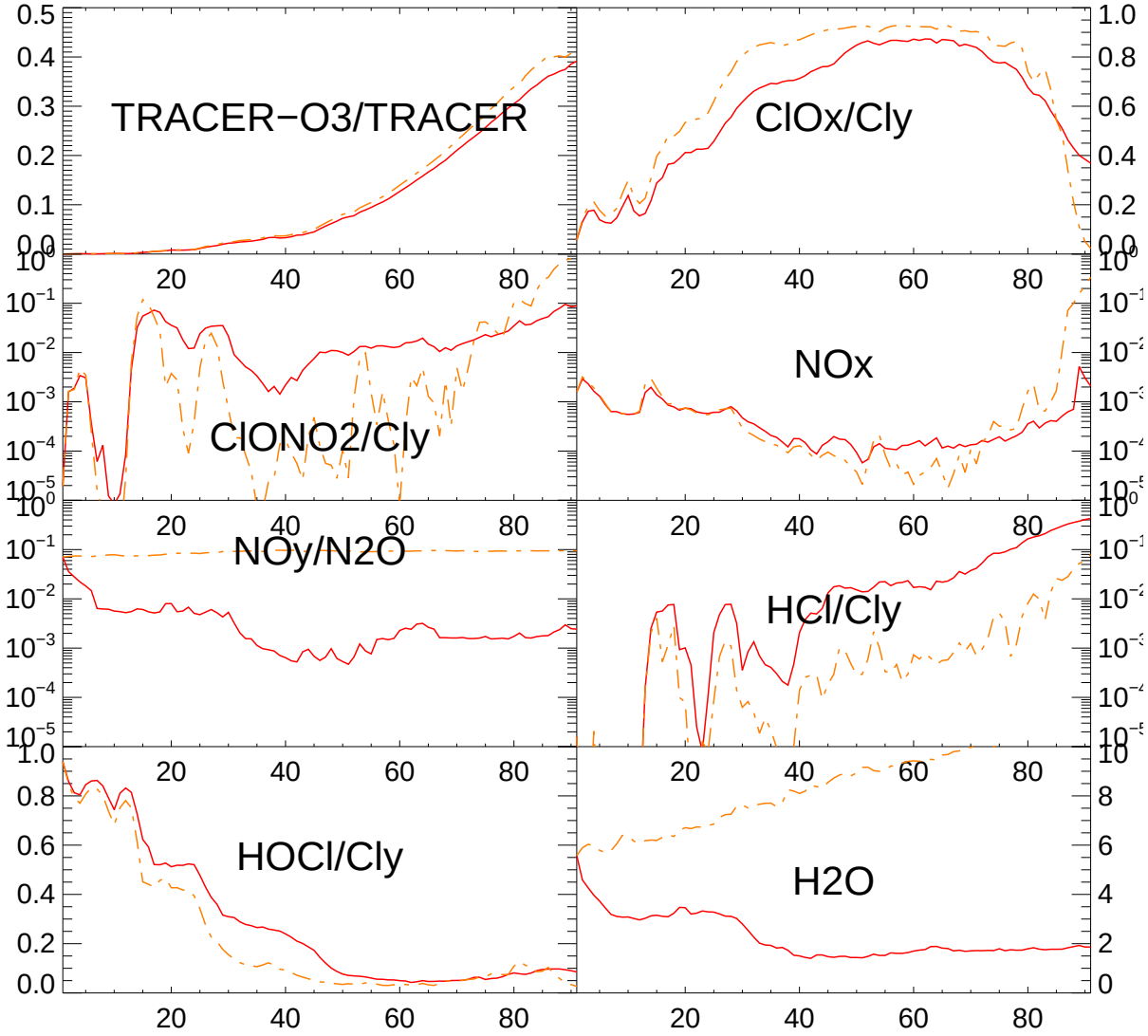

Figure 6.12: As in Figure 6.11, but for two simulations with full chemistry. Tracer relations and mixing ratios from the base scenario A are shown as the broken solid line, from a corresponding simulation without sedimentation as orange broken lines. Volume mixing ratio for H_2O is in units of ppm.

6.5.3 Additional halogen sensitivities

Complementary to the three-dimensional experiments, high-resolution isentropic experiments including and excluding bromine chemistry show the same general feature. Across all experiments, ranging in horizontal resolution from 50 to 400 km, and with critical Lyapunov exponents from 0.2 d^{-1} to 4.0 d^{-1}, the neglect of bromine chemistry leads to an underestimation of ozone loss by 30%, shown in Figure 6.13. Within the vortex, the relative depletion is uniformly 30% with a variation of absolute underesti-

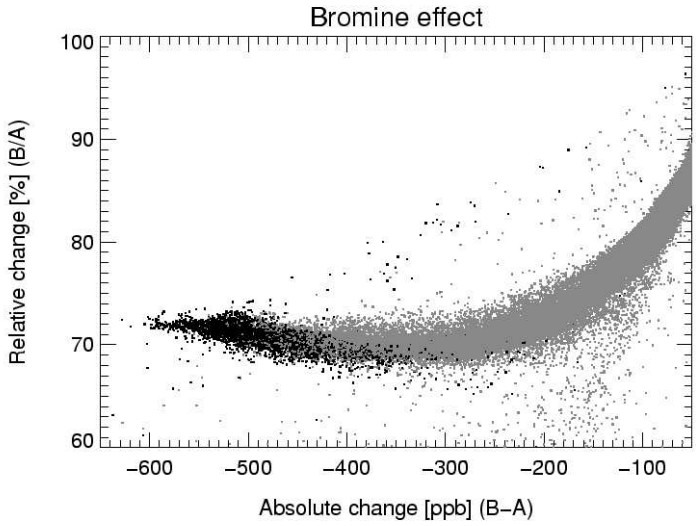

Figure 6.13: Effect of bromine chemistry on ozone loss across all two-dimensional resolution and mixing sensitivity experiments. On the abscissa, the absolute underestimation and on the ordinate axis the simulated fraction of ozone loss of simulations without bromine with respect to a corresponding simulation including bromine chemistry is shown. Black colour indicates vortex data.

mation in the range of 200 to 650 ppb. The relative depletion is approximately 30% for all data where the absolute difference in ozone loss is above 200 ppb.

Figure 6.14 shows the vortex average chemical ozone loss for two-dimensional simulations on the 475 K isentrope with varying chemical setup. The results are similar to those obtained in the three-dimensional simulations; in addition, the accumulated chemical loss for a simulation which includes bromine but excludes chlorine species is shown: simulated mean ozone loss is twice that of the no-halogen scenario (C, 110 ± 34 ppb vs. 60 ± 33 ppb). This additional loss is due to catalytic cycles involving bromine but not requiring chlorine, for example,

$$\mathrm{Br} + \mathrm{O_3} \longrightarrow \mathrm{BrO} + \mathrm{O_2} \tag{6.1a}$$

$$\mathrm{BrO} + \mathrm{O} \longrightarrow \mathrm{Br} + \mathrm{O_2} \tag{6.1b}$$

$$\text{net:}\quad 2\mathrm{O}_x \longrightarrow 2\mathrm{O_2}. \tag{6.1c}$$

The second reaction can be substituted by slow self-reactions of two BrO molecules to O_2 and Br_2 (or 2Br).

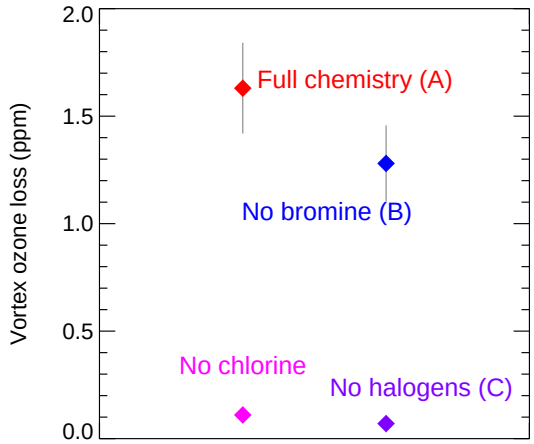

Figure 6.14: Accumulated chemical vortex ozone loss for different constellations of halogen loading on the 475 K isentropic level in two-dimensional simulations on 1 April: full chemistry (scenario A), without bromine (scenario B), without chlorine but including bromine, and without halogens (scenario C). The bars denote one standard deviation (which is very small in the two lower data points). Arbitrary abscissa.

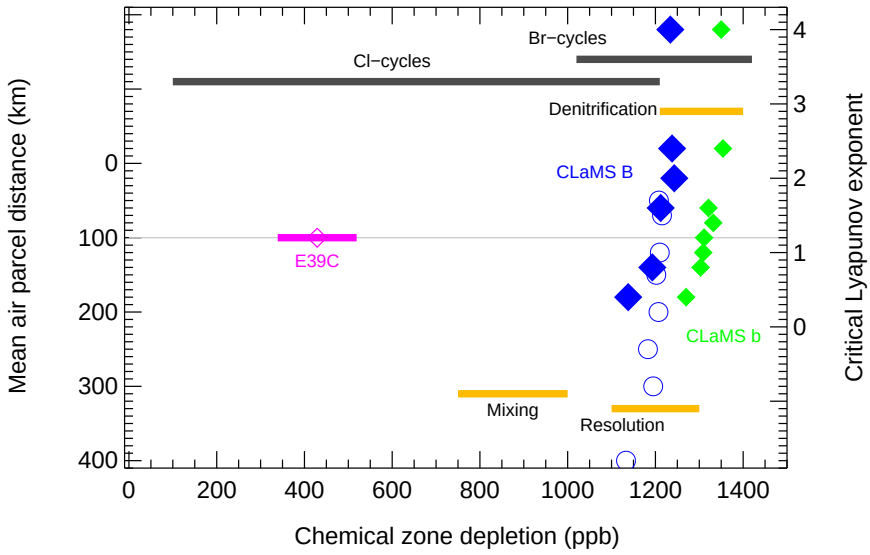

Figure 6.15: Summary plot of accumulated ozone loss (calculated with TRAC) for multiple model sensitivities. Mixing intensity variation is shown for scenario b (green) which excludes bromine and sedimentation; 2D simulations at varying Lyapunov exponents (diamonds) and air parcel distances (circles) are shown in blue for scenario B. Annotated bars indicate the variation introduced in different parameters. In pink colour, the E39C vortex average ozone loss is shown with one standard deviation indicated by horizontal bars.

6.6 Combined sensitivities and comparison to E39C

A summary of sensitivity studies is provided in Figure 6.15. This overview is used to compare CLaMS accumulated ozone loss with accumulated ozone loss inferred from the E39C archived data. All chemical ozone loss mixing ratios shown in the figure are calculated with the tracer-tracer technique and use the same reference correlation, derived in Section 5.4.1; results are reported for the 475 K isentropic surface in CLaMS and the corresponding 490 K level in E39C to correct for mean ascent in E39C (cmp. Section 3.5.3) and to ensure the same level of inactive tracer mixing ratio ($\mu\,(CH_4) = 1.46$ ppm). CLaMS simulated ranges of sensitivity to mixing intensity, resolution and sedimentation are indicated as bars. Bars denoted 'Cl-cycles' and 'Br-cycles' show the magnitude of ozone loss in the base simulation and the further increase obtained by adding bromine (scenario A, not shown).

Individual CLaMS simulations (green: no sedimentation, scenario b, blue: including sedimentation, scenario B) simulate more vortex average ozone loss than is simulated by E39C (roughly 1200 ppb vs. 430 ppb). Sensitivities introduced by varying mixing and resolution are each on the order of 150 ppb; less denitrification (as it is observed in E39C, cmp. Section 5.4.2) tends to increase ozone loss rather than decrease it if deactivation occurs very late and continues until after the end of the simulation. Accumulated chemical ozone loss in E39C is less than calculations based on observations in cold Arctic winters show. Manney et al. (1995), for example, find that chemical ozone loss at 465 K in winter 1996-1997 is 1300 ppb.

7 Future ozone depletion

In the three previous chapters, the influences of chemistry and dynamics on chemical ozone depletion in E39C time slice experiments 1990 and 2015 were analysed. The coldest winter of the time slice experiment 2015 was in detail examined with the CLaMS chemistry transport model.

In this chapter, results from bromine and chlorine loading experiments are viewed in the light of a hypothetical 'road not taken', i.e., as if the Montreal protocol had not been implemented (Prather et al., 1996); at the same time a more generalised approach to bromine loading (and the lack thereof in the E39C simulation) is developed.

The predictions of 2015 ozone loss by E39C and the CLaMS are compared to studies by other authors who use observations of ozone loss during the 1990s to derive relationships between the potential for polar stratospheric cloud occurrence and chemical ozone loss. It is shown how the combination of E39C and CLaMS can result in a more credible prediction of future ozone loss that cannot be achieved with the CCM alone. Finally, an updated value for the minimum Arctic ozone column in 2015 is suggested.

Scenario	loading factor f	enhance. factor e
4	4	6.60
2	2	2.75
A	1	1.00
C	0	0.38
H	2	1.31
B	0	0.71

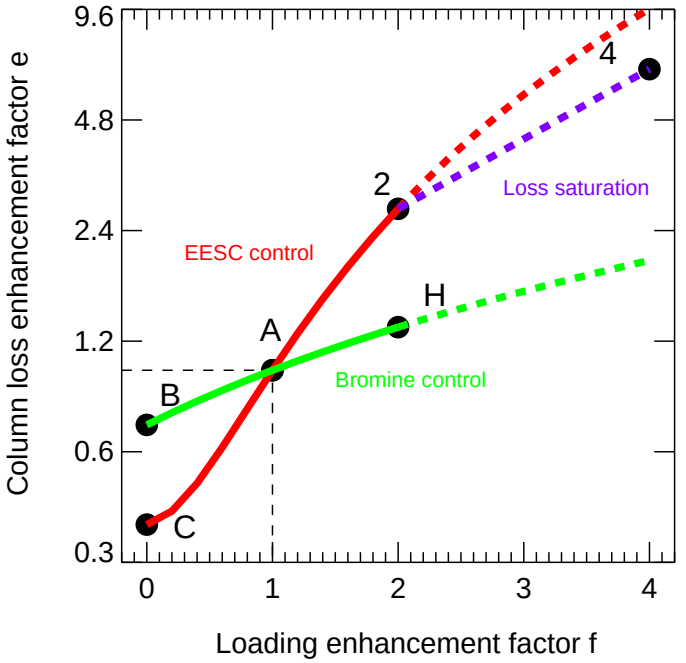

Figure 7.1: Pathways of maximum Arctic column loss for different halogen loadings (variation of EESC and Br_y). Shown is the enhancement factor e of maximum Arctic column loss with respect to the base scenario A; note the logarithmic scaling for the ordinate axis. The adjacent table lists the respective numbers for each scenario. See text for details.

7.1 Halogen loading

Sensitivities of column ozone loss or other measures of ozone loss to a variation of bromine loading or effective equivalent stratospheric chlorine (EESC) are here combined by considering halogen loading factors and enhancement factors for ozone loss. By reducing specific halogen loading scenarios to a simple factor (f) a more generalised view of the previously discussed halogen sensitivities is obtained: the loading f is defined as the ratio of a loading quantity with respect to the base scenario A ($Br_y = 11$ ppt, $Cl_y = 1.83$ ppb, and EESC≈ 2.4 ppb). For zero, doubled and quadrupled EESC (scenarios C, 2, and H) f is 0, 2, and 4, respectively; for zero and doubled Br_y (scenarios B and H), f is 0 and 2.

A further level of abstraction from a specific measure of ozone loss is obtained by introducing a loss enhancement factor (e). e is defined as the ratio of a quantity describing ozone loss relative to ozone loss in scenario A. Simple relationships that can be expressed by polynomial coefficients relate loading factors f to loss enhancement factors e for the various experiments performed with CLaMS: Figure 7.1 summarises these relationships for experiments with variation of Br_y (shown in green colour) and with variation of EESC (shown in red colour). In the adjacent table, the scenarios are listed with their loading factors f and the loss enhancement factor e obtained by relating daily accumulated maximum Arctic column loss to the daily maximum Arctic column loss obtained in the base simulation (loading and enhancement factors for A

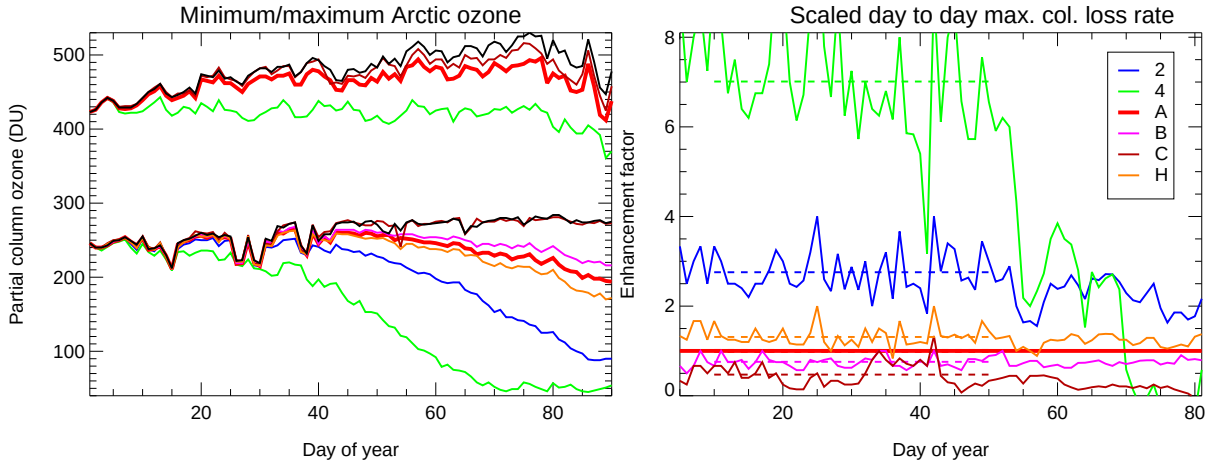

Figure 7.2: (left) Minimum/maximum Arctic ozone column in altitude range 340 to 640 K for different halogen loading scenarios. The lower ensemble of lines shows AMOC, the standard scenario A is printed with bold lines; the upper ensemble shows the respective maximum ozone column. **(right)** Day to day loss rate scaled to the loss rate of the base scenario, showing the relative enhancement (e) of ozone loss. Some numerical noise was removed from the loss rates by applying a ±5-day window running average.

are, by definition $e = f = 1.0$).

A doubling of Br_y results in an enhancement of $e = 1.31$, neglect of bromine to an enhancement of $e = 0.71$. This finding confirms the 25% to 30% effect that is found throughout this thesis and in the literature (e.g. Bregman et al., 1997) for studies that quantify the relative contribution of bromine chemistry to ozone loss. The polynomial expression for the bromine sensitivity is

$$e_{Br_y}(f) = 0.71 + 0.28 \cdot f + 0.01 \cdot f^2 \tag{7.1}$$

and is shown as the green curve in Figure 7.1. This relationship is to a good approximation linear in the range $f = 0$ to $f = 4$, and may justify an extrapolation to higher than simulated loading (shown as the dashed line); Equation (7.1) shows that for a 10% variation of Br_y, ozone loss is expected to change by ≈ 3%.

The response of ozone loss to variations of EESC loading is more than linear in the simulated range of f. A polynomial expression derived from loading factors 0 to 2 is

$$e_{EESC}(f) = 0.38 + 0.06 \cdot f + 0.57 \cdot f^2. \tag{7.2}$$

The quadratic term dominates the relationship for $f > 0.2$, the resulting graph is shown in Figure 7.1 as the red solid line: a doubling of EESC leads to a factor 2.75 in ozone loss. The path from A to H visualises the 'road that has not been taken': compared to a scenario assuming no regulations, ozone loss decreases by a factor $e = 2.75$ in 2015 (in a future very cold winter)

For a loading factor $f = 4$, an enhancement factor $e = 9.6$ is predicted by extrapolation of Equation (7.2), displayed as the broken red line. This high value of the

loss enhancement factor is not observed in the quadrupled EESC simulation, where $e = 6.6$; that is, the sensitivity from $f = 2$ to $f = 4$ follows the dashed violet line.

A more detailed view of the ozone loss during the CLaMS simulation is shown in Figure 7.2. In the left hand panel Arctic maximum (upper ensemble of curves) and minimum ozone column (AMOC, lower ensemble) are shown. While for scenarios B, A, and H the minimum ozone column is monotonically decreasing during March, AMOC stagnates at a low level in scenario 4 from day 70 on. To remove this ozone loss saturation effect from the calculation of enhancement factors (e), alternatively, the day to day change in maximum column loss between day 10 and 50 is used for the calculation of e. This day to day maximum column rate is displayed in the right panel, scaled to the rate of the base scenario which is shown in Figure 6.1 on page 86. The resulting enhancement factors are shown as dotted lines in the right panel of Figure 7.2; they are $e = 7.01, 2.76, 1.31, 0.76, 0.47$ for scenarios 4, 2, H, B, and C, respectively. At $f = 4, e = 7.01$ is still lower than the extrapolated value from the polynomial expression $e_{\mathrm{EESC}}(4) = 9.6$: there may be other saturation effects that influence the rate of ozone loss which are beyond the scope of this thesis.

Loss enhancement factor e increases from 0.38 to 0.47 for scenario C when day to day loss rate during early winter is used instead of accumulated column ozone loss. In the latter measure of ozone loss the relatively low importance of non-halogen chemistry with respect to halogen chemistry for accumulated ozone loss is evident. The former measure considers a larger contribution of non-halogen chemistry to the day to day rate of early winter loss; well-lit regions outside the vortex exhibit chemical ozone ozone loss which are included in the maximum column loss rate when intra-vortex halogen chemistry is absent (cmp. Section 6.3).

The stratospheric chlorine loading in E39C time slice 2015 (for scenario A) is 91% of the respective value in the 1990 time slice. Noting that the response to bromine loading is almost linear, the response to chlorine changes can be estimated from the polynomial expression for EESC changes: the 9% Cl_y decrease from 1990 to 2015 in E39C should decrease the chemical ozone loss by $\approx 11\%$. However, the mean chemical ozone loss averaged over all winters that exhibit ozone loss greater than zero is reduced from 26 ± 13 DU to 13 ± 12 DU (cmp. Tables 4.3 to 4.4 on page 72). This reduction of 50% from 2015 to 1990 cannot be explained by the 9% variation of stratospheric chlorine: dynamical changes in both time slice experiments control ozone loss stronger than the reduction of halogens.

7.2 Comparison to other studies

Recently, studies using Arctic ozone loss information gathered during the 1990s have been published which show that there is a good correlation between measures of total ozone loss and measures of possible PSC occurrence. Rex et al. (2004) establish a very good correlation between possible volume of PSC and partial ozone column loss during Arctic winters 1992–2003. The correlation found by Rex et al. is shown in Figure 7.3 as the grey line, with individual winters shown as grey squares (large and

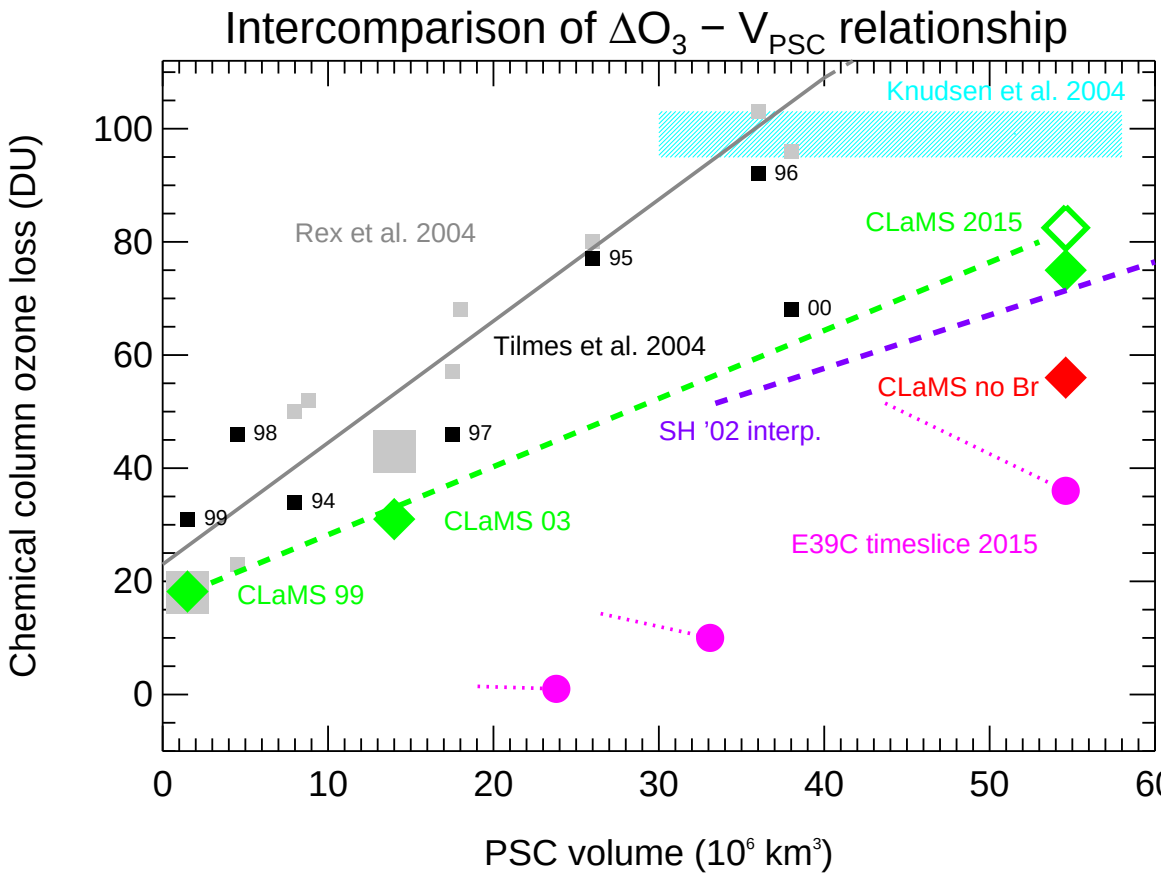

Figure 7.3: Arctic column ozone loss as a function of possible PSC volume. While the possible PSC volume projected by E39C is larger than in any recent winter, the simulated ozone loss does not at all agree with the linear function estimated from 1990's Arctic vortex average data (Rex et al., 2004) or the prediction by Knudsen et al. (2004) for cold Arctic winters in 2015. CLaMS results for 1999 and 2003 are from TOPOZ III (2005) and Grooß et al. (2004). See text for details.

small squares, individual years not labeled for clarity). Partial column ozone loss was determined between 14 and 24 km at equivalent latitudes poleward 67°N with the vortex average method between days 15 and 85 of each year. Results from this vortex average method were compared to SLIMCAT CTM simulations of Arctic winters (not shown), Modelled ozone loss was underestimated by the model for winters with large V_{PSC}, and overestimated for winters with small V_{PSC} (Rex et al., 2004). SLIMCAT simulations have been repeated with updated numerics, meteorology and reaction constants; updated results from SLIMCAT agree well with the relation derived from the vortex average approach (M. Chipperfield, personal communication, 2004).

Knudsen et al. (2004) combine the results by Rex et al. with historical wintertime analyses of the Arctic stratosphere provided by the Free University of Berlin (FUB, 1965–2001) and ECMWF (ERA-40, 1957-2002) to infer from long-term data an ex-

trapolation of Arctic ozone loss up to the year 2030. For those years with largest A_{PSC} in 5 year intervals, they predict for the year 2015 total ozone loss of 43–48 megatonnes (Mt). Using a relation between the data by Knudsen et al., Figure 2, O_3 loss in Mt as a function of hemispheric coverage and Rex et al., Figure 2, O_3 loss in DU as a function of V_{PSC}, this depletion translates to 95–103 DU, shown as cyan shading in Figure 7.3. Knudsen et al. demonstrate that for Arctic winters the correlation between ozone loss and possible PSC area (in percent hemispheric coverage) is even better than the original correlation between ozone loss and V_{PSC} by Rex et al.. Knudsen et al.'s linear extrapolation of Arctic PSC area to Arctic vortex depletion is not valid in general for Antarctic winters: cold winters exhibit ozone loss above the extrapolated value, and ozone loss in warm winters is well represented or overestimated by the extrapolation. For the unusual Antarctic winter 2002 ($\mathrm{Col}(\Delta O_3) \approx 125$ DU, $V_{PSC} \approx 90 \cdot 10^6\,\mathrm{km}^3$, not shown) a linear interpolation to CLaMS '99 is shown as the violet line in Figure 7.3.

The analysis of ozone loss in twelve recent Arctic winters by Tilmes et al. (2004b) is based on observations by the HALOE instrument; ozone loss is derived with tracer-tracer correlations. Tilmes et al. confirm a generally linear relationship between V_{PSC} and ozone loss for low possible PSC volumes; in addition, the amount of sunlight received per V_{PSC} is identified as an important factor which can explain some of the deviation of HALOE observed ozone loss (black squares in Figure 7.3) from a linear interpolation. Pinatubo aerosols after 1991 increased the extent of chemical ozone loss with respect to the linear interpolation. At large V_{PSC} ($30 \cdot 10^6$–$40 \cdot 10^6\,\mathrm{km}^3$), as would be expected in a cold future Arctic vortex, a linear relationship may not hold true (S. Tilmes, personal communication, 2005)

Chemical ozone loss prediction for 2015 based on the E39C time slice 2015 are shown as pink solid circles for winters numbered 46, 53, and 58 (in ascending V_{PSC} order[1]. Ozone loss is derived using the tracer-tracer correlation (cmp. Section 4.3.2). Clearly, in all four E39C winters ozone loss is vastly underestimated within the framework set by the above cited studies. Underestimation by E39C can be understood in part by taking into account that (a) ozone loss is reduced by 11% compared to the 1990s due to chlorine loading; (b) V_{PSC} is probably too large; the cold bias problem (Hein et al., 2001) can be ameliorated by a temperature shift of 3 K[2]; this amount reduces V_{PSC} by $\approx$ 20%; (c) bromine chemistry is missing which should add about 30% to the simulated column. The theoretical corrections described above are shown as dotted pink lines, drawing the E39C model results closer to observational studies.

Results from CLaMS simulations in this thesis (scenario A low $\mathrm{Br_y}$, solid green; and scenario B, no $\mathrm{Br_y}$, red) and other CLaMS studies (Grooß et al. 2004 and S. Bausch in: TOPOZ III 2005) are displayed in Figure 7.3 as solid diamonds. V_{PSC} was calculated as the mean vortex A_{PSC} on the 475 K isentrope[3] scaled with the conversion factor 5.06

[1] for comparison, all possible PSC volumes are calculated based on typical stratospheric values for H_2O and HNO_3. See annotations in Section 5.1.2

[2] Which is consistent with lowering the NAT existence temperature to 192 K as would be expected for the denitrified and dehydrated simulated stratosphere, as opposed to typical stratospheric values of H_2O and HNO_3.

[3] Numerically identical to the mean of A_{PSC} calculated over all isentropic levels between 380 and

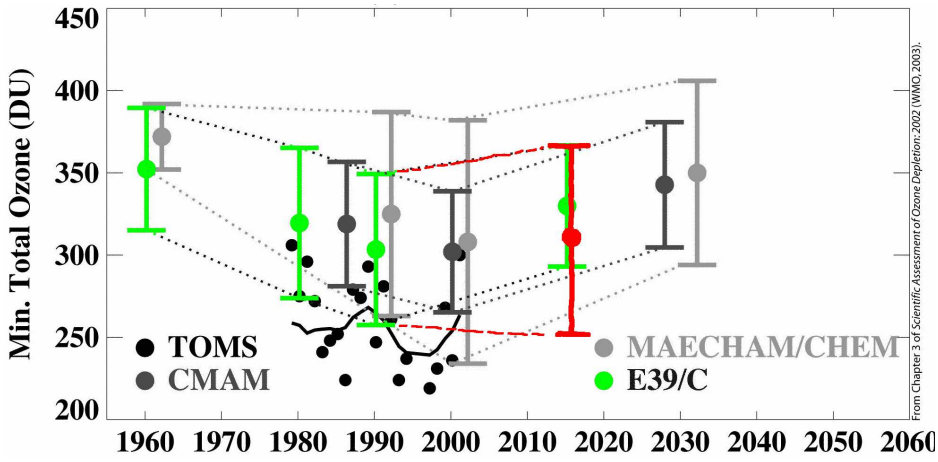

Figure 7.4: Spring Arctic minimum ozone column from a variety of GCM simulations. The four green highlighted experiments were performed with E39C, in red the updated prediction calculated in this thesis is shown (WMO, 2003, updated).

used by Rex et al.. Ozone loss calculated with the tracer-tracer correlation is shown. For winter 1999, CLaMS agrees with Rex et al.; for winter 2003, CLaMS simulates lower partial column ozone loss. Predictions for Arctic ozone loss 2015 are lower than the extrapolation by Rex et al., even taking into account that ozone loss would be 11% larger without EESC decrease from the 1990s to 2015 (shown as open diamond). The CLaMS prediction is also lower than the range of Arctic ozone depletion expected by Knudsen et al. for 2015. The empirical approach used by Knudsen et al. does not include the chemistry climate interaction present in the CCM simulation on which CLaMS is based, nor do they consider in their extrapolation a possible large change in stratospheric circulation, as is apparent in the reversal of the NAO in the E39C 2015 experiments by Schnadt and Dameris (2003).

7.3 A refined prediction of the Arctic minimum ozone column

The discussion in the previous section neglects many differences in the calculation of ozone loss (e.g. methodology, temporal range) and PSC volume (e.g. conversion from PSC area or hemispheric coverage, vortex edge definition, wind data) and provides a very generalised picture of the relationship between Arctic ozone loss and polar stratospheric clouds. Future ozone loss simulated with CLaMS on the basis of the E39C CCM is lower than relationships based on all 1990s Arctic winters suggest; the CLaMS result is in good agreement with HALOE observations in winters 2000 and exceeds a hypothetical relationship based on warm winter Antarctic ozone loss observed in 2002.

550 K, not shown

The CLaMS base simulation can therefore be considered a realistic predictor of minimum ozone loss in a cold winter in the decade around the year 2015. It is proposed to update the prediction of future Arctic minimum ozone column (AMOC) derived from E39C simulations with results from this thesis: The lower bound for the 2015 prediction should be reduced from 296 DU as simulated by E39C in winter 2015/58 to a value of 255 DU, which is the value for AMOC in the CLaMS simulation (scenario A) for the same winter. This update to WMO (2003) is shown in Figure 7.4 as the red coloured bar. No changes are shown here for the upper value of AMOC in 2015: of the four winters that contribute to this value (370 DU, winters 44, 47, 56, 61, cmp. Figure 4.4), one is analysed with severe column ozone loss (28 DU, winter 56, cmp. Table 4.4), the remaining three show no chemical ozone loss in the E39C simulations. A detailed analysis of the four winters 44, 47, 56, and 61 —similar to the calculations for winter 58 demonstrated in this thesis— may give more insight into the upper range of 2015 AMOC.

Dynamical effects are primarily responsible for the apparent recovery of AMOC in the E39C 2015 time slice experiment. A dominance of dynamical effects is also found by Schnadt and Dameris (2003) who demonstrate the link between sea surface temperatures via sea level pressure to changes in the NAO index. The decrease of the NAO index in 2015 compared to 1990 increases stationary wave activity, leading to a weaker and warmer polar vortex, and hence to lower chemical ozone loss. Indeed, in this thesis it is found that the frequency of winters exhibiting chemical ozone loss and the severity of chemical Arctic ozone loss 2015 is reduced with respect to 1990. The increase in dynamical resupply of ozone between these time slices is, however, much stronger than the decrease in chemical loss. The detailed chemistry transport model simulation with CLaMS —which considers bromine chemistry— of cold winter chemistry for 2015 shows that chemical ozone loss in 2015 may well be on the order of cold winter chemical ozone depletion observed in the 1990s, even under the more favourable dynamic conditions for Arctic ozone recovery.

7.4 Outlook

Successfully, the tracer-tracer correlation method has been applied to data from a global circulation model to analyse chemical ozone loss. The applicability of TRAC to GCM data is still debated: results of this thesis are expected to increase confidence in this analysis method, especially for GCM data where potential vorticity, and temperature are readily available at any time to accurately determine the polar vortex edge. In newer generations of GCMs and CCMs, the use of passive ozone tracers becomes increasingly common, such that results from TRAC can be validated within the model. TRAC provides the possibility to determine ozone loss in hindcast, even for many simulations performed over the last decade, where a passive ozone tracer may not be available.

The technical extension of CLaMS to operate on GCM data has been achieved, which now provides the possibility to drive the chemical transport model with GCM

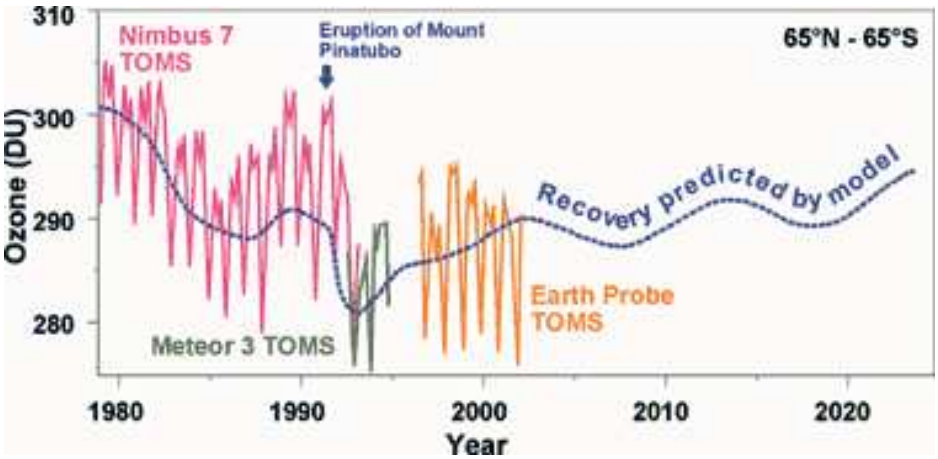

Figure 7.5: Global ozone as observed by the TOMS instrument flown on various satellite platforms and a sketch of the uncertain development of future global ozone. (UNEP, 2005)

simulations of past and future climates. An off-line coupling to other models than those of the ECHAM family should be easy to implement. Specifically, the coupling to a chemistry climate model like E39C has the beneficial effect that partial chemical feedback is already included in the underlying CCM simulation.

Future work is the on-line coupling between CLaMS and global circulation models, where both models are operated in parallel with data synchronisation at specified intervals, such that the GCM obtains the changed chemistry from CLaMS and CLaMS operates on the updated GCM meteorological fields. A second on-line coupling approach is currently discussed in the framework of the MESSy initiative (Jöckel et al., 2005; Sander et al., 2005), where individual CLaMS components could be interactively coupled to the base GCM (ECHAM5).

The coupling of CLaMS to a CCM demonstrated in this thesis is one step forward towards larger global initiatives to construct Earth system models (ESM) in an effort to understand the changing biogeosphere as an entity. ESM combine traditionally separated modelling domains into one large framework. Here, it is demonstrated, however, that even a seemingly small coupling aspect, namely the coupling between an AGCM and stratospheric chemistry, is not yet sufficiently well modelled. Caution with regards to interpreting AGCM results as an indication of the recovery of polar and global ozone is advised.

This study provides quantitative insight into effects of processes like mixing intensity and numerical resolution on chemical ozone loss calculations, which show a small, but non-negligible sensitivity, that should be considered for CCM improvements. The generalised approach of relating halogen loading scenarios to ozone loss enhancement may serve as a corrector to prior simulations that did not consider stratospheric halogen chemistry in full detail, as shown here for an E39C simulation where bromine was missing.

Diverging model results for the evolution and trend of Arctic stratospheric ozone over the next two decades show that the complex interaction between climate and

chemistry is not well understood, yet. The new prediction of the future Arctic minimum column ozone presented in this thesis shows that a recovery is not evident by 2015. Uncertainty is somewhat lower for southern hemispheric and global ozone.

In the recent UNEP progress report on "environmental effects of ozone depletion and its interactions with climate change", a schematic (Figure 7.5) of past and future global ozone is shown, which illustrates that the timing of and path to ozone recovery in models is unclear over the next two decades. Chemistry climate interactions are the focus of upcoming reports by the IPCC and WMO/UNEP. In May 2005, the "Special Report on safeguarding the Ozone layer and the global Climate system" (SROC) will be presented by IPCC. Results from climate chemistry models are expected to play a major role in the Scientific Assessment of Ozone Depletion: 2006.

A Supporting material

A.1 Table of ozone column and chemical loss

Scenario	ℓ_c	Col(O_3)	Col($\hat{O}_3$)	Col(O_3^*)	Col($\Delta\hat{O}_3$)	Col(ΔO_3^*)	
A	1.2	140	207	209	−66	−68	multi 2D
B	1.2	158	207	209	−48	−51	multi 2D
	0.0	—	294	306	12	—	high res
	1.2	—	257	263	6	—	high res
2	1.2	48	250	255	−201	−206	2× EESC
4	1.2	7	252	255	−244	−248	4× EESC
A	1.2	170	245	252	−75	−82	
B	1.2	191	248	254	−56	−62	
C	1.2	252	249	255	2	−3	no Br_y, Cl_y
H	1.2	145	250	255	−105	−110	$2 \times Br_y$
	0.0	—	242	248	6	—	no boundary
	1.2	—	242	248	6	—	no boundary
	1.2	251	245	240	6	11	global correlation
	0.0	—	279	288	9	—	
	0.4	—	241	251	9	—	
	1.2	—	247	254	6	—	
	4.0	—	252	260	7	—	
	0.0	—	221	229	8	—	no mixing
	1.2	—	247	254	6	—	low boundary
	1.2	—	222	227	4	—	low boundary updated
	1.2	—	221	224	2	—	low boundary
E	1.2	209	246	—	−36	—	E39C

Table A.1: April ozone columns for all three-dimensional and multilayer experiments. Ozone column is given in Dobson units and calculated between 380 and 550 K potential temperature within the vortex. O_3^* is passive tracer ozone, $\hat{O}_3$ a proxy for ozone derived from the CH_4-O_3 early winter vortex correlation. To these partial column values (altitude range 380–550 K, an offset column of ≈ 85 DU can be added to obtain the total column.

A.2 CLaMS parameters

Meteorology input time step	12 h
Trajectory mode	forward
Dimensions	2D and 3D
Vertical descent variable	$\dot{\theta}$
Trajectory start	equal
Trajectory end	1 April 00:00:00 UTC
Trajectory time step	60 s
Trajectory length	$\tau = 24$ h

Table A.2: Parameters for trajectory calculations. For three-dimensional calculations, the time derivative of potential vorticity $\dot{\theta}$ was used for vertical velocity.

Chemical time step	600 s
Heterogeneous chemistry	on and off
Particle sedimentation	on and off
Sedimentation distance	250 m
Integration method	IMPACT solver
SZA recalculation	hourly
Albedo	0.4
Ozone profile	Monthly Mainz-2D 2015 projection
Cosmic ray emission	off
Photolysis	Lary and Pyle (1991) and Becker et al. (2000a)

Table A.3: Parameters for chemistry calculations. For several sensitivity studies, heterogeneous chemistry and/or particle sedimentation were switched off.

Std. dev. of particle size log-normal distribution	1.8
Initial liquid aerosol number density	$10\,cm^{-1}$
H_2SO_4 aerosol	0.5 ppb
Constant ice number density	$0.01\,cm^{-1}$
Constant NAT number density	$1.0\,cm^{-1}$
SAT melting upon cooling	none
Heterogeneous parameterisation	Hanson and Ravishankara (1993, 1994); Hanson et al. (1994, 1996)
Rising temperature particle transformations	ice→NAT, NAT→SAT, SAT→STS
Falling temperature particle transformations	STS→NAT or ice, SAT→NAT or ice, NAT→ICE
Supersaturation required	10 for STS→NAT, 1 elsewhere

Table A.4: Parameters for heterogeneous chemistry.

Reaction	on ice	on NAT	on SAT
$ClONO_2$+ HCl	0.3		
$ClONO_2$+ H_2O	0.3		
$ClONO_2$+ HBr	0.3	0.3	
N_2O_5+ HCl	0.03	0.003	
N_2O_5+ H_2O	0.01	0.0003	0.006
$BrONO_2$+ HCl	0.3	0.3	
$BrONO_2$+ H_2O	0.3		
HBr + HOCl	0.3	0.3	
HOBr + HCl	0.3	0.1	
HOBr + HBr	0.1	0.1	
HOCl + HCl	0.3		

Table A.5: Constant sticking coefficients for reactions on NAT, ice, and sulphate aerosol. Sticking coefficients for other heterogeneous reactions are calculated online.

Boundary condition	1 January file/none
Number of tracers	multiple
Mixing	implicit
crit. Lyapunov exponent	$\ell_c \in [0.0; 4.0]$
Max. horizontal AP distance	2.0
Max. vertical AP distance	50 K
Number of adaptation loops	1
Grid switch	shifted every 12 h

Table A.6: Mixing scheme parameters. The reference (recommended) Lyapunov exponent was set at 1.2; for sensitivity studies, this parameter was varied over the range 0.0 to 4.0.

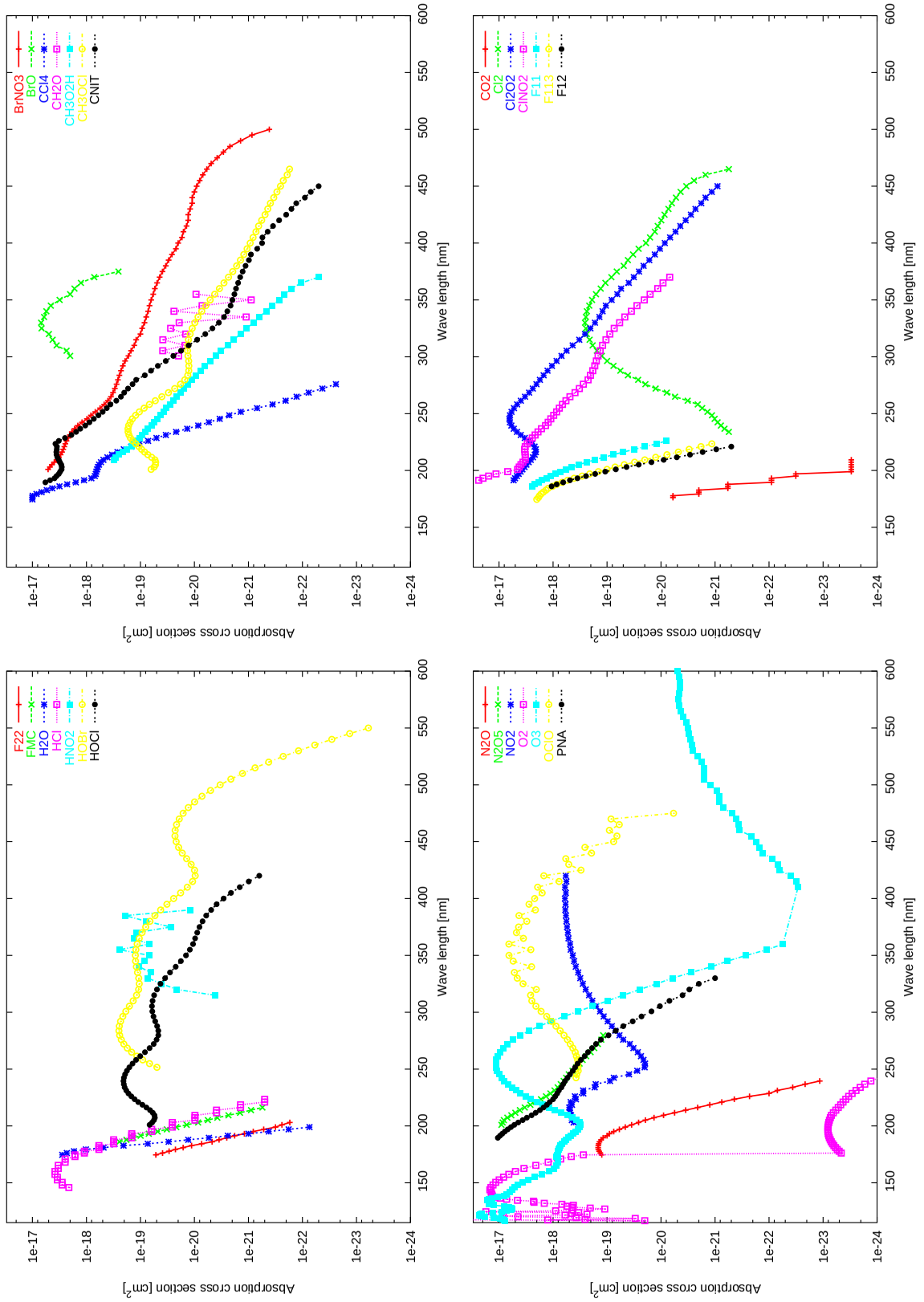

Figure A.1: Absorption cross sections used in CLaMS. Data based on DeMore et al. (1997) with updates from Sander et al. (2000a) and Sander et al. (2003). For CLaMS simulations in this thesis, halocarbon photolysis is not considered.

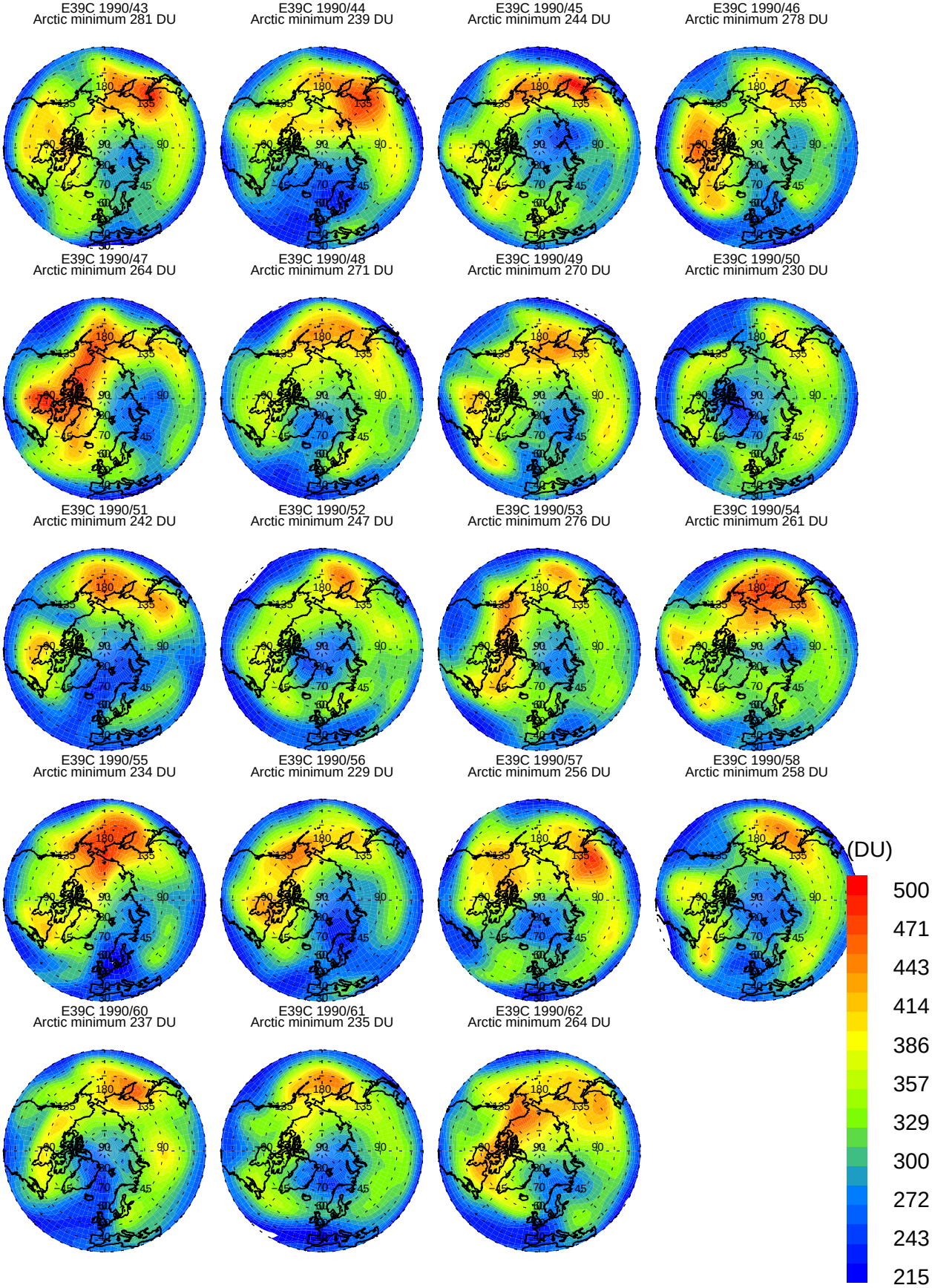

Figure A.2: Total ozone column in time slice 1990, January, numerically integrated over all E39C pressure levels (1 000–10 hPa) for each model grid point. The same color scale applies to the following figures A.3–A.5 and Figure 4.3 on page 69.

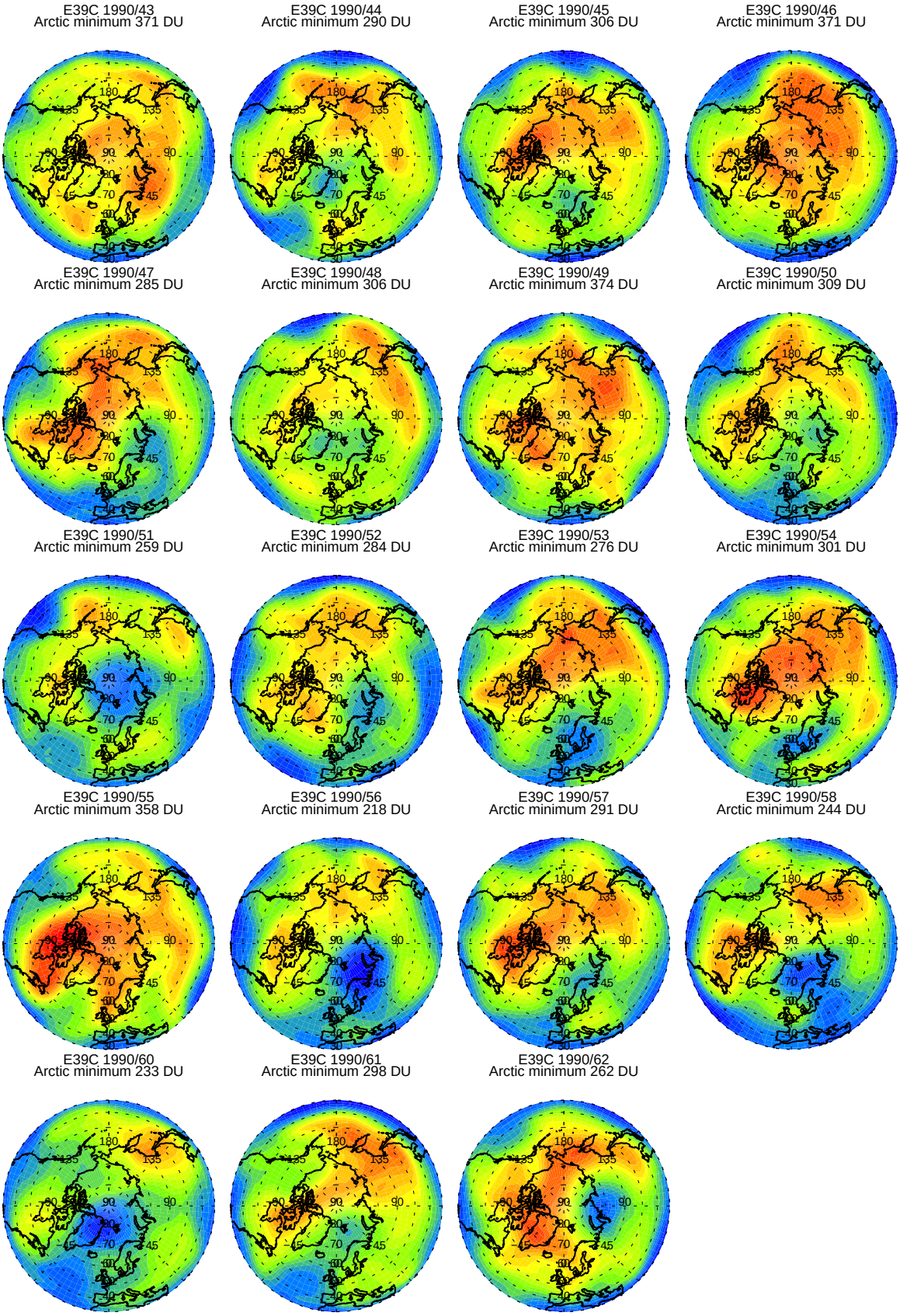

Figure A.3: As Figure A.2, but for time slice 1990, April

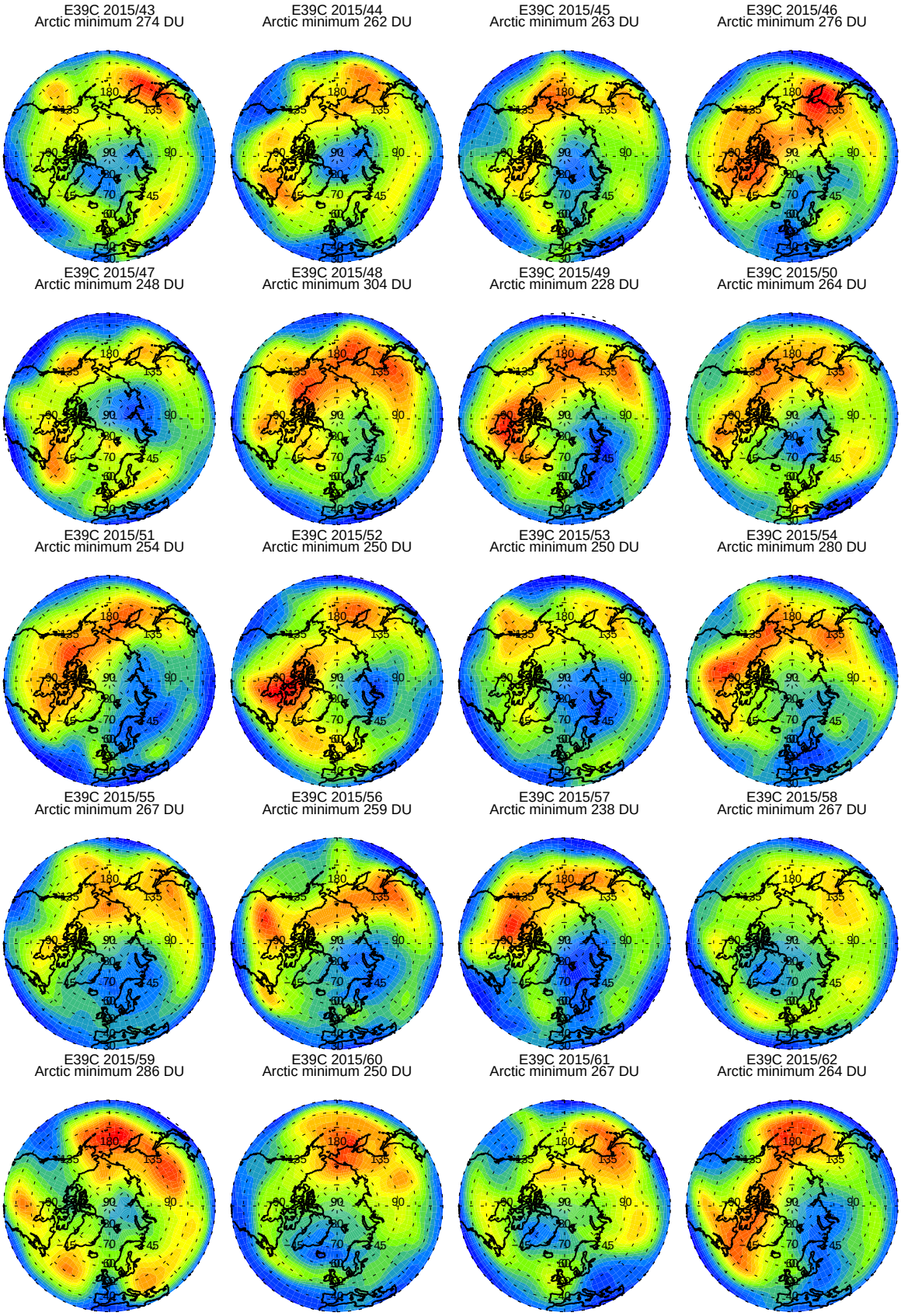

Figure A.4: As Figure A.2, but for time slice 2015, January

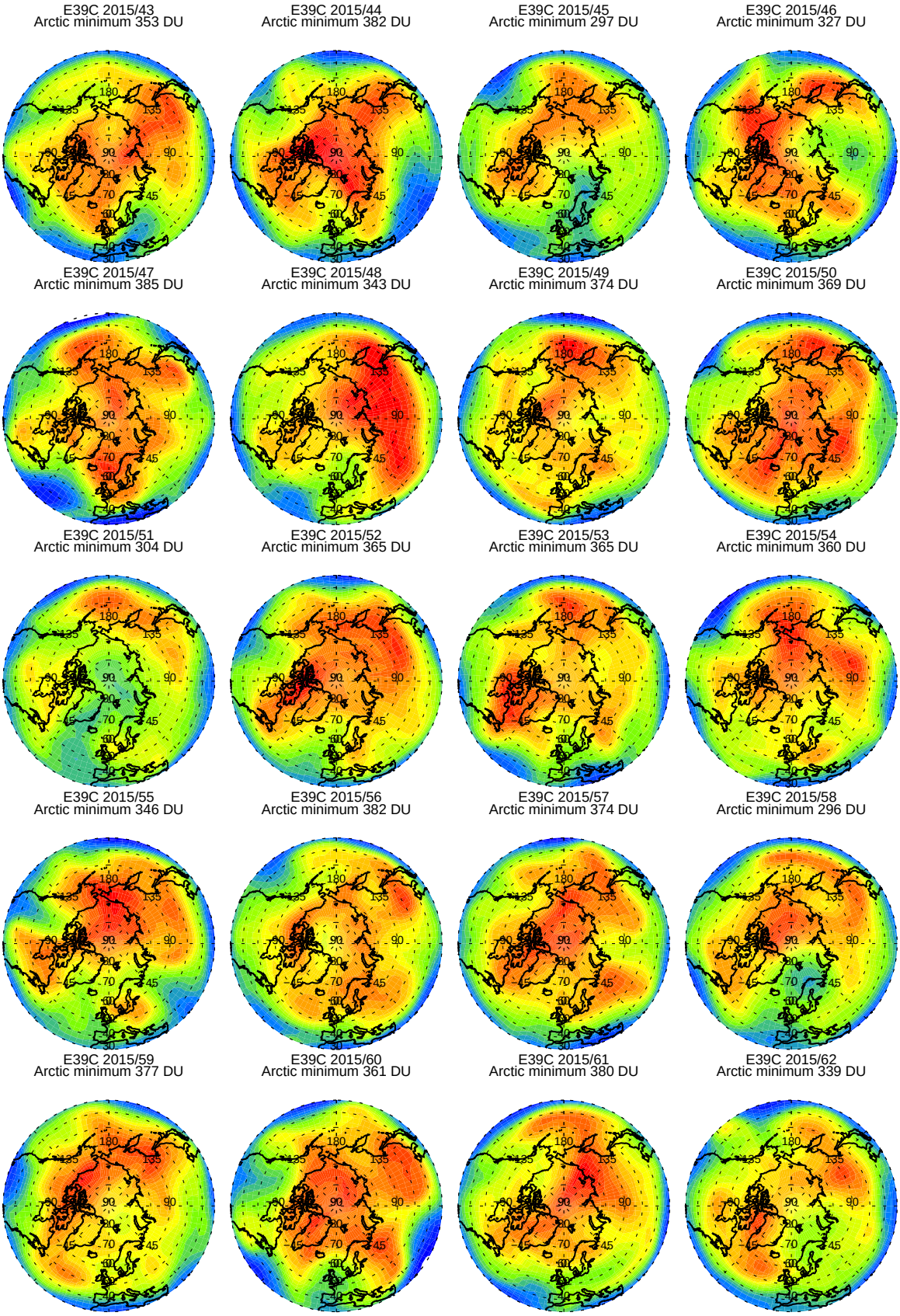

Figure A.5: As Figure A.2, but for time slice 2015, April

Symbols and Abbreviations

Symbol	description	unit, value
A_{PSC}	area of possible PSC occurrence	km^2
a_i	polynomial coefficient	
b	bias in reference column	DU
c_p	specific heat at constant pressure	$\mathrm{J{\cdot}K^{-1}{\cdot}mol^{-1}}$
d	day	
f	Coriolis parameter	$2\Omega \sin\phi$
f	loading factor	
g	acceleration due to gravity	$9.81\,\mathrm{m{\cdot}s^{-2}}$
i	index variable	
k	factor used for scaling of nPV to sPV	$2.65 \cdot 10^5$
ℓ	Lyapunov exponent for mixing	d^{-1}
ℓ_c	critical Lyapunov exponent	d^{-1}
m	specific mass of dry air	$0.028964\,\mathrm{kg{\cdot}mol^{-1}}$
mPV	modified potential vorticity	PVU
N_A	Avogadro's number	$6.02252 \cdot 10^{23}\,\mathrm{mol}^{-1}$
nPV	normalised potential vorticity	
P	polynomial expression	
PV	potential vorticity	PVU
p_0	surface pressure	hPa
p_s	standard pressure	1013 hPa, 1 atm
p_{NAT}	saturation vapour pressure of NAT	hPa
Q	heating rate	K·d−1
q	potential vorticity (all components)	PVU
R	universal gas constant	
r	distance	km
$\bar{r}_{\mathrm{fine}}$	high-resolution mean air parcel distance	km
$\bar{r}_{\mathrm{coarse}}$	low-resolution mean air parcel distance	km
sPV	scaled potential vorticity	
T_0	surface temperature	K
T_s	standard temperature	273 K
T_{NAT}	NAT existence temperature	$\approx 195\,\mathrm{K}$
t	time	s, h
u	zonal wind	$\mathrm{m{\cdot}s^{-1}}$
$\boldsymbol{u}$	wind vector	$\mathrm{m{\cdot}s^{-1}}$

Symbol	description	unit, value
V_{PSC}	volume of possible PSC occurrence	km^3
v	meridional wind	$\mathrm{m{\cdot}s}^{-1}$
W	numbering of time slice winters	
x	passive tracer variable	ppm, ppb, ppt
y	active tracer variable	ppm, ppb, ppt
z	altitude	km
α	horizontal to vertical aspect ratio	250
β	scaling coefficient for modified PV	9/2
Δ	any difference	
∂	partial derivative	
η	vertical component of absolute vorticity	PVU
Θ_r	reference potential temperature layer	$(485 \pm 15)\,\mathrm{K}$
θ	potential temperature	K
θ_r	reference potential temperature	475 K
$\dot{\theta}$	vertical velocity in isentropic coordinates	$\mathrm{K{\cdot}d}^{-1}$
κ	scaling exponent	$R/c_p = 2/7$
λ	wave length	nm
μ	mixing ratio	
ν	frequency	s^{-1}
τ	CLaMS time step	24 h
ρ	density	
ϕ	latitude	°N
ϕ_{eq}	equivalent latitude	°N
ξ	vertical component of relative vorticity	PVU
Ω	magnitude of Earth's angular velocity	$7.292 \cdot 10^{-5}\,\mathrm{s}^{-1}$
$\mathbf{\Omega}$	Earth's angular velocity	

2D	two-dimensional
Acronym	description
AGAGE	Advanced Global Atmospheric Gases Experiment
AGCM	Atmospheric global circulation model
AMOC	Arctic minimum ozone column
AMSU	Advanced Microwave Sounding Unit
AO	Arctic oscillation
AP	Air parcel
ASAD	A Self-contained Atmospheric chemistry code
ATMOS	Atmospheric Trace Molecule Spectroscopy experiment
CCM	Chemistry climate model
CFC	Chlorofluorocarbons
CLaMS	Chemical Lagrangian Model of the Stratosphere
CPT	Cold point temperature
CTM	Chemistry transport model
CRISTA	Cryogenic Infrared Spectrometers and Telescopes for the Atmosphere
DKRZ	Deutsches Klimarechenzentrum
DLR	Deutsches Zentrum für Luft- und Raumfahrt

2D	two-dimensional
Acronym	description
DNA	Deoxyribonucleic acid
DRF	Direct radiative forcing
DU	Dobson units
E39C	ECHAM4.DLR(L39)/CHEM
ECMWF	European Centre for Medium-range Weather Forecasts
EECl	Effective equivalent chlorine
EESC	Effective equivalent stratospheric chlorine
ERA	ECMWF reanalysis
ESM	Earth system model
EUPLEX	European Polar ozone and Lee wave Experiment
GAGE	Global Atmospheric Gases Experiment
GCM	Global circulation model
GHG	Greenhouse gases
GOME	Global Ozone Monitoring Experiment
HALOE	Halogen Occultation Experiment
HAMMONIA	Hamburg Model of the Neutral and Ionised Atmosphere
HCFC	Hydrogenated chlorofluorocarbons
HFC	Hydrogenated fluorocarbons
ICG	Institute for Chemistry and Dynamics of the Geosphere
ILAS	Improved Limb Atmospheric Spectrometer
IMPACT	Implicit Algorithm for Chemical Timestepping
IPCC	Intergovernmental Panel on Climate Change
IRF	Indirect radiative forcing
ITCZ	Inter-tropical convergence zone
IR	Infrared radiation
LMS	Lowermost stratosphere
LS	Lower stratosphere
LSG	Large Scale Geostrophic ocean GCM
MLS	Microwave Limb Sounder
MPI	Max Planck Institute
MPIC	Max Planck Institute for Chemistry, Mainz
MSU	Microwave sounding unit
NAD	Nitric acid dihydrate
NAM	Northern annular mode
NAO	North Atlantic oscillation
NAT	Nitric acid trihydrate
NCEP	National Centers for Environmental Prediction
ODP	Ozone depletion potential
ODS	Ozone depleting substances
OPYC	Ocean model in isopycnic coordinates
PSC	Polar stratospheric clouds
POLARIS	Photochemistry of Ozone Loss in the Arctic Region in Summer
PVU	Potential vorticity units
ppb	parts per billion, 10^{-9}

2D	two-dimensional
Acronym	description
ppm	parts per million, 10^{-6}
ppt	parts per trillion, 10^{-12}
QBO	Quasi biennial oscillation
RF	Radiative forcing
SAD	Surface area density
SAOZ	Système d'Analyse par Observation Zénithale
SAGE	Stratospheric Aerosol and Gas Experiment
SAT	Sulfuric acid tetrahydrate
SBUV	Solar Backscatter UV
SLP	Sea level pressure
SOLVE	Sage II Ozone Loss Validation Experiment
SRES	Special report on emission scenarios
SROC	Special report on ozone and climate
SST	Sea surface temperature
STE	Stratosphere-troposphere exchange
STS	Supercooled ternary solutions
STT	Stratosphere to troposphere transport
sPV	Scaled potential vorticity
TFA	Trifluoroacetic acid
THESEO	Third European Experiment on Ozone
TOMS	Total ozone mapping spectrometer
TRAC	Tracer-tracer correlation method
TROCCINOX	Tropical Convection Cirrus and Nitrogen Oxides experiment
TTL	Tropical tropopause layer
UARS	Upper Atmosphere Research Satellite
UNEP	United Nations Environmental Programme
UT	Upper troposphere
UTC	Coordinated Universal Time
UTLS	Upper troposphere and lower stratosphere
UV	Ultraviolet radiation
VOC	volatile organic carbons
vmr	volume mixing ratio
WMGHG	Well-mixed greenhouse gases
WMO	World Meteorological Organisation

Figures

List of Tables

References cited

ACIA, *Arctic Climate Impact Assessment Overview Report. Impacts of a Warming Arctic*, Cambridge University Press, Cambridge, New York, edited by S. J. Hassol, available online at http://amap.no/acia/, 2004. 22, 31, 36

Anderson, J. G., W. H. Brune, and M. H. Proffitt, Ozone destruction by chlorine radicals within the antarctic vortex: The spatial and temporal evolution of ClO-O_3 anticorrelation based on in situ ER-2 data, *J. Geophys. Res.*, *94*(D9), 1465–11,479, doi:10.1029/89JD00914, 1989. 17

Andrews, D. G., J. R. Holton, and C. B. Leovy, *Middle Atmosphere Dynamics*, Academic Press, San Diego, USA, 1987. 15

Arrhenius, S., On the influence of carbonic acid in the air upon the temperature of the ground, *Philosophical Magazine*, *41*, 237–76, 1896. 2

Austin, J., R. C. Pallister, J. A. Pyle, A. F. Tuck, and A. M. Zavody, Photochemical model comparisons with LIMS observations in a stratospheric trajectory coordinate system, *Q. J. R. Meteorol. Soc.*, *113*, 361–392, 1987. 8

Austin, J., N. Butchart, and K. Shine, Possibility of an arctic ozone hole in a doubled-CO_2 climate, *Nature*, *360*, 221–225, 1992. 7, 8

Austin, J., et al., Uncertainties and assessments of chemistry-climate models of the stratosphere, *Atmos. Chem. Phys.*, *3*, 1–27, sref:1680-7324/acp/2003-3-1, 2003. 7, 8, 9, 40, 66, 67, 73

Baldwin, M. P., and T. J. Dunkerton, Propagation of the Arctic Oscillation from the stratosphere to the troposphere, *J. Geophys. Res.*, *104*(D24), 30,937–30,946, 1999. 19

Barber, C. B., P. D. David, and H. Huhdanpaa, The quickhull algorithm for convex hulls, *ACM Transactions on Mathematical Software*, *22*, 469–483, 1996. 50

Becker, G., R. Müller, D. S. McKenna, M. Rex, and K. S. Carslaw, Ozone loss rates in the Arctic stratosphere in the winter 1991/92: Model calculations compared with Match results, *Geophys. Res. Lett.*, *25*(23), 4325–4328, 1998. 45

Becker, G., J.-U. Grooß, D. S. McKenna, and R. Müller, Stratospheric photolysis frequencies: Impact of an improved numerical solution of the radiative transfer equation, *J. Atmos. Chem.*, *37*, 217–229, doi:10.1023/A:1006468926530, 2000a. 49, 112

Becker, G., R. Müller, D. S. McKenna, M. Rex, K. S. Carslaw, and H. Oelhaf, Ozone loss rates in the Arctic stratosphere in the winter 1994/1995: Model simulations underestimate results of the Match analysis, *J. Geophys. Res.*, *105*, 15,175–15,184, 2000b. 45

Bekker, A., H. D. Holland, P.-L. Wang, I. Rumble, D., H. J. Stein, J. L. Hannah, L. L. Coetzee, and N. J. Beukes, Dating the rise of atmospheric oxygen, *Nature*, *427*, 117–120, doi:10.1038/nature02260, 2004. 32

Benesch, J. A., M. S. Gustin, G. R. Cramer, and T. M. Cahill, Investigation of effects of trifluoroacetate on vernal pool ecosystems, *Environ. Toxicol. Chem.*, *21*, 640–647, 2002. 34

Blake, D., Methane, nonmethane hydrocarbons, alkyl nitrates, and chlorinated carbon compounds including 3 chlorofluorocarbons (CFC-11, CFC-12, and CFC-113) in whole-air samples, in *Trends: A Compendium of Data on Global Change*, Carbon Dioxide Information Analysis Center, Oak Ridge National Laboratory, U.S. Department of Energy, Oak Ridge Tenn., U.S.A., http://cdiac.esd.ornl.gov/trends/otheratg/blake/blake.html, 2004. 33

Brasseur, G., and S. Solomon, *Aeronomy of the Middle Atmosphere*, Reidel Publishing Company, Dordrecht, NL, 1984. 15, 24

Bregman, A., M. van den Broek, K. S. Carslaw, R. Müller, T. Peter, M. P. Scheele, and J. Lelieveld, Ozone depletion in the late winter lower Arctic stratosphere: Observations and model results, *J. Geophys. Res.*, *102*, 10,815–10,828, 1997. 42, 103

Brewer, A. W., Evidence for a world circulation provided by the measurements of helium and water vapor distribution in the stratosphere, *Q. J. R. Meteorol. Soc.*, *75*, 351–363, 1949. 13

Brühl, C., and P. J. Crutzen, Scenarios of possible changes in atmospheric temperatures and ozone concentrations due to man's activities, estimated with a one-dimensional coupled photochemical climate model, *Clim. Dyn.*, *2*(3), 173–203, 1988. 49

Burrows, J. P., et al., The Global Ozone Monitoring Experiment GOME: Mission concept and first scientific results, *J. Atmos. Sci.*, *56*, 151–175, 1999. 43, 66

Carslaw, K. S., and T. Peter, Uncertainties in reactive uptake coefficients for solid stratospheric particles - 1. Surface chemistry, *Geophys. Res. Lett.*, *24*, 1743–1746, 1997. 48

Carslaw, K. S., S. L. Clegg, and P. Brimblecombe, A thermodynamic model of the system HCl-HNO_3-H_2SO_4-H_2O, including solubilities of HBr, from 328 K to $<$ 200 K, *J. Phys. Chem.*, *99*, 11,557–11,574, 1995a. 48

Carslaw, K. S., B. P. Luo, and T. Peter, An analytical expression for the composition of aqueous HNO_3-H_2SO_4-H_2O stratospheric aerosols including gas phase removal of HNO_3, *Geophys. Res. Lett.*, *22*(14), 1877–1880, doi:10.1029/95GL01668, 1995b. 48

Carslaw, K. S., T. Peter, and S. L. Clegg, Modelling the composition of stratospheric aerosols, *Rev. Geophys.*, *35*, 125–154, 1997a. 49

Carslaw, K. S., T. Peter, and R. Müller, Uncertainties in reactive uptake coefficients for solid stratospheric particles - 2. Effect on ozone depletion, *Geophys. Res. Lett.*, *24*, 1747–1750, 1997b. 48

Carslaw, K. S., J. A. Kettleborough, M. J. Northway, S. Davies, R. Gao, D. W. Fahey, D. G. Baumgardner, M. P. Chipperfield, and A. Kleinböhl, A vortex-scale simulation of the growth and sedimentation of large nitric acid hydrate particles, *J. Geophys. Res.*, *107*(D20), doi:10.1029/2001JD000467, 2002. 61

Carver, G. D., and P. A. Scott, IMPACT: an implicit time integration scheme for chemical species and families, *Ann. Geophys.*, *18*, 337–346, sref:1432-0576/ag/2000-18-337, 2000. 48

Carver, G. D., P. D. Brown, and O. Wild, The ASAD atmospheric chemistry integration

package and chemical reaction database, *Computer Physics Communications*, *105*, 197–215, 1997a. 48, 53

Carver, G. D., P. D. Brown, and O. Wild, The ASAD atmospheric chemistry integration package and chemical reaction database: User guide, *Tech. rep.*, Centre for Atmospheric Science, Cambridge University, Lensfield Road, Cambridge CB2 1EW, UK, doi:10.1016/S0010-4655(97)00056-8, 1997b. 48

Chapman, S., A theory of upper atmospheric ozone, *Q. J. R. Meteorol. Soc.*, *3*, 103–125, 1930. 25

Chipperfield, M. P., A three-dimensional model study of long-term mid-high latitde lower stratosphere ozone changes, *Atmos. Chem. Phys.*, *3*, 1253–1265, 2003. 43

Chipperfield, M. P., and J. A. Pyle, Model sensitivity studies of arctic ozone depletion, *J. Geophys. Res.*, *103*, 28,389–28,403, 1998. 9, 55, 90

Copley, J., The story of O, *Nature*, *410*, 862 – 864, doi:doi:10.1038/35073794, 2001. 32

Crutzen, P. J., The influence of nitrogen oxides on the atmospheric ozone content, *Q. J. R. Meteorol. Soc.*, *96*, 320–325, 1970. 29

Crutzen, P. J., Estimates of possible future ozone reductions from continued use of fluro-chloro-methanes (CF_2Cl_2, $CFCl_3$), *Geophys. Res. Lett.*, *1*, 205–208, 1974. 3, 4, 25

Crutzen, P. J., and F. Arnold, Nitric acid cloud formation in the cold Antarctic stratosphere: A major cause for the springtime 'ozone hole', *Nature*, *342*, 651–655, 1986. 4

Crutzen, P. J., and U. Schmailzl, Chemical budgets of the stratosphere, *Planet Space Sci*, *31*, 1009–1032, 1983. 58

Crutzen, P. J., R. Müller, C. Brühl, and T. Peter, On the potential importance of the gas phase reaction $CH_3O_2 + ClO \rightarrow ClOO + CH_3O$ and the heterogeneous reaction $HOCl + HCl \rightarrow H_2O + Cl_2$ in "ozone hole" chemistry, *Geophys. Res. Lett.*, *19*(11), 1113–1116, doi:10.1029/92GL01172, 1992. 49

Crutzen, P. J., J.-U. Grooß, C. Brühl, R. Müller, and I. Russell, J. M., A reevaluation of the ozone budget with HALOE UARS data: No evidence for the ozone deficit, *Science*, *268*, 705–708, 1995. 27

Cubasch, U., K. Hasselmann, K. Höck, E. Maier-Reimer, U. Mikolajewicz, B. D. Santer, and R. Sausen, Time-dependent greenhouse warming computations with a coupled ocean-atmosphere model, *Clim. Dyn.*, *8*, 55–69, 1992. 40

Cubasch, U., G. A. Meehl, G. J. Boer, R. J. Stouffer, M. Dix, A. Noda, C. A. Senior, S. Raper, and K. S. Yap, Projections of future climate change, in Houghton et al. (2001), chap. 9, 2001. 37

Dameris, M., V. Grewe, R. Hein, C. Schnadt, C. Brühl, and B. Steil, Assessment of the future development of the ozone layer, *Geophys. Res. Lett.*, *25*(19), 3579–3582, doi:10.1029/98GL02778, 1998. 41

Dameris, M., V. Grewe, I. Köhler, R. Sausen, C. Brühl, J.-U. Grooß, and B. Steil, Impact of aircraft NO_x-emissions on tropospheric and stratospheric ozone. Part II: 3-D model results, *Atmos. Environ.*, *32*(18), 3185–3199, 1998. 12, 41

DeMore, W. B., S. P. Sander, D. M. Golden, R. F. Hampson, M. J. Kurylo, C. J. Howard, A. R. Ravishankara, C. E. Kolb, and M. J. Molina, Chemical kinetics and photochemical data for use in stratospheric modeling, JPL Publication 97-4, 1997. 48, 50, 114

Dessler, A. E., The chemistry and physics of stratospheric ozone, in *International Geophysics Series*, vol. 74, edited by R. Dmowska, J. R. Holton, and H. T. Rossby, p. 214, Academic Press, London, San Diego, 2000. 15, 25, 30

Dessler, A. E., et al., Balloon-borne measurements of ClO, NO and O_3 in a volcanic cloud: an analysis of heterogeneous chemistry between 20 and 30 km, *Geophys. Res. Lett.*, *20*, 2527–2530, 1993. 27

DKRZ, The ECHAM3 general circulation model, *Technical report*, Deutsches Klimarechenzentrum, Modellbetreuungsgruppe, 1992. 40

Dlugokencky, E. J., B. P. Walter, K. A. Masarie, P. M. Lang, and E. S. Kasischke, Measurements of an anomalous global methane increase during 1998, *Geophys. Res. Lett.*, *28*(3), 499–502, doi:10.1029/2000GL012119, 2001. 32

Dobson, G. M. B., Annual variations of ozone in Antarctica, *Q. J. R. Meteorol. Soc.*, *92*, 549–552, 1966. 22

Ehhalt, D., et al., Atmospheric chemistry and greenhouse gases, in Houghton et al. (2001), chap. 4, 2001. 32, 37

Elwood, J. M., and J. Jopson, Melanoma and sun exposure: an overview of published studies., *Int. J. Cancer*, *73*(2), 198–203, 1997. 22

Engel, A., U. Schmidt, and D. S. McKenna, Stratospheric trends of CFC-12 over the past two decades: Recent observational evidence of declining growth rates, *Geophys. Res. Lett.*, *25*(17), 3319–3322, doi:10.1029/98GL02520, 1998. 3

Engel, A., M. Strunk, M. Müller, H. Haase, C. Poss, I. Levin, and U. Schmidt, Temporal development of total chlorine in the high-latitude stratosphere based on reference distributions of mean age derived from co_2 and sf_6, *J. Geophys. Res.*, *107*(D12), doi:10.1029/2001JD000584, 2002. 5

Ertel, H., Ein neuer hydrodynamischer Wirbelsatz, *Meteorol Z*, *59*, 277–281, 1942a. 16

Ertel, H., Ein neuer hydrodynamischer Erhaltungssatz, *Naturwissenschaften*, *30*, 543–544, 1942b. 16

Esler, J. G., and D. W. Waugh, A method for estimating the extent of denitrification of arctic polar vortex air from tracer-tracer scatter plots, *J. Geophys. Res.*, *107*(6), 1–14, doi:10.1029/2001JD001071, 2002. 61, 83, 92

Eyring, V., et al., Brief report on the workshop on process-oriented validation of coupled chemistry-climate models, *SPARC Newsletter*, (22), 2004. 9

Fahey, D. W., K. K. Kelly, G. V. Ferry, L. R. Poole, J. C. Wilson, D. M. Murphy, M. Loewenstein, and K. R. Chan, In situ measurements of total reactive nitrogen, total water, and aerosol in a polar stratospheric cloud in the Antarctic, *J. Geophys. Res.*, *94*, 11,299–11,315, 1989. 27, 61

Fahey, D. W., et al., The detection of large HNO_3-containing particles in the winter Arctic stratosphere, *Science*, *291*, 1026–1031, 2001. 30, 61

Farman, J. C., B. G. Gardiner, and J. D. Shanklin, Large losses of total ozone in Antarctica reveal seasonal ClO_x/NO_x interaction, *Nature*, *315*, 207–210, 1985. 3, 4

Fears, T. R., et al., Average midrange ultraviolet radiation flux and time outdoors predict melanoma risk, *Cancer Research*, *62*, 3992–3996, 2002. 22

Fioletov, V. E., G. E. Bodeker, A. J. Miller, R. D. McPeters, , and R. Stolarski, Global and

zonal total ozone variations estimated from ground-based and satellite measurements: 1964–2000, *J. Geophys. Res.*, *107*(D22), 4647, doi:10.1029/2001JD001350, 2002. 4

Folkins, I., and C. Appenzeller, Ozone and potential vorticity at the subtropical tropopause break, *J. Geophys. Res.*, *101*, 18,787–18,792, 1996. 13

Folland, C. K., T. R. Karl, J. R. Christy, R. A. Clarke, G. V. Gruza, J. Jouzel, M. E. Mann, J. Oerlemans, and M. J. S. ans S.-W. Wang, Observed climate variability and change, in Houghton et al. (2001), chap. 2, 2001. 36

Forster, P., and M. Joshi, The role of halocarbons in the climate change of the troposphere and stratosphere, *Clim. Change*, *accepted*, 2005. 3, 5, 6, 38

Forster, P., and K. P. Shine, Stratospheric water vapour change as possible contributor to observed stratospheric cooling, *Geophys. Res. Lett.*, *26*(21), 3309 – 3312, doi: 10.1029/1999GL010487, 1999. 6, 35

Fortuin, J. P. F., and H. Kelder, An ozone climatology based on ozonesonde and satellite measurements, *J. Geophys. Res.*, *103*, 31,709–31,734, 1998. 21, 43

Fouquart, Y., and B. Bonnel, Computations of solar heating of the Earth's atmosphere: A new parameterization, *Beitr. Phys. Atmos.*, *53*, 35–62, 1980. 40

Fourier, J. B. J., Remarques générales sur la température du globe terrestre et des espaces planétaires, *Annales de chimie et de physique*, *27*, 136–167, 1824. 2, 32

Gidel, L. T., P. J. Crutzen, and J. Fishman, A two-dimensional photochemical model of the atmosphere; 1: Chlorocarbon emissions and their effect on stratospheric ozone, *J. Geophys. Res.*, *88*, 6622–6640, 1983. 49

Goutail, F., et al., Depletion of column ozone in the Arctic during the winter of 1993-94 and 1994-95, *J. Atmos. Chem.*, *32*, 1–34, 1999. 60, 64

Goutail, F., et al., Early unusual ozone loss during the Arctic winter 2002/2003 compared to other winters, *Atmos. Chem. Phys. Discuss.*, *4*, 5019–5044, 2004. 64

Grewe, V., D. Brunner, M. Dameris, J. L. Grenfell, R. Hein, D. Shindell, and J. Staehelin, Origin and variability of upper tropospheric nitrogen oxides and ozone at northern mid-latitudes, *Atmos. Environ.*, *35*, 3421–3433, 2001a. 41

Grewe, V., M. Dameris, R. Hein, R. Sausen, and B. Steil, Future changes of the atmospheric composition and the impact of climate change, *Tellus B*, *53*, 103–121, 2001b. 41

Grooß, J.-U., Modelling of stratospheric chemistry based on HALOE/UARS satellite data, PhD thesis, University of Mainz, 1996. 20, 42, 49, 51

Grooß, J.-U., and R. Müller, The impact of mid-latitude intrusions into the polar vortex on ozone loss estimates, *Atmos. Chem. Phys.*, *3*, 395–402, 2003. 45

Grooß, J.-U., G. Günther, R. Müller, P. Konopka, S. Bausch, H. Schlager, C. Voigt, C. M. Volk, and G. C. Toon, Simulation of denitrification and ozone loss for the Arctic winter 2002/2003, *Atmos. Chem. Phys. Discuss.*, *4*, 8069–8101, 2004. 16, 46, 49, 58, 64, 84, 96, 105, 106

Grooß, J.-U., P. Konopka, and R. Müller, Ozone chemistry during the 2002 Antarctic vortex split, *J. Atmos. Sci.*, *62*(3), 860–870, 2005. 8, 46

Grooß, J.-U., et al., Simulation of ozone depletion in spring 2000 with the Chemical Lagrangian Model of the Stratosphere (CLaMS), *J. Geophys. Res.*, *107*, 8295, doi: 10.1029/2001JD000456, 2002. 46, 49, 50, 58, 64, 84, 96

Günther, G., C. Schiller, P. Konopka, and M. Krebsbach, Simulation of transport processes in the tropopause region during SPURT using a Lagrangian model, *Geophys. Res. Abs.*, *6*, 02609, sref:1607-7962/gra/EGU04-A-02609, 2004. 46

Hansen, G., and M. P. Chipperfield, Ozone depletion at the edge of the Arctic polar vortex 1996/1997, *J. Geophys. Res.*, *104*, 1837–1845, 1999. 60

Hanson, D. R., and K. Mauersberger, Laboratory studies of the nitric acid trihydrate: Implications for the south polar stratosphere, *Geophys. Res. Lett.*, *15*(8), 855–858, doi:10.1029/88GL00209, 1988. 27, 42, 79

Hanson, D. R., and A. R. Ravishankara, Reaction of $ClONO_2$ with HCl on NAT, NAD, and frozen sulfuric acid and hydrolysis of N_2O_5 and $ClONO_2$ on frozen sulfuric acid, *J. Geophys. Res.*, *98*, 22,931–22,936, 1993. 113

Hanson, D. R., and A. R. Ravishankara, Reactive uptake of $ClONO_2$ onto sulfuric acid due to reaction with HCl and H_2O, *J. Phys. Chem.*, *98*, 5728–5735, 1994. 113

Hanson, D. R., A. R. Ravishankara, and S. Solomon, Heterogeneous reactions in sulfuric acid aerosols: A framework for model calculations, *J. Geophys. Res.*, *99*, 3615–3629, 1994. 113

Hanson, D. R., A. R. Ravishankara, and E. R. Lovejoy, Reaction of $BrONO_2$ with H_2O on submicron sulfuric acid aerosol and the implications for the lower stratosphere, *J. Geophys. Res.*, *101*, 9063–9069, 1996. 113

Harris, N. R., M. Rex, F. Goutail, B. M. Knudsen, G. L. Manney, R. Müller, and P. von der Gathen, Comparison of empirically derived ozone loss rates in the Arctic vortex, *J. Geophys. Res.*, *107*(D20), doi:10.1029/2001JD000482, 2002. 60

Haynes, P., and J. Anglade, The vertical scale cascade in atmospheric tracers due to large-scale differential advection, *J. Atmos. Sci.*, *54*, 1121–1136, 1997. 55

Hein, R., et al., Results of an interactively coupled atmospheric chemistry-general circulation model: Comparison with observations, *Ann. Geophys.*, *19*, 435–457, sref:1432-0576/ag/2001-19-435, 2001. 9, 41, 43, 56, 79, 106

Högbom, A., Om Sannolikheten för sekulära Förändringar i atmosfärens Kolsyrehalt, *Svensk kemisk Tidskrift*, *6*, 169–77, excerpt translation In: Arrhenius (1896), 1894. 2

Holton, J. R., *An Introduction to Dynamic Meteorology*, Academic Press, London, 1992. 15

Holton, J. R., P. Haynes, M. E. McIntyre, A. R. Douglass, R. B. Rood, and L. Pfister, Stratosphere-troposphere exchange, *Rev. Geophys.*, *33*, 403–439, 1995. 14

Hood, L., S. Rossi, and M. Beulen, Trends in lower stratospheric zonal winds, rossby wave breaking behavior, and column ozone at northern midlatitudes, *J. Geophys. Res.*, *104*(D20), 24,321–24,340, doi:10.1029/1999JD900401, 1999. 19

Hoor, P., C. Gurk, D. Brunner, M. I. Hegglin, H. Wernli, and H. Fischer, Seasonality and extent of extratropical TST derived from in-situ CO measurements during SPURT, *Atmos. Chem. Phys. Discuss.*, *4*, 1691–1726, sref:1680-7375/acpd/2004-4-1691, 2004. 13, 14

Hoskins, B. J., Towards a PV-θ view of the general circulation, *Tellus*, pp. 27–35, 1991. 18

Hoskins, B. J., M. E. McIntyre, and A. W. Robertson, On the use and significance of isentropic potential vorticity maps, *Q. J. R. Meteorol. Soc.*, *111*, 877–946, 1985. 15

Houghton, J. T., et al. (Eds.), *Climate Change 2001: the scientific basis. Contribution of Working Group I to the Third Assessment Report of the Intergovernmental Panel on*

Climate Change, Cambridge University Press, Cambridge, UK and New York, NY, USA, 2001. 128, 129, 130, 136

IPCC, *Scientific Assessment of Climate change — Report of Working Group I to the First Assessment Report of the Intergovernmental Panel on Climate Change*, 365 pp., Cambridge University Press, Cambridge, UK, edited by J. T. Houghton and others, 1990. 2

IPCC, *Special Report 1994. Radiative Forcing of Climate Change and An Evaluation of the IPCC IS92 Emissions Scenarios*, 339 pp., Cambridge University Press, Cambridge, UK, edited by J. T. Houghton and others, 1994. 31

IPCC, *Climate Change 1995: the science of Climate Change. Contribution of Working Group I to the Second Assessment of the Intergovernmental Panel on Climate Change*, 572 pp., Cambridge University Press, Cambridge, UK, edited by J. T. Houghton and others, 1995. 2, 31, 42

IPCC, *Emissions Scenarios 2000. Special Report of the Intergovernmental Panel on Climate Change*, 570 pp., Cambridge University Press, Cambridge, UK, edited by N. Nakicenovic and R. Swart, 2000. 31, 37

IPCC, *Climate Change 2001: the scientific basis. Contribution of Working Group I to the Third Assessment Report of the Intergovernmental Panel on Climate Change*, 881 pp., Cambridge University Press, Cambridge, UK and New York, NY, USA, edited by J. T. Houghton and others, 2001. 2, 3, 31, 32, 37, 51

Jöckel, P., R. Sander, A. Kerkweg, H. Tost, and J. Lelieveld, Technical note: The modular earth submodel system (messy) — a new approach towards Earth system modeling, *Atmos. Chem. Phys.*, *5*, 433–444, sref:1680-7324/acp/2005-5-433, 2005. 109

Jones, A. E., and J. D. Shanklin, Continued decline of total ozone over Halley, Antarctica since 1985, *Nature*, *376*, 409–411, 1995. 20

Junge, C. E., C. W. Changnon, and J. E. Manson, Stratospheric aerosols, *J Meteorol*, *18*, 81–108, 1961. 27

Keeling, C. D., The concentration and isotopic abundances of carbon dioxide in the atmosphere, *Tellus*, *12*, 200, 1960. 2

Keeling, R. F., and T. H. Peng, Transport of heat, CO_2, and O_2 by the Atlantic's thermohaline circulation, *Phil. Trans. Roy. Soc.*, *348*, 133–142, 1995. 32

Kirk-Davidoff, D. B., E. J. Hintsa, J. G. Anderson, and D. W. Keith, The effect of climate change on ozone depletion through changes in stratospheric water vapour, *Nature*, *402*, 399–401, doi:10.1038/46521, 1999. 6, 38

Knudsen, B. M., S. B. Andersen, B. Christiansen, N. Larsen, M. Rex, N. R. P. Harris, and B. Naujokat, Extrapolating future arctic ozone losses, *Atmos. Chem. Phys. Discuss.*, *4*, 3227–3248, sref:1680-7324/acp/2004-4-1849, 2004. 7, 8, 64, 79, 105, 106, 107

Knudsen, B. M., et al., Ozone depletion in and below the Arctic vortex for 1997, *Geophys. Res. Lett.*, *25*(5), 627–630, doi:10.1029/98GL00300, 1998. 60

Konopka, P., J.-U. Grooß, S. Bausch, R. Müller, D. S. McKenna, O. Morgenstern, and Y. Orsolini, Dynamics and chemistry of vortex remnants in late Arctic spring 1997 and 2000: Simulations with the Chemical Lagrangian Model of the Stratosphere (CLaMS), *Atmos. Chem. Phys.*, *3*, 839–849, sref:1680-7375/acpd/2003-3-1051, 2003a. 45, 57

Konopka, P., J. U. Grooß, G. Günther, D. S. McKenna, R. Müller, J. W. Elkins, D. Fahey, and P. Popp, Weak impact of mixing on chlorine deactivation during SOLVE/THESEO2000: Lagrangian modeling (CLaMS) versus ER-2 in situ observations., *J. Geophys. Res.*, *108*, 8324, doi:10.1029/2001JD000876, 2003b. 45, 51, 57, 62

Konopka, P., J.-U. Grooß, K. Hoppel, H.-M. Steinhorst, and R. Müller, Mixing and chemical ozone loss during and after the Antarctic polar vortex major warming in September 2002, *J. Atmos. Sci.*, *62*(3), 848–859, 2005a. 46

Konopka, P., G. Günther, D. S. McKenna, R. Müller, D. Offermann, R. Spang, and M. Riese, How homogeneous and isotropic is stratospheric mixing? comparison of CRISTA-1 observations with transport studies based on the Chemical Lagrangian Model of the Stratosphere (CLaMS), *Q. J. R. Meteorol. Soc.*, *131*(606), 565–579, doi:10.1256/qj.04.47, 2005b. 45

Konopka, P., et al., Mixing and ozone loss in the 1999-2000 Arctic vortex: Simulations with the 3-dimensional Chemical Lagrangian Model of the Stratosphere (CLaMS), *J. Geophys. Res.*, *109*, D02315, doi:10.1029/2003JD003792, 2004. 46, 50, 51, 52, 57, 60, 64

Krämer, M., et al., Intercomparison of stratospheric chemistry models under polar vortex conditions, *J. Atmos. Chem.*, *45*, 51–77, doi:10.1023/A:1024056026432, 2003. 45, 48

Labitzke, K., *Die Stratosphäre: Geschichte, Phänomene, Relevanz*, 174 pp., Springer Verlag, Berlin, Germany, 1999. 76

Lait, L. R., An alternative form for potential vorticity, *J. Atmos. Sci.*, *51*, 1754–1759, 1994. 17, 18, 77

Land, C., M. Ponater, R. Sausen, and E. Roeckner, The ECHAM4.L39(DLR) atmosphere GCM: Technical description and model climatology, *Forschungsbericht*, Deutsches Zentrum für Luft- und Raumfahrt e. V., 51170 Köln, Germany, 1999. 41

Landgraf, J., and P. J. Crutzen, An efficient method for online calculations of photolysis and heating rates, *J. Atmos. Sci.*, *55*, 863–878, 1998. 41, 50

Langematz, U., An estimate of the impact of observed ozone losses on stratospheric temperature, *Geophys. Res. Lett.*, *27*(14), 2077–2080, 2000. 36

Langematz, U., M. Kunze, K. Krüger, K. Labitzke, and G. L. Roff, Thermal and dynamical changes of the stratosphere since 1979 and their link to ozone and CO_2 changes, *J. Geophys. Res.*, *108*, 4027, doi:10.1029/2002JD002069, 2003. 6, 36

Lary, D. J., and J. A. Pyle, Diffuse radiation, twilight, and photochemistry - I, *J Atmos Chem*, *13*, 373–406, 1991. 49, 50, 63, 112

Lefèvre, F., F. Figarol, K. S. Carslaw, and T. Peter, The 1997 Arctic ozone depletion quantified from three-dimensional model simulations, *Geophys. Res. Lett.*, *25*, 2425–2428, 1998. 8, 60, 64

Logan, J. A., An analysis of ozonesonde data for the troposphere: Recommendations for testing 3-D models and development of a gridded climatology for tropospheric ozone, *J. Geophys. Res.*, *104*(D13), 16,115–16,150, doi:10.1029/1998JD100096, 1999. 14, 21

Lotze, H. K., B. Worm, M. Molis, and M. Wahl, Effects of Uv radiation and consumers on recruitment and succession of a marine macrobenthic community, *Mar. Ecol. Prog. Ser.*, *243*, 57–66, 2002. 22

Lukyanov, A. N., H. Nakane, and V. A. Yushkov, Lagrangian estimations of ozone loss in the

core and edge region of the Arctic polar vortex 1995/1996: Model results and observations, *J. Atmos. Chem.*, *44*, 191–210, 2003. 60

Lunkeit, F., R. Sausen, and J. M. Oberhuber, Climate simulations with the global coupled atmosphere-ocean model ECHAM2/OPYC, *Clim. Dyn.*, *12*(3), 195–212, doi: 10.1007/s003820050103, 1996. 40

Mann, G. W., S. Davies, K. S. Carslaw, M. P. Chipperfield, and J. Kettleborough, Polar vortex concentricity as a controlling factor in Arctic denitrification, *J. Geophys. Res.*, *107*, 4663, doi:10.1029/2002JD002102, 2002. 30, 38

Mann, M. E., R. S. Bradley, and M. K. Hughes, Global-scale temperature patterns and climate forcing over the past six centuries, *Nature*, *392*, 779–787, doi:10.1038/33859, 1998. 31

Mann, M. E., R. S. Bradley, and M. K. Hughes, corrigendum: Global-scale temperature patterns and climate forcing over the past six centuries, *Nature*, *430*, 105, doi: 10.1038/nature02478, 2004. 31

Manney, G. L., R. W. Zurek, L. Froidevaux, J. W. Waters, A. O. O'Neill, and R. Swinbank, Lagrangian transport calculations using UARS data. Part II: Ozone, *J. Atmos. Sci.*, *52*, 3069–3081, 1995. 60

Manney, G. L., L. Froidevaux, J. W. Waters, M. L. Santee, W. G. Read, D. A. Flower, R. F. Jarnot, and R. W. Zurek, Arctic ozone depletion observed by UARS MLS during the 1994-95 winter, *Geophys. Res. Lett.*, *23*(1), 85–88, doi:10.1029/95GL03591, 1996. 19, 60

Manney, G. L., L. Froidevaux, M. L. Santee, R. W. Zurek, and J. W. Waters, MLS observations of Arctic ozone loss in 1996-97, *Geophys. Res. Lett.*, *24*(22), 2697–2700, doi: 10.1029/97GL52827, 1997. 60

Manney, G. L., et al., Chemical depletion of ozone in the Arctic lower stratosphere during winter 1992-93, *Nature*, *370*, 429–434, 1994. 60

Manney, G. L., et al., Lagrangian transport calculations using UARS data; Passive tracers, *J. Atmos. Sci.*, *52*, 3049–3068, 1995. 100

Manzini, E., and N. A. McFarlane, The effect of varying the source spectrum of a gravity wave parameterization in a middle atmosphere general circulation model, *J. Geophys. Res.*, *103*, 31,523–31,539, 1998. 40

McElroy, M. B., R. J. Salawitch, S. C. Wofsy, and J. A. Logan, Antarctic ozone: Reductions due to synergistic interactions of chlorine and bromine, *Nature*, *321*, 759–762, 1986. 4, 28

McKenna, D. S., J.-U. Grooß, G. Günther, P. Konopka, R. Müller, G. Carver, and Y. Sasano, A new Chemical Lagrangian Model of the Stratosphere (CLaMS): Part II Formulation of chemistry-scheme and initialisation, *J. Geophys. Res.*, *107*(D15), 4256, doi:10.1029/2000JD000113, 2002a. 9, 45, 48, 49, 50, 51, 57

McKenna, D. S., P. Konopka, J.-U. Grooß, G. Günther, R. Müller, R. Spang, D. Offermann, and Y. Orsolini, A new Chemical Lagrangian Model of the Stratosphere (CLaMS): Part I Formulation of advection and mixing, *J. Geophys. Res.*, *107*(D16), 4309, doi: 10.1029/2000JD000114, 2002b. 9, 45, 52, 64

Michelsen, H. A., G. L. Manney, M. R. Gunson, and R. Zander, Correlations of stratospheric

abundances of NO_y, O_3, N_2O, and CH_4 derived from ATMOS measurements, *J. Geophys. Res.*, *103*, 28,347–28,359, 1998. 61

Miller, M. J., T. N. Palmer, and R. Swinbank, Parameterization and influence of subgrid scale orography in general circulation and numerical weather prediction models, *Meteor. Atmos. Phys.*, *40*, 84–109, 1989. 40

Molina, L. T., and M. J. Molina, Production of Cl_2O_2 from the selfreaction of the ClO radical, *J. Phys. Chem.*, *91*, 433–436, 1987. 4, 28

Molina, M. J., and F. S. Rowland, Stratospheric sink for chlorofluoromethanes: Chlorine atom catalysed destruction of ozone, *Nature*, *249*, 810–812, 1974. 3, 26

Montzka, S. A., J. H. Butler, R. C. Myers, T. M. Thompson, T. H. Swanson, A. D. Clarke, L. T. Lock, and J. W. Elkins, Decline in the Tropospheric Abundance of Halogen from Halocarbons: Implications for Stratospheric Ozone Depletion, *Science*, *272*(5266), 1318–1322, 1996. 5, 33

Montzka, S. A., J. H. Butler, J. W. Elkins, T. M. Thompson, A. D. Clarke, and L. T. Lock, Present and future trends in the atmospheric burden of ozone-depleting halogens, *Nature*, *398*, 690–694, doi:10.1038/19499, 1999. 33

Morcrette, J.-J., Radiation and cloud radiative properties in the European Centre for Medium-Range Weather Forecasts forecasting system, *J. Geophys. Res.*, *96*(D5), 9121–9132, 1991. 40, 47

Müller, R., Die Chemie des Ozons in der Polaren Stratosphäre, Dissertation, FU Berlin, 1994. 8, 49

Müller, R., and G. Günther, A generalized form of Lait's modified potential vorticity, *J. Atmos. Sci.*, *60*, 2229–2237, 2003. 17

Müller, R., and G. Günther, Polytropic atmospheres and the scaling of potential vorticity, *Meteorol. Atmos. Phys.*, (online first), doi:10.1007/s00703-004-0087-6, 2004. 16, 17

Müller, R., P. J. Crutzen, H. Oelhaf, G. P. Adrian, T. v. Clarmann, A. Wegner, U. Schmidt, and D. Lary, Chlorine chemistry and the potential for ozone depletion in the Arctic stratosphere in the winter of 1991/92, *Geophys. Res. Lett.*, *21*, 1427–1430, 1994. 49

Müller, R., P. J. Crutzen, J.-U. Grooß, C. Brühl, J. M. Russel III, and A. F. Tuck, Chlorine activation and ozone depletion in the Arctic vortex: Observations by the Halogen Occultation Experiment on the Upper Atmosphere Research Satellite, *J. Geophys. Res.*, *101*, 12,531–12,554, 1996. 61, 64

Müller, R., P. J. Crutzen, J.-U. Grooß, C. Brühl, I. Russell, J. M., H. Gernandt, D. S. McKenna, and A. F. Tuck, Severe chemical ozone loss in the Arctic during the winter of 1995-96, *Nature*, *389*, 709–712, 1997. 60

Müller, R., U. Schmidt, A. Engel, D. S. McKenna, and M. H. Proffitt, The O_3/N_2O relationship from balloon-borne observations as a measure of Arctic ozone loss in 1991-1992, *Q. J. R. Meteorol. Soc.*, *127*, 1389–1412, 2001. 62

Müller, R., et al., Chlorine activation and chemical ozone loss deduced from HALOE and balloon measurements in the Arctic during the winter of 1999-2000, *J. Geophys. Res.*, *107*, 8302, doi:10.1029/2001JD001423, 2002. 62

Nakamura, N., Quantifying asymmetric wave breaking and two-way transport, *J. Atmos. Sci.*, *61*(22), 2735–2748, doi:10.1175/JAS3296.1, 2004. 19

Nash, E. R., P. A. Newman, J. E. Rosenfield, and M. R. Schoeberl, An objective determination of the polar vortex using Ertel's potential vorticity, *J. Geophys. Res.*, *101*, 9471–9478, 1996. 16, 17, 24, 53, 63, 77

Newman, S. J., S. Nicol, D. Ritz, and H. Marchant, Susceptibility of Antarctic krill (*Euphausia superba* Dana) to ultraviolet radiation, *Polar Biol.*, *22*(1), 50–55, doi:10.1007/s003000050389, 1999. 22

Oltmans, S. J., H. Vömel, D. J. Hofmann, K. H. Rosenlof, and D. Kley, Tropical convective outflow and near surface equivalent potential temperatures, *Geophys. Res. Lett.*, *27*(21), doi:10.1029/2000GL012133, 2000. 3, 6

Paeth, H., A. Hense, R. Glowienka-Hense, S. Voss, and U. Cubasch, The North Atlantic Oscillation as an indicator for greenhouse-gas induced regional climate change, *Clim. Dyn.*, *15*(12), 953–960, doi:10.1007/s00382005032, 1999. 37

Paeth, H., M. Latif, and A. Hense, Global SST influence on twentieth century NAO variability, *Clim. Dyn.*, *21*(1), 63–75, doi:10.1007/s00382-003-0318-4, 2003. 37

Peter, T., Microphysics and heterogeneous chemistry of polar stratospheric clouds, *Ann. Rev. Phys. Chem.*, *48*, 785–822, 1997. 28

Petit, J. R., et al., Climate and atmospheric history of the past 420,000 years from the Vostok ice core, Antarctica, *Nature*, *399*, 429–436, 1999. 2, 30

Plumb, R. A., Stratospheric transport, *J. Meteorol. Soc. Jpn.*, *80*(4B), 793–809, 2002. 14, 18

Plumb, R. A., D. W. Waugh, and M. P. Chipperfield, The effect of mixing on tracer relationships in the polar vortices, *J. Geophys. Res.*, *105*, 10,047–10,062, 2000. 61, 62

Popp, P. J., et al., Severe and extensive denitrification in the 1999-2000 Arctic winter stratosphere, *Geophys. Res. Lett.*, *28*, 2875–2878, doi:10.1029/2001GL013132, 2001. 83, 84

Prather, P., M., F. S. R. Midgley, and R. Stolarski, The ozone layer: the road not taken, *Nature*, *381*, 551–554, 1996. 9, 101

Preparata, F. P., and M. Shamos, *Computational Geometry. An Introduction*, Springer-Verlag, 1985. 51

Proffitt, M. H., J. J. Margitan, K. K. Kelly, M. Loewenstein, J. R. Podolske, and K. R. Chan, Ozone loss in the Arctic polar vortex inferred from high altitude aircraft measurements, *Nature*, *347*, 31–36, 1990. 60

Proffitt, M. H., K. Aikin, J. J. Margitan, M. Loewenstein, J. R. Podolske, A. Weaver, K. R. Chan, H. Fast, and J. W. Elkins, Ozone loss inside the northern polar vortex during the 1991-1992 winter, *Science*, *261*, 1150–1154, 1993. 62

Ramaswamy, V., O. Boucher, J. Haigh, D. Hauglustaine, J. Haywood, G. Myhre, T. Takajima, G. Y. Shi, and S. Solomon, Radiative forcing of climate change, in Houghton et al. (2001), chap. 6, 2001. 34, 35, 37

Randel, W. J., F. Wu, J. M. Russell, and J. Waters, Space-time patterns of trends in stratospheric constituents derived from UARS measurements, *J. Geophys. Res.*, *104*, 3711–3727, 1999. 19

Randel, W. J., F. Wu, S. J. Oltmans, K. Rosenlof, and G. E. Nodoluha, Interannual changes of stratospheric water vapor and correlations with tropical tropopause temperatures, *J. Atmos. Sci.*, *61*, 2133–2148, 2004. 6

Randeniya, L. K., P. F. Vohralik, and I. Plumb, Stratospheric ozone depletion at northern midlatitudes in the 21st century: The importance of future concentrations of greenhouse gases nitrous oxide and methane, *Geophys. Res. Lett.*, *29*(4), 1051, doi:10.1029/2001GL014295, 2002. 37

Ray, E. A., F. L. Moore, J. W. Elkins, D. F. Hurst, P. A. Romashkin, G. S. Dutton, and D. W. Fahey, Descent and mixing in the 1999-2000 northern polar vortex inferred from in situ tracer measurements, *J. Geophys. Res.*, *107*, 8285, doi:10.1029/2001JD000961, 2002. 93

Revelle, R., and H. Suess, Carbon dioxide exchange between the atmosphere and the ocean and the question of an increase of atmospheric CO_2 during the past decades, *Tellus*, *9*, 18–27, 1957. 2, 32

Rex, M., Der Ozonabbau in der arktischen Stratosphäre: Ergebnisse einer neuen Meßstrategie (Match), Dissertation, Universität Berlin, 1997. 77

Rex, M., R. J. Salawitch, M. L. Santee, J. W. Waters, K. Hoppel, and R. Bevilacqua, On the unexplained stratospheric ozone losses during cold Arctic Januaries, *Geophys. Res. Lett.*, *30*(1), 1010, doi:10.1029/2002GL016008, 2003. 64

Rex, M., R. J. Salawitch, P. von der Gathen, N. R. Harris, M. P. Chipperfield, and B. Naujokat, Arctic ozone loss and climate change, *Geophys. Res. Lett.*, *31*, L04116, doi:10.1029/2003GL018844, 2004. 28, 38, 79, 104, 105, 106, 107

Rex, M., et al., Prolonged stratospheric ozone loss in the 1995/96 Arctic winter, *Nature*, *389*, 835–838, doi:10.1038/39849, 1997. 60

Rex, M., et al., In situ measurements of stratospheric ozone depletion rates in the Arctic winter 1991/92: A Lagrangian approach, *J. Geophys. Res.*, *103*, 5843–5853, 1998. 17, 18

Rex, M., et al., Subsidence, mixing and denitrification of Arctic polar vortex air measured during POLARIS, *J. Geophys. Res.*, *104*, 26,611–26,623, 1999. 62

Rex, M., et al., Chemical depletion of Arctic ozone in winter 1999/2000, *J. Geophys. Res.*, *107*, 8276, doi:10.1029/2001JD000533, 2002. 60

Richard, E. C., et al., Severe chemical ozone loss in the Arctic polar vortex during winter 1999-2000 inferred from in-situ airborne measurements, *Geophys. Res. Lett.*, *28*(11), 2197–2000, 2001. 60

Röckmann, T., J.-U. Grooß, and R. Müller, The impact of anthropogenic chlorine emissions, stratospheric ozone change and chemical feedbacks on stratospheric water, *Atmos. Chem. Phys.*, *4*, 693–699, sref:1680-7324/acp/2004-4-693, 2004. 6

Roeckner, E., et al., Simulation of the present-day climate with the ECHAM model: Impact of model physics and resolution, *Report 93*, MPI für Meteorologie, Hamburg, 1992. 40

Roeckner, E., et al., The atmospheric general circulation model ECHAM-4: Model description and simulation of present-day climate, *Report 218*, MPI für Meteorologie, Hamburg, 1996. 40

Roeckner, E., et al., The atmospheric general circulation model ECHAM5 part I: Model decription, *Report 349*, MPI für Meteorologie, Hamburg, 2003. 40

Roeckner, E., et al., The atmospheric general circulation model ECHAM5 part II: Sensitivity of simulated climate to horizontal and vertical resolution, *Report 354*, MPI für Meteorologie, Hamburg, 2004. 40

Rowlands, I. H., The fourth meeting of the parties to the Montreal Protocol: Report and reflection, *Environment*, *35*, 25–34, 1993. 4, 5

Ruddiman, W. F., The anthropogenic greenhouse era began thousands of years ago, *Clim. Change*, *61*, 261–293, doi:10.1023/B:CLIM.0000004577.17928.fa, 2003. 2

Ruddiman, W. F., S. J. Vavrus, and J. E. Kutzbach, A test of the overdue-glaciation hypothesis, *Quat. Sci. Rev.*, *24*, 1–100, doi:10.1016/j.quascirev.2004.07.010, 2005. 3

Rummukainen, M., B. Knudsen, and P. von der Gathen, Dynamical diagnostics of the edges of the polar vortices, *Ann. Geophys.*, *12*, 1114–1118, 1994. 16

Salawitch, R. J., D. K. Weisenstein, L. J. Kovalenko, C. E. Sioris, P. O. Wennberg, K. Chance, M. K. W. Ko, and C. A. McLinden, Sensitivity of ozone to bromine in the lower stratosphere, *Geophys. Res. Lett.*, *32*, L05811, doi:10.1029/2004GL021504, 2005. 54

Salawitch, R. J., et al., Chemical loss of ozone during the Arctic winter of 1999-2000: an analysis based on balloon-borne observations, *J. Geophys. Res.*, *107*(D20), 8269, doi:10.1029/2001JD000620, 2002. 61, 62, 93

Sander, R., A. Kerkweg, P. Jöckel, and J. Lelieveld, Technical note: The new comprehensive atmospheric chemistry module MECCA, *Atmos. Chem. Phys.*, *5*, 445–450, sref:1680-7324/acp/2005-5-445, 2005. 109

Sander, S. P., et al., Chemical kinetics and photochemical data for use in stratospheric modeling, Supplement to evaluation 12: Update of key reactions, JPL Publication 00-3, 2000a. 114

Sander, S. P., et al., Chemical kinetics and photochemical data for use in stratospheric modeling, Supplement to evaluation 12: Update of key reactions, JPL Publication 00-3, 2000b. 50

Sander, S. P., et al., Chemical kinetics and photochemical data for use in atmospheric studies, Evaluation number 14, JPL Publication 02-25, 2003. 24, 25, 48, 50, 114

Sankey, D., and T. G. Shepherd, Correlations of long-lived chemical species in a middle atmosphere general circulation model, *J. Geophys. Res.*, *108*(D16), 4494, doi:10.1029/2002JD002799, 2003. 9, 61

Schmidt, H., and G. P. Brasseur, Simulation of the mesospheric ozone response to natural and anthropogenic climate variability, in *Proceedings of the Quadrennial Ozone symposium, Kos, Greece*, 2004. 40

Schmidt, H., et al., The HAMMONIA chemistry climate model: Sensitivity of the mesopause region to the 11-year solar cycle and CO_2 doubling, in preparation, 2005. 40

Schnadt, C., Untersuchung der zeitlichen Entwicklung der stratosphärischen Chemie mit einem interaktiv gekoppelten Klima-Chemie-Modell, Dissertation, Universität München, Institut für Physik der Atmosphäre des DLR, Oberpfaffenhofen, 2001. 40, 42, 43, 44, 58, 64, 67, 74

Schnadt, C., and M. Dameris, Relationship between North Atlantic Oscillation changes and stratospheric ozone recovery in the Northern Hemisphere in a chemistry-climate model, *Geophys. Res. Lett.*, *30*, 1487, doi:10.1029/2003GL017006, 2003. 20, 38, 74, 107, 108

Schnadt, C., M. Dameris, M. Ponater, R. Hein, V. Grewe, and B. Steil, Interaction of atmospheric chemistry and climate and its impact on stratospheric ozone, *Clim. Dyn.*, *18*, 501–517, 2002. 74

Sherwood, S. C., and A. E. Dessler, A model for transport across the tropical tropopause, *J. Atmos. Sci.*, *58*, 765–779, 2001. 13

Shindell, D. T., D. Rind, and P. Lonergan, Increased polar stratospheric ozone losses and delayed eventual recovery owing to increasing greenhouse-gas concentrations, *Nature*, *392*, 589–592, doi:10.1038/33385, 1998. 7, 8, 38

Shindell, D. T., R. L. Miller, G. A. Schmidt, and L. Pandolfo, Simulation of recent northern winter climate trends by greenhouse-gas forcing, *Nature*, *399*, 452–455, doi:10.1038/20905, 1999. 36, 37

Shine, K. P., et al., A comparison of model-simulated trends in stratospheric temperatures, *Q. J. R. Meteorol. Soc.*, *129*, 1565–1588, doi:10.1256/qj.02.186, 2003. 6, 41

Simmons, A. J., A. Untch, C. Jakob, P. Kållberg, and P. Unden, Stratospheric water vapour and tropical tropopause temperatures in ecmwf analyses and multi-year simulations, *Q. J. R. Meteorol. Soc.*, *125*, 353 – 386, 1999. 38

Sinnhuber, B.-M., et al., Large loss of total ozone during the Arctic winter of 1999/2000, *Geophys. Res. Lett.*, *27*, 3473–3476, 2000. 8, 60, 64

Solomon, S., Stratospheric ozone depletion: A review of concepts and history, *Rev. Geophys.*, *37*(3), 275–316, 1999. 28

Solomon, S., The hole truth, *Nature*, *427*, 289–291, doi:10.1038/427289a, 2004. 1

Solomon, S., R. R. Garcia, F. S. Rowland, and D. J. Wuebbles, On the depletion of Antarctic ozone, *Nature*, *321*, 755–758, 1986. 4

Soret, M. J.-L., Sur les relations volumetriques de l'ozone, *Comptes rendus Acad. Sciences*, *57*, 604–609, 1863. 21

SPARC, *Water vapor assessement (WAVAS): 2000*, SPARC Report No. 2, WMO, edited by D. Kley and J. M. Russell, 2000. 6

Steil, B., Modellierung der Chemie der globalen Strato- und Troposphäre mit einem dreidimensionalen Zirkulationsmodell, Dissertation, Universität Hamburg, 1998. 41, 42, 49

Steil, B., M. Dameris, C. Brühl, P. J. Crutzen, V. Grewe, M. Ponater, and R. Sausen, Development of a chemistry module for GCMs: first results of a multiannual integration, *Ann. Geophys.*, *16*, 205–228, sref:1432-0576/ag/1998-16-205, 1998. 41, 50

Steinhorst, H.-M., P. Konopka, G. Günther, and R. Müller, How permeable is the edge of the Arctic vortex - Model studies of the winter 1999-2000, *J. Geophys. Res.*, *110*, D06105, doi:10.1029/2004JD005268, 2005. 17

Sterin, A. M., Tropospheric and lower stratospheric temperature anomalies based on global radiosonde network data., in *Trends Online: A Compendium of Data on Global Change.*, Carbon Dioxide Information Analysis Center, Oak Ridge National Laboratory, U.S. Department of Energy, Oak Ridge, Tennessee, U.S.A., http://cdiac.esd.ornl.gov/trends/trends.htm, 2001. 36

Stimpfle, R. M., First measurements of ClOOCl in the stratosphere: The coupling of ClOOCl and ClO in the Arctic polar vortex, *J. Geophys. Res.*, *109*, D03301, doi: 10.1029/2003JD003811, 2004. 96

Stohl, A., Computations, accuracy and applications of trajectories – a review and bibliography, *Atmos. Environ.*, *32*(6), 947–966, 1998. 46

Stolarski, R. S., and R. J. Cicerone, Stratospheric chlorine: A possible sink of ozone, *Canad.*

J. Chem., *52*, 1610–1615, 1974. 26

Stolarski, R. S., A. J. Krueger, M. R. Schoeberl, R. D. McPeters, P. A. Newman, and J. C. Alpert, Nimbus 7 satellite measurements of the springtime Antarctic ozone decrease, *Nature*, *322*, 808–811, 1986. 4, 23, 65

Suess, E. M., et al., Gas hydrate destabilization: enhanced dewatering, benthic material turnover, and large methane plumes at the Cascadia convergent margin, *Earth Planet. Sci. Lett.*, *170*, 1–15, 1999. 37

Sutton, R. T., H. Maclean, R. Swinbank, A. O'Neill, and F. W. Taylor, High-resolution stratospheric tracer fields estimated from satellite observations using Lagrangian trajectory calculations, *J. Atmos. Sci.*, *51*, 2995–3005, 1994. 48

Tabazadeh, A., R. P. Turco, K. Drdla, M. Z. Jacobson, and O. B. Toon, A study of type I polar stratospheric cloud formation, *Geophys. Res. Lett.*, *21*, 1619–1622, 1994. 27

Terao, Y., Y. Sasano, H. Nakajima, H. L. Tanaka, and T. Yasunari, Stratospheric ozone loss in the 1996/1997 Arctic winter: Evaluation based on multiple trajectory analysis for double-sounded air parcels by ILAS, *J. Geophys. Res.*, *107*(D24), 8210, doi: 10.1029/2001JD000615, 2002. 60

Tett, S. F. B., J. F. B. Mitchell, D. E. Parker, and M. R. Allen, Human influence on the atmospheric vertical temperature structure: Detection and observations, *Science*, *274*(5290), 1170–1173, doi:10.1126/science.274.5290.1170, 1996. 36

Thejll, P., B. Christiansen, and H. Gleisner, On correlations between the North Atlantic Oscillation, geopotential heights, and geomagnetic activity, *Geophys. Res. Lett.*, *30*(6), doi:10.1029/2002GL016598, 2003. 19

Thompson, D. W. J., and J. M. Wallace, The Arctic Oscillation signature in the wintertime geopotential height and temperature fields, *Geophys. Res. Lett.*, *25*(9), 1297–1300, doi: 10.1029/98GL00950, 1998. 19, 38

Tilmes, S., Chemical ozone loss in the Arctic polar stratosphere derived from satellite observations, Dissertation, Johann Wolfgang Goethe Universität, Frankfurt, 2003. 60

Tilmes, S., Chemical ozone loss in the arctic polar stratosphere, *Tech. rep.*, Institute for Chemistry and Dynamics of the Geosphere, Jülich, Germany, 2004. 83

Tilmes, S., R. Müller, J.-U. Grooß, and J. M. Russell, Ozone loss and chlorine activation in the Arctic winters 1991–2003 derived with the tracer-tracer correlations, *Atmos. Chem. Phys. Discuss.*, *4*, 2181–2213, sref:1680-7324/acp/2004-4-2181, 2004a. 9

Tilmes, S., R. Müller, J.-U. Grooß, and J. M. Russell, Ozone loss and chlorine activation in the Arctic winters 1991–2003 derived with the tracer-tracer correlations, *Atmos. Chem. Phys.*, *4*(8), 2181–2213, sref:1680-7324/acp/2004-4-2181, 2004b. 38, 60, 61, 62, 106

Toon, O. B., P. Hamil, R. P. Turco, and J. Pinto, Condensation of HNO_3 and HCl in winter polar stratospheres, *Geophys. Res. Lett.*, *13*, 1284–1287, 1986. 4

TOPOZ III, *Towards the Prediction of Stratospheric Ozone (TOPOZ III) —Scientific Report*, edited by W. Kouker et al., EC Contract No: EVK2-CT-2001-00102, 2005. 105, 106

Tyndall, J., On the absorption and radiation of heat by gases and vapours, *Philosophical Magazine and Journal of Science*, *22*(146), 169–94, 273–85, 1861. 2

Ulbrich, U., and M. Christoph, A shift of the NAO and increasing storm track activity

over Europe due to anthropogenic greenhouse gas forcing, *Clim. Dyn.*, *15*(7), 551–559, doi:10.1007/s003820050299, 1999. 37, 38

UNEP, *Vienna Convention for the Protection of the Ozone Layer*, United Nations Environmental Programme, Nairobi, Kenya, 1985. 3, 4

UNEP, *Montreal Protocol on substances that deplete the ozone layer*, United Nations Environmental Programme, Nairobi, Kenya, 1987. 4

UNEP, United Nations Environment Programme and Environmental Effects Assessment Panel. Environmental effects of ozone depletion and its interactions with climate change: Progress report, 2004, *Photochem. Photobiol. Sci.*, *4*(2), 177–184, doi:10.1039/b418650h, 2005. 109

UNFCCC, *Framework Convention on Climate Change*, United Nations, 1992. 1, 2

UNFCCC, *Kyoto Protocol to the Framework Convention on Climate Change*, United Nations, 1997. 3

von der Gathen, P., et al., Observational evidence for chemical ozone depletion over the Arctic in winter 1991-92, *Nature*, *375*, 131–134, doi:10.1023/A:1010607521870, 1995. 60

von Hobe, M., J.-U. Grooß, R. Müller, S. Hrechanyy, U. Winkler, and F. Stroh, A re-evaluation of the ClO/Cl_2O_2 equilibrium constant based on stratospheric in-situ observations, *Atmos. Chem. Phys.*, *5*, 693–702, sref:1680-7324/acp/2005-5-693, 2005. 28

Waibel, A. E., et al., Arctic ozone loss due to denitrification, *Science*, *283*, 2064–2069, 1999. 30, 58, 84, 96

Walker, G. T., and E. W. Bliss, World weather, V, *Mem. Royal Meteor. Soc.*, *4*, 53–84, 1932. 19

Waple, A. M., et al., Climate assessment for 2001, *Bull. Am. Meteorol. Soc.*, doi:10.1175/1520-0477(2002)083¡0938:CAF¿2.3.CO;2, 2002. 34, 36

Waugh, D. W., and W. J. Randel, Climatology of Arctic and Antarctic polar vortices using elliptical diagnostics, *J. Atmos. Sci.*, *56*, 1594–1613, 1999. 6

Weiss, A. K., J. Staehelin, C. Appenzeller, and N. R. P. Harris, Chemical and dynamical contributions to ozone profile trends of the Payerne (Switzerland) balloon soundings, *J. Geophys. Res.*, *106*, 22,685–22,694, 2001. 3

Wells, N., *The Atmosphere and Ocean: a physical introduction*, second ed., 404 pp., John Wiley and Sons, 1997. 11

Williamson, D. L., and P. J. Rasch, Water vapour transport in the NCAR CCM2, *Tellus A*, *46*, 34–51, 1994. 40

WMO, *Scientific assessment of ozone depletion: 1989*, Report No. 20, Geneva, Switzerland, 1990. 4, 22

WMO, *Scientific assessment of ozone depletion: 1991*, Report No. 25, Geneva, Switzerland, 1992. 19

WMO, *Scientific assessment of ozone depletion: 1994*, Report No. 37, Geneva, Switzerland, 1995. 33, 90

WMO, *Scientific assessment of ozone depletion: 1998*, Report No. 44, Geneva, Switzerland, 1999. 6, 42, 51

WMO, *Scientific assessment of ozone depletion: 2002*, Report No. 47, Geneva, Switzerland,

2003. 4, 5, 6, 8, 20, 22, 23, 31, 33, 34, 37, 39, 51, 54, 67, 73, 75, 107, 108

Wordsworth (Ed.), *Dictionary of science and technology*, 1008 pp., Wordsworth Editions Ltd, Cumberland House, Herfordshire, UK, 1995. 30

Zhong, W., and J. D. Haigh, Improved broadband emissivity parameterization for water vapor cooling rate calculations, *J. Atmos. Sci.*, *52*(1), 124–138, 1995. 47, 56

Zhou, X. L., M. A. Geller, and M. H. Zhang, Cooling trend of the tropical cold point tropopause temperatures and its implications, *J. Geophys. Res.*, *106*(D2), 1511–1522, 2001. 6, 38

Acknowledgements

This thesis was prepared at the Institut für Chemie und Dynamik der Geosphäre: Stratosphäre (ICG-1) at Forschungszentrum Jülich GmbH. The research centre provides an excellent infrastructure, for example, ample computing power and facilities to handle the large data sets necessary for this work. A wide spectrum of electronic journals and original works of the 19th century can be rapidly accessed through the centre's library service.

At ICG-1 I found a productive and helpful working environment; Dr. Gebhard Günther, Dr. Jens-Uwe Grooß, and Dr. Paul Konopka of the CLaMS group demonstrate how to do excellent science based on individual aspirations and teamwork thinking. They were open to the many questions that I posed and technical issues I encountered with the CLaMS model; they always took the time to answer my requests thoughtfully and skillfully. I am especially grateful to my supervisor, Dr. Rolf Müller, who gave me the scientific freedom to investigate those issues that I found most intriguing and at the same time provided me with his professional guidance to not lose the plot of climate chemistry interactions.

I appreciate the commitment of ICG-1's head of department Dr. Martin Riese towards my fellow doctoral students and me. The 'Jülich model' —with Dr. Riese being head of ICG-1 and at the same time holding a professorship at the Bergische Universität Wuppertal— made it easy to conduct my thesis at the research centre and be a doctoral candidate at the university. I thank all my examiners, foremost Dr. Riese and Dr. Martin Dameris, and members of the Bergische Universität Wuppertal for their willingness to review this thesis.

The E39C climate model data were kindly provided by Dr. Dameris' group at Deutsches Zentrum für Luft- und Raumfahrt (DLR) Oberpfaffenhofen. Dr. Fabian Mager worked especially hard to retrieve any data set I requested from the archives and preprocess them for my ease of use. This thesis was conducted in the framework of the KODYACS/LAVERO projects in AFO2000. Several colleagues in this project contributed to my work with their instructive comments during workshops and discussions for the project reports.

During my thesis, I took many opportunities to participate in international conferences. At these conferences, I learned to put a face to the numerous famous names that I kept reading during my bibliographic research. I am grateful for inspiring discussions and encounters, especially with Dr. Susan Solomon, of the National Oceanic and Atmospheric Administration's Aeronomy Laboratory, and Dr. Darrin Toohey, of the University of Colorado.

I benefited greatly from international efforts to promote young scientists. My thanks go to the Third World Academy of Sciences (TWAS), the International Geosphere Biosphere Program (IGBP), the World Meteorological Organisation (WMO) and Stratospheric Processes And their Role in Climate (SPARC) for enabling me to participate in the 1st Young Scientists' Conference on Climate Change in Trieste, the 8th International Conference on Atmospheric Chemistry in Christchurch, and the 3rd SPARC Assembly held in Victoria.

There are those who kept me on track by imposing on me the ritual coffee break: thank

you for your companionship and life support. Especially, I would like to thank Dr. Stefan Bausch, my patient roommate, who never complained about my hammering away on the keyboard; I'll keep my fingers crossed for him. Thanks to Reimar Bauer, Verena Cals, and Nicole Thomas for programming support, data visualisation, Wikis and the like.

Those passages that stray away from stratospheric ozone in this thesis I blame on Dr. Kai Wirtz of Carl von Ossietzky Universität Oldenburg (now at GKSS research centre). As a coauthor, personal mentor and friend he encourages me to think beyond the usual and to cross disciplinary frontiers. He taught me the power and beauty of mathematical models.

At all times, and especially during the write-up of this thesis, my wife Daniela encouraged me to push on beyond the hours on good days and consoled me when I came home frustrated on bad ones. Thank you, Daniela, for the support you gave me; I should have had been the one to support you when our twins deprived you of your sleep and well-being.